UNIVERSITÀ DEGLI STUDI DELL'AQUILA
DIPARTIMENTO DI INGEGNERIA INDUSTRIALE E DELL'INFORMAZIONE E DI ECONOMIA

Dottorato di Ricerca in Ingegneria Industriale e dell'Informazione

Curriculum in Ingegneria Elettronica

XXXII ciclo

RF ELECTROMAGNETIC, THERMAL AND BIOMECHANICAL ENERGY HARVESTING CIRCUITS AND SYSTEMS FOR AUTONOMOUS SENSORS AND BIOMEDICAL WEARABLES

SSD ING-INF/01

Dottorando

Alfiero Leoni

Coordinatore del corso

Prof. Giuseppe Ferri

Supervisor

Prof. Vincenzo Stornelli

A.A. 2018/2019

This page is left blank intentionally

This page is left blank intentionally

Keywords

Antenna;
autonomous device;
batteries;
biomechanics;
biomedical;
electronics;
electromagnetics;
energy harvesting;
low-power;
piezoelectric;
radiofrequency;
sensor;
thermoelectric;
wearable;
wireless sensor node.

Abstract

In recent years, the development of electronics and information technology can be considered among the protagonists of social growth and technological progress, now essential for everyday life. The growing number of applications that require global connectivity is going hand in hand with the increasing demand for portable devices, such as in the IoT (Internet of Things) environment, for the distributed monitoring of environmental parameters, the use of wearable devices for human well-being and health or for sports and leisure activities. These devices need a portable and long-lasting source of energy, reliable over time to guarantee prolonged self-sufficiency as much as possible. Historically, batteries have always been considered the only, indispensable energy source in applications for mobile devices, embedded systems, and remote systems; the use of batteries is, however, constraining for many factors, first of all, the limited capacity to supply energy over time, with consequent need for maintenance for replacement or recharging. Although great strides have recently been made on the development of ever more efficient batteries, both in terms of materials and process, and new electronic technologies are moving towards reducing consumption, to date the use of batteries is still limiting in terms of energy supply over time, for various portable applications. Moreover, they constitute a real problem of environmental impact, being generally composed of toxic and highly polluting materials, which also make their disposal difficult. In this scenario, the activity of this dissertation focuses on the research and development of energy recovery systems from alternative sources, with reduced environmental impact, which can guarantee potentially unlimited autonomy for low-power portable devices, or standalone autonomous sensors, together with eco-sustainability. In particular, the research carried out focuses on the design and implementation of energy harvesting (EH) systems, single-source or multi-source, for the energy support of wearable devices in the biomedical field and for autonomous sensors used in wireless networks, for example for the widespread and distributed monitoring of the environment.

After the introduction to the topic, a chapter dedicated to the review of the literature and the state of the art follows. This step is fundamental, as in any research activity, to identify the various existing techniques as well as the materials used for energy recovery and, moreover, it is fundamental to understand the current problems

and limitations that require further analysis and in-depth studies. From this initial review, the main circuit blocks constituting the energy processing chain have been identified and analyzed.

Many of these materials and methodologies have already been used, in the past and present days, to implement devices such as sensors or communication systems, where the principle that converts the physical quantity into an electrical one is optimized to maximize the signal voltage or current; the latter is generated for the purpose of measurement and evaluation in metrology, while further measures are required to maximize power conversion. The review also covered the analysis of alternative non-standard energy sources, such as, for example, the energy generated by the human body in its daily activities or the energy spread in the surrounding environment, mainly urban, by RF electromagnetic fields for telecommunication systems. The study of the literature was conducted a thorough bibliometric analysis of the main diffusion media for electronic and energy engineering, using online search engines provided by publishers of important international journals and transactions such as IEEE Xplore, Elsevier, Wiley, Springer, and others, or through communication channels and direct confrontation between engineers and researchers working in the field, such as participation in national and international conferences or workshops.

The literature review is followed by the author's contributions to RF electromagnetic, Thermoelectric and biomechanical energy harvesting. In particular, chapter 3 is focused on novel design methods for multi-antenna, multi-band and multi-channel power harvester for autonomous sensors and wearables, as well as practical considerations about matching network and antenna design for RF energy harvesting in the field of biomedical applications. Following, chapter 4 introduces the research works centered on thermoelectric and biomechanical energy harvesting. Specifically, the analysis and design methods of the human body’s heat thermoelectric energy harvesting are investigated ad discussed, as well as the possibility to recover the body motion energy by means of piezoelectric transducers. An example of a multisource energy harvesting system design is also presented and discussed. Finally, chapter 5 summarizes the findings and original contributions of this research. Suggestions for further work in this area are then given.

Table of Contents

List of Figures

List of Tables

List of Abbreviations

ADC	Analog to Digital Converter
BLE	Bluetooth Low Energy
CAD	Computer-Aided Design
CMOS	Complementary Metal Oxide Semiconductor
CVD	Chemical Vapour Deposition
dB	Decibel
dBi	Decibel Isotropic
dBm	Decibel (referenced to milliWatt)
DC	Direct Current
DGS	Defected Ground Structure
DIP	Distal IP
DoF	Degree of Freedom
EBG	Electromagnetic Band Gap
EH	Energy Harvesting
EIRP	Effective Isotropic Radiated Power
EM	Electromagnetic
EMF	Electromotive Force
FEM	Finite Element Method
FM	Frequency Modulation
FOCV	Fractional Open-Circuit Voltage
FSCC	Fractional Short-Circuit Current
FSPL	free space path loss
GPS	Global Positioning System
HC	Hill Climbing

IC	Integrated Circuit
IMU	Inertial Measurement Unit
InC	Incremental Conductance
IoT	Internet of Things
IT	Information Technology
MCU	Microcontroller Unit
MEMS	Micro Electro-Mechanical Systems
MoM	Method of Moment
MOS	Metal-Oxide Semiconductor
MOSFET	Metal-Oxide Semiconductor Field-Effect Transistor
MPP	Maximum Power Point
MPPT	Maximum Power Point Tracking
NASA	National Aeronautics and Space Administration (USA)
NTC	Negative Temperature Coefficient
OC	Open Circuit
Op-Amp	Operational Amplifier
OTA	Operational Transconductance Amplifier
P&O	Perturb and Observe
PBG	Photonic Band Gap
PCB	Printed Circuit Board
PCE	Power Conversion Efficiency
PID	Proportional-Integral-Derivative (controller)
PIP	Proximal IP
PMU	Power Management Unit
PPG	Photoplethysmography
PVD	Plasma Vapour Deposition

PVDF	Polyvinylidene Fluoride
PWM	Pulse Width Modulation
PZT	Lead Zirconate Titanate
PZTc	Piezoceramics
PZTp	Piezopolymers
RF	Radiofrequency
RISC	Reduced Instruction Set Computing
RTG	Radioisotope Thermoelectric Generator
RX	Receive/Receiver/Reception
SCR	Silicon-Controlled Rectifier
sEMG	Surface Electromyography
SMD	Surface Mount Device
SoC	System on Chip
SPDT	Single Pole, Double Throw
TEG	Thermoelectric Generator
TX	Transmit/Transmitter/Transmission
VSWR	Voltage Standing Wave Ratio
WBAN	Wireless Body-Area Network
WSN	Wireless Sensor Network

Acknowledgments

First and foremost, I might want to express my true thankfulness and appreciation to my supervisor, Professor Vincenzo Stornelli, for his assistance and guidance during the past years. He has undoubtedly been the most important person forming my academic evolution: his in-depth knowledge, breadth of vision, dedication, enthusiasm, and unfailing energy are a constant source of inspiration for me. He did a great job of introducing me to the academic world, and I am greatly indebted to him for providing me with many opportunities.

I would also like to thank Professor Giuseppe Ferri for creating and coordinating this fantastic research group and for giving me valuable advice for my research activities and my studies in these years. Thanks also to Professor Leonardo Pantoli, whose expertise and competence have taught me a lot and have been of great help to me for the understanding and resolution of many difficulties.

A huge thanks goes to my dear friends and colleagues Gianluca Barile and Mirco Muttillo, without whom this experience would not have been the same at all, and with whom we shared emotions, joys and difficulties, never giving up and handing us strength one other.

Alessia, I would like to express thanks to you from the heart for having always been close to me, for your support in difficult moments and for having pushed me, with your determination, to always try to improve myself.

A special thanks goes to my family, for their sacrifices, for the unfailing and tireless support that has accompanied me over the years and that has allowed me to achieve my goals.

Chapter 1: Introduction

In recent years, the growing development of IT technologies has opened new growth perspectives that have brought radical changes in modern society, improving communications, productivity, and well-being. In this context, the incessant diffusion of portable devices [1] and autonomous sensors, used for the increase of the connectivity, the monitoring of environmental parameters, but also, in the industrial sphere, for intelligent control of the supply chain and warehouse activities have certainly played an important role [2]. Even in the biomedical field, the development of new wearable devices for monitoring and wireless transmission of vital parameters or for the interaction of the individual with the surrounding environment is now a very interesting area [3][4].

The electronic devices used for this type of application must certainly meet certain functional requirements, as well as energy consumption. This last aspect represents a crucial point of engineering design since the energy source supporting these systems must be portable. Historically, batteries have always been considered as the main means of energy supply for portable electronic devices, so that over the years more and more advanced technologies have been developed, which envisage different implementation techniques and the use of various materials, depending on the required performance. However, the use of batteries represents a limitation in several aspects: the limited capacity to supply energy over time, which therefore requires periodic maintenance, which is expressed in the recharging or replacement process, often difficult to complete if it is about autonomous devices, located in environments hostile to man [5]. Furthermore, the use of batteries increases the size and weight of the portable electronic systems that use them, reducing the comfort of wearable devices for biomedical applications [6]. Finally, the growing demand in the battery market, hand in hand with the spread of new generation portable devices, represents a threat to the environment, since both the manufacturing process and the disposal of batteries produce a high environmental impact, due to the toxic and polluting materials that are commonly used [7]. This last aspect constitutes a strong limitation in the use of batteries on wearable and, above all, implantable biomedical devices, where the toxicity of batteries can represent a threat to human health.

In such a context, the search for alternative sources of energy, renewable, at zero cost and with zero environmental impact is becoming a topic of research of great interest in recent years. The term Energy Harvesting (EH) or energy scavenging refers to a sector dedicated to the exploration of alternative energy sources, present in the surrounding environment, and techniques for recovering this energy, which is converted into electricity that can be used to support or even replace batteries, in various low-power applications. The purpose of the energy harvesting techniques and systems, once the target source has been identified, is to recover as much energy as possible, minimizing the losses due to the conversion and storage processes of the converted electricity.

There are several systems and the circuit architectures that can be adopted for the implementation of an energy harvesting device, also in relation to the type of energy source and therefore to the transduction system, at the top of the conversion chain[8]. Therefore, the choice of the energy source, the transduction process, as well as the design of the energy harvesting system should be carefully fulfilled, according to the requirements of the target portable or autonomous device. In this dissertation, the energy harvesting circuits and systems design and implementation methodologies for autonomous sensors and wearable devices will be investigated and discussed. In the following paragraphs, a deepening about wireless autonomous sensors and wearable biomedical devices is reported, to underline the energy harvesting requirements to be matched.

1.1 WIRELESS AUTONOMOUS SENSORS

The term Wireless Autonomous Sensors or Systems generally refers to a wide range of portable devices, which also includes smartphones, tablets, and consumer electronics devices. However, in this dissertation, I will refer to a series of devices that fall into this category, and that are used in industrial, domestic and environmental contexts, with the aim of monitoring a series of parameters of interest and sending them to a datalogger for the analysis and interpretation of delocalized data. These devices can operate stand-alone (for example a gas detection system in a house), or they can be organized in distributed networks, called Wireless Sensor Networks (WSNs), where each node of the network consists of a sensor or autonomous system [9]. The nodes of a WSN can communicate with each other through various algorithms so that the information can always reach the center of the network, used for

data collection. These distributed networks are commonly used in industry, for example for monitoring the vibrations of machinery in process, or for tracking products in a warehouse; to support the environment, the WSNs are used for the distributed monitoring of geological and environmental parameters, useful for the study of natural phenomena or the prevention of environmental disasters such as landslides or forest fires; at a domestic level, WSNs are applied in the capillary monitoring of information such as temperature, humidity, useful for managing smart systems for air conditioning, or they are used for structural monitoring of buildings [10]. The generic architecture of a wireless sensor node is described in Figure 1.1 and can transform the target physical quantity into an electrical quantity using a sensor. The converted information is appropriately conditioned, sampled and, eventually, simple processing operations are performed, before communicating the information wirelessly to another device or to a datalogger using a transceiver [11].

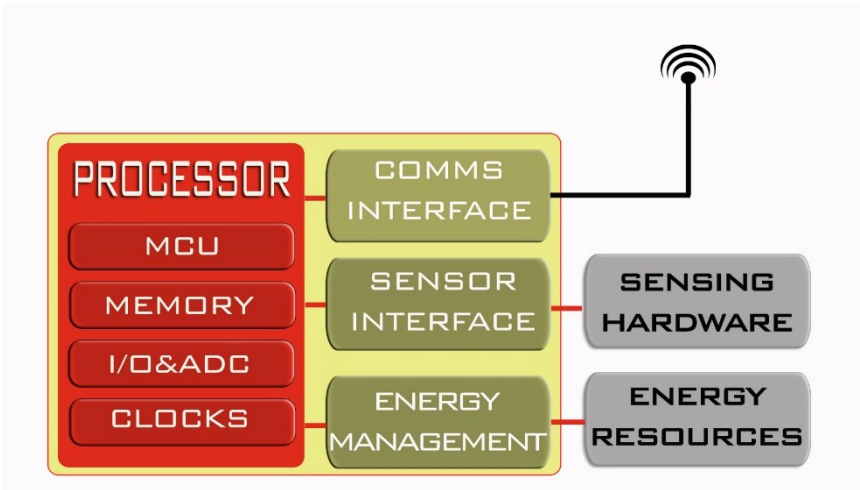

Figure 1.1 General architecture of a wireless sensor node.

In its minimal configuration, a wireless sensor node is equipped with a microcontroller, sensor, power supply system, RF transmitter and possibly a receiver, and an additional support circuit. The firmware, loaded inside the microcontroller, manages the simple operations of the node and is typically written using programming languages such as C / C ++ or ANSI C variants. Some specific operating systems have also been developed for sensor nodes, including TinyOS, an open-source operating system written in a variant of the C language called NesC, which has the particularity of managing the limited amount of memory of the target devices. Other known operating systems are ContikiOS, eMote, MANTIS, LiteOS or Nano-RK RTOS [12].

By definition, wireless sensor nodes must be autonomous and transmit information without relying on wires and wired connections. The same goes for the power supply, so they need a portable power source, like a battery. Nevertheless, the use of batteries constitutes a limitation to the development of this technology because it requires periodic maintenance, also due to wear because of the external exposure of high thermal gradients. The use of energy harvesting technologies, in this scenario, constitutes a valid alternative, offering the possibility of recovering energy from the surrounding environment, avoiding the use of batteries or, at least, prolonging their lifetime [13].

The estimate of the energy needed for the correct operation of a wireless autonomous sensor is, therefore, the first fundamental step to establish whether it is possible to replace the battery with an Energy Harvesting system and identify the energy sources from which to draw enough power. In recent years, although the increase in the functional complexity of modern IT devices has led to a gradual rise in average energy consumption, technological development and research have greatly contributed to the creation of integrated circuits (ICs) with a reduced energy consumption, making it possible to apply energy harvesting techniques to an increasing number of low-power portable devices [14]. Figure 1.2 shows the current scenario of average consumption for various electronic devices.

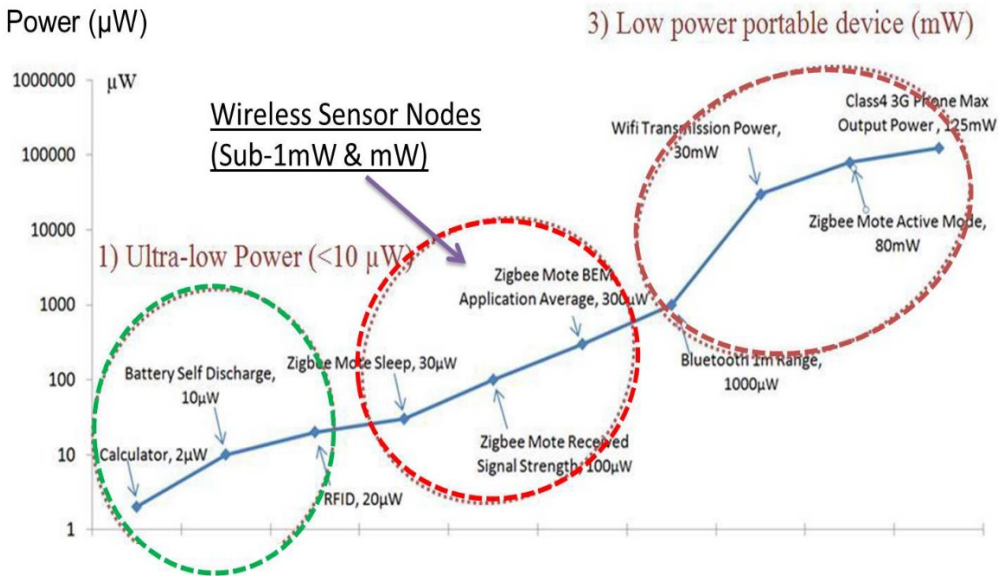

Figure 1.2 Typical power consumption scale of IT devices [15].

The energy consumption of a wireless sensor node is not constant but depends on the operation it is carrying out, or on the logical-functional state in which it is located. Generally speaking, for a node, it is possible to define four operational states, each of them with an estimated average consumption of energy: the sleep mode is the state in which the node is sleeping, reducing functionality and energy consumption to a minimum; in running mode the node is active, but it is not transmitting or receiving information; Radio TX and Radio RX are the states in which the system is transmitting or receiving. The last two states are those that involve a greater expenditure of energy, so the trend is to limit as much as possible the number of transmissions that the node performs over a day, in accordance with the application requirements. To understand the order of magnitude for the involved power consumptions, in Table 1.1 are reported four commercial wireless sensor nodes and the related power consumption, for each functional state. Looking at the table it can be noticed how the transition from sleep mode to running mode (nominal current draw) involves an increase in current of approximately one order of magnitude.

Node	**Bpart [16]**	**.NOW [17]**	**CoSeN [18]**	**FireFly [19]**
Year	2014	2012	2012	2012
Program Memory	256 KB	128/1024 KB	1K	4K
Supply Voltage	3.0 V	2.0 - 3.3 V	2.7 - 3.0 V	3.0 V
Sleep current	20 µA	360 µA	3.0 - 3.6 µA	0.2 µA
Nominal Current	1-5 mA	9 - 30 mA	0.6 - 0.7 mA	24.8 mA
TX Current	8 mA	16 mA	8.9 - 13.2 mA	18.8 - 19.7 mA
RX Current	8 mA	16 - 26 mA	10.4 - 14.4 mA	17.4 mA

Table 1.1 Features and power consumption of commercial wireless sensor nodes.

The amount of time spent by the node in sleep mode with respect to the time in which the node is in running mode, therefore, leads to considerable variations in the node's energy consumption [20]. By indicating *D* as the percentage of time in which the node is active, with respect to the total operating time, the reduction of the average energy consumption ER will be equal to:

$$ER = D\left(1 - \frac{P_{sleep}}{P_{runnig}}\right) \tag{1.1}$$

where P_{sleep} and P_{runnig} are the power consumptions in sleep and running mode, respectively.

The analysis of the energy consumption for a wireless sensor node in its four operating states, together with the estimate of how it operates over time and, therefore constitutes a crucial preliminary phase in the design of an energy harvesting system to support a wireless autonomous sensor.

1.2 WEARABLE DEVICES

The evolution of technology and the development of portable devices and autonomous sensors, described in the previous paragraph, has not only affected the industrial and environmental world, but also that of human health and personal wellness. In recent years, in fact, the technologies for wearable devices had strong growth and development among the population, thanks to the advantages and possibilities offered to improve the quality of life [21]. Wearable devices, in general, are miniaturized electronic systems equipped with one or more sensors, which can be integrated into accessories or clothes and are comfortable to wear [22]. Wearable devices include various categories of electronic devices (Figure 1.3), such as smartwatches, smart glasses, head-mounted displays, activity trackers, contact lenses, smart jewels, headbands, bracelets, etc. They can, therefore, be very complex systems, minicomputers capable of performing advanced functions, but there are also simpler, cheaper and smaller systems, which generally have the purpose of acquiring information on a particular activity performed by our body and send it to a data collection unit where this information is processed [22].

In its minimal form, like a normal wireless autonomous sensor, a wearable system is equipped with a small processing unit capable of acquiring information from

the sensors, eventually processing and sending it to a data collection device through a wireless communication module.

Figure 1.3 Representation of several wearable device categories.

The uses of a wearable device include:

- remote health monitoring of patients;
- disease-specific design, for the everyday monitoring of particular user conditions, such as sleep apnea, pulmonary disease, diabetes, cardiovascular diseases, mosquito-borne diseases, renal failure, skeletal system disease, etc.;
- heart and breath rate monitoring for clinical purposes or sports activities;
- position tracking;
- movements characterization;
- Calories burned;
- Blood pressure;
- Steps walked.

Many of these applications are implemented through wearable devices in the form of bracelets, accepted by users among the most comfortable wearables [23]. This wide range of features that a wearable system can perform involves the use of different types of sensors, which are increasingly miniaturized and low-power today. Among these, the most commonly used are GPS sensors, 3-axis accelerometers, gyroscopes, digital compass, PPG optical system, altimeter, ambient light sensor, vibration and motion sensor, mio continuous optical heart rate, etc.. [24].

Wearable devices, being portable, must necessarily be equipped with a wireless RF communication system for information transmission and a portable power source. Communication generally takes place at short range, given that most wearable devices are designed to transfer the information acquired to other, more advanced, portable systems, such as smartphones, capable of collecting large amounts of data and to perform complex calculations and elaborations to extract the desired information from the received data [25]. End-to-end communication between wearable and datalogger is not the only option; recently, similarly to the WSNs, the so-called Wearable Body Area Networks (WBANs) are being developed, i.e. smart communication networks made up of wearable devices interconnected with each other and with the data logging system [26]. This type of network has recently become an object of great interest, offering, for example, the possibility of distributed monitoring of patients inside a hospital, without the use of cables or wired interconnections [27]. Whether it is end-to-end communications or WBANs, the technologies and communication protocols commonly used must guarantee a short range of action but at the same time reducing power consumption, to minimize battery consumption and to extend the durability of such devices as much as possible [28]. Among these, the most commonly used are MICS, ANT, Zigbee, Bluetooth Low-Energy (BLE) and IEEE 802.15.6, whose main specifications and average consumption are summarized in Table 1.2.

The table highlights how consumption in RF transmission is certainly lower than that reported in the previous table 1.1 relating to wireless autonomous sensors since the communication range is reduced, as there is no need to cover large distances. However, the activity and transmission time for wearable devices, especially when applied to health monitoring, is certainly greater [29], so energy consumption over time once again represents a limitation in the design and use of this type of portable electronic equipment.

	IEEE 802.15.6 [30]	ANT [31]	MICS [31]	BLE (5.0) [31]	Zigbee [31]
Standard	IEEE 802.15.6	custom	FCC and ETSI	IEEE 802.15.1	IEEE 802.15.4
Frequency Band	402–405/420–450/863–870/902–928/950–956/2,360–2,400/2,400–2,483.5 MHz UWB: 3–10 GHz HBC: 16/27 MHz	2,4–2,524 GHz	402–405 MHz	2.4 – 2.4835 GHz	868 MHz/ 915 MHz/ 2.4 GHz
Data rate	57.5–485.7 Kbps UWB: 0.5–10 Mbps	-	Up to 500 Kbps	Up to 2 Mbps	20–250 Kbps
Range	2 m	Up to 10 m	2 m	> 100 m	30 m
RF transmission Power	0.1 μW	0.01-1 mW	25 μW	10 – 500 mW	30 mW

Table 1.2 Summary of communication technologies for wearables and WBANs.

In this scenario, energy harvesting technologies can again be of help, allowing you to increase battery life and even remove it, reducing the overall size and weight, with the aim of obtaining a wearable device totally powered by energy recovered from the surrounding environment.

decibels, wearable devices have the possibility to use the energy that the human body itself generates continuously through daily activities, so the recovery of this alternative energy would enable new prospects for developing and using these devices.

1.3 RESEARCH OBJECTIVES

Energy harvesting systems clearly play a key role in the development of wireless autonomous sensors and wearable devices, as highlighted in the previous sections 1.1

and 1.2, in order to improve the performance and above all the durability and usability of such portable devices. Exponential growth is expected for the market of sensors and microelectromechanical systems (MEMS), as key components in portable devices, from US $48.74 billion in 2018 to a forecast of US $122.83 billion by 2026 [32]. As a result, the possibility of being able to have a perpetual energy source that can guarantee potentially unlimited autonomy is surely a huge advantage, if we consider the enormous and growing diffusion on the market today of portable and autonomous devices applied to WSNs, to human health and well-being.

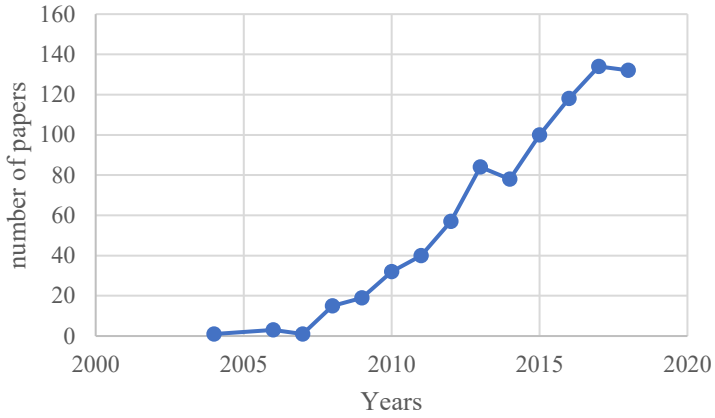

a)

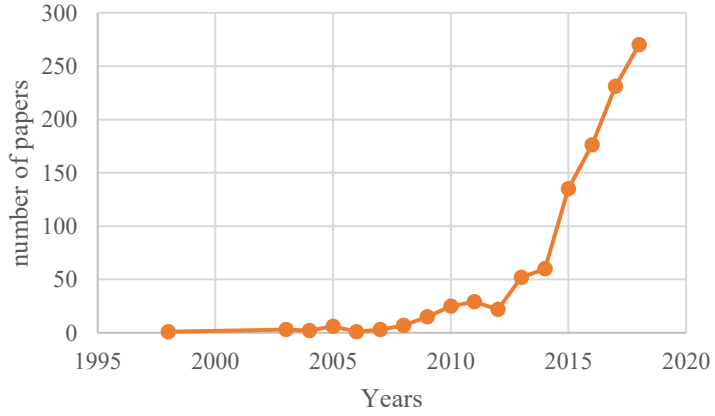

b)

Figure 1.4 Trend of the global research activity for a) energy harvesting for WSNs and b) energy harvesting for wearable devices. Source: Scopus.

However, the current solutions proposed are not yet able to guarantee these requirements and suffer from some drawbacks, so research in this area is of great interest and still finds ample space. Figure 1.4 shows the overall trend for the produced

scientific papers over the years about energy harvesting for autonomous sensors and WSNs (Figure 1.4a) and energy harvesting for wearable devices (Figure 1.4b). These analytic results have been extracted from the Scopus website, which is one of the most accredited scientific databases. By observing these graphs, it is clear that there is an increasing scientific interest in these topics.

The objectives of this research, therefore, aim to propose new solutions for energy harvesting systems, with particular reference to:

- identify and characterize alternative sources valid for low-power portable applications;
- determine the requirements, in terms of the amount of needed energy, that must be respected;
- analyze the limits of current technologies through a depth review of the state of the art in literature;
- identify new design strategies in order to overcome these limitations;
- design and develop prototypes through the use of the new proposed methodologies;
- characterize and analyze the performance of these devices, in order to validate the identified strategies and to compare the results with the literature.

1.4 THESIS OUTLINE

The structure of this text is divided into 5 chapters and the outline of each one is as follows:

- Chapter 1 sets the framework for this project and discusses the main objectives and goals.
- Chapter 2 gives a thorough literature review, identifying the current state of the art and the challenges that this thesis will address. Different applications and energy sources for harvesting are discussed before going further into the topics of this dissertation. Strategies radiofrequency, thermoelectric and biomechanical energy harvesting are laid out.

- Chapter 3 describes all the contributions achieved during Ph.D. studies about RF electromagnetic energy harvesting. Novel design methods for multi-antenna, multi-band and multi-channel power harvester for autonomous sensors and wearables are discussed, as well as practical considerations about matching network and antenna design for biomedical applications.
- Chapter 4 introduces the research works focused on thermoelectric and biomechanical energy harvesting. In particular, the analysis and design methods of the human body's heat thermoelectric energy harvesting are investigated ad discussed, as well as the possibility to recover the body motion energy by means of piezoelectric transducers. An example of a multisource energy harvesting system design is also presented.
- Chapter 5 summarises the findings and original contributions of this research. Suggestions for further work in this area are then given.

Chapter 2: Energy Harvesting Literature Review

Recent advances and state-of-the-art techniques and methodologies will be comprehensively reviewed and discussed in this chapter, in order to delineate various theoretical positions about current EH technologies, and from these to develop a conceptual framework for the generation of hypotheses and setting up the research questions.

Energy harvesting is known to be a viable solution to the problem of sustainability and the need for green power, to face the energy impact due to the growing diffusion of new generation portable low-power devices. This involves capturing ambient energy and converting it into electrical power, in order to recharge batteries or directly feed sensors or IT systems.

Category	Power Range	Description
Ultra-low-power	$\leq 1\ mW$	Energy consumption typically ranges from sub μW to few mW and includes appliances like smart homes, surveillance, environmental monitoring, and biomedical implantable devices
Low-power	$1\ mW - 1\ W$	Most of the wireless sensor node and IoT devices fall in this category, because of the RF transmission of the information
Medium power	$1\ W - 10\ W$	Portable devices with high computational capabilities and high power demand for communication and processing purposes, such as smartphones, some types of smartwatches, etc…
High power	$\geq 10\ W$	Appliances that are typically grid-connected, such as household devices or industrial machinery.

Table 2.1 Classification of power consumption for electric devices [33].

The EH capabilities to power portable devices, or at least to prolong the usability, is related to their power consumption level and to the energy available for the target source. Electric devices can be classified into four distinct categories, according to their power consumption [33]. Table 2.1 reports the estimated power range of each group since there is no standard definition that sets guidelines for this purpose. This dissertation will focus on ultra-low-power and low-power ranges.

While portable devices that fall in the medium power range can rely mainly on high-density energy sources, like solar or wind, the low-power and ultra-low-power devices can take advantage of a higher number of energy sources. A comparison of power sources for these power ranges is reported and summarized in Table 2.2, according to the information reported in [33], [34] and [35].

Power source	**Type**	**Typical Power Density**	**Transducer**
Wind	Mechanical	$28.5\,mW/cm^2$	Wind turbine
Solar	Electromagnetic	$15\,mW/cm^2$	Solar panels (outdoor)
Thermal	Thermal	$15\,\mu W/cm^3$	Thermoelectric generators (TEG)
Vibration	Mechanical	$145\,\mu W/cm^3$	Electromagnetic
	Mechanical	$330\,\mu W/cm^3$	Piezoelectric materials
	Mechanical	$50\,\mu W/cm^3$	Electrostatic
Microbial	Biochemical	$2.6\,\mu W/cm^2$	Microbial fuel cell
Indoor lights	Electromagnetic	$15\,mW/cm^2$	Solar panels (indoor)
Direct RF	Electromagnetic	$50\,mW/cm^2$	Antenna
Acoustic	Mechanical	$96\,\mu W/cm^3$	Microphones/Piezoelectric
Ambient RF	Electromagnetic	GSM: $0.1\ \mu W/cm^2$	Antenna
		WI-FI $1\ mW/cm^2$	

Table 2.2 A comparison of power sources for portable devices.

From this table, it can be noticed that the typical power density lever for ambient RF energy harvesting is quite low if compared with other sources like vibration,

thermal or solar. However, differing from other sources, the RF electromagnetic energy is widely available, and performance can be improved with a direct, dedicated energy source.

The block diagram of a typical EH system is depicted in Figure 2.1. The first part of the chain is the sensor, which has the role to convert the source energy into an electric signal with the highest possible efficiency. The acquired signal has to be processed, in order to be converted into a DC constant voltage level, therefore a suitable conversion circuit is needed. Consequently, a DC/DC voltage converter takes the input DC signal and adjusts the voltage amplitude, in accordance with the standard power supply value that is needed for the target application. Finally, the electric power can be stored into a proper energy storage element or can be directly sent to the system. The last part is accomplished with a Power Management Unit (PMU).

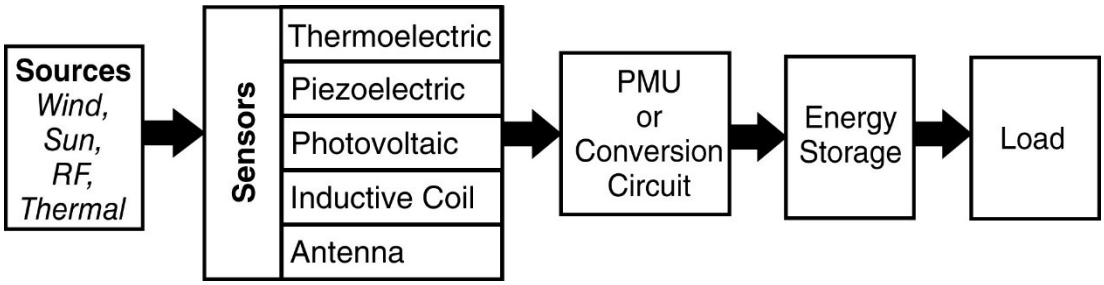

Figure 2.1 Typical block diagram of a generic energy harvesting system.

For low-power and ultra-low-power systems, the power is usually expressed either in μW/mW or in dBm. The latter is the acronym of decibel milliWatts and is computed from the power in milliWatts as follows [36]:

$$P_{dBm} = 10 \log_{10}(P_{mW}) \tag{2.1}$$

2.1 HISTORICAL BACKGROUND

Although energy harvesting is a very popular topic with an increasing interest in the recent days, its origins date back to the early eighteenth century, with the discovery of the thermoelectric effect. In 1826, Thomas Johann Seebeck observed that, by joining two different metal wires and heating one connection point while keeping cold the other joint, a current would flow through the closed-circuit [37].

The photovoltaic effect was observed for the first time by Edmund Becquerel during an experiment involving an electrolytic cell with metal electrodes [38]. After this, Charles Fritts in 1894 built the first solar cell, which was composed of selenium

covered with a thin layer of gold [39]. The full comprehension of the photovoltaic effect was achieved only with the formulation of quantum theory, in the earlies of the eighteenth century.

The electromagnetic energy harvesting sets its origins with the discovery of the electromagnetic induction by Joseph Henry, contemporarily with Michael Faraday in 1831 [40]. After that, Faraday built the first electromagnetic generator to convert kinetic energy into electricity by means of copper plates rotating between magnet poles [41].

For what regards the vibration energy harvesting, it dates back to the discovery of the piezoelectric phenomenon, that was experientially observed by Pierre and Jacques Curie in 1880. They found that some crystals would present a surface charge if mechanically stressed [42].

One of the first attempts in the field of radiofrequency (RF) electromagnetic energy harvesting is attributable to Nikola Tesla with his idea of wirelessly transmit energy. Although he was mainly famous for his advances in the alternating current systems, he also gave a contribution to the RF field, as he presented his high-frequency alternator device with a scientific publication in 1891 [43].

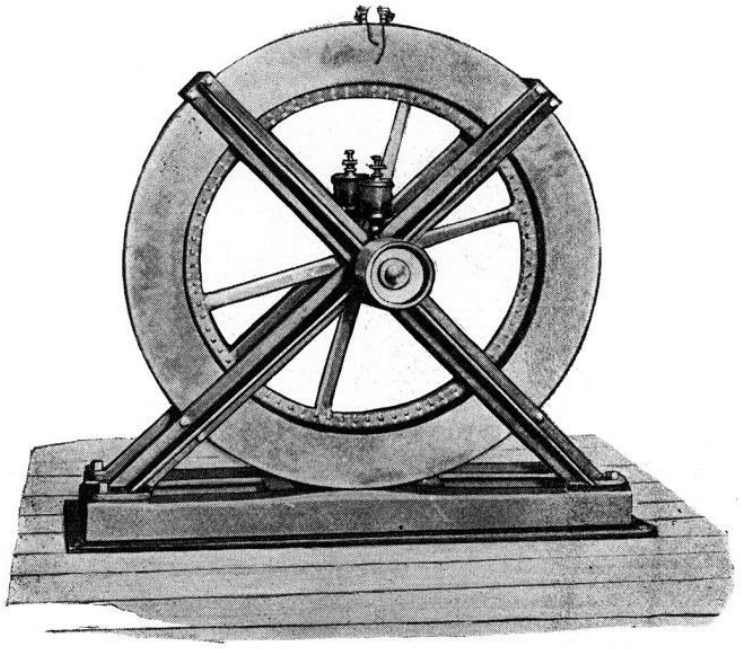

Figure 2.2 Representation of Tesla's high-frequency alternator [7].

He was considered a visionary at that time, but today his ideas of alternating current (ac) transmissions systems and wireless power were the foundations of the

energy harvesting technology we are using today. To support his concepts, Tesla built the Wardenclyffe Tower between 1901 and 1917 in Shoreham, New York, a tower for wireless power generation and communication at the same time.

Figure 2.3 Drawing concept of the Wardenclyffe Tower.

He believed in the possibility of wirelessly power devices like vehicles or flying dirigibles by transmitting energy in the form of alternated radio frequency waves. He also predicted that fossil fuels like petroleum were not a long-time viable because it is an exhaustible source of energy that requires expensive storage and managing systems and, therefore he felt that the idea of RF wireless power transfer was the solution [44].

2.2 RF ELECTROMAGNETIC ENERGY HARVESTING

The radiofrequency energy harvesting (RF EH) aims to recover energy from the ambient high-frequency electromagnetic fields, mostly presents in urban scenarios due to the growing demand for telecommunication infrastructures and services, such as TV broadcasting, mobile phones communications, FM radio or Wi-Fi. Figure 2.4 depicts a typical structure of an RF energy harvesting system, which is composed by an RF energy source (could be dedicated or ambient energy), the receiving antenna, a matching network that ensures the perfect matching between the antenna and the following circuitry, the voltage rectifier which converts the captured RF signal into a DC voltage, a power management block and, finally, the application load.

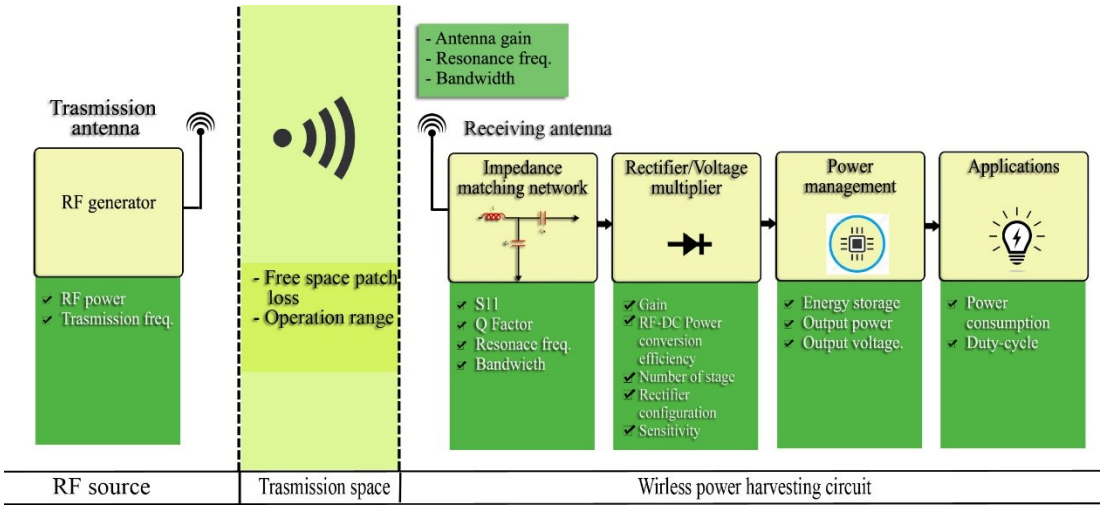

Figure 2.4 Block scheme of a generic RF energy harvesting system.

The key components of an RF power harvesting system are the antenna and rectifier circuit that allows the RF power to be converted into DC energy. Regardless of its low power density in the environment, a dedicated source can be added for more efficient power transmission and an enhancing circuit can be built to suit the requirements of the load request. This feature supports research to realize RF EH technology to support portable or autonomous applications, such as wireless sensor networks and the Internet of Things (IoT).

One of the problems that affect the RF EH is the distance between the source and the harvesting system, due to the Free Space Path Loss (FSPL), which is the loss of the power signal while propagating in free space. Here, the effect differs according to the behavior of the electromagnetic waves, which can be classified in far-field and near-field [45]. While the electromagnetic wave shape at the far-field is relatively uniform, the near-field is characterized by very strong and independent electric and magnetic components, therefore one component can dominate the other. The delimitation between the far-field region and the near-field region is identified with the Fraunhofer's distance, as depicted in Figure 2.5, that is defined as

$$d_f = \frac{2d^2}{\lambda} \tag{2.2}$$

where d_f is the Fraunhofer's distance, d is the length of the antenna (for filar radiators) or the effective diameter of the antenna (for aperture radiators), and λ is the wavelength of the electromagnetic wave. The Fraunhofer's distance is not an abrupt limit, but a

transition region can be defined between the d_f and $\sqrt[3]{d/2\lambda}$, which is known as the Fresnel region or radiative near-field. In this region, the reactive comportment of electromagnetic waves is not leading but the phases of E and H fields still vary with distance.

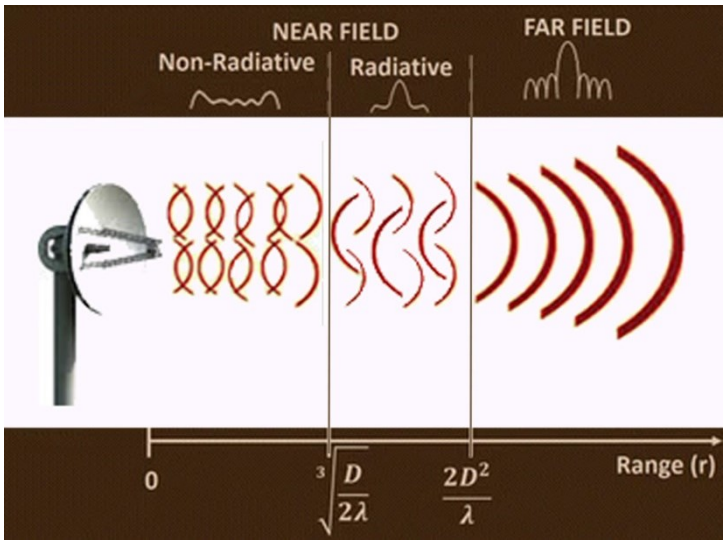

Figure 2.5 Representation of near-field and far-field propagation.

While in the near-field, the relationship between electric and magnetic field is unpredictable, which leads to a difficult estimation of the power density, in the far-field space, the power propagation between a transmitter and a receiver antenna can be easily identified with the well-known Friis formula, as [45]:

$$P_{RX} = \frac{P_{TX} \cdot G_{TX} \cdot G_{RX} \cdot \lambda^2}{(4\pi D)^2} \tag{2.3}$$

where P_{RX} and P_{TX} are the received and transmitted power, respectively; G_{RX} represents the gain of the receiving antenna expressed in dBi (with respect to the isotropic radiator); G_{TX} is the gain of the transmitting antenna expressed in dBi; D is the distance between transmitting and receiving systems.

Given the formula 2.3, it is possible to compute the FSPL for the far-field as follows

$$P_L = \frac{P_{TX}}{P_{RX}} = \frac{(4\pi D)^2}{G_{TX} G_{RX} \lambda^2} = \frac{(4\pi f D)^2}{G_{TX} G_{RX} c^2} \tag{2.4}$$

where P_L represents the power losses, f represents the working frequency and c is the speed of light in vacuum. The representation of the above equation is also widely utilized and can be expressed as

$$P_L(dB) = 20\log_{10}(f) + 20\log_{10}(D) + 20\log_{10}\left(\frac{4\pi}{c}\right) - G_{TX} - G_{RX} \qquad (2.5)$$

The equation 2.4 and 2.5 can be employed to estimate available power at the input of the harvesting system; to increase the accuracy for the power loss computation, other phenomena should be taken into accounts, such as absorption, diffraction, and reflection. However, for ambient RF EH, it is difficult to achieve a high level of accuracy, since the source characteristics are usually unknown, and an empirical measurement of the available average power density should be performed.

The FSPL evaluation procedure is crucial to properly design the energy harvesting system. The knowledge of the amount of power that the system is required to manage is a piece of important information for the designer in order to suitably select the appropriate technology and method.

Once the target RF source has been identified and considerations about the power availability have been made, the first element of the harvesting system chain that should be selected or designed is the antenna. Presuming a free space and isotropic transmitting source, the spreading of the electromagnetic waves is uniform in all directions. Therefore, the energy isosurface is a sphere and the power per unit area at a certain distance R from the source can be computed as

$$S_{isotropic} = \frac{P_{TX}}{4\pi R^2} \qquad (2.6)$$

where $S_{isotropic}$ is the power density of the isotropic radiator, expressed in $\frac{W}{m^2}$, at a certain distance R.

On the other hand, the isotropic radiator is an ideal condition, since a real antenna cannot transmit power uniformly (spherically), but the energy concentration is higher in some directions than others, according to the design. Therefore, the gain of a generic antenna G can be defined as the ratio between the maximum power density of the antenna, with respect to a certain distance, and the power density of the isotropic radiator at the same distance. This information describes the directivity of the antenna, which is a function of the propagation direction. Consequently, the power density of a

generic real antenna is a function of propagation direction as well, i.e. $S(\vartheta, \varphi)$. Therefore, the gain of a real antenna, at a given direction, can be defined as

$$G(\vartheta, \varphi) = \frac{S(\vartheta, \varphi)}{S_{isotropic}} = \frac{4\pi R^2 S(\vartheta, \varphi)}{P_{TX}} \tag{2.7}$$

and the general form for the power density, at a given distance R, can be expressed as follows

$$S(\vartheta, \varphi) = \frac{P_{TX} G_{TX}(\vartheta, \varphi)}{4\pi R^2} \tag{2.8}$$

The antenna gain is usually expressed in dBi, i.e. decibels with respect to the isotropic radiator, therefore the ideal isotropic antenna would have $G_{TX} = 0\ dBi$, while a high-directivity antenna would have a much higher gain. If the RF source is known, in terms of position and irradiated power, a high-gain antenna is preferred, since it can be oriented towards the propagation direction to collect higher power level for energy harvesting purposes. On the contrary, if the characteristics of the RF transmission are unknown or if the harvester is intended to be moved in the space (e.g. a wearable device for sports activity), an omnidirectional antenna with a lower gain is preferable, in order to collect power from various directions.

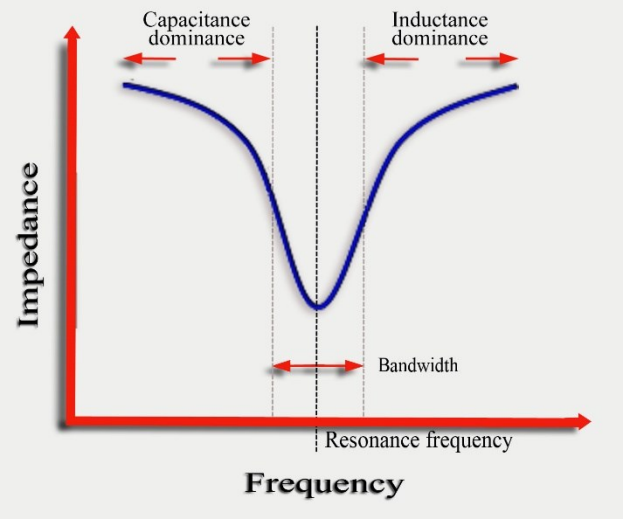

Figure 2.6 Resonance frequency representation for a generic antenna.

Another important parameter for the antenna is the frequency of operation, i.e. the resonance frequency, which is related to the reactive behavior of the antenna

impedance. At the resonance frequency (Figure 2.6), the inductive and capacitive parts of the antenna cancel each other out, minimizing the impedance.

The frequency and the physical dimensions of the antenna affect its capacitive and inductive behavior; generally speaking, the resonance frequency is inversely proportional to the dimensions of the antenna. Therefore, low-frequency energy harvesting applications require large antennas, which could be not suitable for portable or wearable applications. The authors in [46] proposed a high-efficiency broadband antenna with a sensitivity down to -35 dBm, represented in Figure 2.7, but the drawback is the large dimension, with an area of about 49 cm^2.

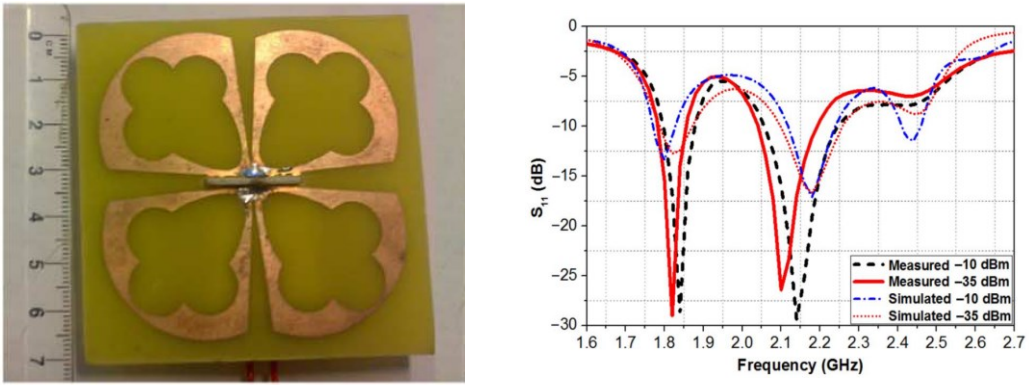

a) b)

Figure 2.7 The energy harvesting antenna proposed in [46] with its a) physical dimensions and b) resonance frequencies characterization. ©2015 IEEE. All rights reserved.

The antenna bandwidth denotes the working frequency range. As shown in Figure 2.6, at the resonance frequency the antenna impedance reaches its minimum value and the highest sensitivity, but the region close to the resonance still presents a good impedance behavior, which provides acceptable performance. The authors in [47] considered an acceptable threshold value for the VSWR (Voltage Standing Wave Ratio) as 1.5, which corresponds to about 13.9 dB. Therefore, if the return loss is under the considered threshold value, the performance of the antenna is acceptable. A wideband antenna presents a large frequency region under the threshold value and can collect power signals from different frequency emitters, while a multiband antenna presents several resonance frequencies, like that represented in Figure 2.7b.

The antenna theory and design methodology have been consolidated over the years, but there is still a great interest to study new techniques and fabrication methods to reduce dimensions and increase the overall efficiency, especially in the field of

portable applications and, therefore, for energy harvesting purposes. The authors in [48] reported a comparison of different energy harvesting antennas, here listed in Table 2.3.

Ref.	Type	Gain (dBi)	Freq. (GHz)	Dimension (mm)	Sensitivity	RF-DC PCE
[49]	Air-substrate patch	7	2.45	261 × 5	–	30% @ 1 μW/cm^2
[50]	Polarization patch	–	5.1–5.8 5.8–6.1	90 × 160	–	23.8%–31.9% 22.7%–24.5%
[51]	Patch	–	2.45	100 × 70	–	73.9% @ 207 μW/cm^2
[52]	Dual-linearly polarized patch	7.45–7.63	2.45	70 × 47.5	–	78% @ 295.3 μW/cm^2
[53]	Microstrip	5.3	160	–	–	8.5% @ −2.46 dBm
[54]	Patch	–	1.9–3.2	40 × 40 × 0.8	20 μW/cm^2	70% @ 50 μW/cm^2
[55]	Patch	−20.20	0.915	Π × 6 × 1.584		~ 60%
[56]	Patch, metal strip	4.33 6.64	4.9 5.9	68 × 34	–	65.2% 64.8%
[57]	Stack differential	–	5.8	120 × 40	–	44.1% @ 0.041 W/m^2
[46]	Cross dipole	–	1.8–2.5	70 × 70 × 13.2	−35 dBm	55% @ −10 dBm
[58]	Dual-polarized patch	–	2.45	100 × 100 × 3.8	–	82.3% @ 22 dBm
[59]	1 × 4 quasi-Yagi	10.9 13.3	1.8 2.2	300 × 300 × 1.6	–	40% @ 455 μW/cm^2
	Dipole	–	0.915 2.45	60 × 60 × 60	1 μW/cm^2	48% @ 0 dBm 39% @ 0 dBm
[60]	Microstrip	8.6	2.45	–		83%
[61]	Patch	4	2.45	–	–	70%
[62]	Patch	2.19 3.6	2.45 5.8	40 × 43	–	65% @ 10 mW/cm^2 46 % @ 10 mW/cm^2

Table 2.3 Comparison of published work about energy harvesting antennas, reported in [48].

Guidance about the fundamental limits of antenna dimensions and efficiency was determined by Wheeler in [63], where he asserted that the maximum size of a small antenna in less than $1/k = \lambda/2\pi$ and should be enclosed in a sphere of radius a, with $ka < 1$. The efficiency of a harvesting antenna can be evaluated with the Q factor, which expresses how much energy is stored against the energy dissipated per cycle. It can be also expressed as the ratio between the resonance frequency and the bandwidth of resonance as

$$Q = \frac{f_c}{BW} \tag{2.9}$$

where f_c is the frequency resonance and BW indicates the frequency bandwidth of the antenna. The minimum Q factor needed for a compact antenna, in order to have minimum losses, was determined by Chu in [64] and the relation is reported below:

$$Q \geq \frac{1}{k^3 a^3} + \frac{1}{ka} \tag{2.10}$$

where $k = 2\pi/\lambda$ is the angular wave number and a is the sphere radius that contains the antenna.

The antenna dimension is, therefore, a crucial aspect for the designer, especially in energy harvesting systems for portable applications, as the antenna size could affect performance, as well as the user comfort. One simple method to reduce the antenna dimensions without degrading efficiency is choosing a flat, microstrip design and to use high dielectric constant materials, as in [54], [55] and [62]. The usage of such materials allows to reduce the patch size, but it also determines a narrow frequency bandwidth and reduces gain, because of the surface waves excitation within the substrate [65]. Other techniques for antenna miniaturization by preserving performance is the geometric optimization, such as the use of slot, slits and shorting. The authors in [62] designed a dual-frequency energy harvesting system with two custom ring slot antennas. The regular design has been improved by means of the meander line structure technique, as shown in Figure 2.8, which allows reducing the antenna size to 52% with respect to the regular design. The final reported size is of 40 × 43 mm and the achieved power density is of 10 mW/cm^2. As stated in [65], the introduction of slots is a very common method used to reduce the antenna size, since the fringing at the slots ends increases the current path and, therefore, the equivalent optimal dimension of the antenna can be reduced. The meandering technique is another

diffused method for antenna size reduction. The authors in [55] implemented a miniature three-layer planar inverted-F antenna with five meanders and two radiator layers (Figure 2.9), achieving a dimensions of $\pi \times 6 \times 1.584$ mm^3, with a resonance frequency of 915 MHz.

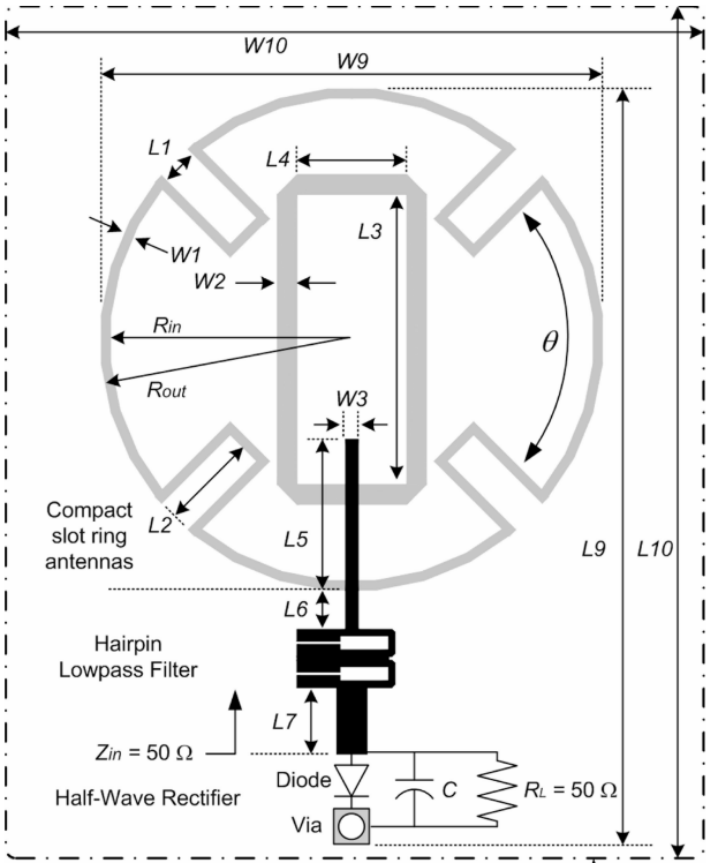

Figure 2.8 Example of EH slot ring antenna size reduction by using the meander line structure technique, presented in [62]. ©2007 IEEE. All rights reserved.

One of the problems occurring when slots are used for the miniaturized antenna design is the mismatch of the source impedance with respect to the input impedance of the system, because of the compensation that slots and meanders perform against the high reactive impedance of the electrically small antennas. This effect can be mitigated by designing external matching circuitry, which leads to an increase in the overall system dimensions [66]. Regarding meanders, they also lead to narrowband operation and impedance mismatch degradation. Moreover, the spacing between meanders is a crucial parameter, since it can produce cross-polarization and antenna efficiency degradation, if not properly designed. For this purpose, usually, CAD software based on the Finite Elements Method (FEM) or similar are employed to

properly design such antennas and verify the proper electromagnetic behavior with simulations.

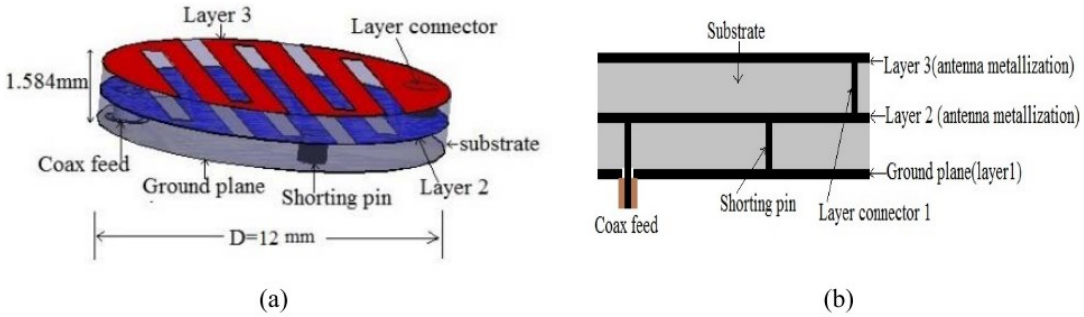

Figure 2.9 Example of meander technique in a miniature three-layer planar inverted-F antenna (a), and its cross-section (b) presented in [55]. ©2015 IEEE. All rights reserved.

As stated previously, narrowband antennas can achieve very good resonance behavior at the working frequency, but the amount of gathered power is low. On the contrary, broadband or multiband antennas can acquire more RF power from the surrounding, but they require complex matching networks [67]. The total input RF power for a multiband/broadband antenna EH system is the summation of every RF power at each working frequency, as

$$P_{AV} = \sum_{i=1}^{N} P_{fi} \tag{2.11}$$

where P_{AV} is the total available RF power, while P_{fi} is the power associated with the working frequency f_i and N is the number of frequencies.

In the above table, the listed parameter PCE represents the Power Conversion Efficiency, which is an important parameter for the evaluation of the energy harvesting system performance. It characterizes the overall efficiency of the whole harvester, from the antenna to the power management block and it is defined as the ratio between the power delivered to the equivalent output load and the power gathered by the antenna [68]:

$$\eta_{PCE} = \frac{P_L}{P_{AV}} = \frac{P_{AV} - P_{loss}}{P_{AV}} \tag{2.12}$$

where P_L is the power provided to the output equivalent load and P_{loss} represents the power dissipated by the antenna and the harvesting circuitry.

Recently, new techniques have been investigated to improve the antenna efficiency, in terms of operating frequency, low impedance bandwidth, low gain, larger dimensions, and polarization issues. These methods involve the usage of Electromagnetic Band Gap (EBG), Photonic Band Gap (PBG), Metamaterial, and Defected Ground Structure (DGS) [69].

The Photonic Band Gap are periodic structures directly created on the ground plane and allow to affect the propagation of electromagnetic waves and the current distribution along with the structure. Therefore, the PBG permit to control the propagation of electromagnetic waves and radiation pattern. The peculiarity of PBG is to present periodic imperfections, which can be considered as resonant cavities which form free mode inside the forbidden band-gap and provides a stopband at specified frequencies. PBG has been described in the literature for enhancing the directivity of antennas, surface wave's inhibition, and harmonics inhibition, as reported in [70].

The EBG technique is quite similar to the PBG, as it consists of the realization of periodic structures such as dielectric rods, holes and metal patches [71]. As stated in, [72], the EBG is very diffused in the low-profile, high-efficiency antenna design.

	PBG	**EBG**	**DGS**
Definition	Photonic Band Gap (PBG) structures are periodic structures etched on the ground plane and have the ability to control the propagation of electromagnetic waves	The EBG technique is based on the PBG phenomena and also realized by periodical structures but compact in size	Single or few compact geometrical slots embedded on the ground plane of microwave circuits are referred to as Defected Ground Structure (DGS)
Geometry	Periodic etched structure	Periodic etched structure	One or few etched structures
Parameter extraction	Very difficult	Very difficult	Relatively simple
Size	Large	Smaller than PBG and larger than DGS	Much more compact than PBG and EBG
Fabrication	Difficult	Difficult	Easy

Table 2.4 Comparison of PBG, EBG, and DGS reported in [73]. ©2017.

Finally, the DGS consists of periodic or aperiodic defects, i.e. slots embedded on the antenna ground plane, that affect the current propagation and, therefore, lower the overall antenna optimal size. They can be modeled as RLC circuits, which modify the effective line (microstrip, coplanar weave guide, etc..) impedance. An example of antenna design and performance with a single DGS structure is depicted in Figure 2.10. The authors in [73] described a comprehensive comparison between EBG, PBG, and DGS techniques, here reported in Table 2.4.

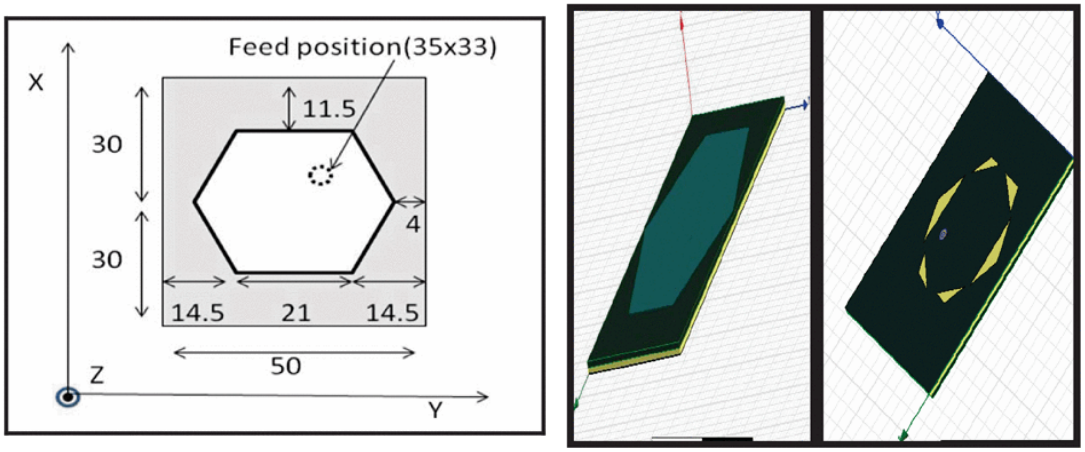

a) b)

Figure 2.10 Comparison of a regular hexagonal patch antenna (a) and a hexagonal patch antenna with DGS (b), reported in [74]. ©2015 IEEE. All rights reserved.

Metamaterials (MTMs) are gaining popularity in the field of microwave engineering, thanks to the great advantages they provide form many applications [75]. They are formed by embedding different materials in the host medium in order to achieve new materials with interesting physical behaviors, that are not available in nature. With metamaterials, it is possible to achieve negative permittivity or permeability for the working frequency by including spaced elements with dimensions and distance lower than the wavelength of interest. In the antenna field, this property leads to a gain enhancement if the metamaterial structure is placed over the antenna, or between the antenna and the ground plane, as it behaves like a lens, magnifying the gain and increasing the efficiency for the EH system.

Antenna polarization is another crucial aspect of EH purposes. A linearly polarized receiving antenna can achieve broadband property and high gain, but the polarization mismatch with the gathered signal can reduce the overall efficiency for the EH system, especially if the RF power source is unknown or for mobile EH

applications. Therefore, the circularly polarized antenna can be a good solution, since it can receive an RF signal with any polarization [76]. To achieve circular polarization behavior, several techniques have been investigated, such as stub loading, patch corner truncation, slits or stub loading. As stated in [76], the main drawback of circular polarized antenna design is the resulting narrowband behavior. In order to mitigate this phenomenon, several novel methods have been proposed in the literature, such as stacked structures with parasitic elements, or the usage of metamaterials. The authors in [77] implemented a stacked, single feed patch antenna with two patches and two different substrates. The top patch has a square shape while the bottom patch is triangular. They also inserted T-slots at both patches, as shown in Figure 2.11, to improve the bandwidth.

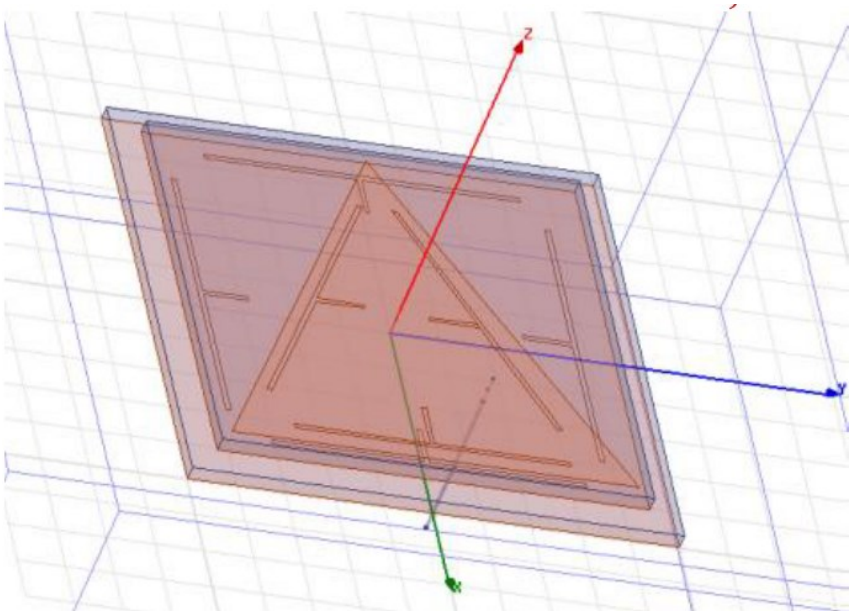

Figure 2.11 Stacked patch antenna with triangular and square shape patches, proposed in [77]. ©2012.

The next block in a typical EH circuit architecture is the matching network. The antenna, from the EH system point of view, behaves like an RF source generator, with a series input impedance, which is resistive and known, at the working frequency range of operation. On the other hand, the EH following circuitry typically has a complex impedance. Moreover, the rectifier circuit has a non-linear behavior, therefore its impedance changes with frequency and input power. Here, the role of the matching network is crucial to ensure the same impedance between the antenna and the load, since an impedance mismatch can lead to backward power reflection, reducing the PCE of the EH system. The design requirements for matching networks are to keep a

low form-factor and reduce as low as possible the losses due to the parasitic resistance. Both lumped element or distributed microstrip electromagnetic component can be employed to design matching circuits; the main drawback of lumped elements is the low-quality factor Q at higher frequencies, while the distributed components are not indicated for low-frequency operations, because of the resulting electrically dimensions that would affect the miniaturization of the system.

As stated before, the Q factor is inversely proportional to the energy dissipated by the component per cycle. It is possible to compute the specific Q factor for capacitance and inductance, at a specific frequency, as follows

$$Q_C = \frac{1}{\omega R_C C} = \frac{X_C}{R_C} \tag{2.13}$$

$$Q_L = \frac{\omega L}{R_L} = \frac{X_L}{R_L} \tag{2.14}$$

where $\omega = 2\pi f$ is the working frequency, R_C and R_L are the parasitic resistance of the capacitor C and the inductor L, respectively.

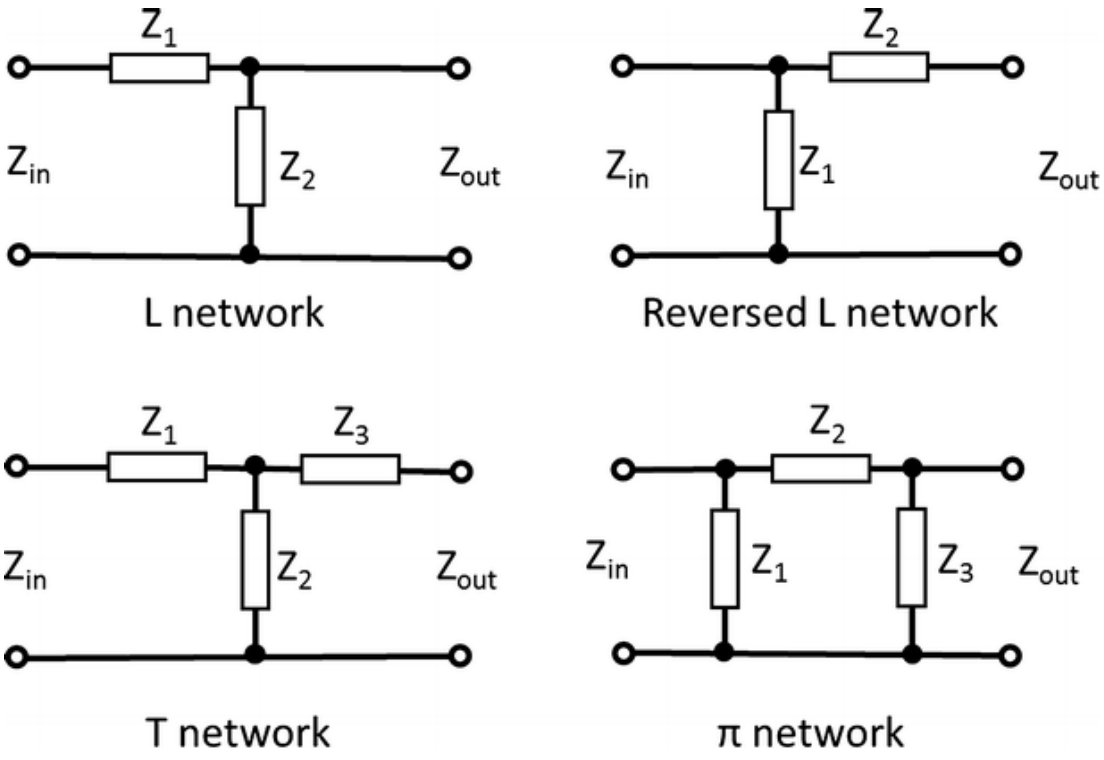

Figure 2.12 First and second-order matching circuits commonly employed for EH.

First-order matching circuits are commonly used for EH systems since the reduced number of matching components minimized losses, however, it results in a

narrow band matching operation. A broadband behavior can be achieved with a second-order matching network, while greater order can negatively affect the EH performance because of the energy dissipation and bandwidth degradation [78].

The typical lumped elements matching circuit architectures, depicted in Figure 2.12, are the L and reverse L networks for the first order, T and Pi networks for the second order. The L network configuration is chosen according to the load impedance value, compared with the source impedance. Generally speaking, if the load impedance is larger than the source impedance, that the configuration a) should be adopted, while the configuration b) should be employed if the load impedance is lower than the source [79]. In this way, the quality factor of the circuit, at the working frequency, is equal to

$$Q = \sqrt{\frac{R_{large}}{R_{small}} - 1} \tag{2.15}$$

As an example, considering an equivalent complex load as depicted in Figure 2.13.

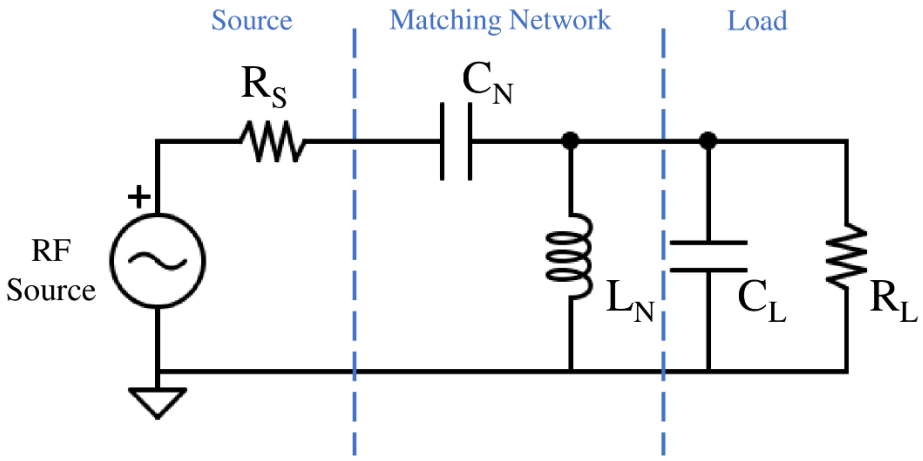

Figure 2.13 L matching network configuration for a complex capacitive load.

The quality factor Q of such a configuration, at the working frequency, can be expressed as

$$Q = \sqrt{\frac{R_L}{R_S} - 1} = \frac{Im(Z)}{Re(Z)} \approx \frac{R_L}{\omega_0 L_N} - \omega_0 C_L R_L \tag{2.16}$$

where ω_0 is the working frequency. Therefore, the inductive and capacitive part of the matching network, L_N and C_N respectively, can be calculated as

$$L_N = \frac{R_L}{\omega_0(Q + \omega_0 C_L R_L)} \tag{2.17}$$

$$C_N = \frac{R_L}{L_N(R_L + R_S)\left(\omega_0^2 - \frac{1}{L_N C_L}\right)} \tag{2.18}$$

The above formulations show that the matching criteria can be satisfied for a single working frequency, therefore a broadband behavior can't be fulfilled with an L network and an additional lumped element must be added, forming a T or Pi network. In [80] the authors conducted a performance analysis of Pi matching network for EH systems. In the schematic representation of the system (see Figure 2.14), the rectifying diode was replaced with an equivalent series of a resistor R_L and a capacitive reactance X_C.

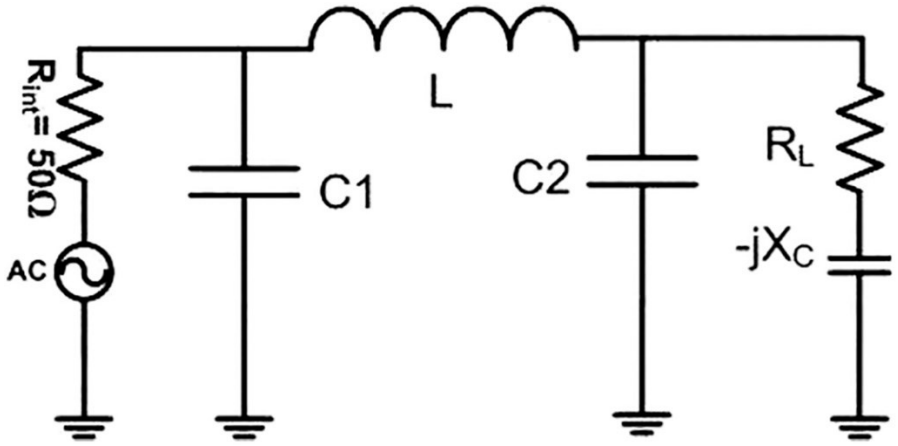

Figure 2.14 Energy harvesting circuit using a Π-type matching network, analyzed in [80]. ©2015 IET. All right reserved.

The limitation in bandwidth shown by the L-type matching network is due to the fixed Q factor, while a Pi matching network provides an extra degree of freedom, which allows selecting the proper Q for the circuit, as well as suitable impedance matching condition [79]. The equation for the Pi-network design can be expressed as

$$Z_{in} = \left\{\left[(R_L - jX_L) \parallel \left(\frac{1}{j\omega C_2}\right)\right] + j\omega L\right\} \parallel \left(\frac{1}{j\omega C_1}\right) \tag{2.19}$$

The power losses correlated to parasitic elements increase with frequency, while the capacitive behavior changes into inductive as frequency increases. As depicted in Figure 2.15d, Agrawal et al. in [80] shown the capacitive and inductive variations with respect to the Q factor. As the latter increases, the optimal inductance value decreases, enabling the possibility to implement a lumped element matching network for high-

frequency applications. In fact, high value lumped inductors with a good quality factor is difficult to implement.

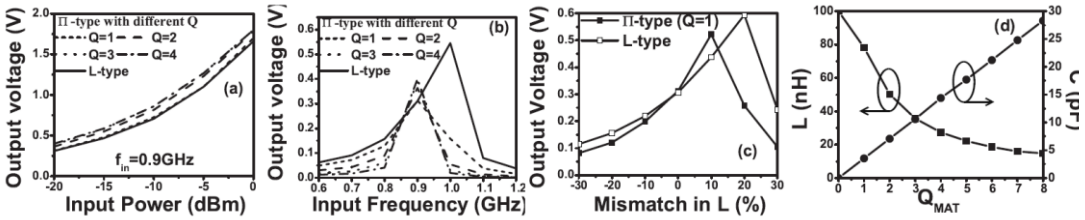

a) b) c) d)

Figure 2.15 Output voltage of half-wave rectifier using L and Π-type matching network as a function of (a) input power (b) frequency (c) mismatch in matching network's inductor value and (d) variation in the inductor and capacitor value with Q factor of the matching network. Presented in [80]. ©2015 IET. All right reserved.

Moreover, Figure 2.15a denotes the performance enhancement for an EH system with PI-network, compared with a simple L matching network.

For complex loads, a broadband matching is quite difficult, however, a method to identify the limitations of impedance matching exists [81][82]. The Bode-Fano criterion, for parallel and series resistive/capacitive load, asserts that

$$\int_0^\infty \ln\left(\frac{1}{|\Gamma(\omega)|}\right) d\omega < \frac{\pi}{R_L C_L} \tag{2.20}$$

$$\int_0^\infty \frac{1}{\omega^2} \ln\left(\frac{1}{|\Gamma(\omega)|}\right) d\omega < \pi R_L C_L \tag{2.21}$$

where Γ represents the reflection coefficient of the network. Since $|\Gamma(\omega)|$ is ideally equal to 1 outside the frequency bandwidth of interest, the term $\ln\left(\frac{1}{|\Gamma(\omega)|}\right)$ will be equal to 0 in that frequency range. As a consequence, for the desired bandwidth $\Delta\omega$, the Bode-Fano criterion applied to a parallel load will be

$$\Delta\omega \cdot \ln\left(\frac{1}{|\Gamma(\omega)|_{min}}\right) < \frac{\pi}{R_L C_L} \tag{2.22}$$

The equation 2.22 represents a compromise between matching performance and bandwidth.

To overcome some of the limitations and issues coming from the impedance matching network design, like precise impedance matching and narrow bandwidth, several methods have been investigated in recent years. One technique consists of

designing a tunable matching circuit, in order to adjust the impedance for the real implemented circuit. Hoarau, Corraro et al. proposed in [83] a tunable network consisting of a Π-structure with tunable components, implemented with varactors in series with inductors.

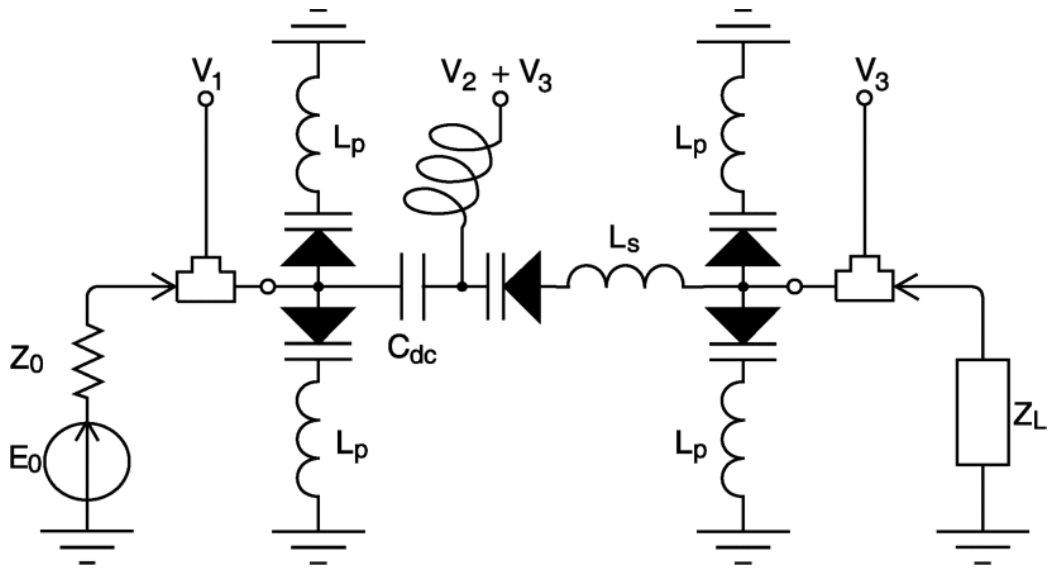

Figure 2.16 Equivalent circuit of the tunable Π-structure matching network, proposed in [83].

The network is able to implement complex impedances with magnitudes varying from 6 Ω to 1 kΩ, which can be matched at 1 GHz and tuned in a 50% bandwidth. The main disadvantage of this strategy is the need for external control voltages, to properly tune the network. Moreover, the matching condition can be achieved only for a narrow band. Other methods to mitigate matching issues consists of removing the matching network and directly design the harvesting antenna with a conjugate impedance of the rectifier circuit. This is a very interesting technique since it eliminates losses and efficiency degradation due to the matching network components and reduces the EH size, but it requires high-level design skills, in order to implement an efficient antenna with the desired impedance. Moreover, it is necessary to know exactly the load impedance and, therefore, the rectifying diode non-linear behavior. Authors in [84] reviewed some recent antenna design techniques to achieve a suitable conjugate impedance matching with the equivalent complex load. In Figure 2.17 a planar dipole antenna in T-match configuration and its equivalent circuit model are depicted. It is composed of a large radiator of length l and width w, while a second smaller radiator of length a and width w' is placed at the antenna source and very close to the main dipole, at a distance b.

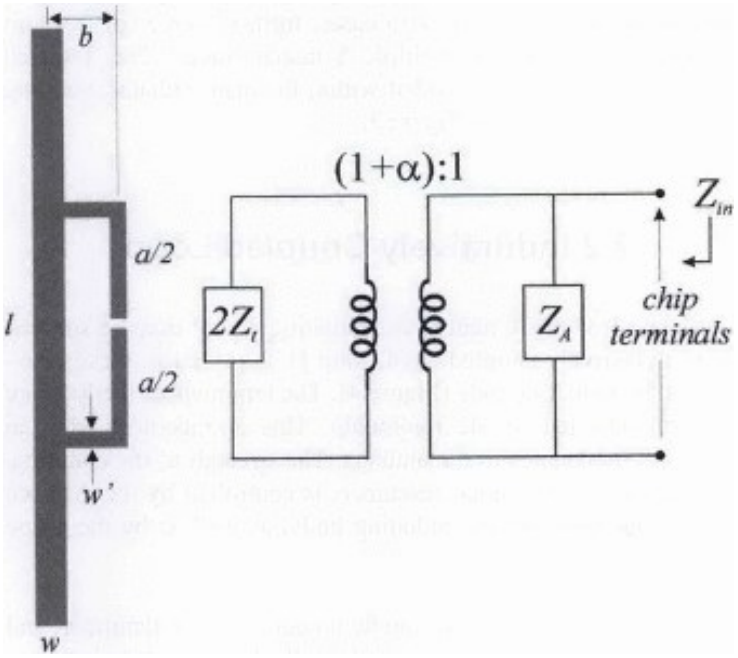

Figure 2.17 Example of antenna impedance matching for a planar dipole in a T-match configuration, presented in [84]. ©2008 IEEE. All rights reserved.

In this configuration, according to [84], [85] and [65], it can be demonstrated that the antenna impedance can be calculated as

$$Z_{in} = \frac{2Z_t(1+\alpha)^2 Z_A}{2Z_t + (1+\alpha)^2 Z_A}, \qquad \alpha = \frac{\ln\left(\frac{b}{r_e'}\right)}{\ln\left(\frac{b}{r_e}\right)} \tag{2.23}$$

$$Z_t = jZ_0 \tan\left(\frac{ka}{2}\right) \tag{2.24}$$

$$Z_0 \cong 276 \log_{10}\left(\frac{b}{\sqrt{r_e r_e'}}\right), \quad r_e = 0.25\omega, \quad r_e' = 8.251\omega' \tag{2.25}$$

where Z_t is the input impedance of the short-circuited stub constituted of the T-match traces and part of the main dipole, Z_0 is the characteristic impedance, Z_A represents the main dipole impedance without the T-match connection, r_e and r_e' are the equivalent radii of the antenna traces, while α is the current division factor between the main radiator and the T-match connection.

The above equations demonstrate that it is possible to tune the complex impedance of the antenna shown in Figure 2.17 by changing the design parameters a, b, w and w'. As stated in [84], The tunable matching impedance for the T-match dipole is inductive if the main radiator wavelength is equal to $\lambda/2$, while for smaller

dipole the impedance can be both capacitive or inductive. In Figure 2.18 the authors reported an impedance tuning chart for the abovementioned dipole, in the case of $l = \lambda/2$, $w = \lambda/100$, $w' = w/3$ and $Z_A = 75\Omega$.

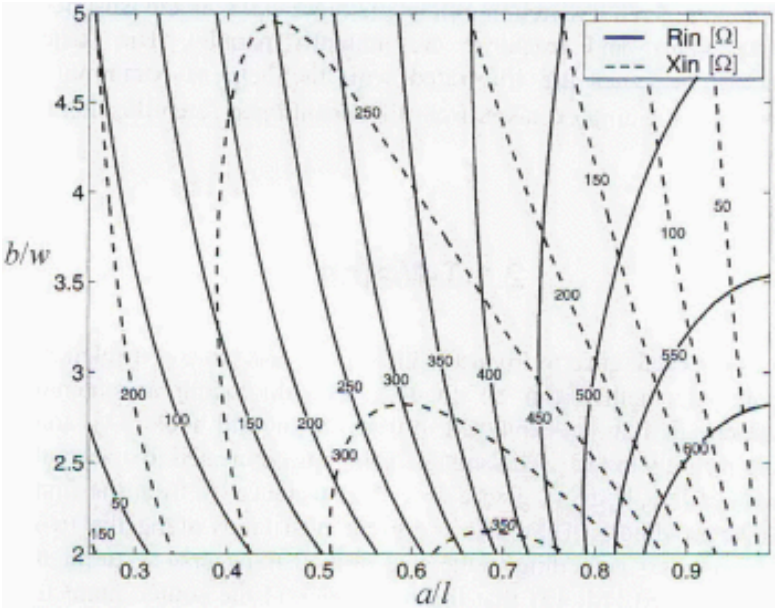

Figure 2.18 T-match dipole impedance tuning chart, as reported in [84]. ©2008 IEEE. All rights reserved.

The last block of an RF EH system is the rectifier, which has the role to convert the RF input power into a DC voltage signal. The latter is then handled by a power management block, such as a DC/DC converter and/or battery charger, which is a common final stage for every energy harvesting device.

The AC-to-DC conversion stage is the most critical part of the EH system, since it introduces non-linearity and, therefore, it imposes several design constrains for the other block of the EH chain, as stated in the previous paragraphs. The goals for the rectifier block are to ensure low power losses, high sensitivity for low RF input power conversion and high output DC voltage. Rectifiers for RF EH can be classified according to the non-linear component used, i.e. diode or MOSFET.

Diode-based rectifier circuits are very popular, because of the low forward voltage drop, in comparison with MOSFET based architecture. The forward voltage drop V_F is a crucial parameter, since it contributes to lower the PCE, especially for low RF input power, so as the voltage amplitude of the RF signal is lower than the diode V_F, which significantly increases the diode impedance. Moreover, the non-linearity of the rectifier generates high order harmonics, which are reflected backward and

reradiated by the harvesting antenna, lowering the conversion efficiency. To mitigate these problems, one possible solution is to design a harmonic rejection low pass filter between the antenna and the rectifier, as proposed in [86]. The rectifier power handling limits are also imposed by the diode breakdown voltage V_{br}; as the RF input voltage amplitude exceeds the V_{br} of the rectifying diode, the PCE is drastically degraded. The critical input power level for a single diode rectifier circuit can be computed as [87]:

$$P_{in}|_{max} = \frac{V_{br}^2}{4R_L} \tag{2.26}$$

where R_L represents the equivalent output load resistance of the EH system.

The combination of diode forward voltage, breakdown effect, and high order harmonics generation defines the maximum efficiency of the rectifier [87], as depicted in Figure 2.19.

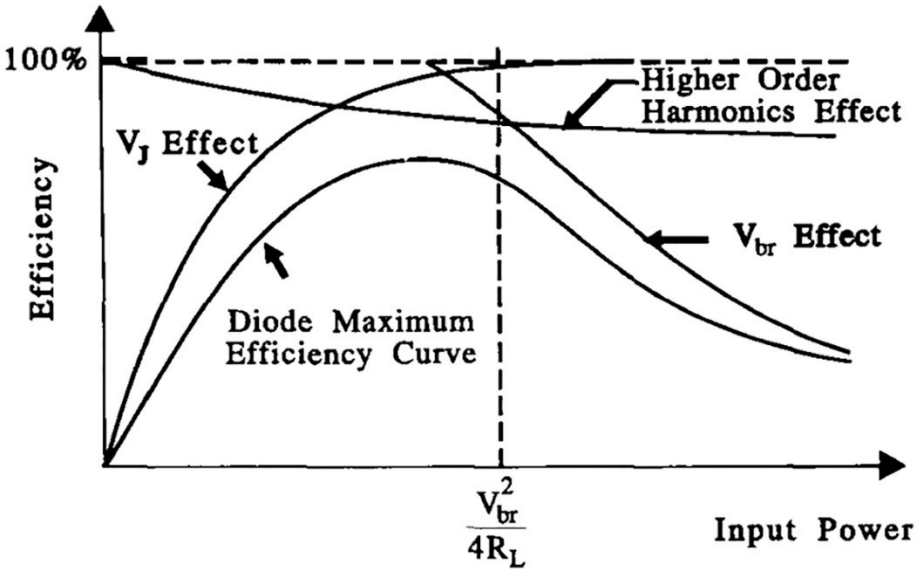

Figure 2.19 Diode maximum efficiency versus RF input power, as presented in [87]. ©2011 IJEST. All rights reserved.

To overcome the forward voltage issue, that limits the minimum input power for the EH system, a low V_F diode must be selected. For this reason, Schottky barrier diodes (Figure 2.20) are very popular for RF EH purposes [67], because of their intrinsic low threshold voltage. The PCE of a Schottky diode-based EH architecture is related to the diode junction capacitance C_{j0} that affects also the diode speed, its breakdown voltage V_{br}, the equivalent series resistance R_s and the forward threshold voltage V_F.

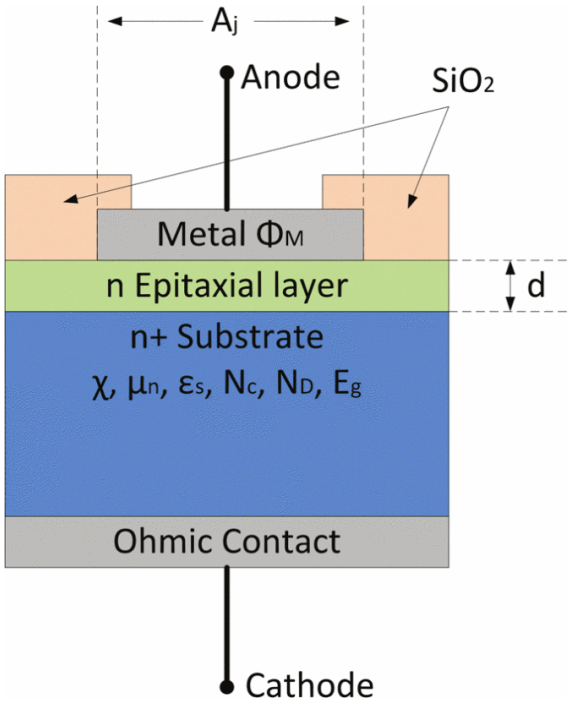

Figure 2.20 Physical structure of a Schottky diode, reported in [88]. ©2015 IEEE. All rights reserved.

The breakdown voltage V_{br}, which affects the maximum input power, can be varied, at semiconductor level, by changing the doping density N_d. An example of performance variation for a platinum-gallium arsenide Schottky diode was reported C. Valenta in [88] and is depicted in Figure 2.21.

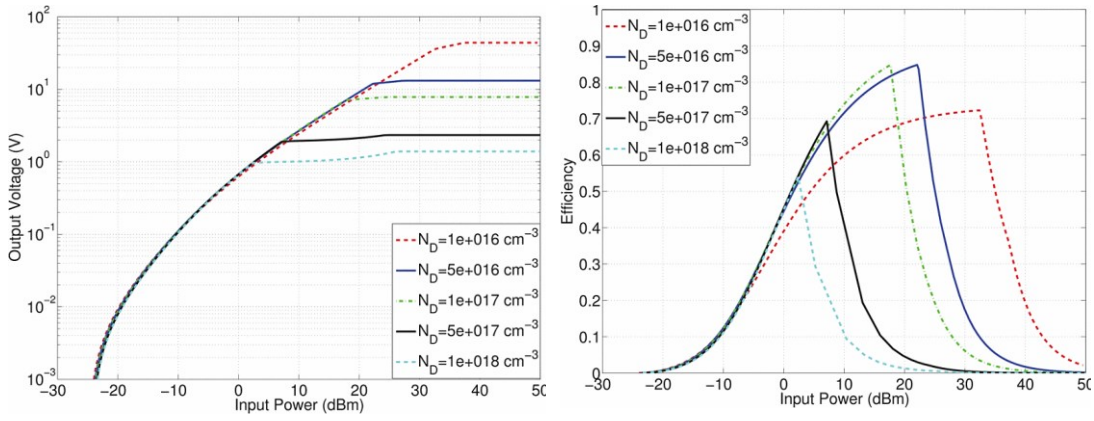

a) b)

Figure 2.21 Variation of doping concentration N_d versus (a) the maximum output voltage and (b) the conversion efficiency for a platinum-gallium arsenide Schottky diode, as reported in [88]. ©2015 IEEE. All rights reserved.

In Table 2.5, the typical parameters of the most diffused Schottky diodes for RF energy harvesting are reported.

Diodes	SMS 7630 [89]	HSMS 2820 [90]	HSMS 2850 [91]	HSMS 2860 [92]
$R_s[\Omega]$	20	6	25	6
$C_{j0}[pF]$	0.14	0.7	0.18	0.18
$V_F[V]$	0.34	0.65	0.35	0.65

Table 2.5 Typical parameters comparison of the most diffused Schottky diodes for EH.

Power losses must be lowered as low as possible, especially for low input power applications, therefore the EH rectifiers tend to be implemented with the lowest number of lumped elements. For this reason, the most popular rectifier topologies for low-power RF EH are the half-wave single diode, full-wave voltage doubler, and bridge architectures, as shown in Figure 2.22.

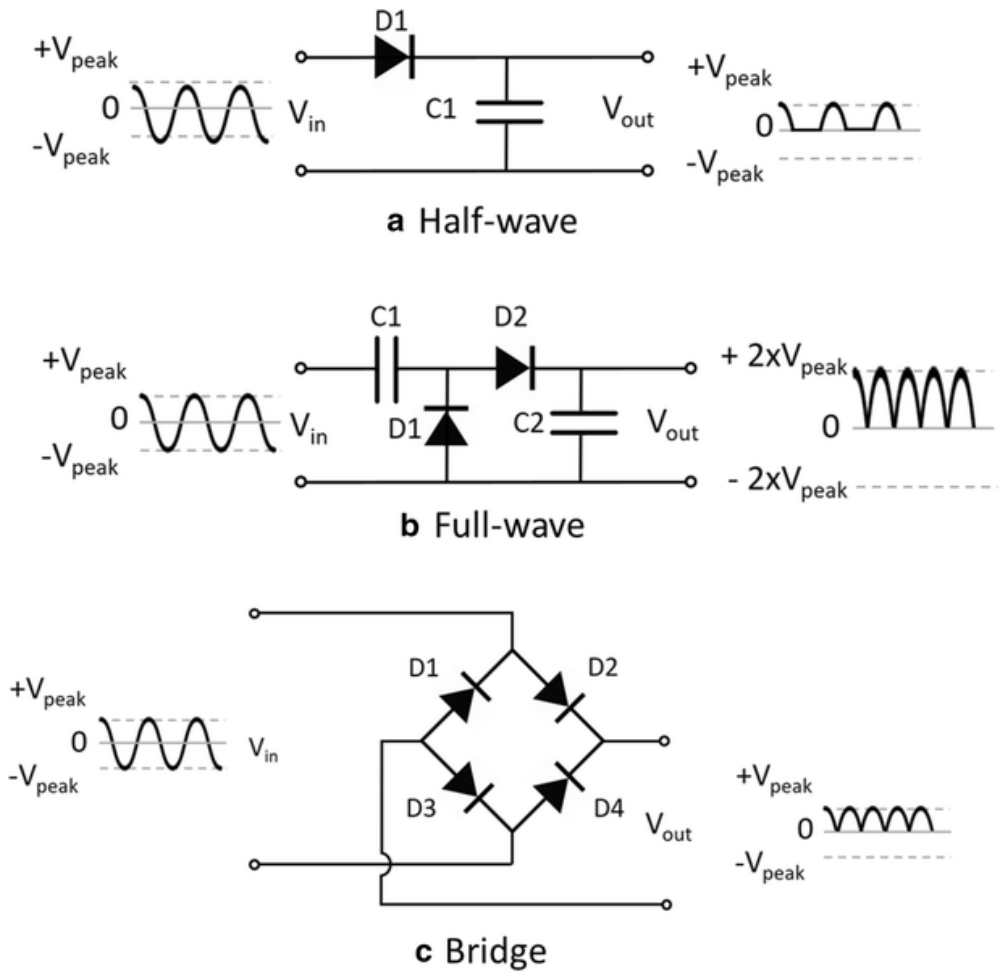

Figure 2.22 RF EH rectifier architectures for low input power applications: (a) half-wave single diode; (b) full-wave voltage doubler; (c) full-wave bridge rectifier.

Among them, single-stage voltage doubler (Figure 2.22b) is an interesting configuration, since it allows to both rectify the RF input signal and double the output

DC voltage. This is very important, especially for very low input power EH applications, since a converted DC voltage with higher amplitude helps the DC/DC converter stage to boost the supply signal more efficiently [93]. The voltage multiplication effect can be increased by adding further rectifying stage, at the cost of greater power dissipation [94]. Among the multistage voltage multiplier architectures, the Cockcroft–Walton is one of the most diffused (Figure 2.23). The architecture is quite similar to the voltage multiplier shown in Figure 2.22b, but it presents more stages, in order to increase the output voltage [95]. However, series-connected capacitors can lead to parasitic effects, which can degrade performance for low input power applications. To mitigate this problem, a modified scheme of the Cockcroft–Walton has been developed by Dickson, i.e. the Dickson voltage multiplier (see Figure 2.24), which employs shunt capacitors [96]. For these configurations, the high number of diodes and, therefore, the sum of threshold voltages and power dissipation lead to a PCE degradation.

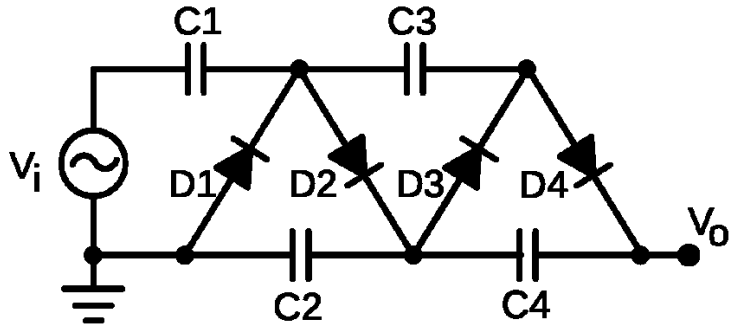

Figure 2.23 The Cockcroft–Walton voltage rectifier and multiplier.

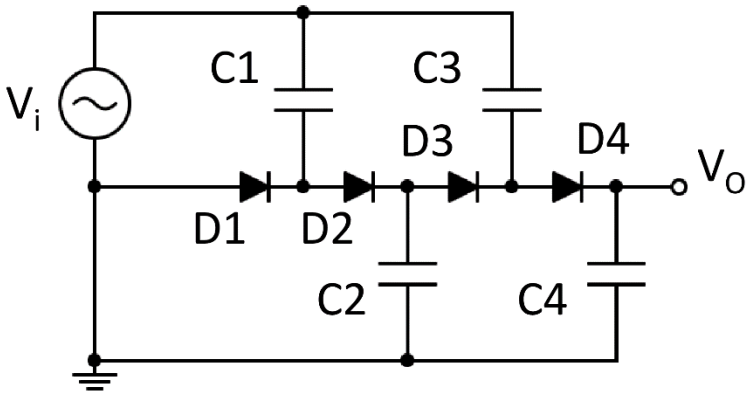

Figure 2.24 The Dickson voltage rectifier and multiplier.

On the other hand, the performance of a multistage rectifier is better for high input power EH applications, since the single diode architectures are limited by the

breakdown voltage of the diode itself. A compromise between output voltage gain, PCE degradation, and input power handling range should be fulfilled for the choice of the suitable number of diode rectifying stages.

The MOSFET technology can be employed, instead of Schottky diodes, for the design of RF EH AC/DC rectifier. The main advantages are the higher switching speed, which is better for very high-frequency energy harvesting applications, and the possibility to be integrated into IC designs, together with other parts of the system, such as DC/DC converters, power management blocks and so on. In figure 2.25, an example of a Dickson voltage rectifier, implemented with diode-connected MOS transistors is shown. The main drawback of MOSFET technology is the higher threshold voltage, which degrades the PCE, particularly for low input power EH. Several techniques have been investigated to overcome this disadvantage. Hashemi et al. in [97] presented a full-wave rectifier that uses a bootstrapped capacitor method to significantly reduce the threshold voltage of the MOS transistors.

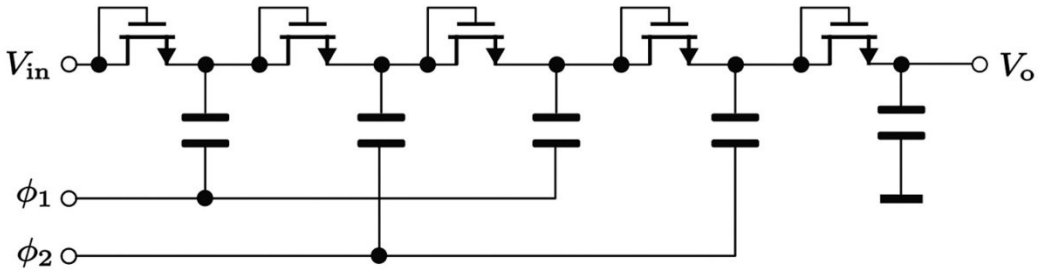

Figure 2.25 MOSFET based Dickson voltage rectifier and multiplier.

Another threshold compensation technique is the cross-coupled architecture, depicted in Figure 2.26. Here, the gate of each transistor is biased by the differential RF input signal. As Chouhan and Halonen stated in [98], "the transistor $N1$ is forward biased during negative half cycle of V_a, while V_b in positive half cycle gives a positive gate bias voltage to $N1$ transistor. This decreases the threshold voltage of the transistor and reduces the on-resistance. Similarly, when V_a is in the positive half cycle and V_b is in the negative half, the transistor becomes reverse biased and the gate voltage decreases, this raises threshold voltage, which reduces reverse leakage current".

Therefore, the output voltage amplitude of the architecture depicted in Figure 2.26 is doubled with respect to the input RF voltage signal, by neglecting the voltage losses in the transistors during switching operations.

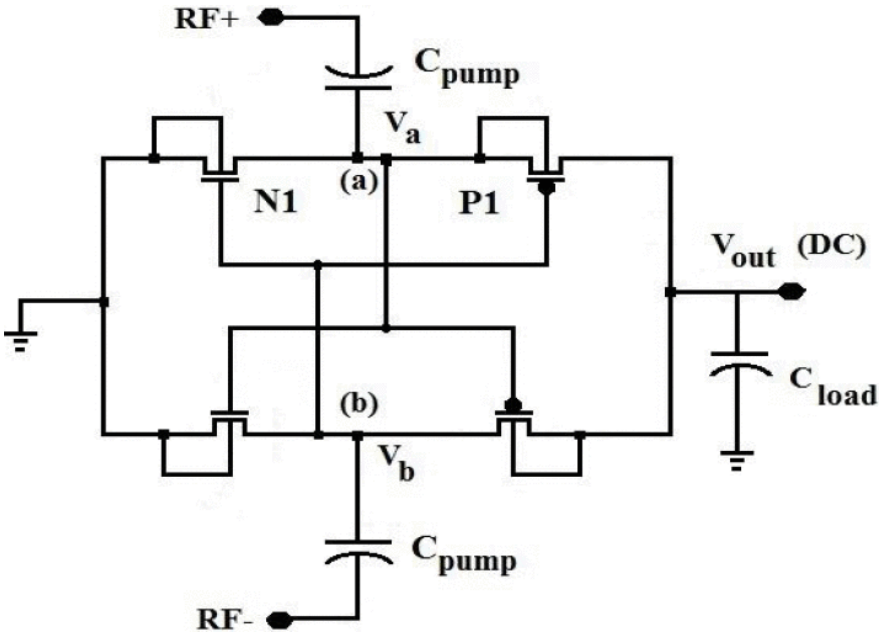

Figure 2.26 Topology of a cross-coupled MOSFET rectifier, reported in [98]. ©2015 IEEE. All rights reserved.

Finally, a comparison of different rectifier topologies and related performance is given in Table 2.6, as reported in [68].

Rectenna	Rectifier	Frequency (GHz)	OLR (kΩ)	Output voltage (V)	Efficiency
[60]	Diode based Grienarcher voltage multiplier	0.9, 1.8, 2.1, 2.45	11	1.5 at pin = −10 dBm	55% at pin = −10 dBm
[99]	Single stage diode based voltage multiplier	2.45	-	5.5	75% for pin = 19 dBm
[100]	VD type rectifier	2.45	1	6.1	55% for RL = 1 K
[101]	Single stage diode based voltage multiplier	0.700-0.900 (broadband)	-	0.5 at pin = −6 dBm	50% at −10 dBm input power
[102]	Single stage diode based voltage multiplier	0.45-0.85 (broadband)	1.5	-	25%at −20 dBm
[103]	9 stage Dickson charge pump based on MOSFETs	0. 84-0 0.975 (broadband)	-	2 at pin = −16 dBm	60% at pin = 10 dB

Rectenna	Rectifier	Frequency (GHz)	OLR (kΩ)	Output voltage (V)	Efficiency
[104]	5 stage MOSFET based rectifier for high power and 10 stage rectifier for low input power	0.9	-	1.5	-
[105]	16 stage Cockroft Watson multiplier	0.45	1 M	3	10.94% at pin = 63.1 W
[106]	Diode connected zero threshold NMOS transistor	0.9	500	1.52	13% at pin = −14.7 dBm
[107]	Single stage shunt diode rectifier	1.8-2.5 (broadband)	0.5	-	60% at pin = 0 dBm
[108]	Schottky diode based rectifier	2.45	2.8	3 at pin = −15 dBm	60% at pin = −15 dBm
[109]	Schottky diode based rectifier	2-18	0.1	-	20% at pin = 0.1 mW/cm^2
[110]	Full wave Greinacher circuit	1.8	1.2	1.8 V at pin = 10 μW/cm^2	60% at pin = 10 μW/cm^2
[111]	0.18 μm CMOS	0.95	1	-	-
[112]	0.18 μm differential CMOS	0.935	-	1.8	67.5% at −12.5 dBm
[113]	Bridge rectifier (HSMS2820)	0.9-2.45	200	6.5	78% at 23 dBm
[114]	HSMS 285C	0.945	0.1	4.5	52% at −10 dBm
[115]	Sub rectifier circuits with HSMS 2822 and HSMS 2860	2.4	0.82 and 1.2	-	50% at 0-20 dBm

Table 2.6 Comparison table for different RF EH architectures, reported in [68].

2.3 THERMAL ENERGY HARVESTING

Thermal energy harvesting is mainly based on the thermoelectric effect, by means of thermoelectric generators (TEG). A TEG module allows converting heat into

electrical energy through the Seebeck effect, for which a temperature difference across the module causes motion of charge carriers, i.e. electrons and holes.

Among all the alternative sources, thermoelectric harvesting has a great relevance, since it produces green energy, it doesn't need maintenance because of high reliability of employed solid-state modules, it's environmental efficient since it recovers energy from wasted heat and it is scalable, according to the source and the amount of energy needed [116].

In order to gather thermal energy and convert it into electricity, a temperature gradient is needed, while the heat flow provides the amount of power. Unlike conventional heat engines, the efficiency of thermoelectric devices is constrained, according to the Carnot limit [117], under 15%, therefore the produced energy could be lower, but still suitable for low-power devices.

A typical thermoelectric EH systems is depicted in Figure 2.27 and it is composed of a thermoelectric module, which is placed between a thermal gradient; the TEG produces a DC voltage that is proportional to the harvested heat, therefore no particular conversion circuit is needed before a DC/DC converter, which adjusts the voltage level for the output load.

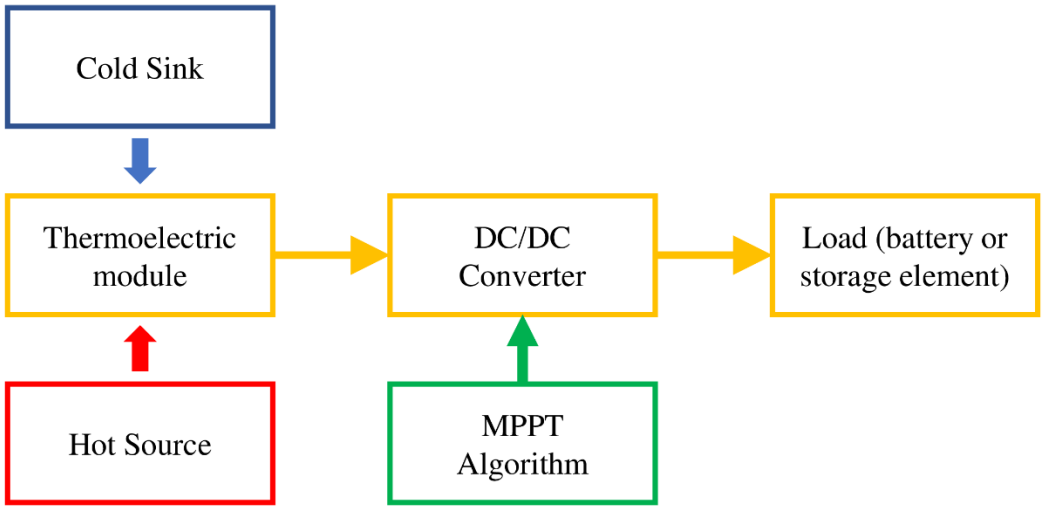

Figure 2.27 Block scheme of a typical Thermoelectric Energy Harvesting System.

A maximum power point tracking (MPPT) algorithm controls the DC/DC operation, in order to extract all the available power from the TEG source.

The Seebeck effect is a phenomenon that occurs when a temperature difference is applied between the joints of two different electric conductors. This leads to the motion of charge carriers and, therefore an electromotive force (EMF) is created along the circuit, so the electrons tend to move towards the lower potential while the positive ions move on the other side. This movement of electric charges induces an electric voltage at the ends of the joint conductors, which is proportional to the applied temperature difference [116], times the Seebeck coefficient α. Therefore, the voltage generated by a TEG module under a temperature gradient con be computed as

$$V_{TEG} = \alpha(T_h - T_c) \tag{2.27}$$

where α is expressed in $[V/K]$ and $T_h - T_c = \Delta T$ is the temperature difference, where T_h is the hot temperature while T_c represents the cold temperature.

The Seebeck phenomenon can be observed with every couple of different conductive, semi-conductive or insulator materials, according to the electron behavior of the material valence layer [118], but the efficiency of power generation can be quite different. In order to increase the heat to electricity conversion efficiency, the choice of the target materials for the TEG module that has to be employed for EH purposes aim to maximize the Seebeck coefficient, as well as the electrical conductivity σ $[S/m]$ and to minimize the thermal conductivity k $[W/(m \cdot K)]$. The latter helps to keep constant the temperature difference between the hot junction and the cold junction of the TEG module, avoiding the two temperatures to equalize [119].

To evaluate the performance of a thermoelectric material, the above-mentioned parameters can be combined to establish a figure of merit Z [120], which is defined as

$$Z = \frac{\alpha^2}{k \cdot \rho} \tag{2.28}$$

where ρ $[\Omega/m]$ expresses the electrical resistivity of the joined materials. To express the figure of merit as a dimensionless parameter (*ZT*), it can be multiplied by the average temperature $\bar{T}$ [120], where

$$\bar{T} = \frac{T_h - T_c}{2} \tag{2.29}$$

Although there is no theoretical limit to the *ZT* value, typical high-performance materials tend to reach the unity value. However, *ZT* is not constant with temperature, which affects all the parameters, therefore different material exists, based on the

working temperature range [118]. In Figure 2.28, the correlation between the *ZT* parameter and temperature is depicted, as reported in [118].

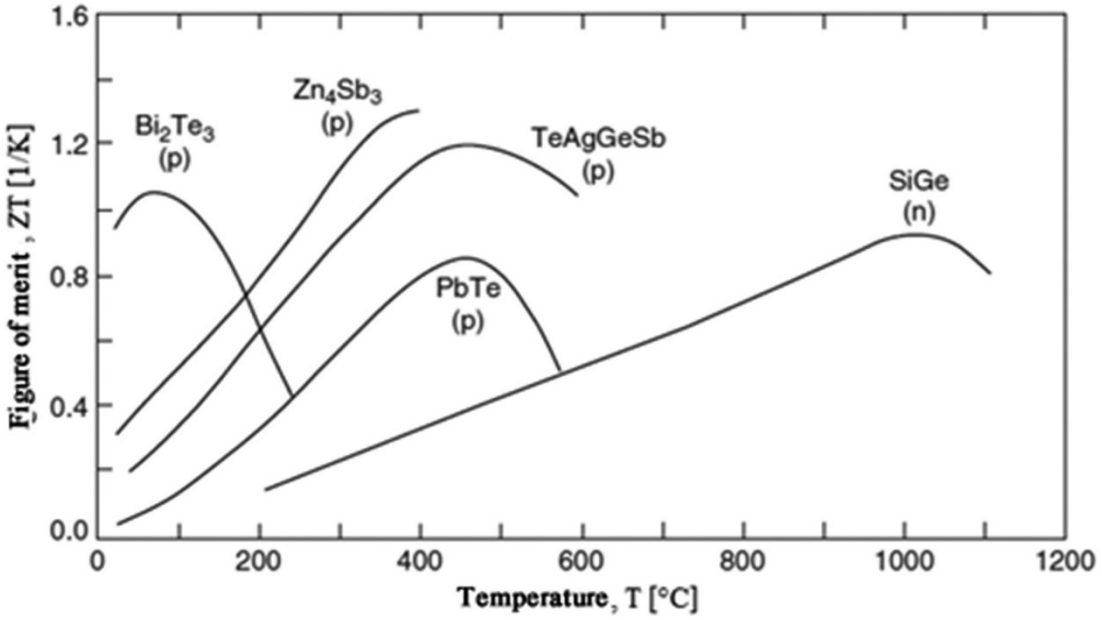

Figure 2.28 Relationship between the figure of merit *ZT* and temperature variation for the most common high-efficiency thermoelectric materials, reported in [118]. ©2002 IEEE. All rights reserved.

It has been demonstrated that metals cannot achieve a high figure of merit *ZT* values since it is not possible to increase one characteristic parameter without affecting the others. For this reason, semiconductors showed to be a good candidate for high conversion efficiency, because of their intermediate concentration of charge carrier [121]. The above figure shows the most diffused semiconductor thermoelectric materials, according to the working temperature range. It can be noticed that the bismuth telluride (Bi_2Te_3) denotes high efficiency for low-temperature ranges, while Lead telluride (PbTe) and silicon-germanium (SiGe) are the good candidates for high temperatures applications. Recently, new thermoelectric materials have been investigated to achieve higher *ZT* values, around 3 or 4, such as quantum wells, quantum dots and quantum wires [119], [121].

The thermal to electrical energy conversion efficiency η is also correlated to the *ZT* parameter, as demonstrated by the following equation [122]:

$$\eta_{max} = \frac{\Delta T}{T_h} \frac{\sqrt{1 + Z\bar{T}} - 1}{\sqrt{1 + Z\bar{T}} + \frac{T_c}{T_h}} \tag{2.30}$$

where the term $\Delta T/T_h$ express the Carnot efficiency. The equation 2.30 states that the maximum conversion efficiency is limited by *ZT* of the material. Figure 2.29 shows the relationship between different values of *ZT* and the conversion efficiency, as reported in [119]:

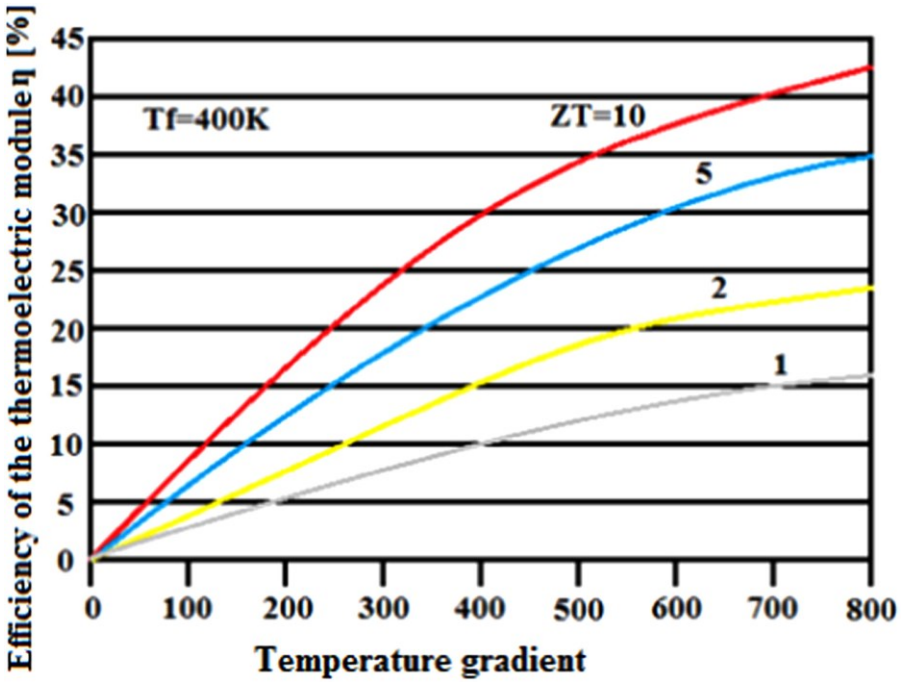

Figure 2.29 Relationship between efficiency, temperature difference, and *ZT,* as reported in [119].

While the research is focusing on new high-performance thermoelectric materials with higher *ZT*, recently some advances have been conducted for existing TEG. Bitschi in [123] achieved a conversion efficiency of up to 25% by adding 1% of cerium or ytterbium to Bi_2Te_3.

A TEG module is generally composed of a matrix of thermoelectric junctions, that are electrically connected in series while parallelly connected from a thermal point of view so that the output voltage and current can be increased [121]. Each pillar of every thermal joint couple is n-doped and p-doped, respectively, forming a junction of two different semiconductor types (see Figure 2.30). The connection between semiconductor couple is made with copper plates, so as the upper side of the plates form the cold side, while the downside constitutes the hot surface. Both sides of the TEG module are covered by ceramic layers or other high thermal conductivity materials.

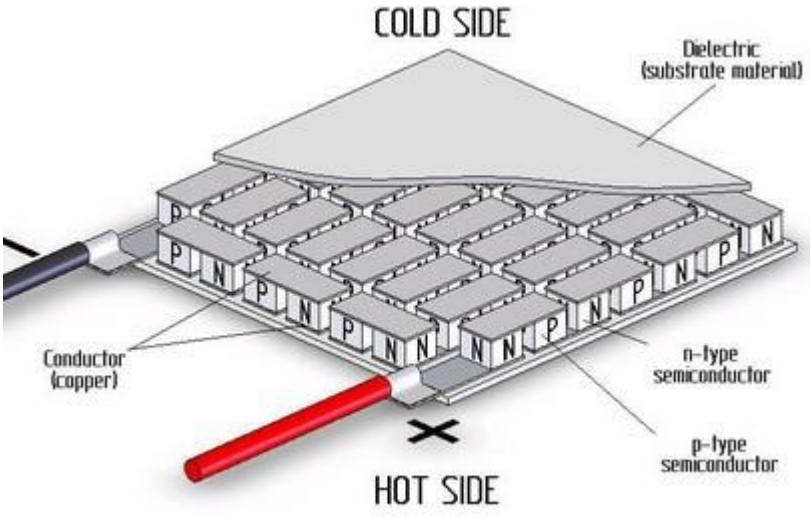

Figure 2.30 Typical structure of a TEG module [124].

The operating temperature range for a TEG module is also important since excessive thermal expansion could cause mechanical stress that could damage the device [125].

Recent advances in electrical energy generation by means of thermoelectric materials provided a large space of application for thermoelectric energy harvesting in many fields of interest. In automotive, for instance, the BMW company developed in 2005 a TEG EH system which is able to produce up to 200W of electric power, with a temperature difference of 207 °C, that is generated directly from the exhaust part of the engine [126].

Figure 2.31 TEG EH system for battery charging in a BMW [126].

Also, in the aerospace industry, the TEG EH is a great field of interest for many years. The first application of thermoelectric energy harvesting was employed to

support the Voyager I, the robotic spacecraft developed by NASA (National Aeronautics and Space Administration) on September 5th, 1977 [127]. The system, called Radioisotope Thermoelectric Generator (RTG) relies on the natural decomposition of the radioactive plutonium-238 ad a thermal source, while the space provides the cold temperature, in order to establish a consistent temperature gradient for TEG module of the EH system. The system was then improved and utilized in other space missions, as for the famous space research mission Cassini-Huygens (see Figure 2.32).

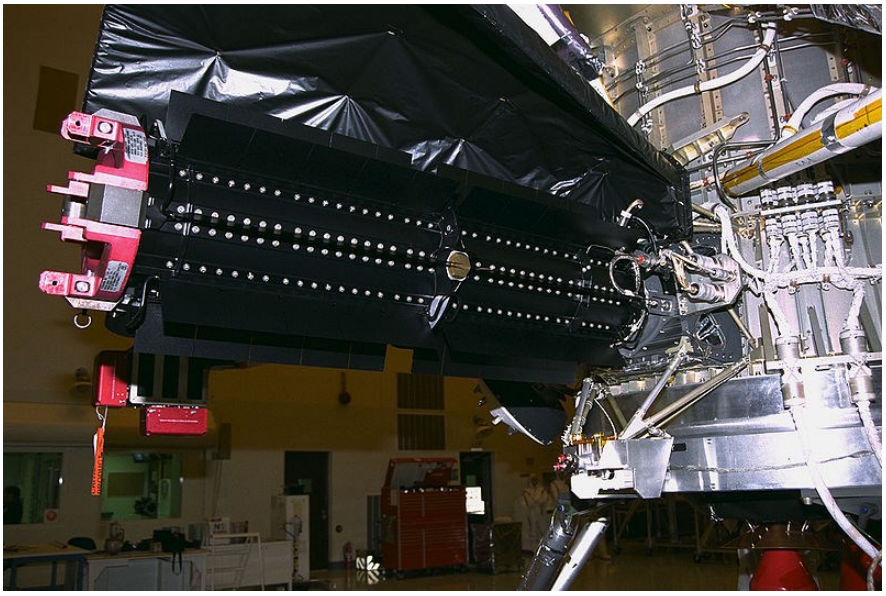

Figure 2.32 RTG employed for the Cassini-probe in 1997.

The thermoelectric energy harvesting was also applied for in-house generation and building installations. Ghaddar and Shihadeh in [128] proposed to exploit thermoelectric EH with a domestic woodstove. They applied a custom thermoelectric module on a woodstove with controlled fire rate and temperatures, while exploited commercial heat sink to cool the external side of the TEG by means of natural convection. The achieved maximum power, at a matched load, was 4.2 W for a single module. In Figure 2.33 the whole system is showed, with a section view of the cooling heatsink (Figure 2.33b), that was tightened to the TEG module, in order to improve the heat exchange with the ambient and increase the thermoelectric efficiency.

Azarbayjani and Anderson in [129] demonstrated the feasibility of a TEG EH system for building, in order to gather energy from the temperature difference between the indoor and outdoor environment.

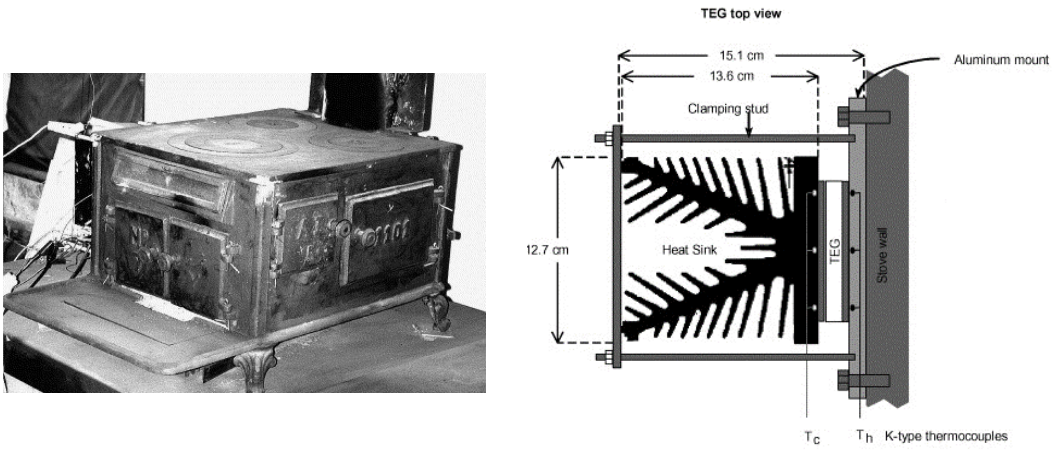

a) b)

Figure 2.33 Domestic woodstove TEG EH system (a) and TEG cooling installation (b) presented in [128].

The 3 cm × 3 cm modules were applied to the wall of an office and the collected power was employed to supply the room, which was equipped with computers, monitors, electric lights, printer, and scanner. The authors measured a maximum output power of 5W per module, with an average temperature difference of 18°C for six months. A total number of 90 TEG modules were employed to properly supply enough energy for the whole office.

As demonstrated, the advantages of thermoelectric EH were widely studied and applied in many fields, where high-temperature gradients can be exploited to generate power. Recently, the possibility to harvest power from low-temperature difference were investigated, in order to feed autonomous sensors or portable and wearable devices. As stated before, the thermoelectric conversion efficiency is strongly related to the material characteristics and to the working temperatures. Generally speaking, standard and widely used thermoelectric media are intended for high-temperature difference applications, therefore their figure of merit *ZT* is quite low for low-temperature gradients [118]. Hence, the study of new thermoelectric materials and new EH architectures and systems to improve the energy conversion efficiency constitute a great field of interest, considering the great diffusion and the increasing demand for portable electronic applications and autonomous sensors.

In this perspective, novel fabrication techniques have been investigated recently, in order to implement thin-film thermoelectric devices, including electrochemical MEMS (Micro Electro-Mechanical Systems) [130], CVD (Chemical Vapour

Deposition) [131] and plasma sputtering PVD (Plasma Vapour Deposition) [132], [133]. The authors in [131] implemented a superlattice Bi_2Te_3 that was grown by a metallorganic chemical vapor deposition process, that was employed to realize a 4x4 array of p-n couples in a 2.5 mm × 2.5 mm × 0.3 mm TEG module. Measurements demonstrated that the module is able to produce 1 W and 31 mW with a temperature difference of 200 °C and 5 °C, respectively, showing superior performance even at low-temperature gradients.

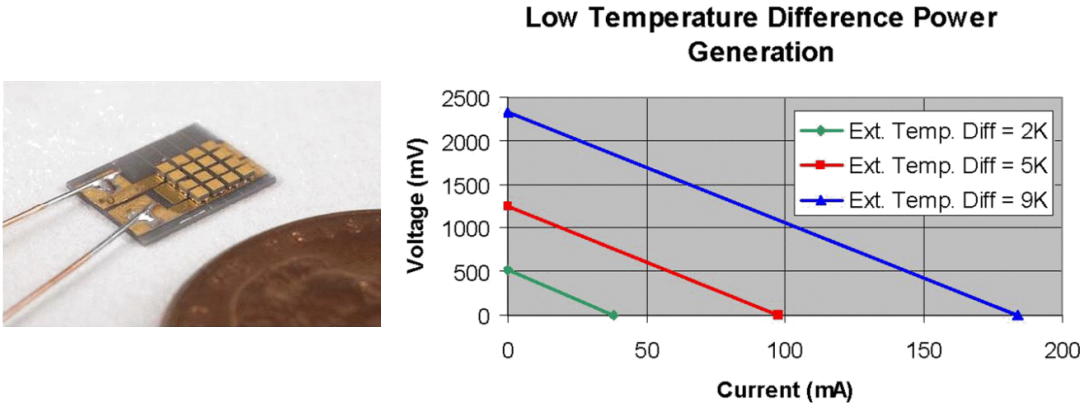

a) b)

Figure 2.34 The 4x4 array TEG module (a) and its power generation performance at low-temperature difference (b) [131]. ©2007 IEEE. All rights reserved.

Bottner, Nurnus et all in [132] implemented the first micro-thermogenerator module based on the V-VI-groups Bi2Te3 and (Bi,Sb)2Te3 for enhanced performance. The authors measured a maximum out power, at matched load, of 0.67 µW at a temperature difference of 5 °C. The active area of the implemented TEG is of 1400 µm × 800 µm, resulting in a minimum power density of 0.60 $\mu W/mm^2$.

Research institutes and companies recently presented some portable applications with thermoelectric generators. Seiko and Citizen implemented two wristwatch models that are directly supplied by the human body's heat, which is converted into electricity by means of a micro-TEG directly embedded inside the watch [118]. The Seiko "Thermic" watch is able to produce an open-circuit voltage of 300 mV with only 1.5 °C of temperature difference, and a maximum output power of 22 µW, while the Citizen "Eco-Drive" wristwatch is equipped with 1242 thermoelectric junctions that are able to generate 13.8 µW per degree centigrade of temperature difference.

Gyselinckx et al in [134] studied the possibility to implement micro-thermoelectric generators that can gather energy from the human body's heat, in order

to support wearable for a wireless body area network. According to Gyselinckx's statistic results, the average heat flow produced by the human body is $19\ \mathrm{mW/cm^2}$, as shown in Figure 2.35. Based on this characterization, they exploited the MEMS technology to implement a wearable bracelet with a thermoelectric generator based on commercially available BiTe thermopile, thermally matched with the human body and the surrounding. The module can produce an average output power of 100 µW and an output voltage up to 2.4 V.

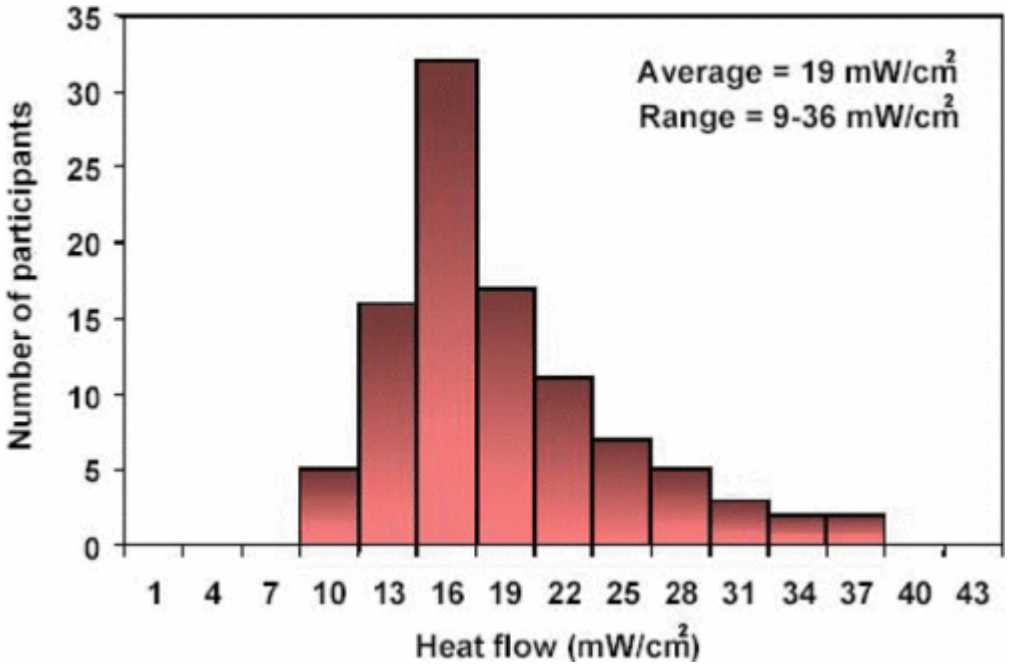

Figure 2.35 Heat flow from human body measurement at t_{room}(avg) = 22 °C, t_{skin}(avg) = 30 °C. [134] ©2005 IEEE. All rights reserved.

Thermal energy harvesting from the human body's heat represents nowadays a great field of interest because it could be a solution to potentially provide endless energy for the new generation, low-power wearable devices, such as health monitoring or activity tracking systems, as described in chapter 1. It consists to exploit the body heat as a thermostatic source [135], in order to convert it into electrical energy by means of the temperature difference that establishes between the human body and the external surrounding. This thermal gradient could be very low, and also both the skin temperature and the air temperature could vary along with time and weather conditions[136], therefore the realization of a Thermal EH system could be a challenge. Wang et al, in [137], presented the realization of a wearable miniaturized TEG for human body applications based on a surface micromachined poly-SiGe thermopile. One of the major advances presented in this work consists of the

improvement of the thermal resistance presented by the thermocouple array. Indeed, the conceived human body power generation system can be modeled, from a thermal point of view, with an equivalent circuit where the TEG is connected in series with the ambient and the human skin, as shown in Figure 2.36.

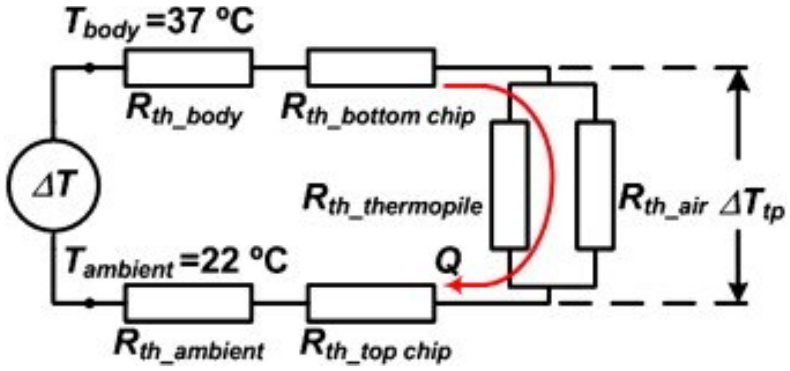

Figure 2.36 Equivalent thermal circuit model of a typical TEG EH system for human body heat energy conversion [137]. ©2009 Elsevier. All rights reserved.

Both the human skin and the ambient present a high thermal resistance [136], while the micromachined TEG is typically characterized by a very small resistance, caused by the short height of the thermoelectric couples and by the parallel connection, from a thermal point of view, which further decreases the thermal resistance. For these reasons, the temperature difference across the thermopile is significantly decreased, with respect to the temperature gradient between the human body and the air. As shown in figure 2.36, the thermal resistance of the thermoelectric couples is in parallel with the air resistance, which fills the gap between junctions. Therefore, a possible solution is to significantly increase the air thermal resistance by adding thicker space between the skin contact and the air contact of the TEG module. Wang et al featured the thermopile with a high rim structure, standing of Si substrate (see Figure 2.37), in order to increase the air gap and, therefore, the overall thermal resistance of the active area. With a total number of 2350 of thermocouples, results demonstrated that the chip was able to deliver an open-circuit voltage of $12.5\ \mathrm{V/(K \cdot cm^2)}$ and an output power of $0.026\ \mu\mathrm{W/(K^2\ cm^2)}$ on a matched external load. The final system realization is shown in Figure 2.38, where a heatsink is also added to lower the air thermal resistance.

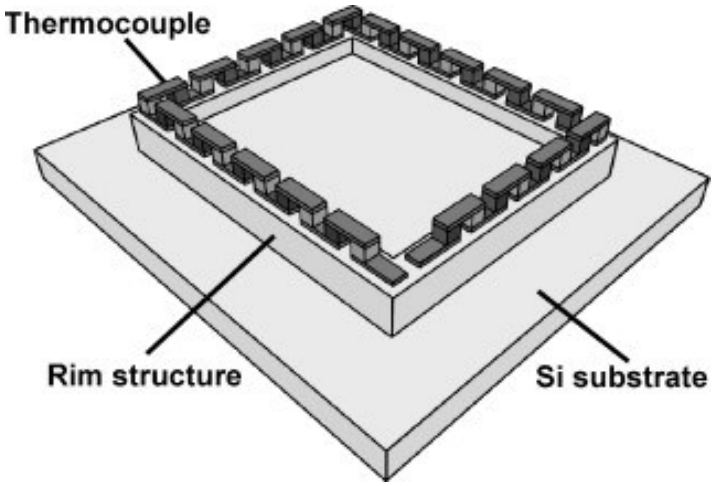

Figure 2.37 Rim structure for the thermopile realization, proposed in [137]. ©2009 Elsevier. All rights reserved.

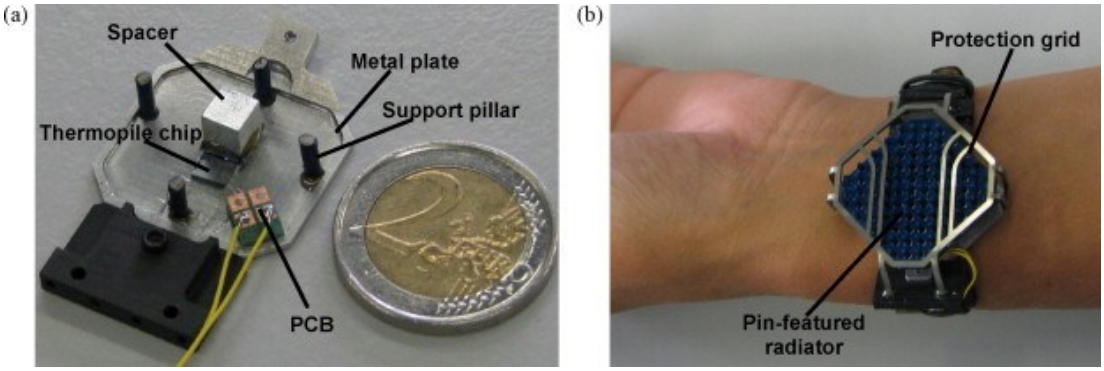

Figure 2.38 Implementation of the thermal EH system proposed in [137]: (a) TEG being assembled; (b) TEG being worn on the human body. ©2009 Elsevier. All rights reserved.

2.4 BIOMECHANICAL ENERGY HARVESTING

Biomechanical energy harvesting is another promising field where the aim is to gather electrical energy directly from the human body motion, which could represent a leading technology to directly feed wearable sensors and devices, together with the human body heat energy harvesting, as stated in the previous paragraph. It was demonstrated by McArdle et al in [138] that the amount of energy expended by the human body is about $1.07 \cdot 10^7$ J per day, which is approximately equivalent to 800 AA (2500 mAh) batteries. The total weight of such an amount of batteries is about 20 kg, while the same energy produced by our body can be obtained from just 0.2 kg

of fat. Therefore, the efficiency of the human source of energy (carbohydrates, fats, and proteins) is typically 35 to 100 times higher than the efficiency provided by the currently available batteries [139].

The amount of energy released by the human body is the combination of heat and motion. Winter in [140] estimated that the human body mechanical efficiency is about 15-30%, which means that the majority of energy released as heat in the environment. This result suggests that the best way to harvest the human body produced energy is to convert heat into electrical energy by means of thermoelectric generators. However, to harvest this energy, it would be necessary to cover the body with a thermoelectric material (perhaps a jacket or a garment like a diving suit). The design of an item of clothing with an embedded thermoelectric material that would cover part of the body (or the whole body) is obviously a challenge [141]. Since in cold weather, the device would have to function as a thermal insulator; however, currently available thermoelectric materials have a much higher thermal conductivity than typical coat material [141]. This would result in a coat that would be too heavy to wear or in a need for an additional layer of thermal insulation material, thereby reducing the temperature difference along with the device. In addition, such a device would have to allow sweat evaporation; however, this would mean that some of the sensible heat would flow out through the openings, causing a loss of available energy [141]. The above statements imply that this technology would be more convenient for low power applications, for which it would be necessary to cover only a small part of the human body.

Therefore, biomechanical energy harvesting could be a complementary solution to obtain free and green energy from the human body's daily activities, to power portable devices. When considering a particular human motion as a candidate for energy harvesting, the following main factors must be taken into consideration. First, muscles perform positive and negative mechanical work within each motion: During the positive work phase, the muscles generate the motion, and in negative work phases, the muscles absorb energy and act as brakes to retard or stop the motion [141]. The negative and positive muscle work has been described in [140] as follows: positive work is the work performed by the muscles during a concentric contraction, i.e., shortening of the muscle when the torque applied by the muscle at the joint acts in the same direction as the angular velocity of the joint [141]. When the muscle performs

positive work, it generates motion. Consequently, the use of positive energy will always increase the metabolic cost. On the other hand, negative work is the work done during an eccentric contraction, i.e., lengthening of the muscle, when the muscle torque acts in the direction opposite to the angular velocity of the joint [140]. An energy harvesting device should, therefore, replace part of the muscle activity during negative work and create resistance to retard the motion, similar to "generative braking" in hybrid cars. Theoretically, such a device will allow energy generation with minimal or no interference with natural motions [140].

For the analysis of the energy generated by the human motion, i.e. the produced work, formulas of the force acting through a displacement and the product of torque and angular displacement can be employed, and are defined as [141]:

$$W = \int_0^S F \cdot ds \tag{2.31}$$

$$W = \int_0^\theta \tau \cdot d\theta \tag{2.32}$$

where F is the applied force, τ represents the torque, while S and θ indicate the linear and angular displacement.

To harvest biomechanical energy produced by the human motion, several techniques have been investigated in the literature, which involves different transducing processes and conversion methods. The most diffused are piezoelectric, electrostatic, electromagnetic and triboelectric [142].

The piezoelectric phenomenon consists of the electric charge accumulation in specific materials, i.e. piezoelectric media when a strain is applied [143]. In particular, the force applied to the material induces the reconfiguration of the dipole ions in the lattice, which generates an electric field and, therefore, a potential difference between the material terminals. Among the availability of piezoelectric media, inorganic compounds such as Zinc oxide (ZnO) and the lead zirconate titanate ($PbZr_{0.42}Ti_{0.58}O_3$) also known as PZT, are the most used in mechanical energy harvesting applications [143], [144]. The PZT is also strongly diffused for sensors and actuators implementation, while the presence of lead limits its application for implantable devices, because of the toxicity for human health. On the contrary, the ZnO is

biocompatible [145] and offers high piezoelectric capability [146] and high electron mobility [147].

Even Though inorganic piezoelectric materials present a higher piezoelectric effect, compared to the organic materials, they present some limitations regarding the fabrication process and the substrate for deposition, which limits their application, especially when flexibility is needed [142]. For this reason, the organic piezoelectric materials could represent a good choice for implantable and wearable devices, because of their flexibility, low-cost fabrication process, lightness and biocompatibility [142].

The polyvinylidene fluoride (PVDF) and the polyvinylidene-fluoride-trifluoroethylene (PVDF-TrFE) are two of the most investigated organic piezoelectric material for biomechanical energy harvesting applications, but also for sensors and actuators [148], [149] and [150].

Among all the joints and locations of the human body for biomechanical energy harvesting, one can be mention heel strike, leg motion, arm motion, and center of mass motion. Heel strike refers to the part of the walk cycle during which the heel of the forward foot contacts the ground [141]. This motion can be considered as a perfectly elastic collision [151], but some researchers state that there is an elastic percentage in the collision [152]. Shorten in his work computed the energy loss in a running shoe, relating it to a linear displacement of the shoe sole. He predicted that for a typical runner moving at 4.5 m/s, the value of the dissipated energy could range from 1.72 to 10.32 J during a single step and that most of the energy loss would occur during the heel strike [141], [152]. By using a viscoelastic model and assuming a displacement of 4 mm in the shoe sole, the work for the heel compression results equal to 2 J/step, for an 80 kg of body weight. Since a complete stride at natural walking speed has a frequency of approximately 1 Hz (two steps per second), the theoretical maximal power will be 4 W. Moreover, if 50-80% of the energy during walking is stored as elastic energy in the shoe [141], [152], the maximum available energy that could be recovered is equal to 2 W.

The heel strike is not the only part of the walking activity that produces energy; human muscles generate also torques, along with three axes, at the ankle, knee and hip joints for leg motion [141]. In Figure 2.39, the typical magnitudes for the whole leg torques are reported for a subject mass of 58 kg, speed 1.3 m/s and a walking frequency of 0.9 Hz [140], [141]. Winter et al, in their research [153] calculated the work

performed at different leg joints during a single step and normalized it by the subject's weight. In addition, they divided the net work done by the muscles at the joints into several phases of motion [141], and the resulting classification is reported in Table 2.7, where A1-4 are phases of work that are performed in the ankle joint, K1-4 are phases for the knee, and H1-3 are for the hip joint.

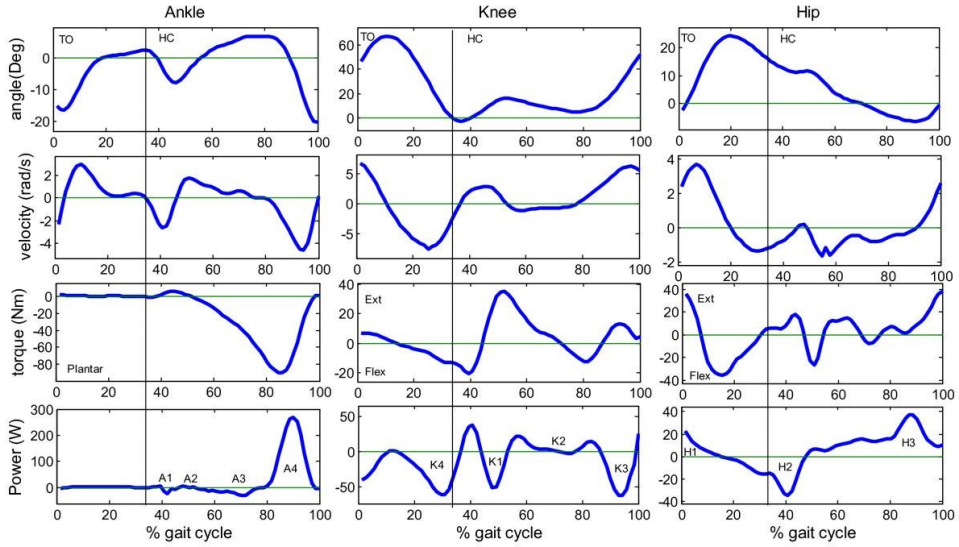

Figure 2.39 Typical kinematics and kinetics during a walking cycle, as reported in [141].

work during the phase (J/kg)	average (J/kg)	standard deviation (J/kg)
Ankle A-1	-0.0074	0.0072
Ankle A-2	0.0036	0.0046
Ankle A-3	-0.111	0.042
Ankle A-4	0.296	0.051
Knee K-1	-0.048	0.032
Knee K-2	0.0186	0.026
Knee K-3	-0.047	0.015
Knee K-4	-0.114	0.015
Hip H-1	0.103	0.047
Hip H-2	-0.044	0.029
Hip H-3	0.090	0.027

Table 2.7 Work performed at the leg joints during a walking step normalized by the subject's mass, as reported in [141].

According to the above outcomes presented by Winter et al in [153] and the calculations performed by Riemer and his colleagues in [141], the resulting energy, for an 80 kg person walking at normal speed, is 33.4 J for the ankle, 18.2 J for the knee and 3.52 J for the hip motion.

Arm motion refers to the backward and forward swinging movement of the arm that occurs during walking and running. The arm motion is composed of two sub-motions: the relative motion between the forearm and the upper arm (change of angle of the elbow) and the relative motion between the trunk and the upper arm (change of angle at the shoulder) [141]. As for the leg joints, Riemer et al conducted an experiment, based on the method applied by Winter and its colleagues in [153], to compute the energy released for the arm motion, involving three male subjects of average weight of 82 kg who walked at a speed of 1.1 m/s and six-camera motion capture systems at a sample rate of 100 Hz [141]. They reported a maximum work of 1.07 J for the elbow, with a maximum power of 2.1 W, and a maximum work of 1.3 J for the shoulder, with 2.2 W of maximum power.

In the literature, several examples of biomechanical energy harvesting system implementations have been presented. Kymissis et al in [154] proposed three different devices that can be integrated into a shoe to gather energy coming from the heel strike and convert it into usable electrical energy.

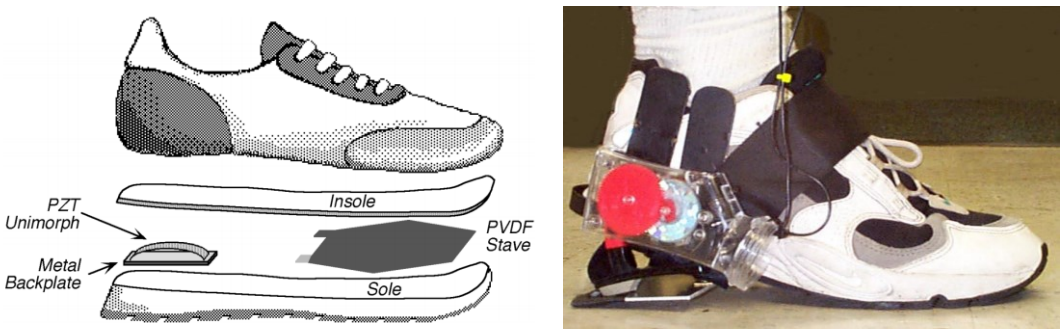

a) b)

Figure 2.40 Structure of the biomechanical EH system from the foot movements and strike, where in (a) shows the PZT and PVDF integrations into the sole and (b) depicts the external electromagnetic generator. [154] ©1998 IEEE. All rights reserved.

Here, two different piezoelectric materials were integrated into the shoe sole, while an external electromagnetic generator was coupled with the shoe heel (see Figure 2.40). The resulting EH system was applied to power an RF tag device, in order to

transmit information such as the identification code of the user. The adopted conditioning circuit for the energy conversion, shown in Figure 2.41, represents the typical architecture for piezoelectric energy harvesting from mechanical motion. The output alternated voltage produced by the piezoelectric devices in fully-rectified by means of a diode full-bridge arrangement. The DC charge is then stored into the electrolytic capacitor C1. The circuit mainly composed of transistors *Q1* and *Q2*, and the 12 V Zener diode *D2*, acts like an SCR with supercritical feedback, as stated in [154]. Basically, it allows the capacitor *C1*, to self-charge until it reaches 12.6 V, then the stored energy id discharged towards the voltage regulator *U1*, which was set for 5 V operation. During the output voltage regulation period, the RF transmission is performed by means of an encoder and an RF transmitter.

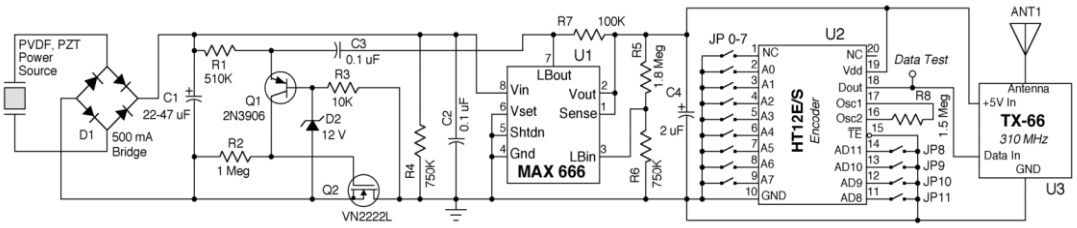

Figure 2.41 Schematic diagram showing power conditioning electronics for PZT and PVDF energy harvesting, presented in [154]. ©1998 IEEE. All rights reserved.

The above piezoelectric EH system showed an average output power of 1.1 mW for the PVDF stave, 1.8 mW for the PZT heel and 0.23 W for the electromagnetic generator. The authors considered an equivalent output power-matched load of 250 kΩ for the piezoelectric devices and a 10 Ω of equivalent load for the EM generator.

Another example of biomechanical EH applied to the knee rotation was proposed by Niu et al in [155] and implemented by Donelan et al in [151]. The device is an orthopedic knee brace that is configured such that knee rotation drives a gear train (113:1) through a unidirectional clutch, transmitting only knee extension motion to a DC brushless motor that functions as electric generator [141]. The system, depicted in Figure 2.42, is able to generate 2.5 W per knee at a walking speed of 1.5 m/s, while the metabolic cost of producing energy is 4.8 W. As stated in [141], the major drawback of this work is that only a small part of the knee motion is exploited for energy generation, i.e. the end of the swing phase. In fact, during the walking cycle, the work produced in the knee is about 34 W, while the device is able to harvest power only in the final period of the knee rotation, with a conversion efficiency of 65%.

Riemer et all stated that the remaining available energy for harvesting purposes is about 16.8 W. Furthermore, the proposed device weighs 1.8 kg and presents a considerable encumbrance. The added metabolic cost to face the inertia of the harvester was not taken into account for the computations of the efficiency, but it can be relevant.

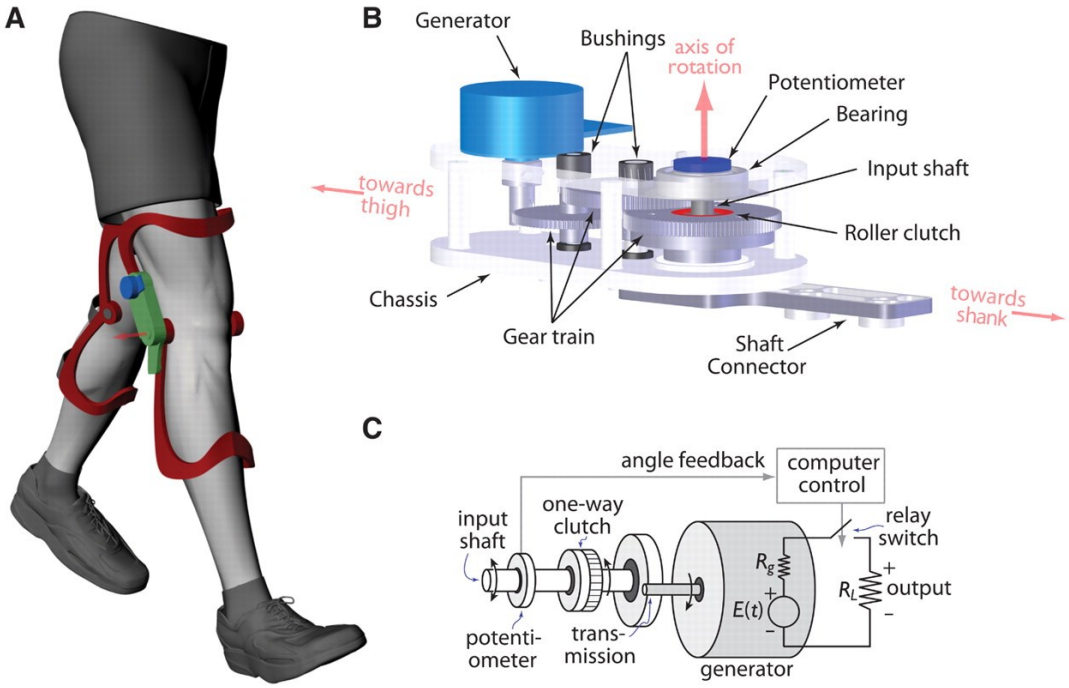

Figure 2.42 Biomechanical energy harvester from the knee motion, as presented in [156].

2.5 SUMMARY AND IMPLICATIONS

The literature review presented in the previous paragraphs underlines how energy harvesting for low-power applications is gaining great importance for the present and next generation of autonomous systems and both wearable and implantable devices. In particular, RF electromagnetic, thermoelectric and biomechanical energy harvesting are currently considered as leading technologies to provide free and zero environmental impact energy, in order to support low-power devices as mentioned before. Although the research in this field achieved promising results, there are several issues and challenges that should be solved, with the aim to further improve the efficiency of the energy extraction and conversion processes. Techniques and methods for the RF EM energy harvesting and conversion need a relatively high complexity system architectures, involving the antenna design, conditioning, and conversion

circuitry. Here the major issues are related to the amount of power that can be captured by the system and to the high-frequency impedance matching requirements, which have to satisfy both the input power and the working frequency specifications. As stated in paragraph 2.2, it is difficult to fulfill both matching requirements, since the two parameters are not independent. Moreover, increasing the matching network complexity can result in an additional degree of freedom, but the energy conversion efficiency is negatively affected, because of the parasitics introduced by the high number of matching components, i.e. lumped element or distributed EM structures.

Regarding thermoelectric energy harvesting, the conditioning circuit for the EH system is simpler, compared to the RF EH method, but the power transfer efficiency from the heat source to the storage element still impose matching requirements. The performance of the overall TEG EH system could be affected if the impedance matching is not properly treated during the system design, especially for low-temperature gradient sources, as the human body for wearable applications. Here, a good representation of the equivalent electrical model for the transducer, i.e. the thermoelectric generator, can help the design to improve the conversion efficiency, taking into account the internal impedance of the TEG, without considering it as an ideal generator. The same consideration can be inferred for biomechanical energy harvesting, where also encumbrance is the main problem.

In the next chapter, several solutions regarding RF electromagnetic, human body thermoelectric and biomechanical energy harvesting are presented, as a result of the research work conducted during Ph.D. studies and activities.

Chapter 3: RF Energy Harvesting Contributions

In this chapter, the author's contribution to novel methods, design procedures and implementation of RF electromagnetic energy harvesting systems for autonomous sensors and wearable biomedical applications are reported.

3.1 DUAL BAND RF HARVESTER WITH RECONFIGURABLE POWER CHANNELS

One of the problems related to the RF Energy harvesting design is the amount of available input power, which is related to the RF power density that occurs around the harvesting space, at the working frequency, as stated in chapter 2. In case of environment long-range RF energy harvesting sources, e.g. mobile-phone communication networks, or TV telecommunication broadcasting, the signal power strength could be very low, since the source may be located at a long distance. If the received power is not enough, the RF-to-DC converter of the EH system could not be able to work properly, since the received signal is below the rectifying diode voltage threshold. Therefore, a method to gather more energy is required. On the other hand, if the input available power is higher than the predicted power level during design optimization, the impedance of the rectifying section could change significantly, because of the non-linearity of the diode. Therefore, the impedance matching requirement is not satisfied anymore, which results in an efficiency degradation for the RF-to-DC power conversion. To overcome these limitations, a possible solution is to implement a multi-band RF energy harvester with reconfigurable power conversion channels. The multiband feature allows gathering energy from many RF sources, thus increasing the input available power, while the multichannel property ensures the maximum conversion efficiency for a wider input power range. In this contribution, a suitable system for energy harvesting, based on a dual-band architecture and able to handle both GSM and WiFi signals is proposed, with the aim to capture the largest amount of EM radiation in the urban environment. The key points of the designed

circuit are the capability to manage input signals over a wide power range together with the high energy conversion efficiency in the full band. It has been conceived as a dual-channel receiver, tuned at 936 MHz and 2.4 GHz, so to catch the largest amount of EM radiation in the surroundings. Defining the harvester efficiency as the ratio between rectified and input power, the proposed circuit shows an efficiency greater than 50% for an incoming power between −5 dBm and 15 dBm thanks to a suitable design both of the networks and of the control system. A prototype board has been fabricated and tested and the final board rendering is also presented. Finally, some experimental results are herewith shown.

3.1.1 Architecture Overview

The considered autonomous sensor as the target application equivalent load for the proposed EH system is a commercial gas sensor for carbon dioxide (CO_2) detection showing the system capability for wireless sensors networks. In Figure 3.1, a rendering of the final board is depicted. Each block of the board, including the commercial CO_2 sensor, is described in the following.

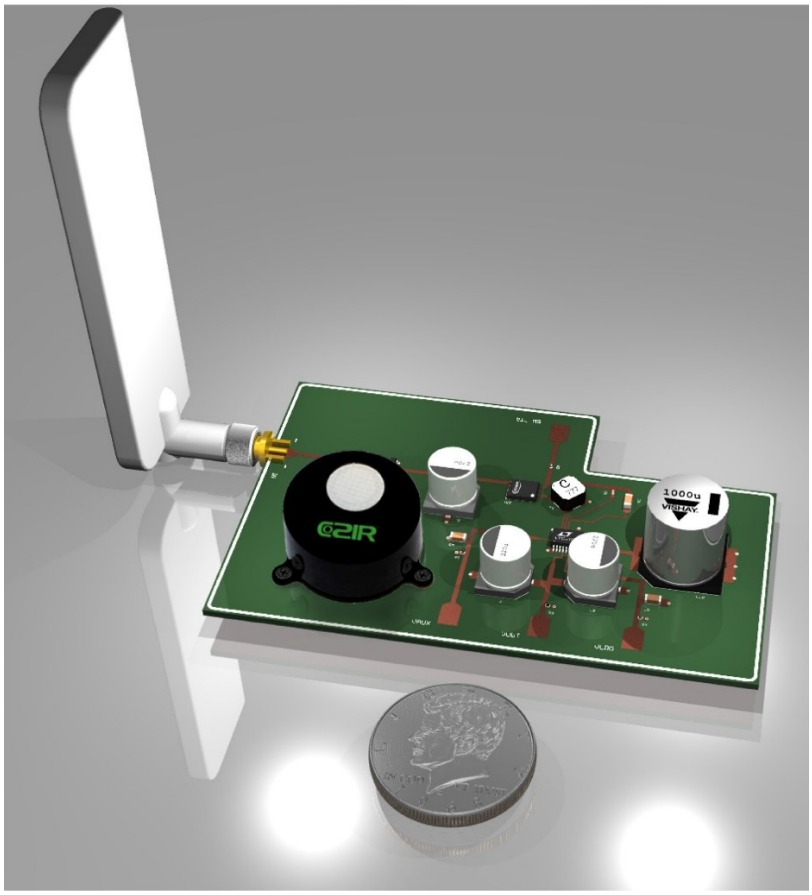

Figure 3.1 The implemented prototype EH system with a gas sensor for wireless sensor networks. [157]© 2016 Elsevier B.V. All rights reserved.

The harvester novel architecture block scheme is reported in Figure 3.2. It is formed by two energy conversion channels (named “Low Power” and “Medium Power”), each of which designed both to manage different power levels at both the reference frequencies and to collect the recovered energy into a common regulation and storage section. The “Low Power” channel is set as the default path by the voltage comparator that, through feedback control, compares the rectified voltage with an internal reference.

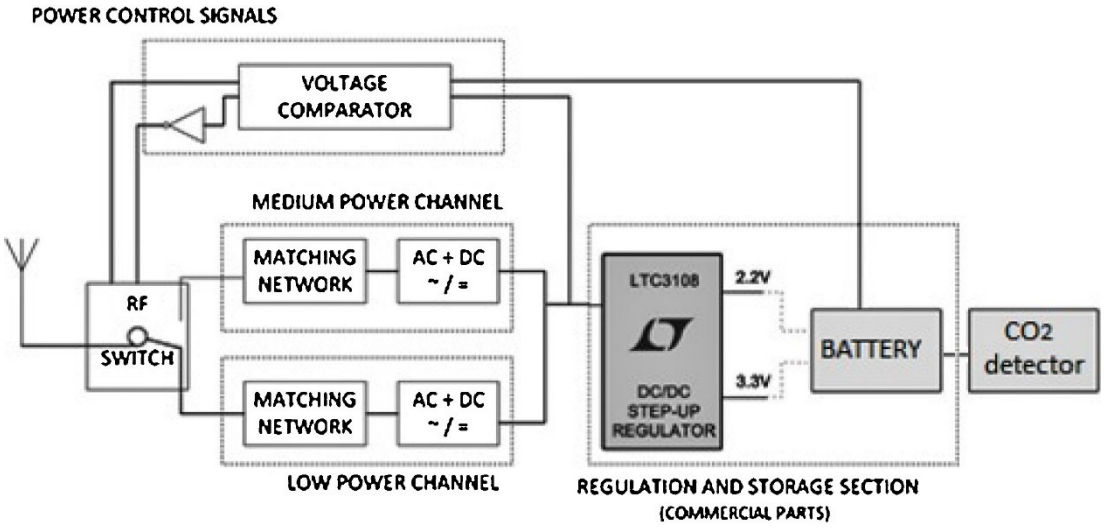

Figure 3.2 Proposed dual-band harvester block diagram with reconfigurable RF-to-DC medium and low power conversion channels. [157]

According to the incoming power level, the ultralow-power voltage comparator selects the suitable channel of the receiver to properly handle the EM radiation. The comparator can be easily realized by a couple of op-amps with the goal of minimizing the requested power to able the switch. The very low amount of required power (<1 μW) is recovered from the storage section itself. Both the channels foresee an AC/DC converter and a suitable matching network, implemented with a “T” configuration using two series inductors and a shunt capacitor. The “Low Power” channel has been optimized to handle an input power from −20 dBm to 5dBm, while the “Medium Power” one relates to power levels going from 5 dBm to 20dBm. The following regulation and storage sections consist of an ultralow voltage Step-Up Converter, the LT3108 provided by Linear Technology in this work, that boosts the input voltage to the regulation section and also decouples the harvester from the storage and load section. Finally, a common load as a “storing section” is used for further utilization. The harvester has been designed and optimized for its simultaneous operation at two

main frequencies: 936 MHz (that is typical for mobile GSM transmissions) and 2.4 GHz (utilized in Wi-Fi broadcasting connections).

As typical for field applications load, we have considered a gas sensor for Carbon Dioxide (CO_2) detection. The "GSS Technology COZIR" Carbon Dioxide Sensor, see Table 3.1, looked the most suitable for the practical applications among a huge number of devices available on the market because the detector integrates an innovative CO2 sensor technology, suitable for a wide range of applications, together with a very low power consumption (less than 3 mW) and an idle capacity. In other words, the full device is able to power the sensor using energy harvesting technology, mainly as a battery recharger. In fact, while a battery can often be required to get more energy during the "in use" windows, the harvester will contribute to continuously recharge it, so that the whole system becomes a real "long life autonomous device". The solution will allow economical revenues by avoiding maintenances or battery replacements to the sensor, always without losing any real-time monitoring of CO_2 concentration levels and always providing the required energy into the proper time windows. The harvester indeed is able to support the whole system in a "long-life" use of the sensor and directly answers the growing demand for sensors that need to be integrated either into batteries (that become in our case rechargeable) or into totally self-powered wireless systems.

Sensor property	Value
Measurement range	5-100%
Accuracy	±70 ppm @ ± 5% of reading
Communication protocol	Serial 9600/8/1/N
Weight	8 g
Warm-up time	<10 ns
Operating conditions	0 °C to 50 °C, 950 mbar to 10 bar
DC supply voltage	3.3 V
DC Power	<3.5 mW

Table 3.1 CO2 COZIR sensor characteristics as reported in [157]

3.1.2 Design Methodology and Simulation Results

Generally, the good performance of harvesting systems can be evaluated by maximizing the RF-to-DC conversion efficiency, defined as the ratio between the total amount of power delivered to the load and the amount of power that the receiving antenna could inject in a perfectly matched circuit. In order to achieve this goal, accurate design of the antenna and rectifier sections is mandatory.

In this case, a commercial omnidirectional, multi-band dipole antenna was selected for harvesting purposes. The multi-band property for an antenna can be achieved by implementing multiple resonance frequencies. As an example, the schematic representation of a dual-band antenna is reported in Figure 3.3.

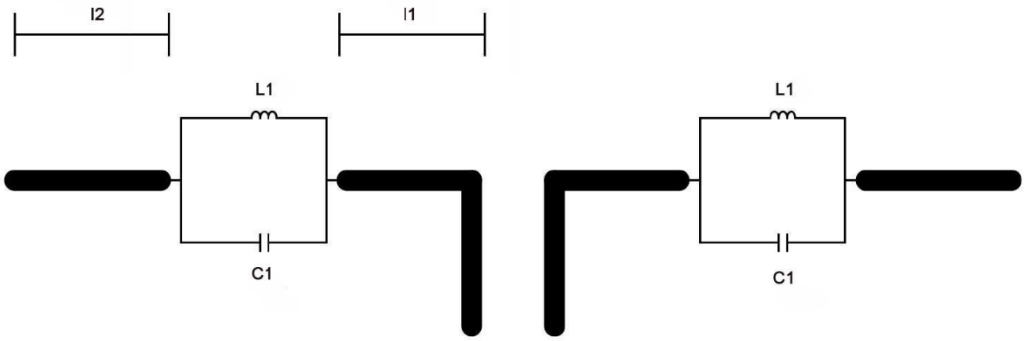

Figure 3.3 Schematic representation of a dual-band dipole antenna.

The two symmetric L-C networks divide the dipole antenna branches into two segments of length l1 and l2, respectively. The impedance of the resonant network can be computed as:

$$Z_1 = \frac{1}{\frac{1}{j\omega L_1} + j\omega C_1} = \frac{j\omega L_1}{1 - \omega^2 L_1 C_1} \tag{3.1.1}$$

where $\omega = 2\pi f$ represents the frequency, while L_1 and C_1 are the inductive and capacitive components of the resonant equivalent network for the dipole branches.

For the impedance Z_1, the resonance condition will be equal to $\omega_0 = \frac{1}{\sqrt{L_1 C_1}}$, therefore if the working frequency matches the resonance condition of the L-C network, i.e. $f_1 = \frac{1}{2\pi\sqrt{L_1 C_1}}$, the impedance will ideally increase to infinite, acting as an open-circuit. Under this condition, the effective dipole branch length will be equal to $l_1 = \frac{\lambda_1}{4}$ and the antenna will behave as a $\lambda_1/2$ dipole. If lower working frequencies are

considered, the capacitive part of the L-C network can be seen as an open circuit, resulting in a prevalent inductive behavior. Under this condition, the antenna resonance frequency will occur at a lower frequency $f_2 < f_1$.

The employed commercial antenna for this application is a TG.30.8112W by TAOGLAS, whose characteristics are reported in Table 3.2.

Frequency (MHz)	**700-800**	**824-960**	**1575.42**	**1710-1880**	**1850-1990**	**1710-2170**	**2400-2700**
Peak Gain (dBi) free space	2.7	2.1	0.3	3.5	3.6	3.6	5.3
Peak Gain (dB) PCB edge	3.2	1.9	2.4	3.2	3.3	3.6	4.7
Average gain – free space	-0.7	-1.2	-1.2	-0.4	-0.4	-0.2	-0.6
Average gain – PCB edge	0.8	-1.9	-0.9	-0.6	-0.6	-0.6	-0.8
Efficiency – free space	85%	75%	76%	90%	90%	90%	87%
Efficiency – PCB edge	86%	87%	81%	86%	86%	86%	84%
Impedance	50 Ω						
Polarization	Linear						
Radiation pattern	Omnidirectional						

Table 3.2 Characteristics of the TG.30.8112W antenna by TAOGLAS.

The reflection coefficient of the antenna has been measured, as shown in Figure 3.4, in order to verify the effective resonance frequency of the real radiator, in order to properly design the matching network for the RF-to-DC conversion channels.

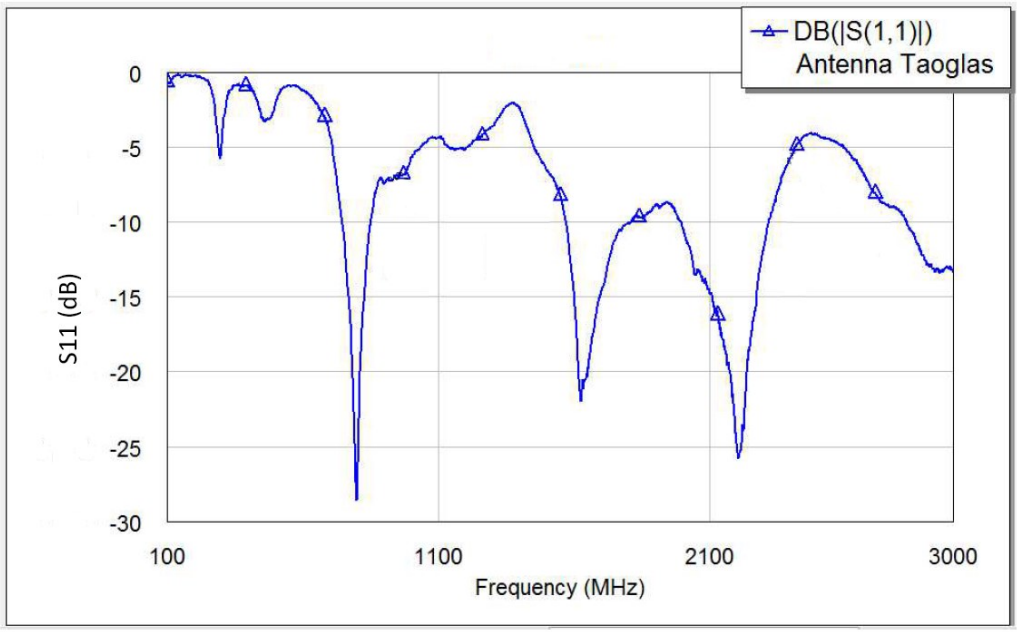

Figure 3.4 Measured reflection coefficient of the employed commercial multi-band antenna.

In this work, the RF-to-DC conversion stage has been designed independently on the two channels, obtaining in the full bandwidth the maximum achievable power transfer, considering either a “Low Power” or a “Medium Power” input. The detailed schematic of the rectifiers is shown in Figure 3.5a while Figure 3.5b shows the equivalent model used for diodes simulations. Then, Figure 3.5c depicts the implemented prototype board used for test measurements. The low power signal handling is achieved through a Schottky diode characterized by a very low threshold voltage. The selected device is the HSMS2850 provided by Avago Technologies; it is a zero-bias detector, series-mounted and able to provide high sensitivity to the circuit response. Conducted simulations demonstrated that the designed “Low Power” circuit shows good behavior for low levels of power, between −20 dBm and about 5 dBm, but at higher power levels its performance drops because the rectified power transfer lost its incremental growth and changes slope tending to a constant limited value. This is because of the diode characteristics, not performing well for relatively high voltages. This consideration justifies the use “Medium Power” channel, suggesting the need to use a more complex configuration. This channel implements, in fact, a voltage multiplier designed with two detector diodes HSMS2865, always provided by Avago. This architecture, as stated in chapter 2, is more efficient for higher input power levels and also ensure higher output DC voltage level.

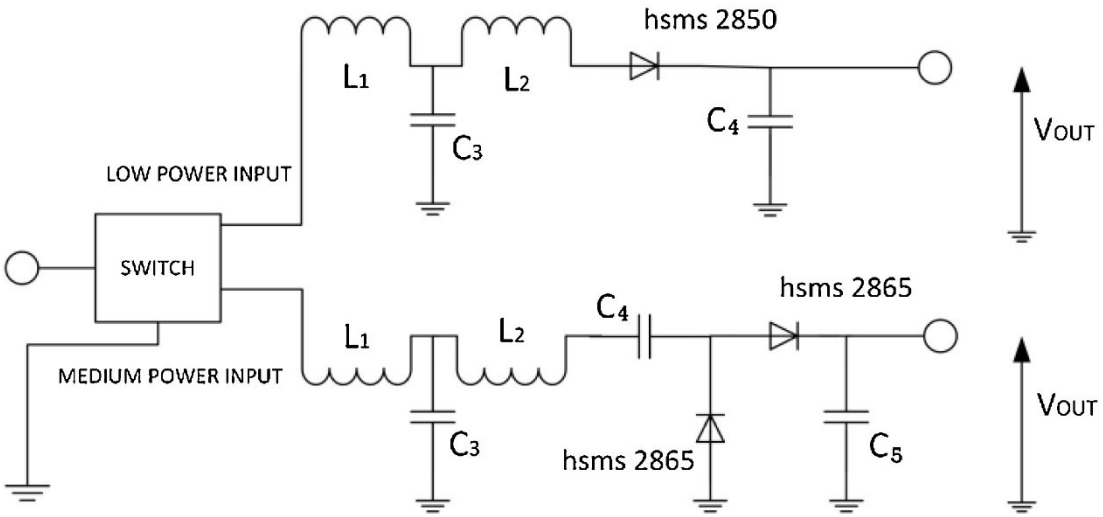

a)

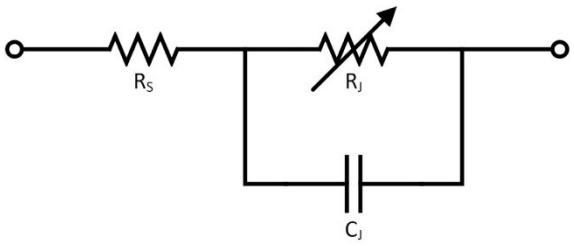

R_S = Series resistance
C_J = Junction capacitance
$R_J = (8.33x10^{-5}nT)/(I_b+I_s)$
where
I_b = Externally applied bias current in amps
I_s = Saturation current;
T = Temperature, °K
n = Ideality factor

b)

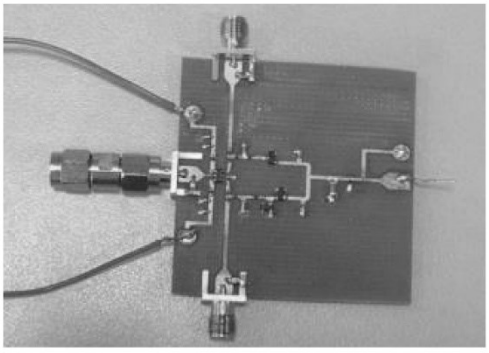

c)

Figure 3.5 Multi-power harvester scheme; b) Equivalent circuit model for the diodes c) Implemented block prototype board, as reported in [157].

In both cases, the input matching is done with LC network configuration and optimized using commercial CAD software, in order to take also into account the layout design, obtaining a high conversion efficiency both at 936 MHz and 2.4 GHz and for different incoming powers. It is definitely interesting to note that with this

double channel approach the power supplied to the load will remain constant and quite high with respect to the different incoming powers levels.

Finally, a commercial RF SPDT switch HMC544 by Analog Device is employed to change from “Low-Power” to “Medium-Power” channel, and vice-versa. The switch has an insertion loss of 0.25 dB and isolation lower than -15 dB below 2.4 GHz. Moreover, it presents two control terminals A and B for the RF output selection, which is 3.3 V CMOS compliant, such as the “Low-Power” channel is selected when the A terminal is at the logic state “low” and the B terminal is at the logic state “high”, while the “Medium-Power” channel is enabled when A is at the “high” logic state and B is at the “low” logic state. By default, some pull-up and pull-down resistors enable the “Low-Power” channel when the EH system is turned on. The channel selection process is managed by means of a window voltage double complementary comparator circuit. The latter compares the open-circuit output voltage of the RF-to-DC conversion circuit with a voltage reference, that was fixed at a proper threshold value. If the output DC value is above the threshold, it means the “Low-Power” channel is in saturation condition since the input available power is higher than the considered range. In this case, the output signals of the comparator circuit will toggle, enabling the “medium-Power” operation.

3.1.3 Prototyping and Measurement Results

Experimental measurements have confirmed theoretical and simulated results. Figure 3.6 shows the output power of the “Low Power” channel when an input signal at −20 dBm at different frequencies is applied. It can be noted that the maximum input power is located at the two main frequencies, 936 MHz (low GSM band) and 2.4 GHz (WiFi), according to design parameters. In Figure 3.7 the RF-to-DC energy conversion efficiency as a function of the incoming power is plotted for both these two frequencies.

The proposed structure reaches its maximum conversion efficiency of about 65% for an input power of 15 dBm in the “Medium Power” range and of 60% at 5 dBm in the “Low Power” range. Despite the few percent difference within the two frequencies, it is important to notice that the overall system shows good results for both low power and medium power signals. Definitively, we have an efficiency greater than 50% for an incoming power between −5 dBm and 15 dBm that decreases outside even though

remains sufficiently high due to a suitable design of both the matching networks and the control system.

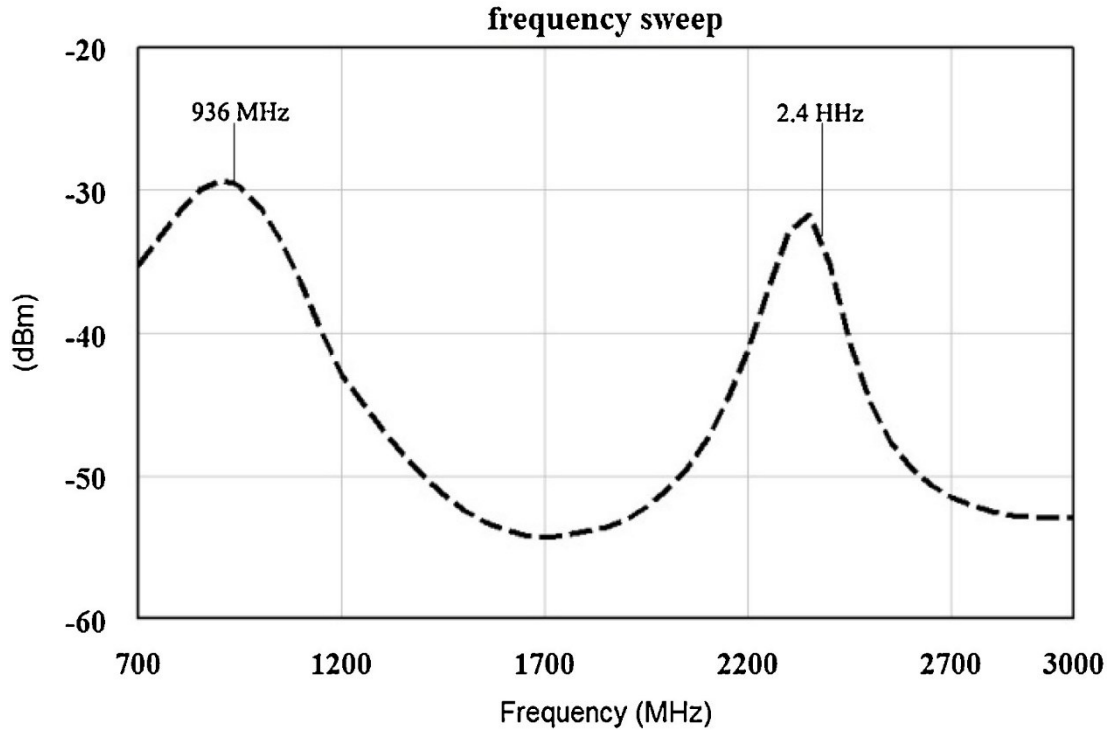

Figure 3.6 Frequency response of the "Low Power" channel for an input signal at −20dBm. [157] © 2016 Elsevier B.V. All rights reserved.

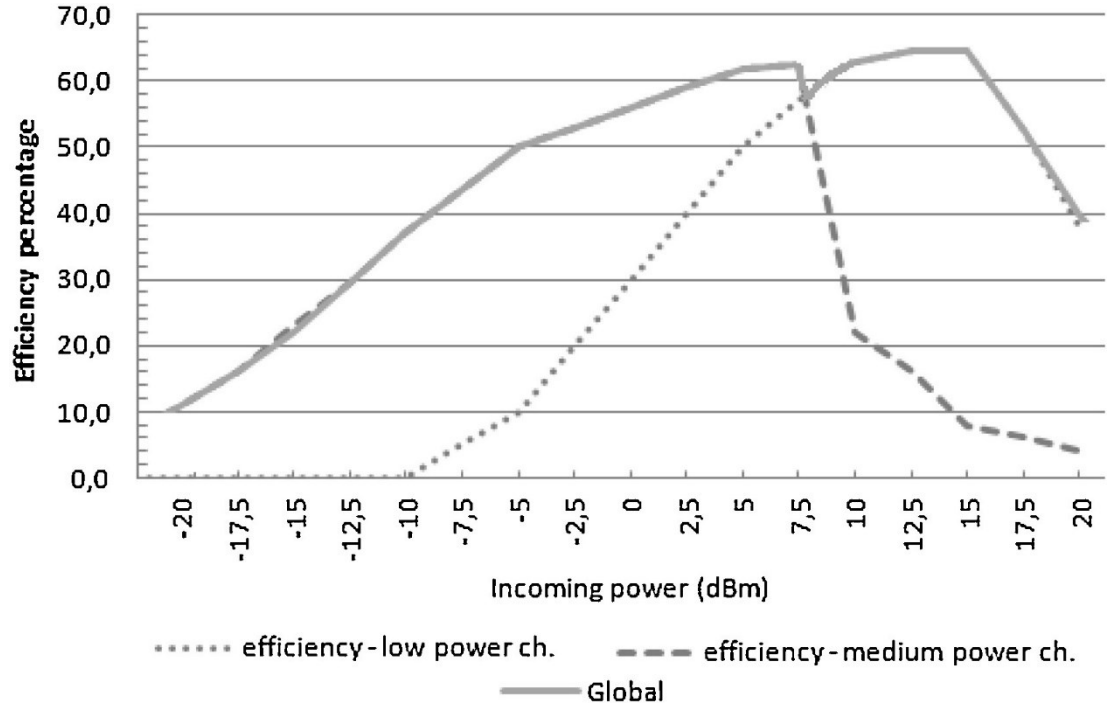

Figure 3.7 Conversion efficiency of the proposed EH system combining the "Low-Power" and "Medium-Power" channels benefits. [157] © 2016 Elsevier B.V. All rights reserved.

All the block parts of Figure 3.8 after the Medium and Low Power channels have been also fabricated in a preliminary printed circuit board so to allow standalone functionality tests. Later, a first testing prototype board has been realized employing a Taconic TLX8 substrate and SMD passive components provided by Murata, as shown in Figure 3.9. The basic functionalities of the regulation and storage section are guaranteed by a commercial highly integrated DC/DC converter, the LTC3108. This device has been verified to be really ideal for harvesting and managing surplus energy coming from extremely low input voltage sources. The step-up topology operates from input voltages as low as 20 mV. Using a small step-up transformer, the LTC3108 provides a complete power management solution for wireless sensing and data acquisition. Extremely low quiescent current and high-efficiency design ensure the fastest possible charge times of the output battery.

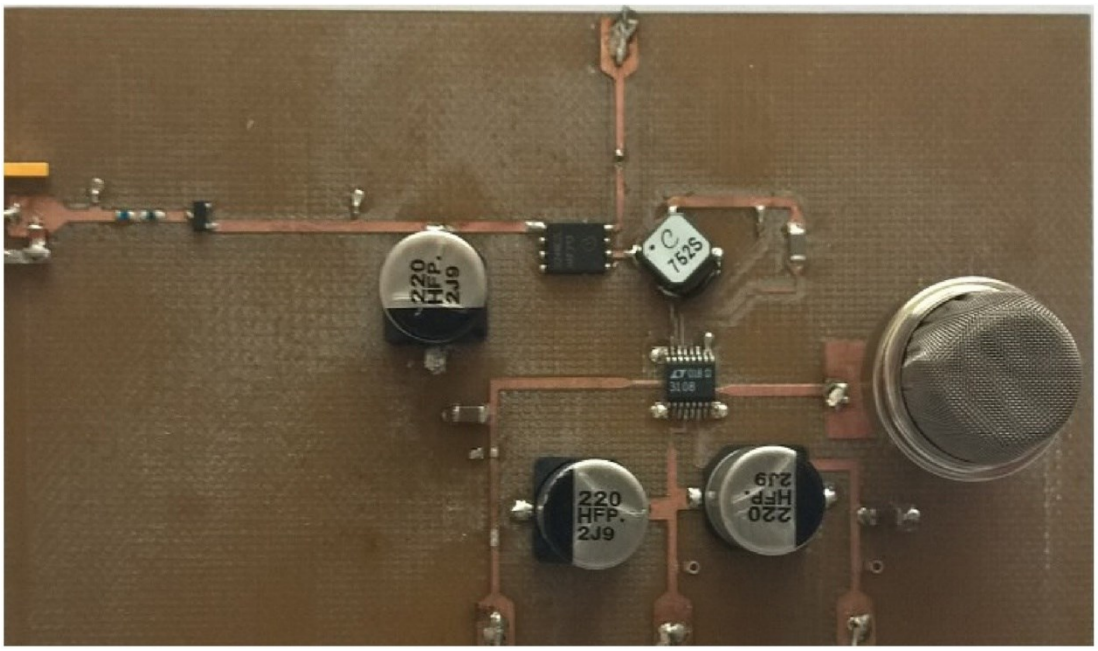

Figure 3.8 The implemented prototype board of the proposed EH system with the CO2 sensor. [157]

The equivalent antenna input impedance has been fixed at 50 Ohm. Figure 3.9 shows the simulated and measured RF-to-DC energy conversion efficiencies of the full system as a function of the input power for the “Low Power” channel and at both the considered frequencies. Moreover, Figure 3.10 reports the simulated and measured RF-to-DC energy conversion efficiency as a function of the input power for the “Medium Power” channel, always at both the considered frequencies.

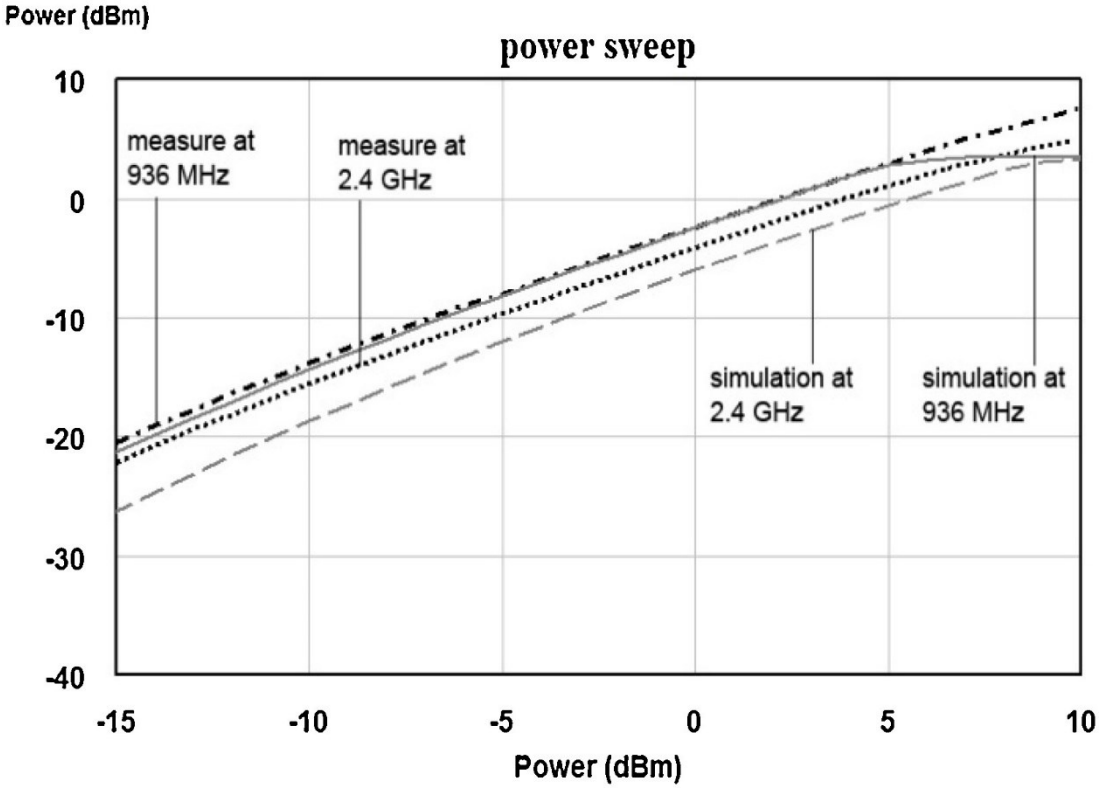

Figure 3.9 Comparison between measured and simulated power transfer function at 936 MHz and 2400 MHz − "Low-Power" channel. [157] © 2016 Elsevier B.V. All rights reserved.

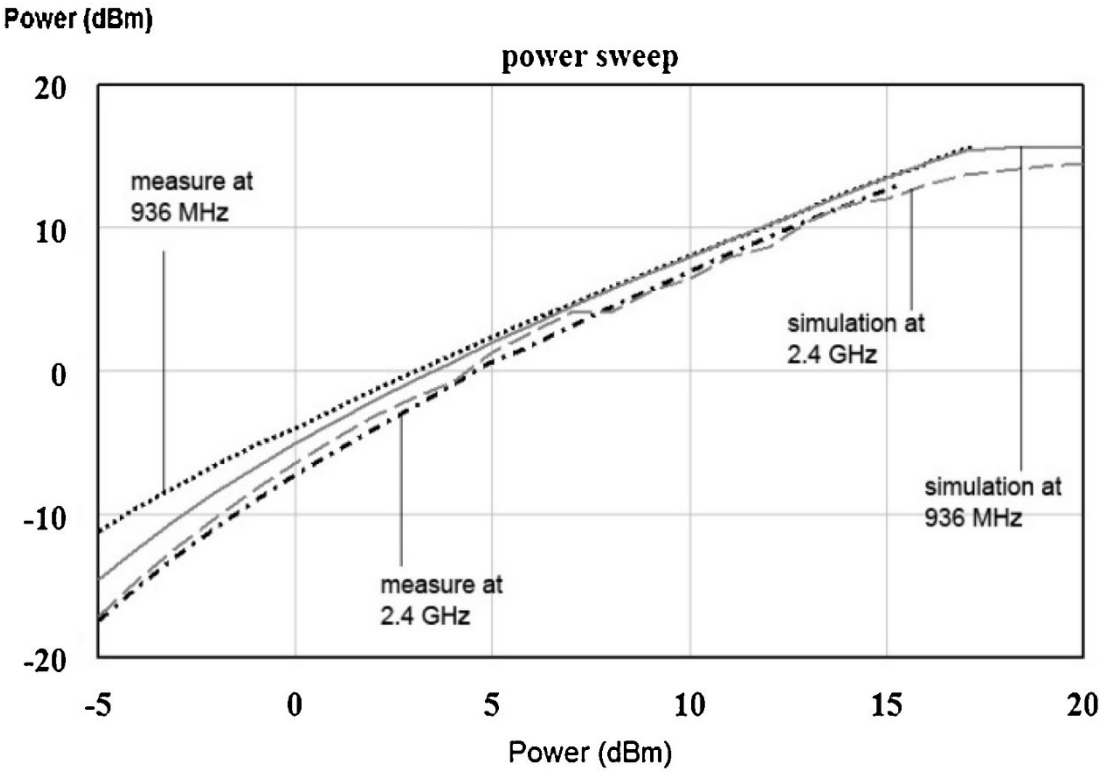

Figure 3.10 Comparison between measured and simulated power transfer function at 936 MHz and 2400 MHz − "Medium-Power" channel. [157] © 2016 Elsevier B.V. All rights reserved.

Finally, the complete hybrid prototype of the harvester has been fabricated and assembled in our laboratory. On-field experimental measurements on the full system have been performed considering free sources provided by commercial devices as a mobile GMS phone and a Wi-Fi router, as shown in Figure 3.11. A simplified set up with no obstacles has been considered. Even though it couldn't be considered a typical scenario in a real residential environment, it is the more general as possible for demonstration purposes being independent form building materials and device position. The two sources have been considered both separately (one feeder per time) and simultaneously by feeding the harvester at different distances. For experimental purposes, considering the radiation diagram of the antenna, their position has been optimized to obtain the maximum power transfer.

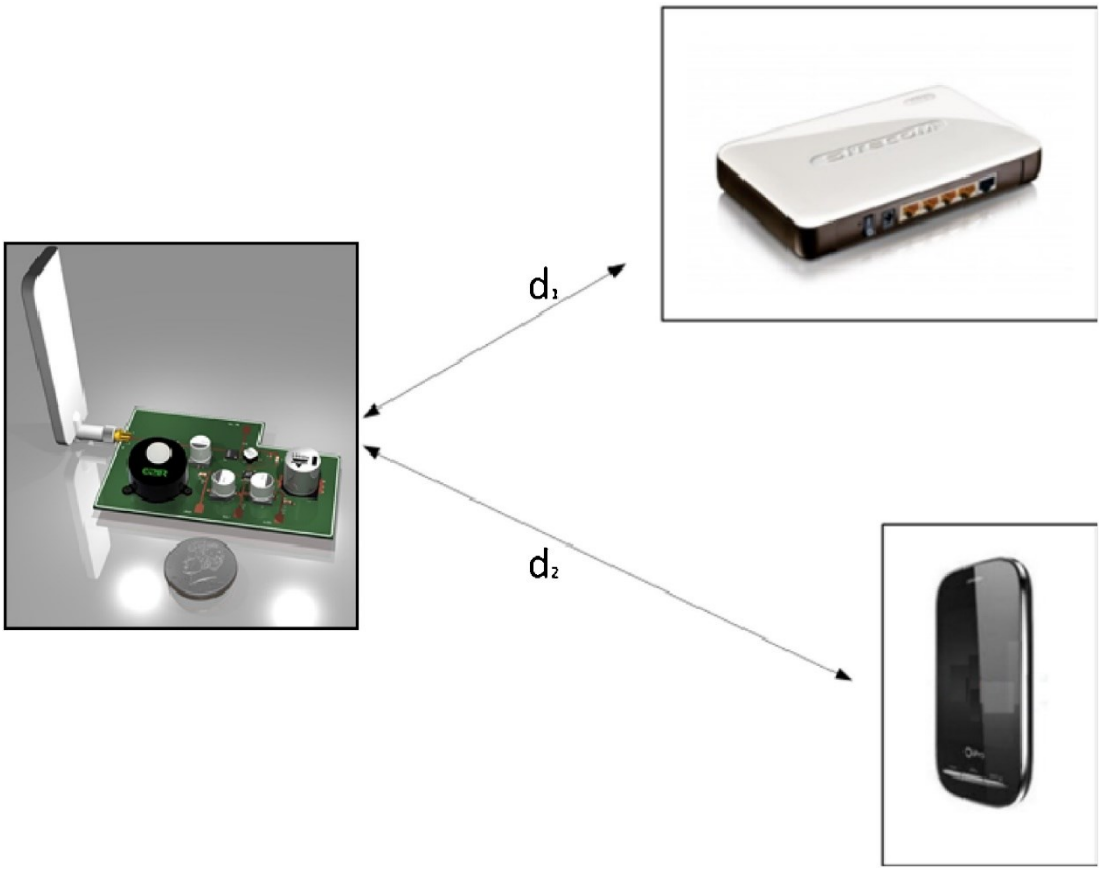

Figure 3.11 Experimental setup for the proposed dual-band EH, gathering RF energy from WiFi and GSM mobile phone signals. [157] © 2016 Elsevier B.V. All rights reserved.

In Figure 3.12 experimental results, in terms of recovered power at different distances, are reported. Data have confirmed the energy efficiency diagrams shown in Figure 3.9 and Figure 3.10. Concerning the presented case study, in order to guarantee the application in an autonomous sensor network, it has been considered an equivalent

sensor load. As typical for field applications load, we considered a gas sensor for Carbon Dioxide (CO_2) detection. The "GSS Technology COZIR" Carbon Dioxide Sensor has looked the most suitable to the practical applications among a huge number of devices available on the market, because the detector integrates innovative CO_2 sensor technology, suitable for a wide range of applications, together with very low power consumption (less than 3.5 mW).

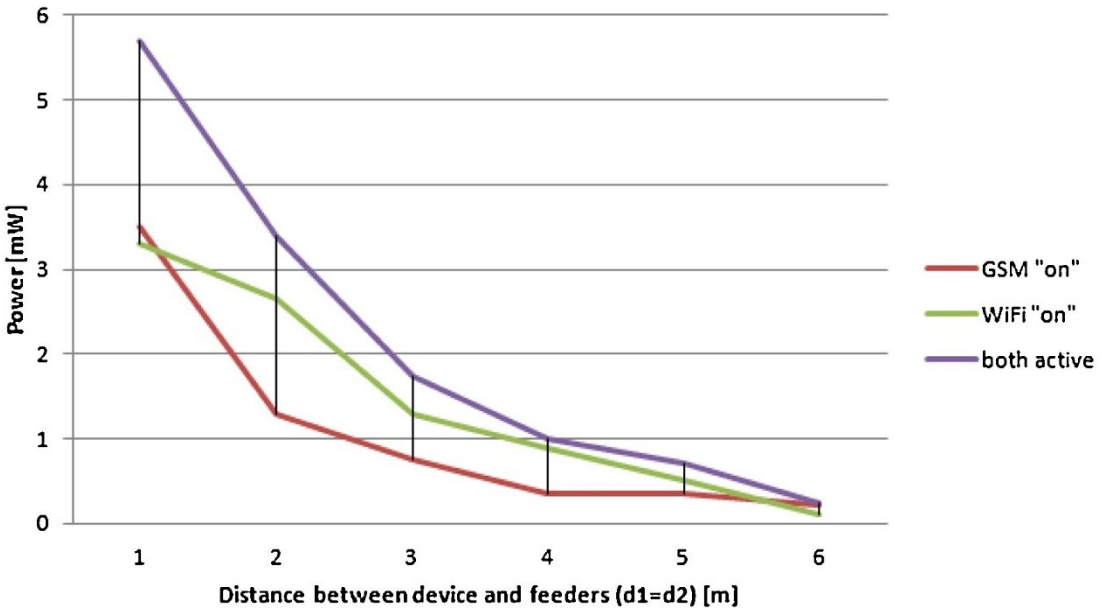

Figure 3.12 Harvester output power for the considered test bench at various distances. [157] © 2016 Elsevier B.V. All rights reserved.

Measured results have confirmed that the combination of extremely low power consumption and instantaneous warm-up capability gives a technical advantage and makes the sensor able to working fine together with our energy harvesting system. The complete device will be able to power the COZIR sensor using energy harvesting technology, mainly as a battery recharger. The sensor has been inserted in the prototype board by means of through-hole and external wires and also the external sensor interface, battery and microcontroller have been separately mounted, at this stage, since it is not the aim of the paper to describe the interface properties.

In fact, while a battery can often be required to get more energy during the "in use" windows, the harvester will contribute to continuously recharge them, so that the whole system becomes a real "long life autonomous device". The solution will allow economical revenues by avoiding maintenances or battery replacements to the sensor, always without losing any real-time monitoring of CO_2 concentration levels and always providing the required energy into the proper time windows.

The sensor is equipped in the designed architecture as already depicted in Figure 3.1. Finally, it must be underlined that the whole system, designed as a discrete element board, has been conceived with particular care in order to be completely integrated into standard CMOS technology.

3.1.4 Integrated IC Architecture Design

The concept of dual-channel RF energy harvester has been also investigated for the IC integration with a 0.18 μm CMOS SMIC technology, reported in [158]. The system has been conceived and optimized to operate only at the GSM band frequency, with a custom-designed folded dipole antenna.

The evaluation is performed at the simulation level using a 0.18μm CMOS SMIC technology and considering a reference frequency of 900 MHz that is used for both mobile phone service and digital television. In particular, the attention has been focused on the simplified architecture of Figure 3.2, paying attention to the rectifiers, the voltage comparator and the DC/DC boost converter that are the most critical parts, in order to catch and manage the incoming radiation (Figure 3.13).

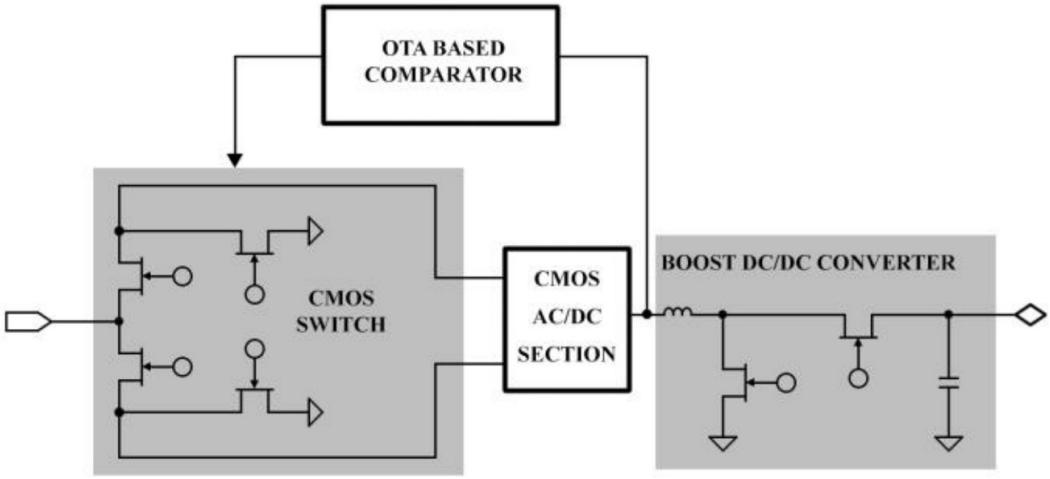

Figure 3.13 Block scheme of the integrated version of the harvester. [158]

About the antenna, a dipole antenna has been taken into account since it shows good performance on a wider bandwidth and can be successfully miniaturized adopting more complex geometry, as for instance in [159], [160]. In particular, a geometry folded dipole antenna similar to that proposed in [159] has been considered and is shown in Figure 3.14. For system simulation purposes, the antenna has been

simulated with Momentum software also considering a 1:100 RF transformer and represented by a Thevenin equivalent source considering its impedance.

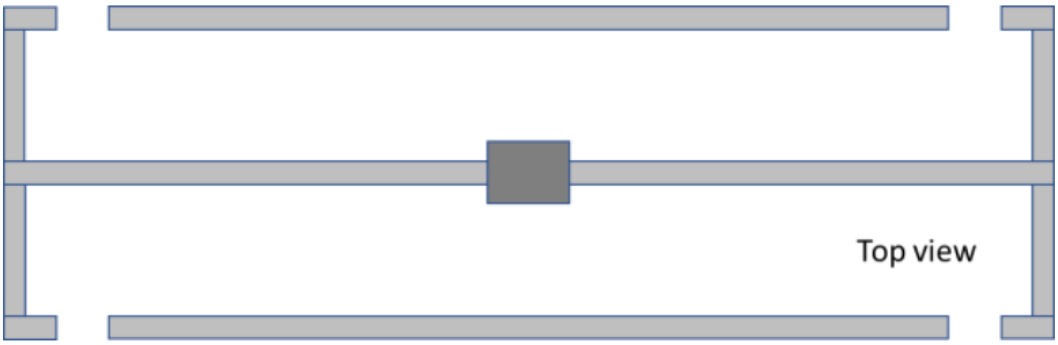

Figure 3.14 Simplified representation of the considered folded dipole antenna. [158]

The RF Switch can be easily realized with parallel MOS transistors controlled by means of gate voltages, as shown in the miniature of Figure 3.13. The comparator is a crucial element in the RF chain since even if it makes possible to double the power management chains, it requires a bias voltage and a reference voltage to set a suitable voltage threshold. The proposed solution concerns the realization of the comparator with a couple of low-voltage, low-power operational transconductance amplifiers (OTAs) [161], [162] that allow minimizing the requested power to drive the switch. The circuit here adopted for the OTA is shown in Figure 3.15 and it requires a very low biasing level (<1 μW) that can be easily recovered from the storage section itself.

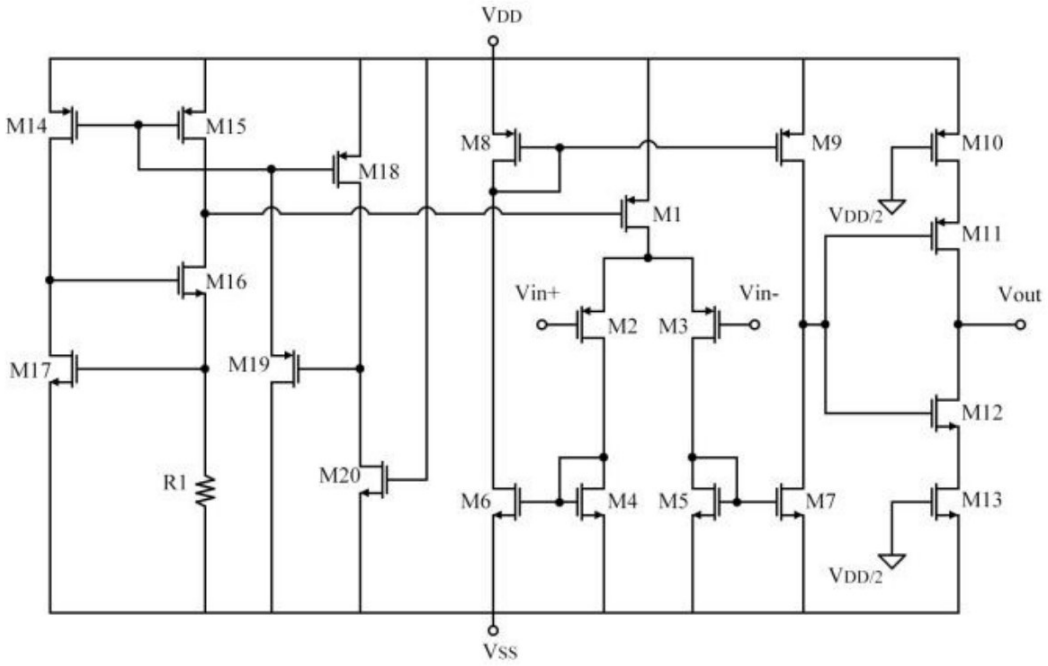

Figure 3.15 Designed LV-LP OTA used for the comparator [158].

Obviously, we are supposing the system will be provided of a rechargeable battery pack, initially charged, so avoiding the use of an external supply voltage for a while, until the incoming RF radiation arises to a sufficient value to auto-sustain the circuit functionality. In detail, the OTA has two stages: an input symmetrical OTA (*M1–M9*) that decreases systematic and random offsets; a source degenerated output stage (*M10–M13*) that allows obtaining a full dynamic output range. Compensation is ensured by the RC series network, while a high slew-rate value is obtained properly dimensioning a suitable Vth-dependent current generator through (*M14–M17*, *R1*). This current reference uses a "start-up" circuit.

Concerning the voltage rectifier, being the two channels of the harvester dimensioned to handle quite different input power levels, it has been necessary to develop different solutions for this building block in order to have at the same time good sensitivity and the capability to manage large input power levels, so ensuring a wide dynamic range. The solution adopted for the medium-power channel is reported in Figure 3.16 and derived by the architecture proposed in [97]. It is a full-wave gate cross-coupled rectifier where the transistors in the two main branches are cross-coupled. This configuration limits the associated voltage drop due to the voltage threshold of the MOS transistor and allows to obtain a higher power efficiency towards classical diode-based solutions. The low-power channel has been conceived with a different scheme, keeping advantages of the solution always proposed in [97] (see Figure 3.17). Since this channel is devoted to handling low-power levels, improved performance in term of efficiency and sensitivity are necessary. The adopted solution implements two MOS switches with very low effective threshold voltage to replace the classical diode-connected pMOS transistors usually employed. In addition, this architecture also takes advantage of the cross-coupled structures that are applied to the MOS transistors and this allows to drive the transistors with a larger voltage swing, increasing the output voltage and improving the power conversion efficiency. A dynamic bulk biasing circuit for diode-connected transistors M5 - M6 is also used for reducing the circuit dropout voltage and power dissipation at startup.

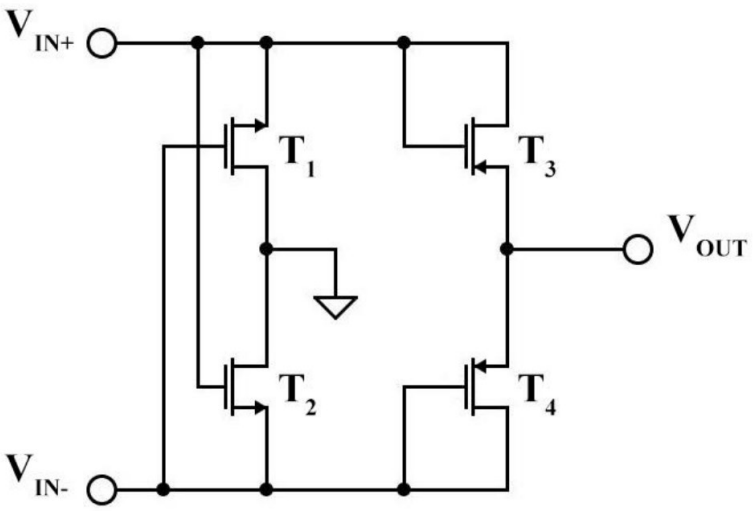

Figure 3.16 Schematic of full-wave medium-power channel rectifier as proposed in [97]. © 2012 IEEE All rights reserved.

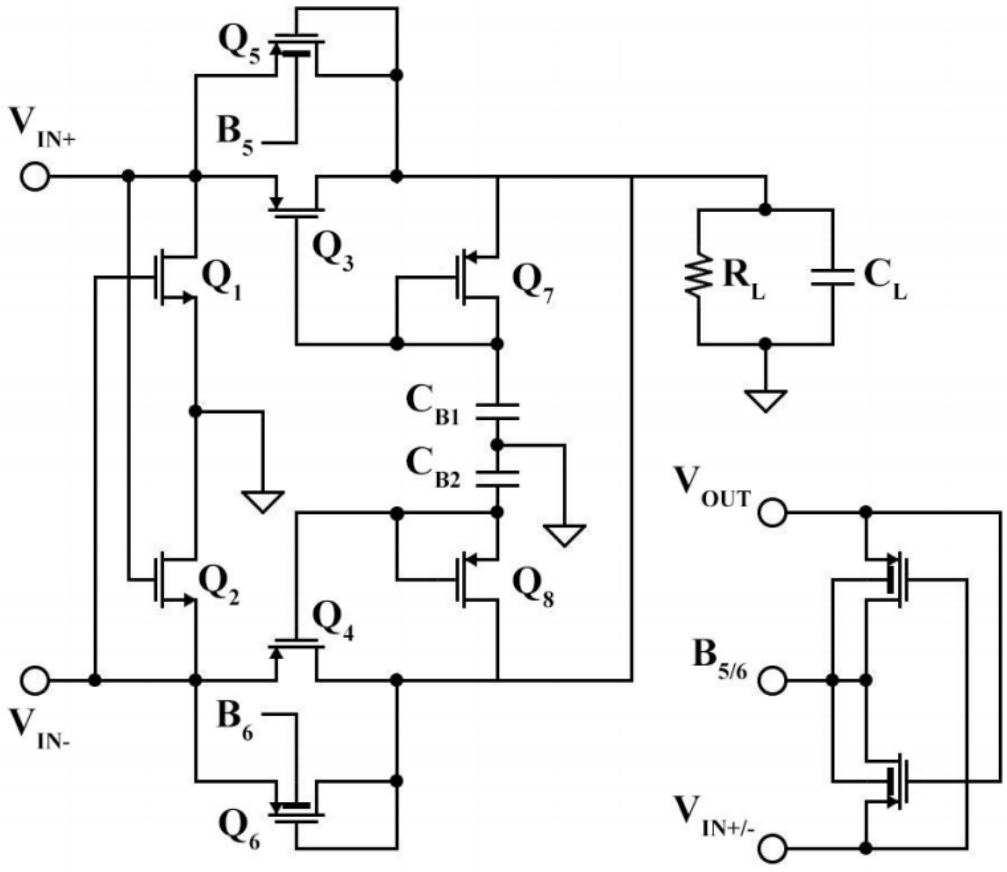

Figure 3.17 Schematic of full-wave low-power channel rectifier as proposed in [97]. © 2012 IEEE All rights reserved.

Finally, the solution illustrated in Figure 3.18 has been adopted for the Boost DC/DC converter [163]. In this design, two instances of the low-power OTA (that is

shown in Figure 3.15) are used in a charge pump configuration to multiply the input voltage.

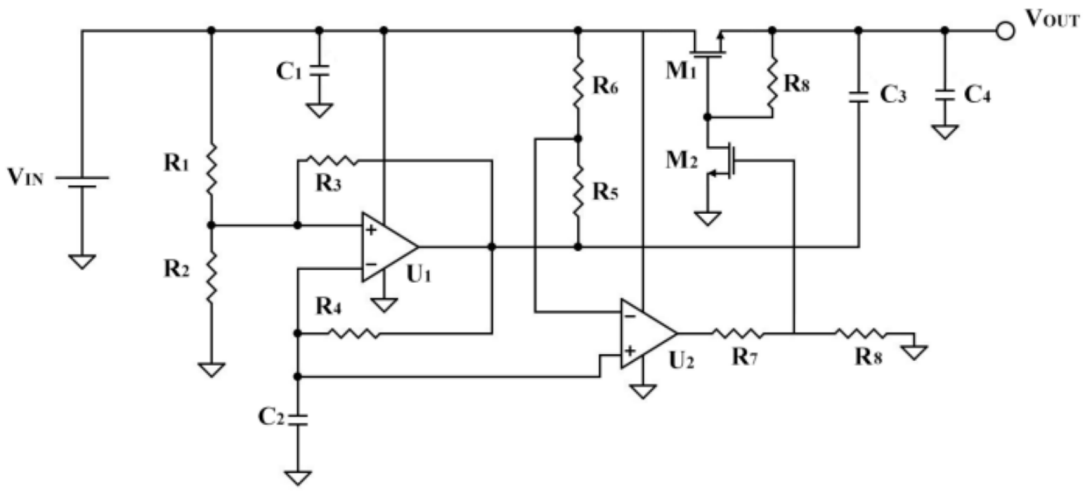

Figure 3.18 Simplified schematic of the boost DC/DC converter [158].

The first OTA acts as a relaxation oscillator, serving as the master charge-pump clock, while the second amplifier is configured as a comparator slaved to the timing cycle established by the first one.

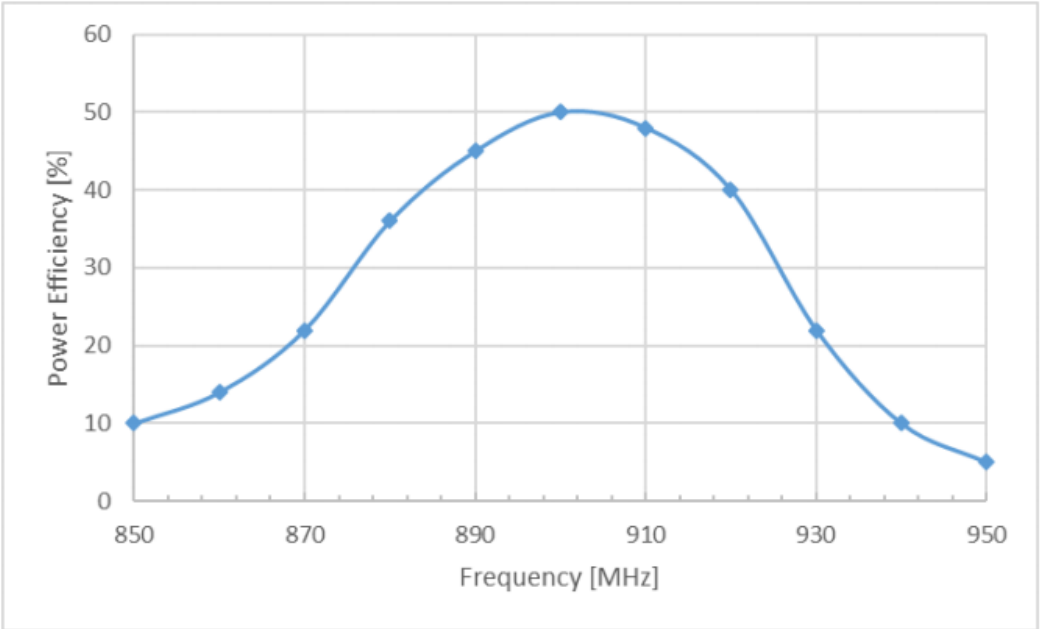

Figure 3.19 Conversion efficiency for the low power channel at 0 dBm input power [158].

Considering the same definition of the Efficiency parameter as in [157], that is, the ratio between the incoming power and the rectified power, preliminary simulation results have confirmed that the integrated system handles an incoming power typically

ranging from -25 dBm to 5 dBm by rectifying the variable input signals into a DC voltage source with an overall efficiency up to 50%. In Figure 3.19 and Figure 3.20, simulation results concerning the conversion efficiency on the two channels are shown confirming the suitability of the proposed circuits towards portable system applications. The chip area estimation for the proposed system is as low as 3 x 3 mm^2.

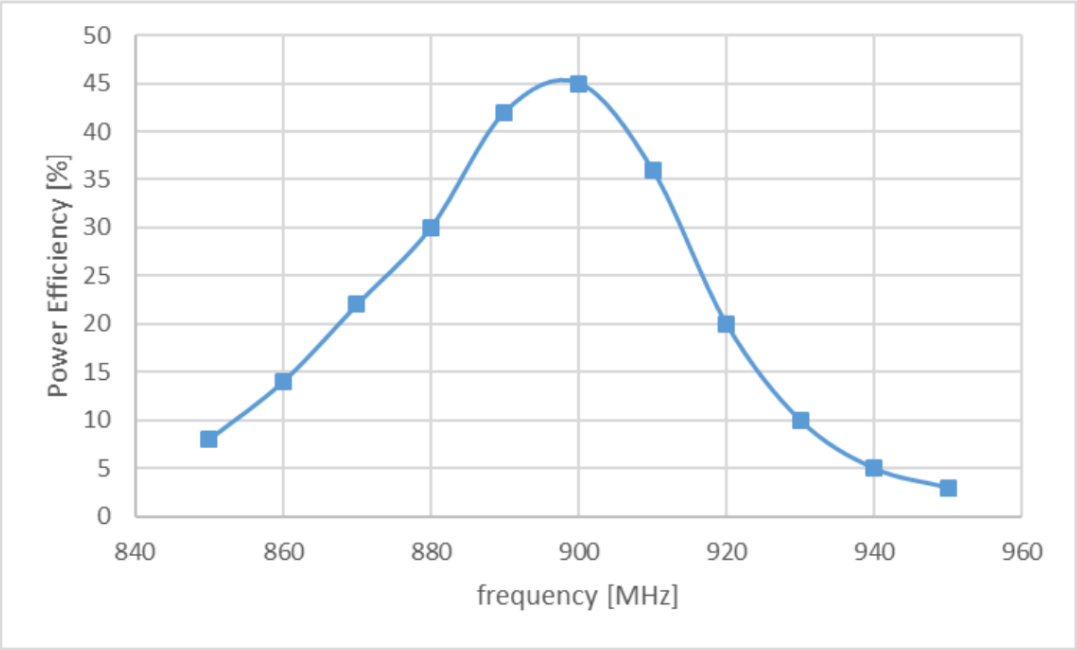

Figure 3.20 Conversion efficiency for the medium power channel at 10 dBm input power [158].

3.2 MULTI-ANTENNA RF ENERGY HARVESTER

In this contribution, a dual-band RF energy harvester with dual input antennas is presented, to gather energy from both the GSM signal and the FM 88-108 MHz radio broadcasting [164]. In this research work, since the two working frequencies are too distant each other, the design or the availability of a single, multi-band antenna for harvesting purposes is quite difficult [165], therefore two distinct antennas have been employed for the two working frequency bands. Moreover, the usage of multiple antennas can help to increase the total received input power. Here the equation 2.6 for the power density of an ideal transmitting isotropic radiator, is recalled:

$$S_{ISOTROPIC} = \frac{P_{TX}}{4\pi D^2} \tag{3.2.1}$$

The paragraph 3.2 is based on the published paper Leoni, A., Pantoli, L., Stornelli, V., Ferri, G., Solic, P. and Russo, M. (2018). A Combined 90/900 MHz IC Architecture for Smart Tag Application. Journal of Communications Software and Systems, 14(1). doi: https://doi.org/10.24138/jcomss.v14i1.451. As the author of this article, reuse permissions are not required.

where P_{TX} is the transmitted power and D is the distance from the radiator. According to equation 3.2.1, the transmitted power is uniformly spread over the spherical isosurface of the isotropic radiator. Therefore, only a small quantity of transmitted power will reach the user receiving antenna, which diminishes with distance (see Figure 3.21).

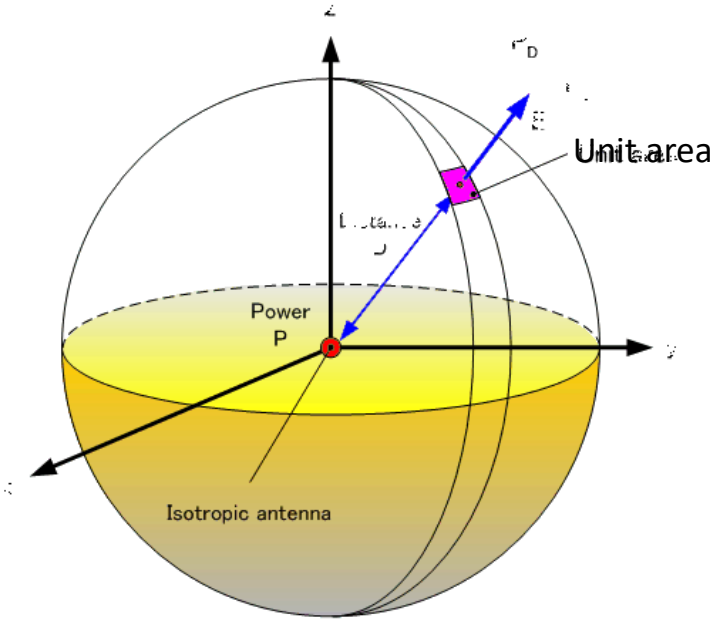

Figure 3.21 Distribution of the power density for an isotropic transmitting radiator [166].

The amount of received power from the EH system is then related to the transmitted power, the distance between harvester and source, and the effective area of the receiving antenna. The latter is a theoretical value which is a measure of how effective an antenna is at receiving power, and is related to the antenna dimension and gain [165]. Once the power density of the receiving signal, at a given distance, is known, the effective received power from the EH system will be equal to:

$$P_R = A_{eff} \cdot S_{TX} \tag{3.2.2}$$

where A_{eff} is the effective area of the receiving antenna, expressed in $[m^2]$ and S_{TX} is the power density related to the transmitted signal. From equation 3.2.1 it can be noticed that the region of the space occupied by multiple distinct antennas is greater, compared to a single, multiband antenna, therefore the effective received power will be higher. However, one of the challenges with the multi-antenna EH system is to efficiently combine received power, so the advantages are not compensated by efficiency degradation.

In this contribution, a novel power combiner has been designed, in order to passively sum the RF signals, which are then converted by means of a single rectifier, minimizing losses. The key points of the designed circuit are the capability to manage input signals over a wide power range together with the high energy conversion efficiency in the full band. First, the application scenario and analytical and experimental analysis on present ambient GSM and FM power levels are given. In fact, since the GSM signal consists of uplink and downlink channels, each of them should be observed. While the downlink power level is always present and relatively constant (small power variations during the day), uplink power depends on the number of mobile phones close to the GSM energy harvester. Due to uncertainty of the number of mobiles, we use for the optimization of the EH circuits a probabilistic approach used for modeling the possible amount of GSM energy that could be harvested

3.2.1 Input Power Level Estimation Method

In this paragraph, the specifications of each working band for the RF EH are analyzed. It is important to note that this separate analysis should be applied whenever both downlink and uplink appear as a part of the communication system.

Generally, throughout the world, the FM broadcast band falls within the VHF part of the radio spectrum. Usually, the frequency range from 87.5 to 108.0 MHz is used, or some portion thereof, with few exceptions.

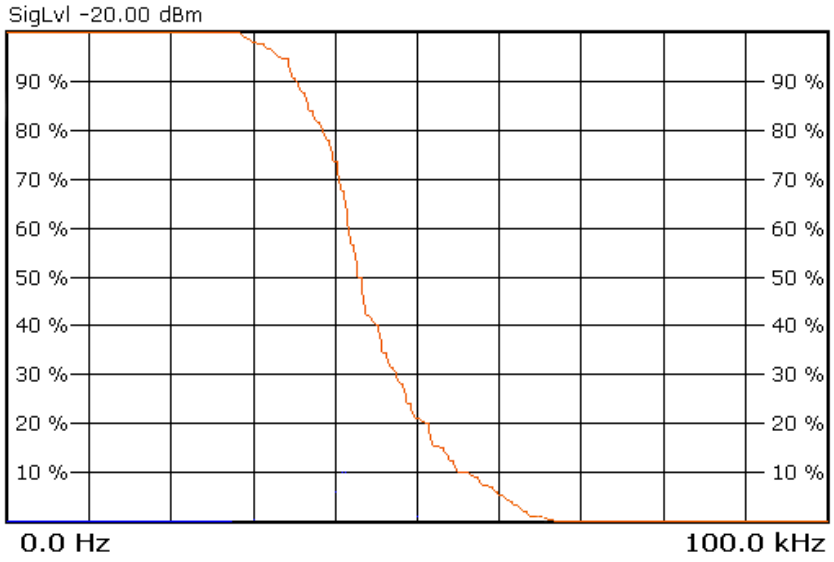

Figure 3.22 Measured power level of a single channel FM radio.

The radiated power, for each channel, is regulated in each country and remains fixed in the downlink. The measured average power level for a single channel FM radio in L'Aquila, Italy, is showed in figure 3.22, which oscillates around -20 dBm.

On the other hand, the GSM allows the use of duplex operation, since each band has a frequency range for the uplink and a separate range for the downlink. In the case of harvesting GSM energy, one should consider the contribution from both downlink and uplink GSM bands. For this purpose, the same approach in [167] has been used and given as follows: in order to characterize the available free power, a GSM-900 signal spectrum has been observed by means of a spectrum analyzer, performing measurements with a quarter-wave ground plane antenna (3 dBi gain). An example of GSM channel is depicted in Figure 3.23a when the mobile phone is ringing one meter far from the measuring antenna of the spectrum analyzer. A trivial example of integrating such a channel shows that an additional power of 10 dBm (100 μW) which can be used to be harvested is obtained.

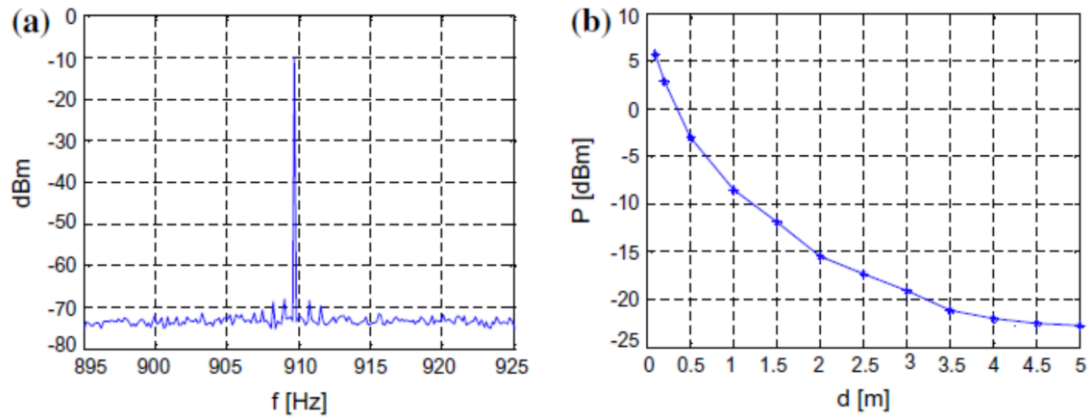

Figure 3.23 a) GSM signal strength when mobile phone calling is active 1m away from the measuring antenna and b) GSM signal strength when the mobile phone is moving away from the measuring antenna [167].

When the ringing mobile phone is moving away from the initial point, the picture changes as depicted in Figure 3.23b, where the signal level is exponentially dropping. As a consequence, moving the mobile phone to the harvester during the ringing can provide additional power. If the EH system is near GSM base station or there are more mobile phones in the neighborhood of the harvester, more energy, of course, could be harvested. As these available levels highly depend on the environment, this has to be modeled appropriately and analyzed with respect to distance from the base station and the number of mobiles around the EH system. On the other hand, GSM Downlink

energy is always available and is dependent on the existing number of near base stations and the distance from them. In this case, the total downlink GSM power was measured with a spectrum analyzer at a fixed location [167]. It oscillates around -26 dBm (2.5 μW) as shown in the histogram in Figure 4. Measured data can be well fitted with log-normal distribution with parameters μ=0.95 and σ=0.1. Concerning the uplink GSM power, it is dependent on the number of nearby mobile phones in an active call.

This number inside a determined radius distance can be modeled with the Poisson distribution. Since downlink and uplink power distributions can be considered independent, the probability distribution of total power can be obtained by their convolution and is shown in Figure 3.25. By taking advantage of the previously probabilistic description of the GSM available power and the FM regulated emitted power, the EH architecture depicted in Figure 3.24 has been designed and optimized. By using this approach, it is possible to consider the amount of available power that can be harvested in terms of its probability available in the spectrum.

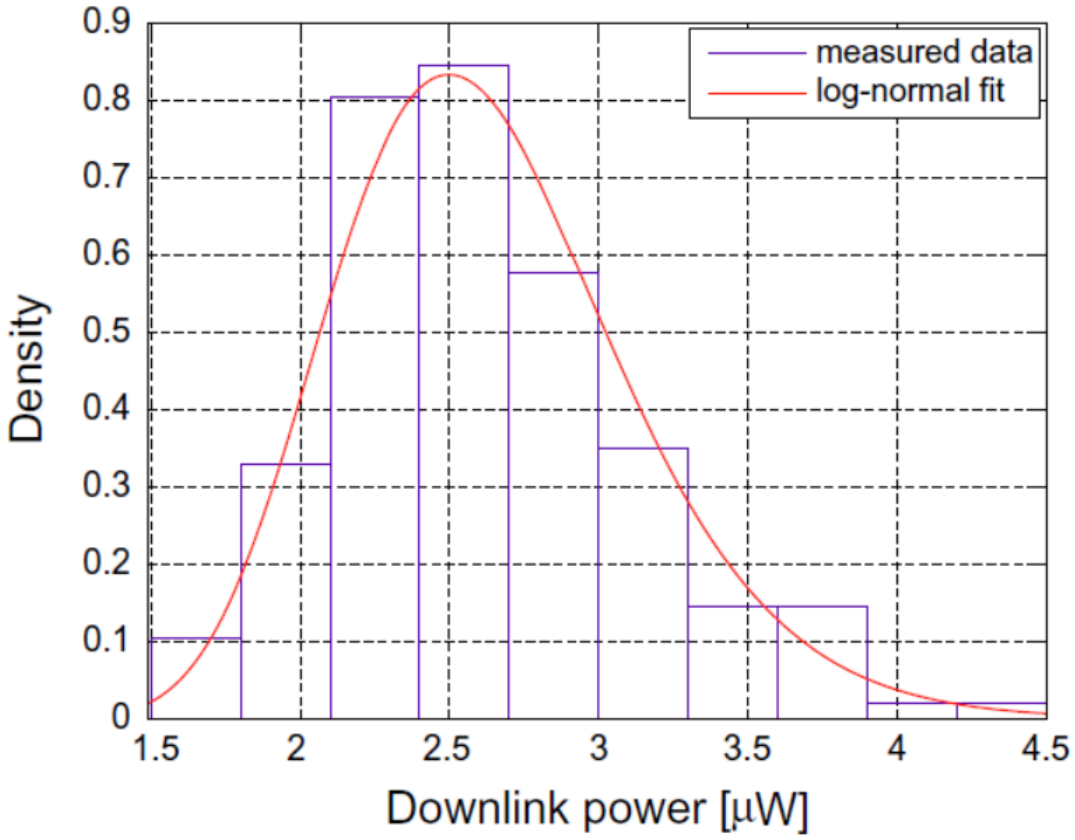

Figure 3.24 GSM downlink power distribution [164].

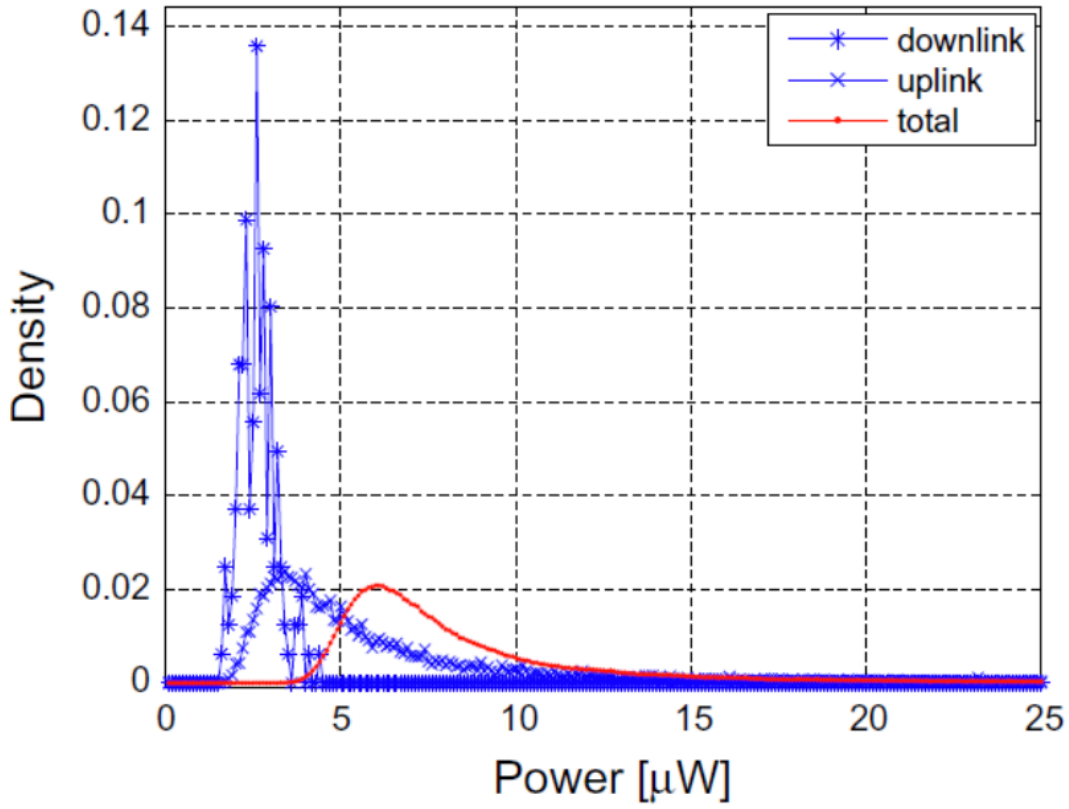

Figure 3.25 GSM power density: uplink, downlink, and total power [164].

3.2.2 Lossless Power Combiner Design Method

In Figure 3.26 the complete block scheme of the conceived architecture is shown. The RF front end of the device is composed of two external antennas, an RF transformer and a matching network designed to match the antenna to the rest of the system with a minimum of power reflection. Since a single, dual-band antenna design is very difficult to achieve, because of the large frequency distance between the two RF bands, two discrete external antennas have been simulated to harvest energy from the two RF mentioned sources.

In order to perform the summation of the two received signals, a custom power combiner has been designed. A passive power combiner (o its dual, power splitter) is a three-port RF network, with two inputs and one output, that has the role to sum the received signals at port 2 and 3 in a resulting signal, provided at port 1 (see Figure 3.27). The passive power combiner, as every passive RF circuits where the transmission of a signal is independent of its direction [165], is a reciprocal network. However, the theory of microwaves states that it is impossible for a three-port network to be lossless, matched and reciprocal at the working frequency, therefore losses or

mismatch condition is inevitable, which can both significantly degrade the EH performance [165].

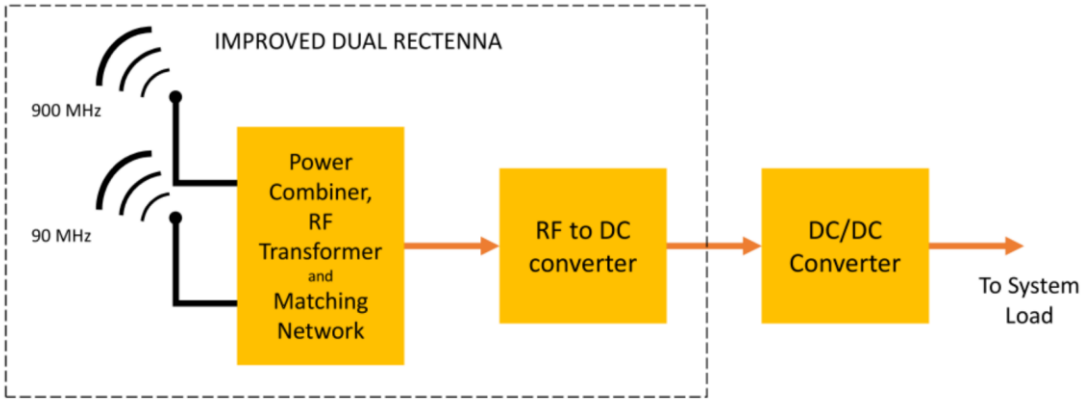

Figure 3.26 Proposed architecture for the dual-antenna harvester [164].

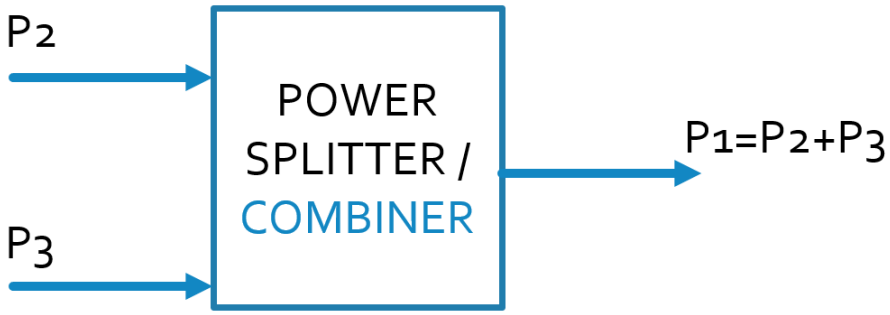

Figure 3.27 RF Power combiner architecture.

As an example, one of the commonly employed power combiners/splitters relies on Wilkinson architecture [165]. In case of equal balancing between the two input port, and satisfied matching condition, the associated scattering matrix can be expressed as:

$$S = \frac{1}{\sqrt{2}}\begin{bmatrix} 0 & j & j \\ j & 0 & 0 \\ j & 0 & 0 \end{bmatrix} \tag{3.2.3}$$

where S represents the scattering matrix. By observing the equation 3.2.2, it can be inferred that the summation process of two input signals occurring at port 2 and 3, will result in an output RF signal where the power of each input wave is decreased of -3 dB, which means that the power is halved, for each received signal. The power losses are dissipated through the isolation resistor between the two input ports (see Figure 3.28). This condition severely affects the amount of harvested energy, vanishing the advantages of a multi-antenna configuration.

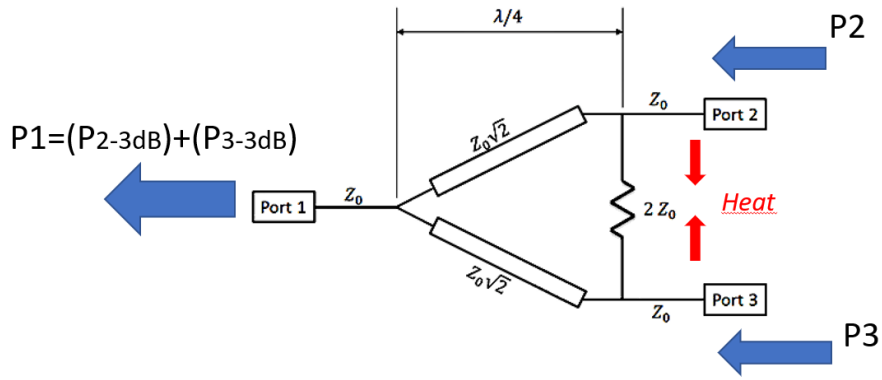

Figure 3.28 Losses in a Wilkinson power combiner operation, with balanced input ports.

The solution here proposed to overcome this problem is the design of a lossless power combiner, which relies on the fact that the working frequencies are quite distant from each other in the spectrum axis. For each working frequency, a dedicated input port is associated and for that port, the requirements to be fulfilled are matching condition and no losses, regardless of the other input port and vice-versa, according to the considered target frequency.

Supposing that the port 2 is linked to the FM band, the S_{21} and the S_{12} parameters, which represents the transmission from input port 2 towards output port 1, should be equal to 1 since all the power received at port 2 should transit towards the output port. Therefore, the scattering matrix for the power combiner, at the FM frequency, can be expressed as:

$$S_{FM} = \begin{bmatrix} 0 & 1 & S_{13} \\ 1 & 0 & 0 \\ S_{31} & 0 & S_{33} \end{bmatrix} \tag{3.2.4}$$

According to microwave theory and as reported by Pozar in [165], the lossless condition is satisfied when the sum of the square modulus for each element of the S parameters matrix must be equal to 1. By imposing the lossless condition and substituting the known terms in equation 3.2.3, it results from that

$$\begin{aligned} |S_{11}|^2 + |S_{21}|^2 + |S_{31}|^2 = 1 &\implies |S_{31}| = 0 \\ |S_{12}|^2 + |S_{22}|^2 + |S_{32}|^2 = 1 &\implies |S_{32}| = 0 \\ |S_{13}|^2 + |S_{23}|^2 + |S_{33}|^2 = 1 &\implies |S_{33}| = 1 \end{aligned} \tag{3.2.5}$$

By combining equations 3.2.3 and 3.2.4 and performing the same considerations for the port 3, which must be associated to the GSM band, the S matrices for the power combiner, at the two working frequencies, must be equal to:

$$S_{FM_{port2}} = \begin{bmatrix} 0 & e^{j\vartheta_1} & 0 \\ e^{j\vartheta_1} & 0 & 0 \\ 0 & 0 & e^{j\varphi_1} \end{bmatrix}, \quad S_{GSM_{port3}} = \begin{bmatrix} 0 & 0 & e^{j\vartheta_2} \\ 0 & e^{j\varphi_2} & 0 \\ e^{j\vartheta_2} & 0 & 0 \end{bmatrix} \quad (3.2.6)$$

The equations 3.2.5 establish the design requirements for the lossless power combiner, applied to the FM and GSM dual antenna EH application here proposed.

The power combiner has been designed with discrete capacitive and inductive lumped elements and its simplified circuit architecture is shown in Figure 3.29, while its prototype implementation is depicted in Figure 3.30.

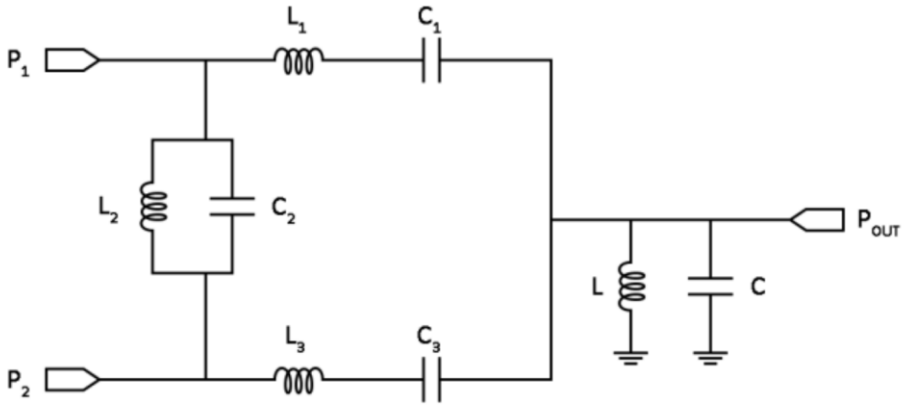

Figure 3.29 Simplified schematic representation of the proposed power combiner [164].

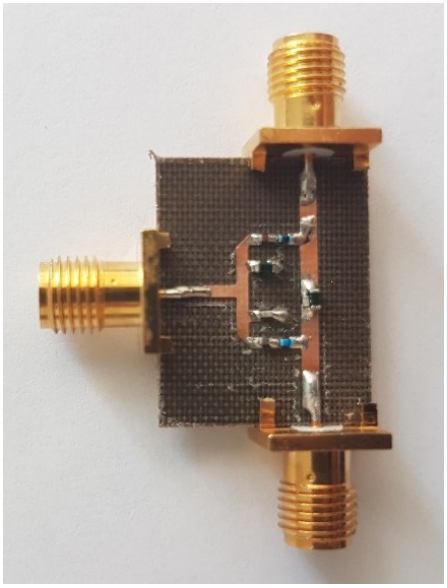

Figure 3.30 Prototype realization of the proposed lossless power combiner

For the matching condition, a reference impedance value of 50 Ω has been considered for all the ports, which means that the adopted antennas for EH should have the same radiation impedance.

In Figure 3.31, the simulated and measured performance of the implemented power combiner are shown. Results prove that the matching conditions are fulfilled for both input ports, with a power loss of 0.41 dB for the FM port and 0.14 dB for the GSM port. The isolation between the two input ports (dashed dark-blue trace in the graph) is also satisfied, being below -20 dB for the considered frequencies of operation.

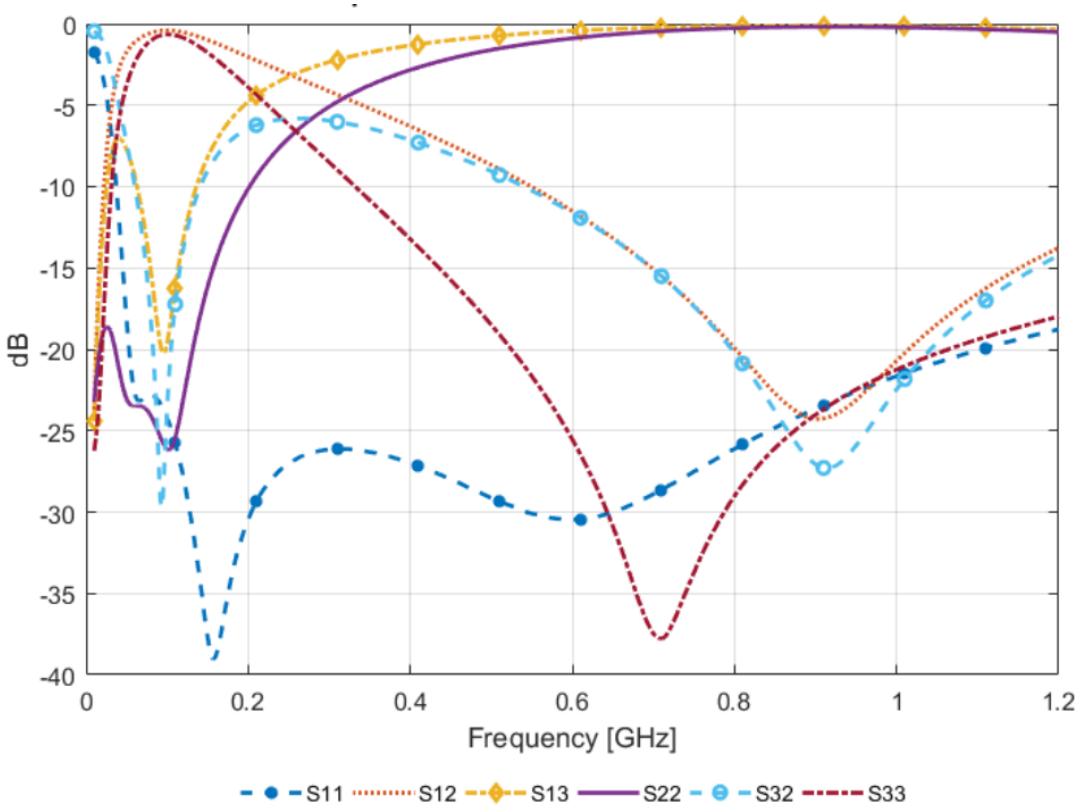

Figure 3.31 Measured and simulated power combiner results [164].

3.2.3 Matching Network and Rectifier Design Method, Simulations and Results

The custom-designed power combiner must be followed by a proper matching network. Since the expected incoming power is a dual-tone RF signal, where each tone has a different, time-variant power level, particular attention must be taken for the matching circuit design. In this research work, a three order L-network has been adopted, in order to achieve a dual-band matching for the considered power level of each signal. The higher-order also allows a wider band matching condition for each

frequency of operation. In Figure 3.32, the complete schematic and block diagram representation of the proposed harvester is represented.

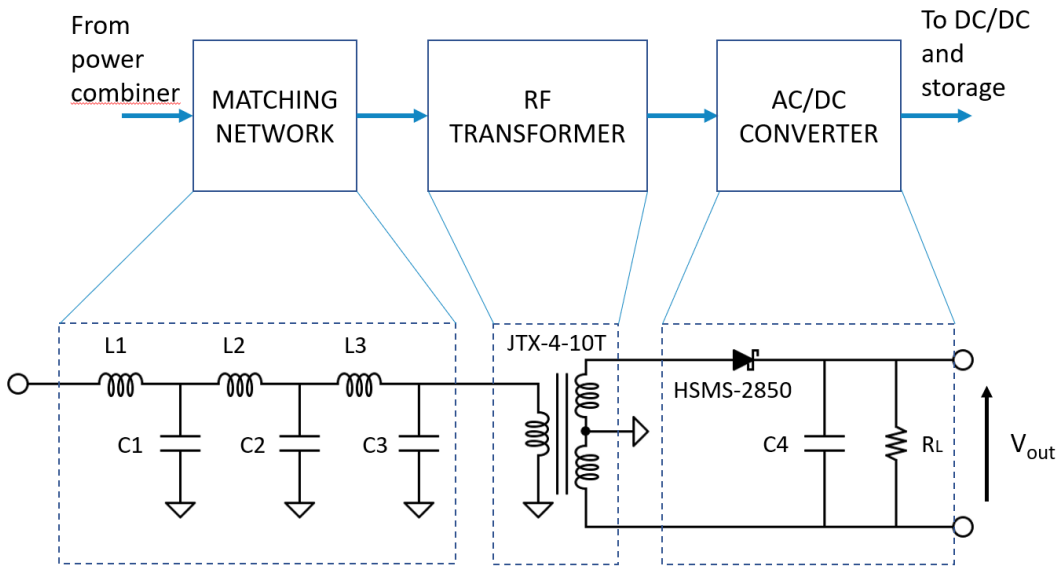

Figure 3.32 Simplified schematic and block diagram of the proposed EH system.

As can be noticed in the above figure, the matching network is also composed of an RF 1:4 transformer, JTX-4-10T+ by Mini-Circuits, whose characteristics are reported in Table 3.3. The role of the transformer is crucial, since it acts as an impedance transformation, helping to reach the matching condition [79], [165]. It also multiplies the RF voltage amplitude, which results 4 times greater than the input amplitude; this ensures that the voltage amplitude is always above the threshold voltage value of the rectifying diode, for the considered input power ranges. Finally, it decouples the RF antenna stage from the DC stage, providing a closed path for the DC current. Indeed, every antenna can be modeled with its Thevenin equivalent circuit, i.e. a voltage generator in series with an internal resistance [165]. However, from the DC point of view, the antenna represents an open circuit which does not permit the rectified DC current to circulate. A possible solution is to place a high-value shunt inductor near the antenna; the inductor represents a short circuit connection for the DC current circulation but can affect the matching network behavior [168]. Similarly, the secondary winding of the transformer acts as a short circuit connection for the DC current, which can circulate only in the rectifier stage, without affecting the antenna and matching network stage.

The selected component for the proposed rectifier circuit is the Schottky diode HSMS-2850 by Avago Technologies. Because of the high frequency and power level

variation of the EH system, the matching network design based on the non-linear model of the diode could be not enough to guarantee an optimal working condition, because of the model imperfections. Therefore, an S-parameter based approach is preferred. On the other hand, vendor's S parameter files are provided for different voltage and current biasing conditions of the diode, since it is generally intended for different applications, like signal peak detector, or input RF video decoding, where the diode is biased to always work in the active region. For an RF EH system, the only operative condition of the diode is the zero-bias, since no DC biasing signal is injected. Therefore, a custom room temperature test session has been performed, to extract the S-parameters at different RF power levels of the considered diode (see Figure 3.35). Moreover, a microstrip board has been implemented and the connectors and microstrips' S-parameters have been removed with a de-embedding operation, as proposed in [169].

Frequency (MHz)	**Insetion Loss (dB)**	**Input Return Loss (dB)**	**Amplitde Unbalance (dB)**	**Phase Unbalance (Deg.)**
50	1.42	20.84	0.06	0.35
130	1.38	22.75	0.00	1.77
210	1.40	20.52	0.09	2.44
300	1.43	18.71	0.16	2.76
425	1.48	17.75	0.22	2.82
550	1.52	18.42	0.26	2.61
675	1.54	20.24	0.25	2.16
800	1.57	24.59	0.18	1.69
925	1.65	32.84	0.03	1.23
1000	1.73	24.64	0.22	1.10

Table 3.3 Typical performance data of the JTX-4-10T+ RF transformer by Mini-Circuits [170].

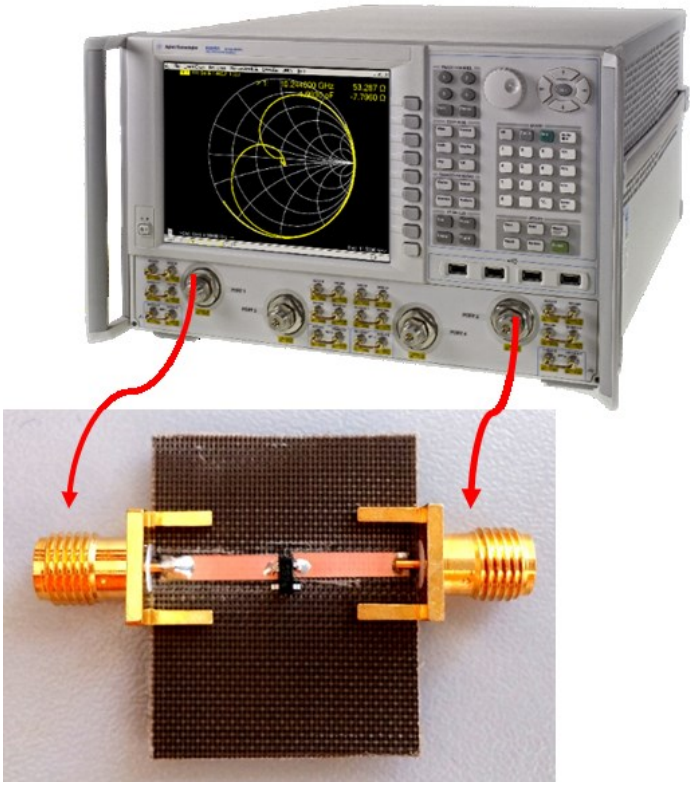

Figure 3.33 HSMS-2850 Schottky diode test board for zero-bias S-parameter extraction with de-embedding operation.

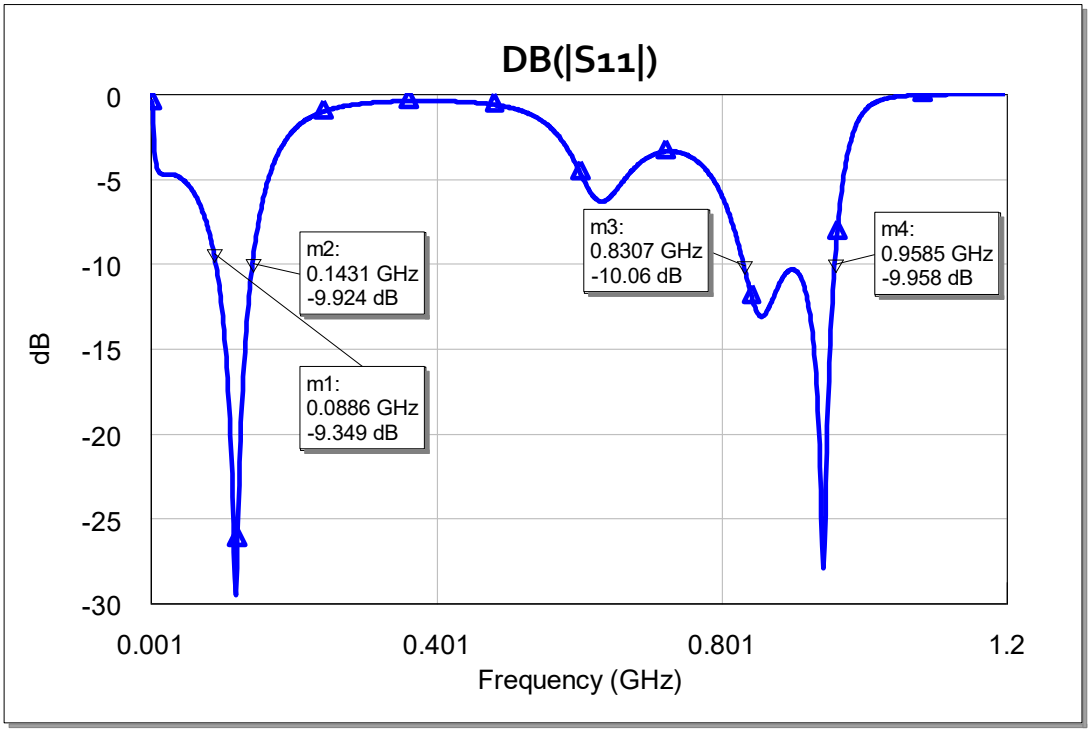

Figure 3.34 Simulated reflection coefficient of the designed matching and rectifying stage of the EH system, with an equivalent matched load of 3.5 kΩ.

In Figure 3.34, the simulated performance of the matching and rectifying stage, in terms of input reflection coefficient, are depicted, for an equivalent matched load of 3.5 kΩ. The conceived EH system shows good matching performance for both FM and GSM working band, with particularly high-matching conditions for 90 MHz and 900 MHz.

To improve the rectifier stage performance, a voltage doubler architecture was also designed (see Figure 3.35), which helps to improve the conversion efficiency for higher input power levels. Simulated performance of both single diode rectifier and voltage doubler architecture are depicted in Figure 3.36 and 3.37.

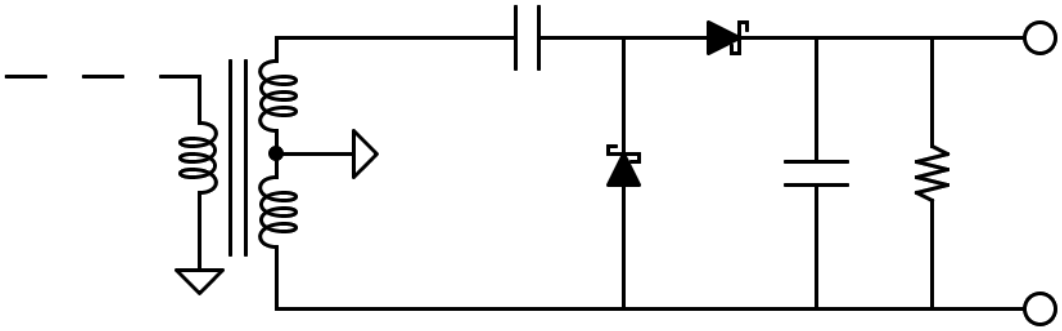

Figure 3.35 Voltage doubler architecture proposed as an alternative EH design.

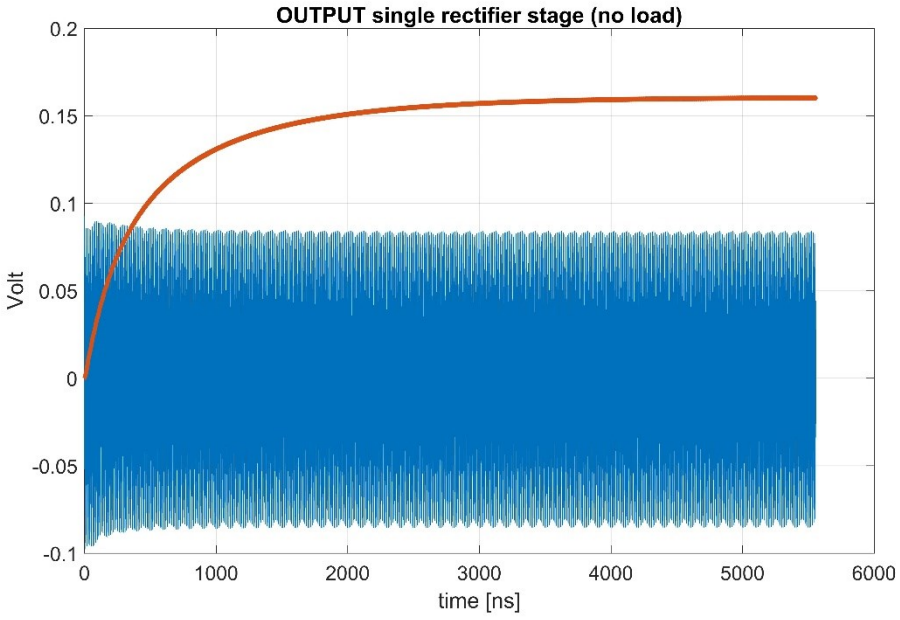

a)

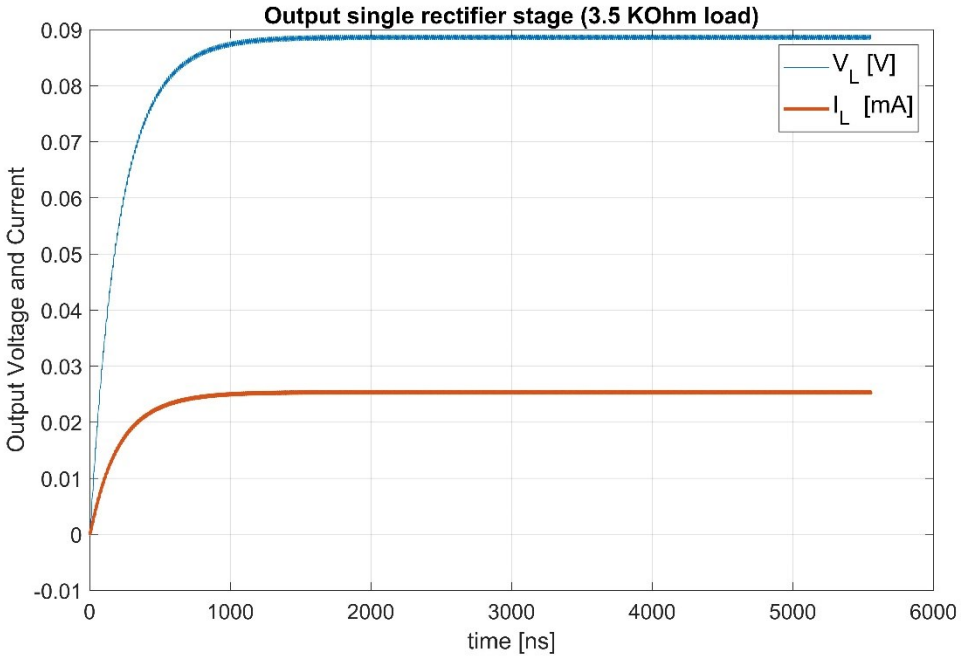

b)

Figure 3.36 Simulated performance of the single rectifier stage with no load (a) and with a matched 3.5 kΩ equivalent load, for an FM and GSM power level of -20 dBm and a and -23 dBm, respectively.

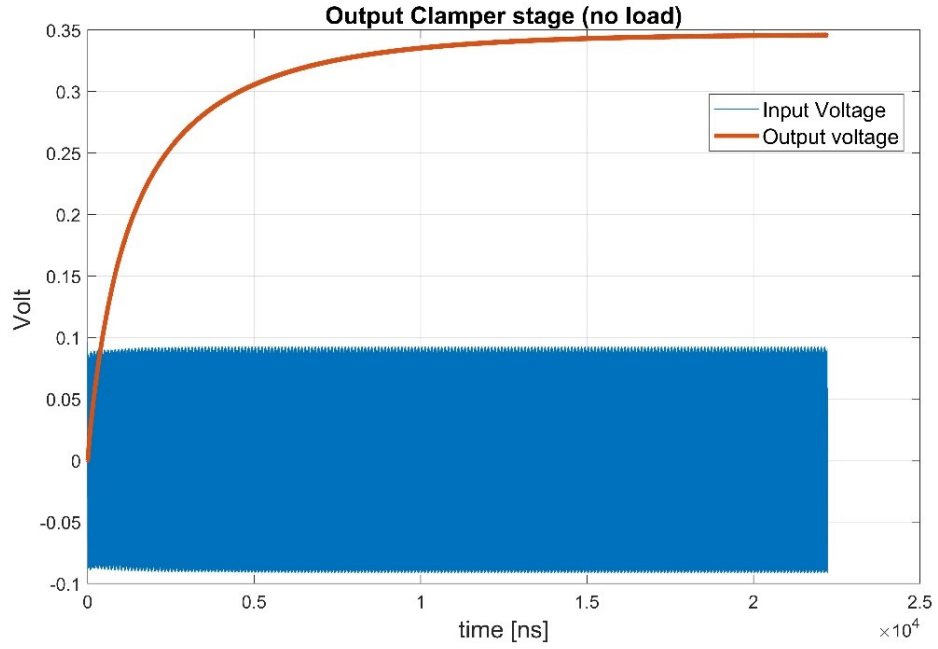

a)

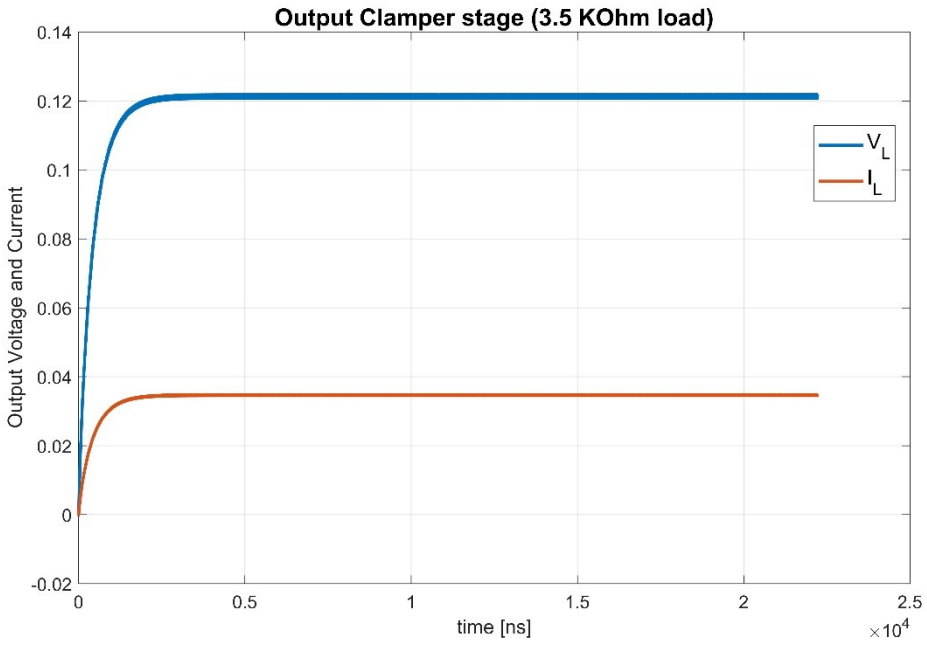

b)

Figure 3.37 Simulated performance of the voltage doubler rectifier stage with no load (a) and with a matched 3.5 kΩ equivalent load, for an FM and GSM power level of -20 dBm and a and -23 dBm, respectively.

Finally, a discrete prototype board has been implemented (Figure 3.38a) and tested (Figure 3.38b). The conversion efficiency of the system is depicted in figure 3.39 denoting a peak value of 52% for the GSM band and 50% for the FM received signal. Moreover, the probability density of the GSM signal related to the harvested efficiency and the total GSM power is showed in Figure 3.40.

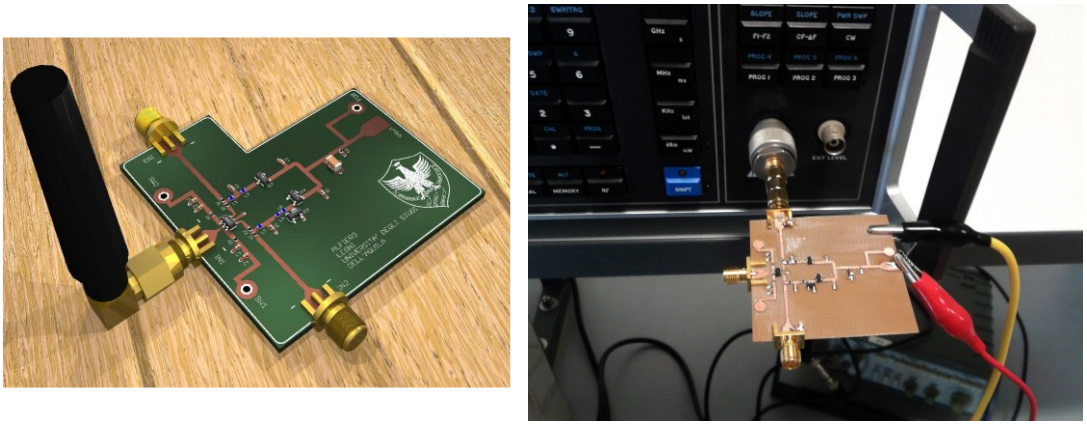

a) b)

Figure 3.38 Rendering of the conceived prototype board (a) and the realized board under tests (b).

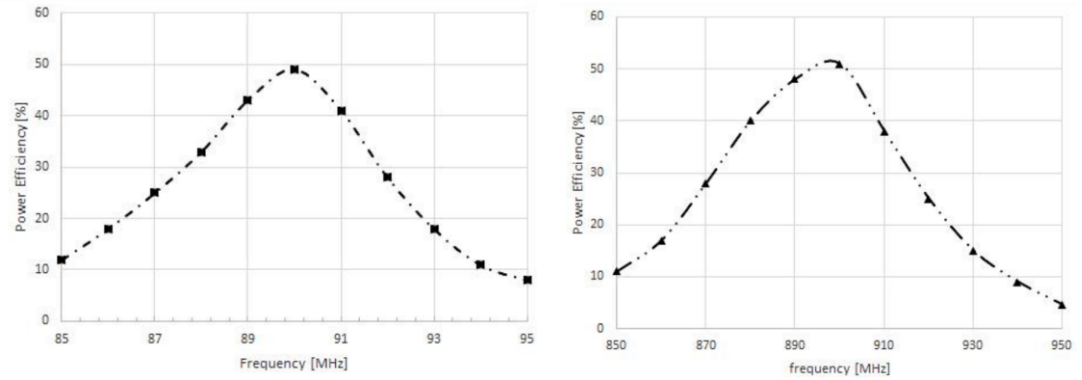

a) b)

Figure 3.39 Conversion efficiency for (a) the FM input signal and (b) the GSM input signal [164].

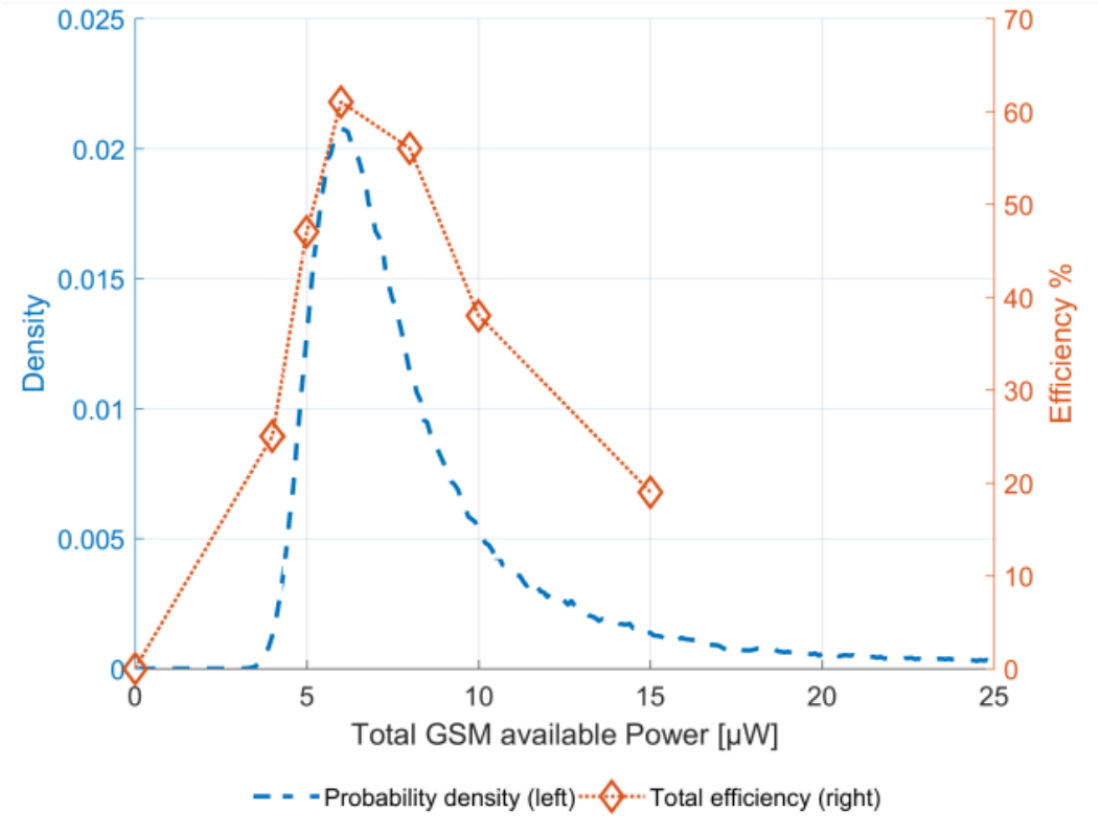

Figure 3.40 Probability Density and Harvester Conversion Efficiency vs Total GSM power [164].

3.3 RF ENERGY HARVESTER FOR SENSORY HEADWEAR

In this contribution, an RF energy harvester with a dedicated, indoor RF source for a wearable, biomedical device is reported. The supported device is a battery-operated sensory headwear, which uses an inertial measurement unit to detect the head movements and wirelessly transmits the acquired data. The maneuverability with the

head, without the use of hands, makes it ideal for the autonomous use by people with reduced motor skills, such as quadriplegics, for home automation and direct control of actuators. A 915MHz Radio Frequency energy harvester provides additional power to the system, thus increasing the usable time of the headwear and permitting the adoption of a smaller lightweight battery. This research has been conducted in collaboration with Prof. Saggio and his team, from the University of Rome "Tor Vergata".

Quadriplegia and paraplegia are disabilities that are caused by severe injuries to the spinal cord and neuromuscular disorders such as cerebral palsy [171]. Patients suffering from quadriplegia have different levels of compromised body movements, therefore, performing daily tasks like controlling home devices could be difficult. Therefore, quadriplegics require specific wearable devices to exploit their residual capacity of movement [171] and, for these reasons, a sensory headwear could be suitable to use the acquired information from the movement of the head for the home automation and the control of actuators, thus enhancing the autonomy of quadriplegic persons. Appropriate design of the system guarantees the required lightness and small dimensions; the use of novel miniaturized electronic components provides ultra-low power consumption. Moreover, in order to limit the overall dimensions and weight of the wearable devices, the general trend is to use smaller and lighter batteries, but this also leads to a shorter usable time of the wearable system. A solution to such a problem can be the energy recovery from the surrounding environment by means of energy harvesting techniques.

3.3.1 Headwear Architecture Overview

The system includes, as shown in Figure 3.41, two main blocks: the first regards the powering of the system; the second block acquires the information concerning the movement of the head and sends the data on a Bluetooth connection for the subsequent use in home automation. Measurements of the movements are made by the Bosh® BMI055 low-noise inertial measurement units (IMU). A Microchip's ATmega328PB 8-bit AVR® RISC-based microcontroller (MCU) permits the IMU timing, thus collecting measurement data. The acquired data is then transmitted using the Nordic® Semiconductor nRF8001 Single-chip Bluetooth® low energy solution. The choice of Bluetooth communication and its diffusion on most portable devices makes the system easily compatible also for the development of third-party applications achievable on smartphones, smartwatches, and tablets [172].

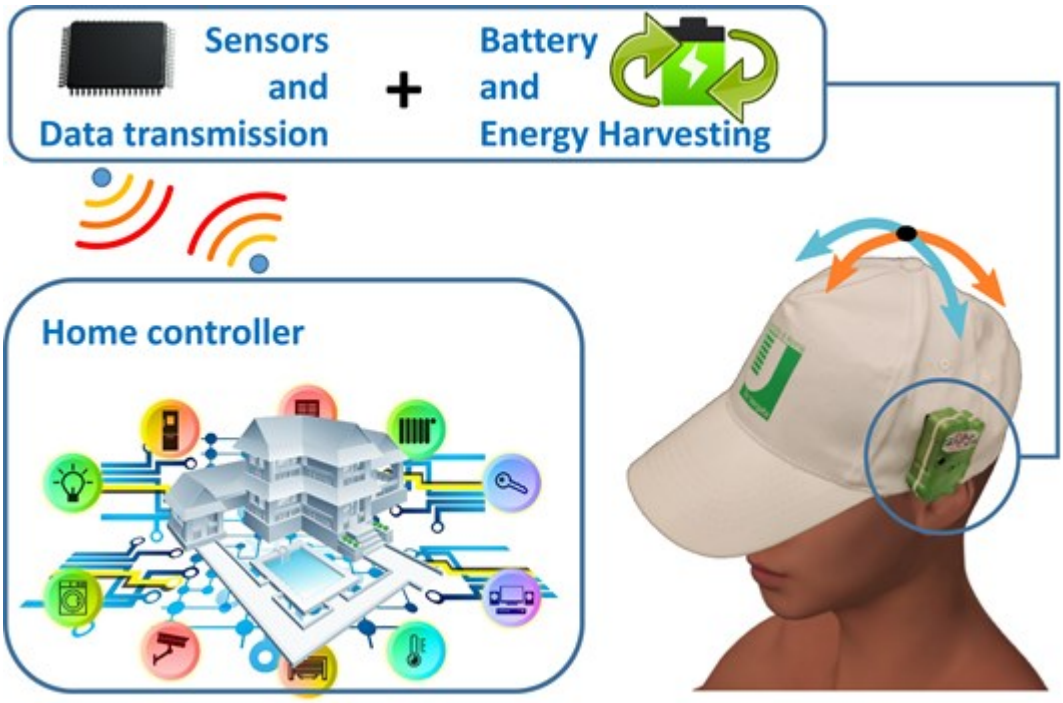

Figure 3.41 Block scheme of the proposed headwear system. The sensory headwear is equipped with an IMU for head motion tracking, a source battery, and an energy harvesting circuitry. Data gathered from the head movements are wirelessly sent to a receiver and converted into home automation commands [172].

The schematic connections of the main building blocks composing the data management part of the sensory headwear are shown in Figure 3.42. The logical center of the system is represented by the MCU Atmega328PB, which collects the movement data coming from the IMU BMI055 and makes them available for the implementation of home automation functions via the integrated nRF8001 which provides wireless transmission with Bluetooth Low Energy® (BLE) standard. All the integrated units are powered at the same voltage of 2.9 V so as to allow the natural compatibility of the voltage logic levels associated with the communication lines and the expected interrupt levels. The BMI055 is a sensor with 6- degree of freedom (6-DOF) which includes a 12-bit triaxial accelerometer and a 16-bit triaxial gyroscope with a range up to ± 2000 °/ s. The BMI055 admits the I2C or SPI serial communications by setting appropriately the voltage value on the PS pin. In particular, by setting PS to the reference voltage, the integrated acts according to the SPI protocol on the output pins at a maximum speed of 10 MHz (obtainable for supply voltages higher than 1.62 V, as in our design). By setting a dedicated register, BMI055 provides the designer with the possibility to opt for a 3 or 4-wire SPI communication. Using 4-wire communication, by means of dedicated slave-select pins (SDO1 and SDO2), the accelerometer and gyroscope behave as independent parallel slaves communicating on two separate lines.

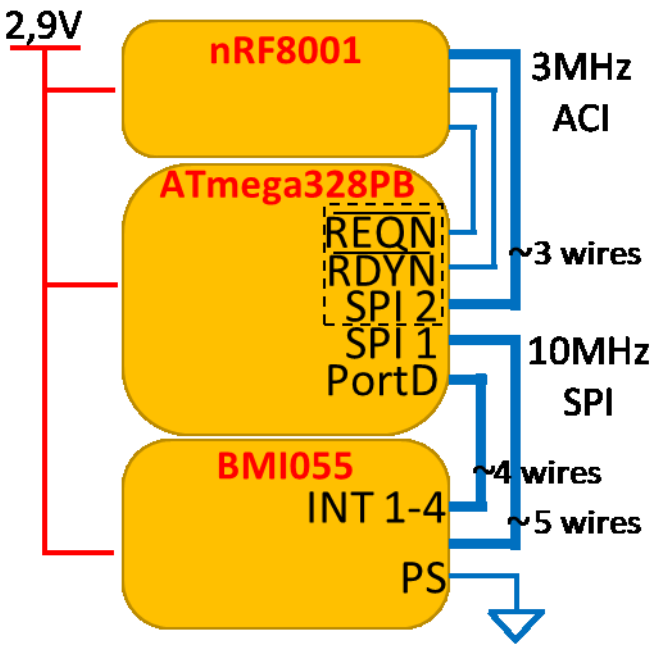

Figure 3.42 Simplified block scheme of the communication and control interface for the microcontroller, the Bluetooth transmitter, and the IMU sensor.

With the aim to minimize the number of PCB tracks, in our implementation, we use the 3-wire configuration, with a common MISO line. Additionally, the BMI055 has four programmable interrupt pins. Two of these are associated with the accelerometer and the other two with the gyroscope. One of the two accelerometer interrupt lines is used to define a wake-up signal on the microcontroller in the case of acceleration values overshot a fixed threshold value. This way, the microcontroller is in "idle mode" if no significant movement measures occur, thus allowing considerable power-saving without affecting the functionality of the device. The other interrupt lines connected to the microcontroller allow the development of dedicated functions *e.g.* the recognition of specific motor patterns or angular or linear acceleration peaks, also useful for defining auxiliary commands for implementing advance features for the sensorized headwear. The nRF8001 is a SoC that implements BLE® wireless communication and has a serial communication interface called Application Controller Interface (ACI). This interface is similar to the classic SPI standard, with the addition of two active handshake signals on the pins called REQN and RDYN (as reported in Figure2). REQN is the handshake signal from the MCU to nRF8001, whereas the RDYN is the handshake signal from nRF8001 to the application controller. The handshake signals terminated on the MCU interrupt pins permit to maintain the nRF8001 SoC ready for communication by activating it when data is available while

maintaining the MCU into idle mode when not needed, thus saving battery power. The nRF8001 maximum interface communication speed is 3 MHz. Since this communication speed is different from that of the BMI055 (that is at 10 MHz), we have used both the SPI ports available on the Atmega328PB, thus achieving the advantage to optimize the data rate of both the IMU and Bluetoooth® SoC by using two different SPI clock frequencies, as well as improving the power management by selecting appropriately the active/idle states of the various integrated circuits involved since they can be managed separately.

3.3.2 RF Harvester Antenna Design Method

In this RF energy harvesting application, a custom antenna has been designed, in order to overcome problems related to the wearability, i.e. encumbrance and weight, but also the effect that the human body has to the antenna radiation pattern.

One of the reasons to consider a dedicated 915 MHz source for RF harvesting is that the human body presents a low absorption rate for electromagnetic waves with frequency below 1 GHz [173], resulting in a low harmful wireless power transfer for the headwear user. However, the human body and so the human head can be considered as a conductor medium from the EM point of view, therefore the RF harvesting antenna performance can be negatively affected, if the environmental conditions are not properly considered during the design process [173].

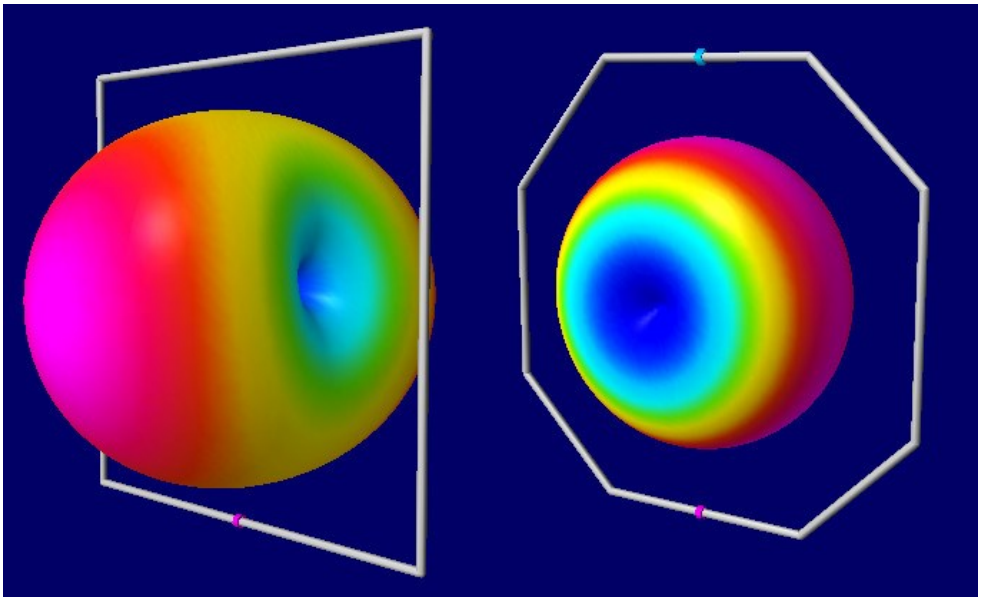

Figure 3.43 Typical far-field 3D radiation patterns of a square (left side) and octagon (right side) shape loop antennas.

The selected antenna type for this application is a simple loop antenna, which is similar to a folded dipole behavior. Microstrip antennas or other planar antennas with ground plane can be also considered, due to the presence of the ground plane that acts as a shield from the antenna and the human body. On the other hand, they are bulky and difficult to fit in a wearable hat, differing from a loop antenna which has the advantage to present the minimum encumbrance and lightness. Here we choose the full wavelength dimension for the loop circumference, in order to maximize the antenna receiving efficiency [174].

Moreover, the loop antenna presents a linear polarization, which is not preferable for environmental RF energy harvesting, since no information is generally given about the energy source transmitter. However, in this application there is control on the RF energy emitter, hence a transmitting antenna with linear polarization can be selected as well, in order to match the harvester requirements. Furthermore, the loop antenna far-field radiation pattern is quite similar to that of a dipole, i.e. a dual, omnidirectional lobe (see Figure 3.43). Differing from a simple or folded dipole, the loop antenna has a lower transmission gain towards the ground or the sky, presenting about 1.5 dB higher gain in the horizontal direction, thus increasing the amount of harvested power [174].

One of the main drawbacks is the feeding method that requires a differential, balanced connection. On the contrary, typical RF energy harvesting circuits are implemented by mean of microstrip structures, that are unbalanced planar waveguides. Therefore, a proper balun structure must be designed.

In order to take into account the human head presence near the antenna for the design process, electromagnetic simulations must be performed and a suitable EM model representing the average dielectric properties of the head has to be implemented. However, the human head is a complex, inhomogeneous medium which is difficult to be modeled and EM simulations algorithms, such as FEM or MoM (Method of Moments), can require high-performance computing resources and long simulation times to solve such a physical model of the system. According to [175] and [176], a human head for EM simulation purposes can be modeled as a homogeneous material phantom whose properties are set to the 2/3 of the permittivity and conductivity of the human muscle tissue at the frequency of operation. Houzen et al in [176] proved that the 2/3 muscle model is a good approximation for the real human head.

According to studies conducted by Gabriel et al. [177], Schwan [178] and Athey et al. [179], the considered EM properties for the 2/3 model of the human muscle tissues are relative permittivity $\varepsilon_r = 36$ and conductivity $\sigma = 0.657\ S/m$, at the operating frequency of 915 MHz.

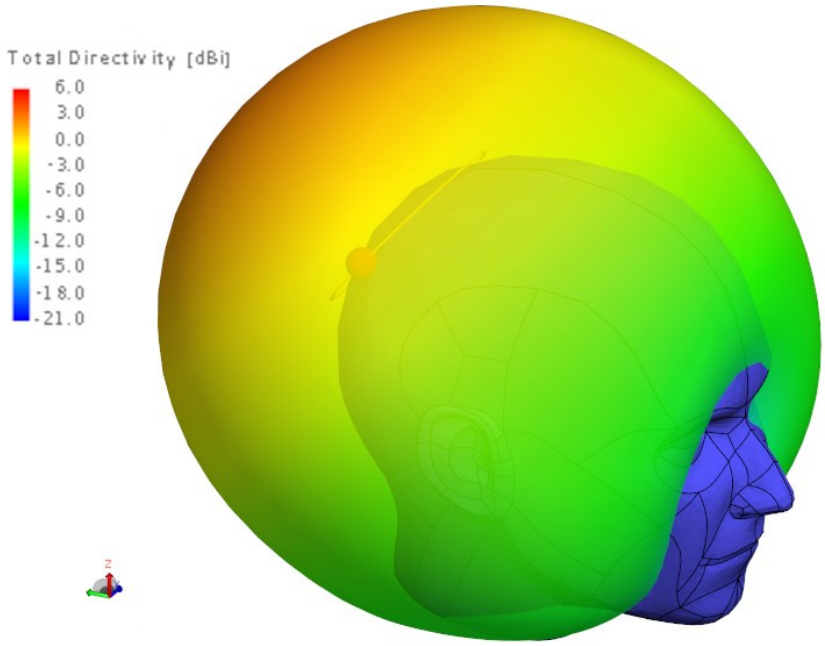

a)

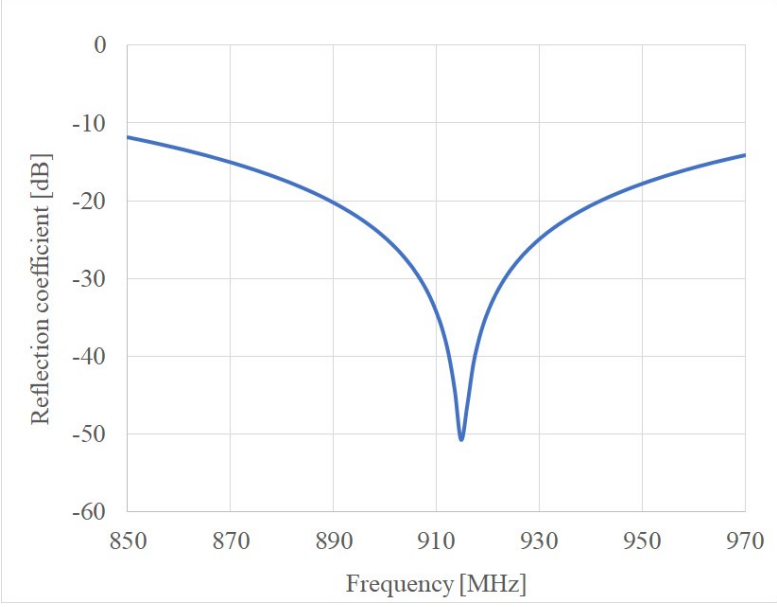

b)

Figure 3.44 The implemented human head phantom with the custom loop antenna place between the occipital and parietal zone (a) and simulations of the obtained reflection coefficient (b).

An average-sized human head phantom with those properties has been implemented in the CAD software Altair FEKO for EM simulations and a loop antenna, placed between the occipital and parietal zone, has been designed (see Figure 3.44a). The presence of such a high permittivity medium permits to reduce the overall dimensions of the antenna [180]–[182], that has a radius of 49,6 mm, with a resonance impedance of 148 Ω and a reflection coefficient of -51 dB at 915 MHz, as shown in Figure 3.44b.

As stated before, a differential antenna structure, as the loop-shaped antenna, needs a balun transformer to be connected with an unbalanced waveguide froth both measurements and usability in EH systems. One of the main goals for the impedance transformation is to provide a 180° phase difference between the two balanced ports of the antenna, and matched differential impedance, in order to guarantee proper functionality [165]. A Wilkinson-type balun is one of the commonly adopted choices, but additional circuits are needed for phase unbalancing [183], which results in increased size and losses. To overcome these issues, the procedure described by Park in [184] was followed to implement a Wilkinson-type balun, presenting a typical structure of a Wilkinson power divider where a conventional $\lambda/4$ transmission line is used for -90° phase shifting, while a composite right/left-handed $-\lambda/4$ transmission line (CRLH-TR) is employed for +90° phase shifting (see Figure 3.45), resulting in a 180° difference between the two balanced ports [184].

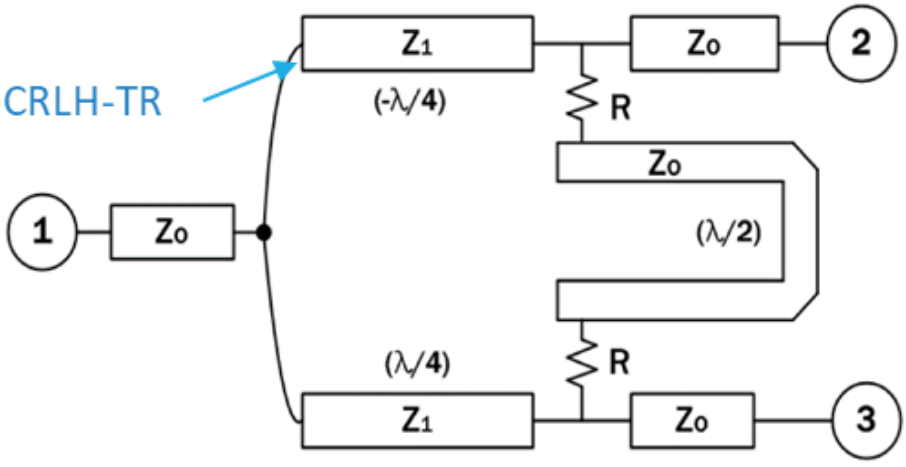

Figure 3.45 Block diagram of the Wilkinson-type balun proposed in [184].

The implemented antenna and balun, with measurements of the obtained reflection coefficient, are shown in Figure 3.46. Results validated the design method since a good resonance behavior is obtained around 915 MHz.

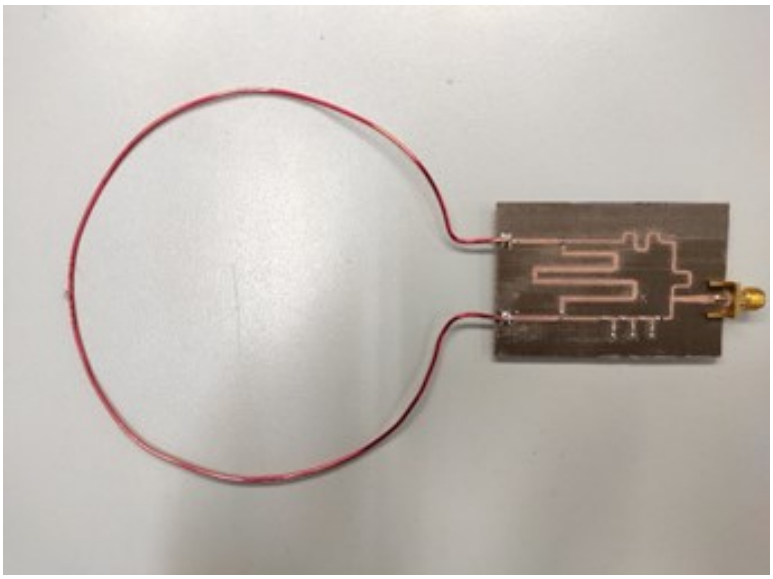

a)

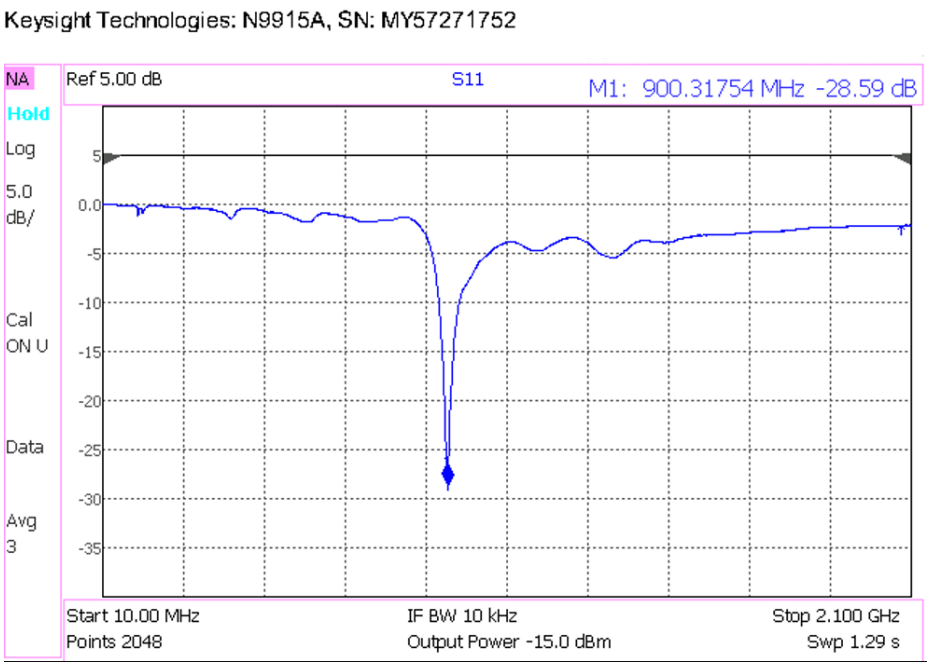

b)

Figure 3.46 The implemented loop antenna with the Wilkinson-type balun (a) and measurements of reflection coefficient (b).

3.3.3 RF Harvester System Design and Implementation

For this application, a custom RF energy harvesting system has been designed and compared with a commercial solution, the P2110B Evaluation Board from Powercast®, to demonstrate the advantages of the adopted method.

For the RF energy source, the Powerspot transmitter from Powercast® has been employed, whose main characteristics are listed in Table 3.4.

Features	Data
Frequency of operation (MHz)	915
Effective Isotropic Radiated Power (W)	3
Antenna gain (dBi)	6
Antenna polarization	Linear
Beam pattern angle (Deg.)	70
Power supply (V)	5
Dimensions (mm^3)	$185.4 \times 53.3 \times 35.6$

Table 3.4 Main characteristics of the RF power transmitter Powerspot from Powercast® [185].

As a first step, the system setup with the commercial energy harvester P2110B was connected to the custom loop antenna (see Figure 3.47) and performance has been measured, in terms of effective conversion efficiency, for a matched load of 5 kΩ.

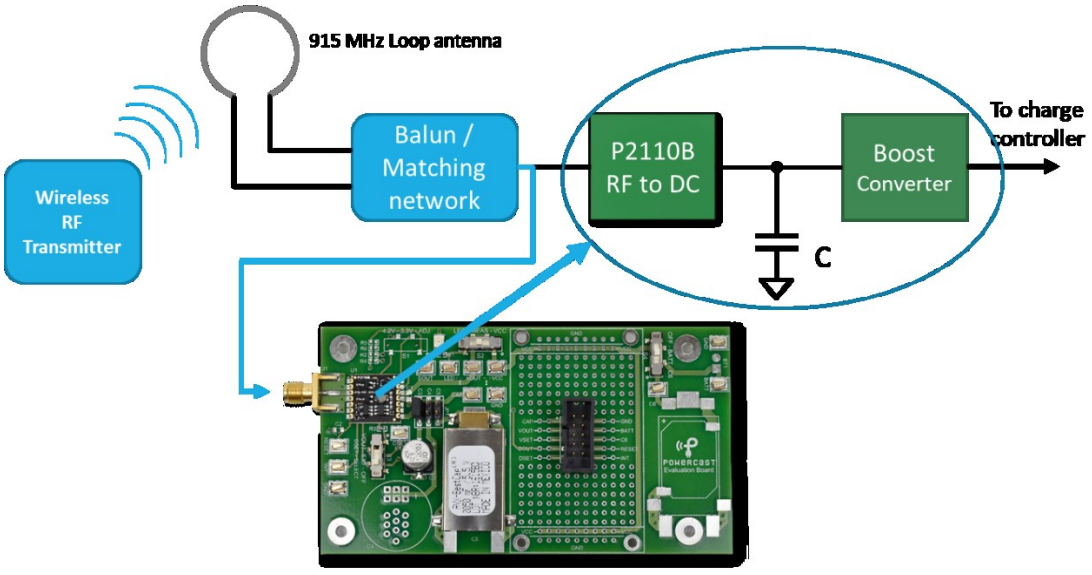

Figure 3.47 RF energy harvester setup with commercial P2110B Eval Board from Powercast®.

For test conditions, the DC/DC and battery charge regulator was disconnected, while the internal reference resistance, that is intended for RF-to-DC output voltage measurement and regulation, was disabled, so that an external load could have been applied, in order to test only the rectifier performance. In order to characterize the device efficiency versus the input power, the antenna was not connected at first, while an RF signal generator was employed to inject the test signal, at the frequency of 915 MHz, with different power levels.

According to the RF power source characteristics, reported in Table 3.4, and recalling the equation 3.2.2, the resulting available power spectral density is much higher, compared to environmental long-range RF energy harvesting capabilities, showing a theoretical value of 0.238 W/m^2 for a distance of 2 m between the source and the user, which rises up to 3.8 W/m^2 for a distance of 50 cm. Therefore, efficiency measurements were taken in the range -6 dBm to 10 dBm. The resulting performance of the commercial EH board, represented in Figure 3.48, denotes an efficiency peak of 43%, with an input power of about 7.5 dBm; after that value, the efficiency soddenly decreases because of the rectifying diode saturation. Below -4 dBm, the efficiency falls to zero, indicating that the harvester is not working anymore.

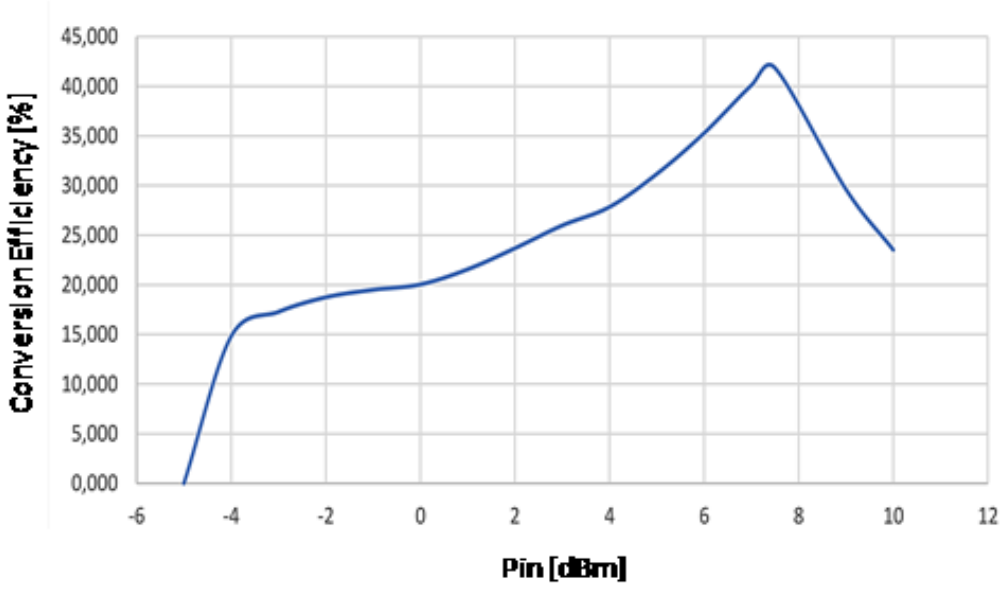

Figure 3.48 Measured conversion efficiency of the commercial harvester P2110B from Powercast®.

Results of the commercial harvester characterization suggest that the system is not able to handle the available amount of power due to the internal diode limitations. Therefore, proper architecture should be selected for the RF-to-DC rectifier block. For

these reasons, a dual-stage Dickinson voltage multiplier has been chosen for the custom design (see Figure 3.49), since this architecture can guarantee high voltage gain and high-power handling capabilities [96].

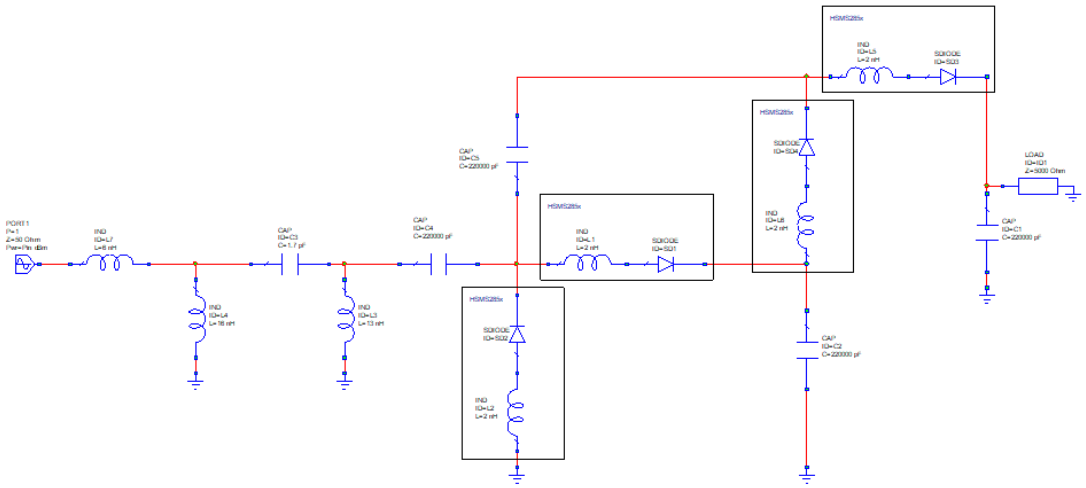

Figure 3.49 Proposed architecture for the custom RF EH system.

For the matching network, a Pi-configuration has been selected, while the Schottky diode HSMS-2852 from Avago Technologies has been chosen for the rectifier architecture. Here, the non-linear Spice model has been employed for simulations, and its typical parameters are reported in Table 3.5.

Parameter	Value
I_S (μA)	3
R_S (Ω)	25
N	1.06
TT (ns)	0.01
C_{J0} (pF)	0.18
M	0.5
E_G (eV)	0.69
XTI	2
B_v (V)	3.8
I_{BV} (μA)	300
V_J (V)	0.35

Table 3.5 Spice model parameters of the Schottky diode HSMS-2852 [186].

Because of the non-linearity of the conceived rectifier, the matching network should be carefully designed, in order to obtain the best efficiency at the frequency of operation and considering the desired input power range, which is fixed from -10 dBm to 10 dBm. For these reasons, a first non-linear simulation of the sole rectifier was performed, under the NI AWR environment, by varying the output DC load, the input power and tuning the conjugate input impedance, in order to keep the efficiency at the maximum possible level. The results of the simulation are shown in Figure 3.50.

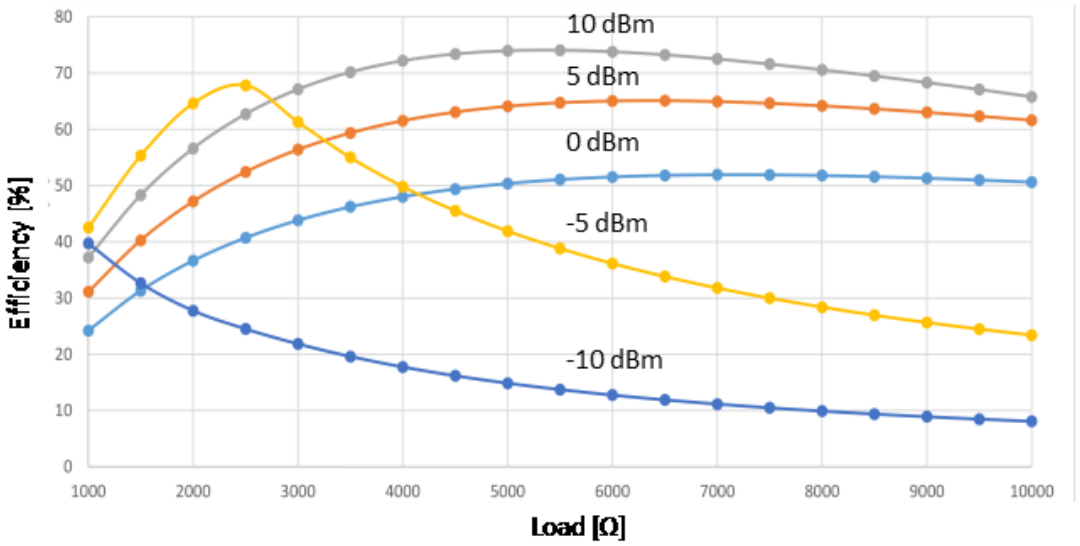

Figure 3.50 Non-linear large S-parameter simulation of the conceived rectifier, obtained by varying the output DC load, the input RF power, and the matching tuner impedance, to maximize the efficiency.

Simulation results show that the best efficiency value can be achieved with high loads, for this configuration. As a compromise for all the considered input power levels, a DC load value of 5 kΩ has been selected as a reference for the matching network design and the optimal impedance was chosen to be 201 + j139 Ω based on the nonlinear characterization. All the simulations have been conducted with real design parameters, thus the TLX-8 RF substrate from Taconic has been selected and its characteristic parameters are listed in Table 3.6.

Material	Dielectric constant@ 10 GHz	Losses (tanδ)@ 10 GHz	Substrate thickness	Coper Thickness
TLX-8 laminate	2.55 ±0.4	0.0019	0.76 mm	0.35 µm

Table 3.6 Dielectric properties and thicknesses of the TLX-8 RF substrate from Taconic.

The obtained matched impedance was employed to design the Pi-configuration matching network and the validation of the implemented matched impedance with the reference DC output load of 5 kΩ was proved by means of a further non-linear simulation. Here, the input impedance of the harvester was simulated by fixing the reference load and changing the input RF power, at the frequency of operation. Simulation results have been reported on a Smith chart (see Figure 3.51), that was normalized at the considered matched impedance.

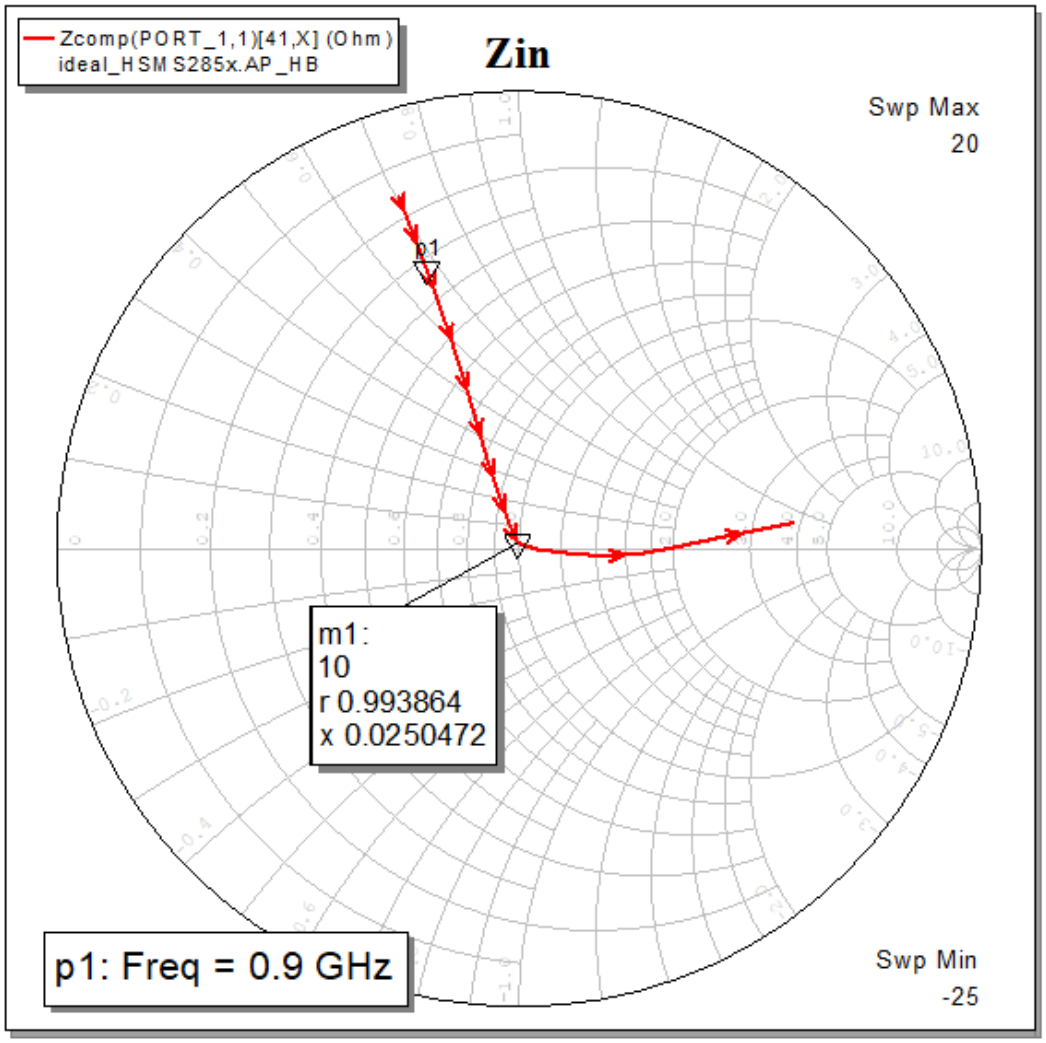

Figure 3.51 Input impedance of the conceived RF energy harvester, with the optimal matching condition at 10 dBm of input power.

From the figure, it can be noticed that the simulation indicates a perfect matching for a 10 dBm of input power. The power compression point was also evaluated in this design, in order to evaluate the saturation behavior of the designed RF harvester. Results of the non-linear simulation input power versus DC output power (see Figure 3.52) locate the 1 dB power compression point at 11 dBm of RF input power. In fact,

greater values of the received Rf power cause a complete flatness of the characteristic curve, degrading the efficiency.

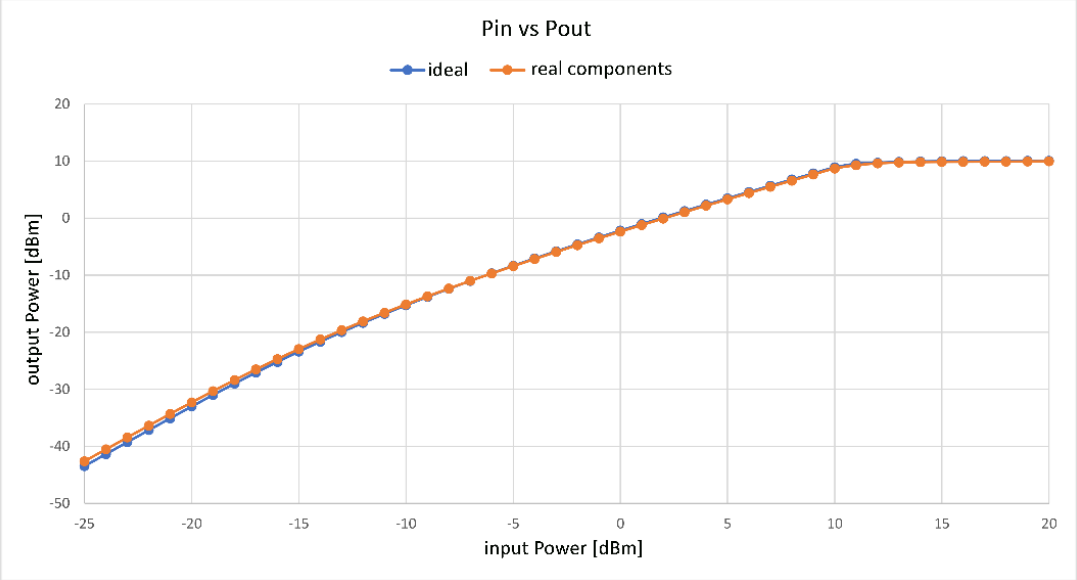

Figure 3.52 Input power vs output power non-linear simulation of the proposed RF multistage harvester.

Finally, a prototype board has been implemented with lumped elements (see Figure 3.53) and characterized. Firstly, the reflection coefficient of the proposed RF energy harvester was measure, with the reference DC load, in order to validate the matching performance at the frequency operation. Results denote a little down-shift of the resonance frequency, which is still in the optimal working range (see Figure 3.54). Consequently, a measurement campaign has been conducted by injecting the input power with the RF signal generator MS2830A from Anritsu, to both the commercial board P2110B and the custom-designed energy harvester, with the considered optimal DC load, in order to compare the performance. The tests were done for both the frequencies of 900 MHz and 915 MHz and results proved the better performance of the custom-designed harvester for all the measuring conditions, with an efficiency peak of up to 75%, as shown in Figure 3.55.

To conclude the characterization, a comparison test with the dedicated 3 W RF transmitter was done, to emulate a real scenario of operation. For this experiment, the custom loop antenna was employed, and measurements were conducted outdoor, in order to avoid reflection and interferences of an indoor environment which could affect the characterization. The results have been reported in Table 3.7.

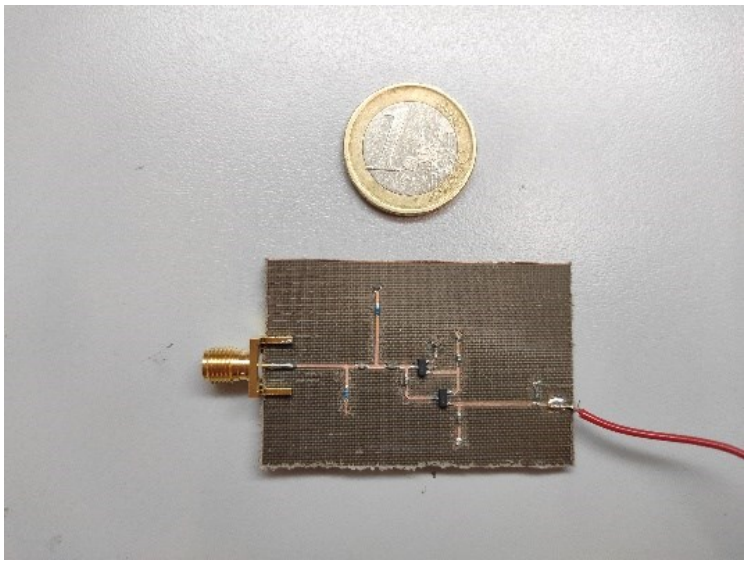

Figure 3.53 The implemented prototype board of the proposed multi-stage RF energy harvester.

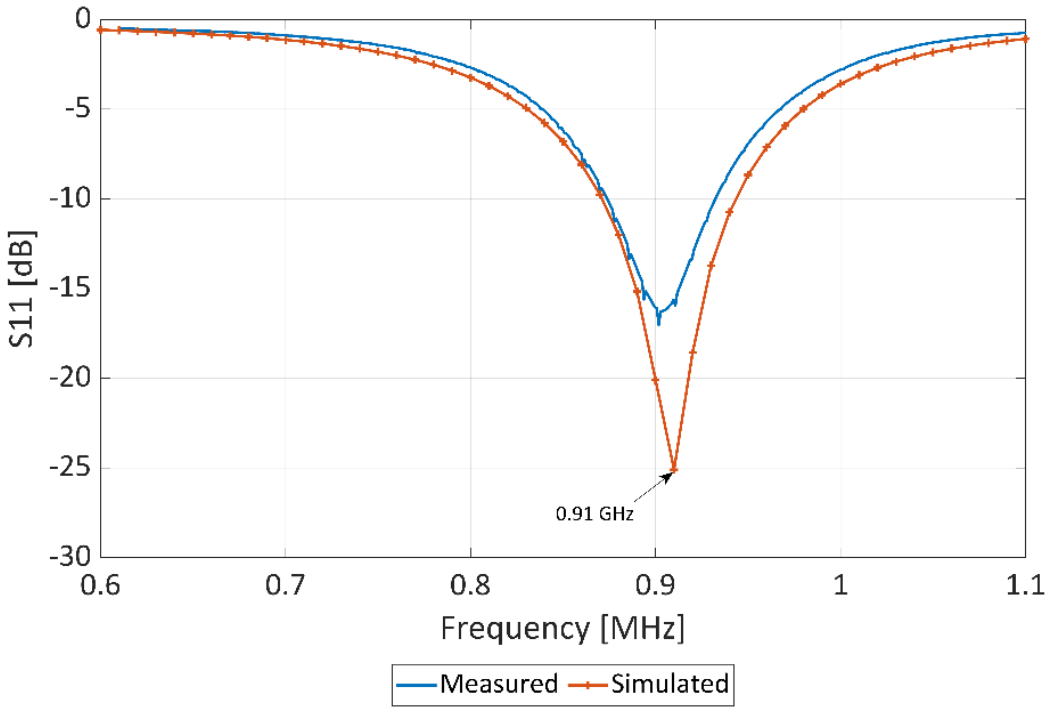

Figure 3.54 Measured vs simulated reflection coefficient of the custom-designed RF EH system.

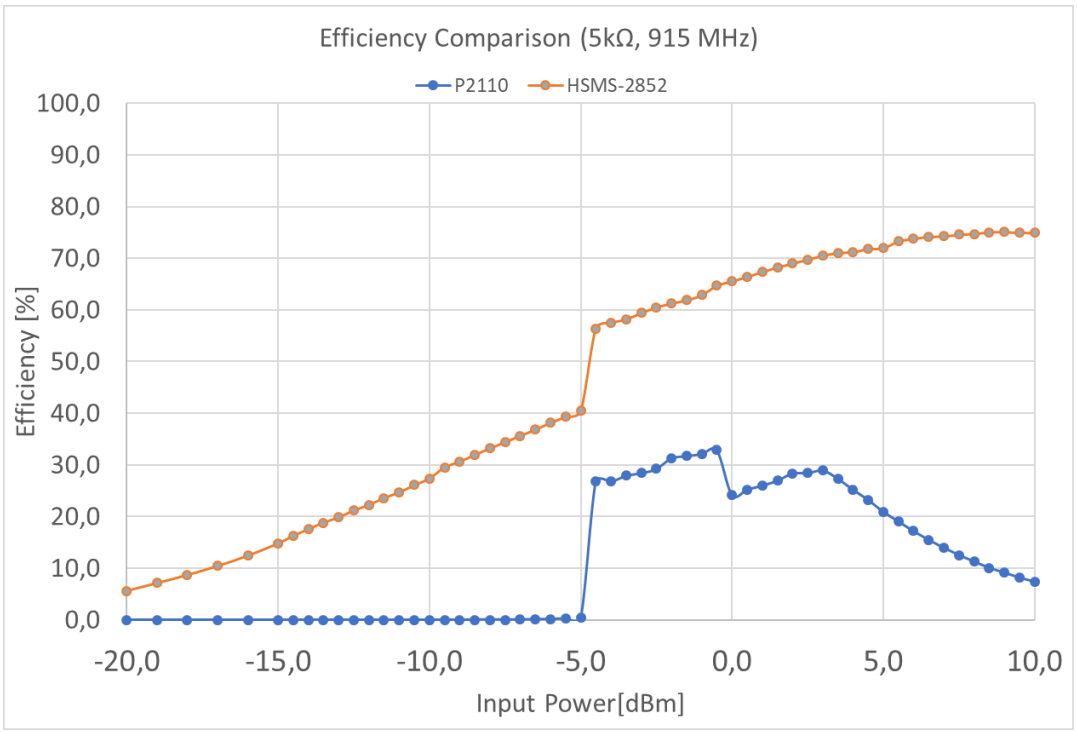

a)

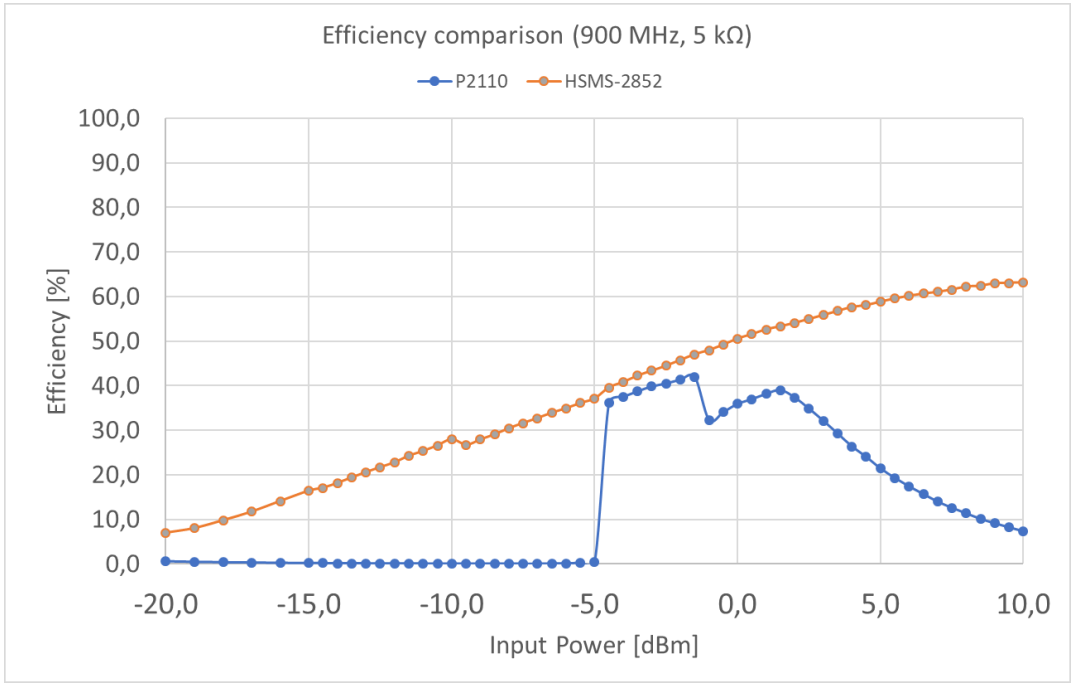

b)

Figure 3.55 Comparison of the measured efficiency between the commercial P2110B harvester board and the proposed energy harvester at (a) 915 MHz and (b) 900 MHz.

Distance [cm]	P2110 Output @ 5 kΩ (V)	Custom design Output @ 5 kΩ (V)
25	2,040	13,450
50	1,980	9,300
75	1,918	5,680
100	1,892	4,680
150	1,814	2,700
200	1,810	2,110
250	1,830	2,770
300	1,600	1,990
400	0,252	0,331
680	0,720	0,900
800	0,850	0,870
1000	0,730	0,740
1500	0,134	0,256
2000	0,002	0,075
2200	0,000	0,050

Table 3.7 Comparison of outdoor harvesting test with the dedicated 3 W RF transmitter.

Chapter 4: Thermoelectric and Biomechanical EH Contributions

In this chapter, the author's contribution to novel methods, design procedures and implementation of thermoelectric and biomechanical energy harvesting systems for wearable biomedical applications are reported.

4.1 MODELLIZATION OF LOW-COST TEG MODULE FOR MULTI-CELL, LOW-TEMPERATURE THERMOELECTRIC EH

In this work, an identification technique of a simple Spice model, measurements-based, is presented for small low-cost Peltier cells used in Thermoelectric Generator (TEG) mode for low-temperature differences, such as for human body heat energy recovery. The collection of electric energy from thermal sources is an alternative solution of great interest to the problem of energy supply for low-power portable devices. However, materials with thermoelectric characteristics specifically designed for this purpose are generally expensive and therefore often not usable for low cost and low power applications. For these reasons, in this paper, we studied the possibility of exploiting small Peltier cells in TEG mode and a method to maximize the efficiency of these objects in energy conversion and storage since they are economical, easy to use and available with different characteristics on the market. The identification of an accurate model is a key aspect for the design of the DC / DC converter, in order to guarantee maximum efficiency. For this purpose, the Spice model has been validated and used in a design example of a DC / DC converter with a Maximum Power Point Tracking (MPPT) algorithm with fractional open-circuit voltage (FOCV).

4.1.1 Materials and Methods

The behavior of a Thermoelectric Generator has been firstly analyzed and reported in this section, in order to understand what the best electrical equivalent model is, suitable for low-power, low-temperature difference applications.

A thermoelectric generator is generally constituted by several junctions in series between semiconductors that are n-doped and p-doped, in order to achieve different Seebeck coefficients. In Figure 4.1, a block scheme of a single n-p couple is represented. The hot-side of the couple has a temperature T_H while the cold side presents a temperature T_C, lower that T_H and because of the Seebeck effect, and electromotive force (emf) $-S\Delta T$ is generated, where S is the total Seebeck coefficient, and a current I flows in the closed circuit, composed by the single n-p couple and the load R_L.

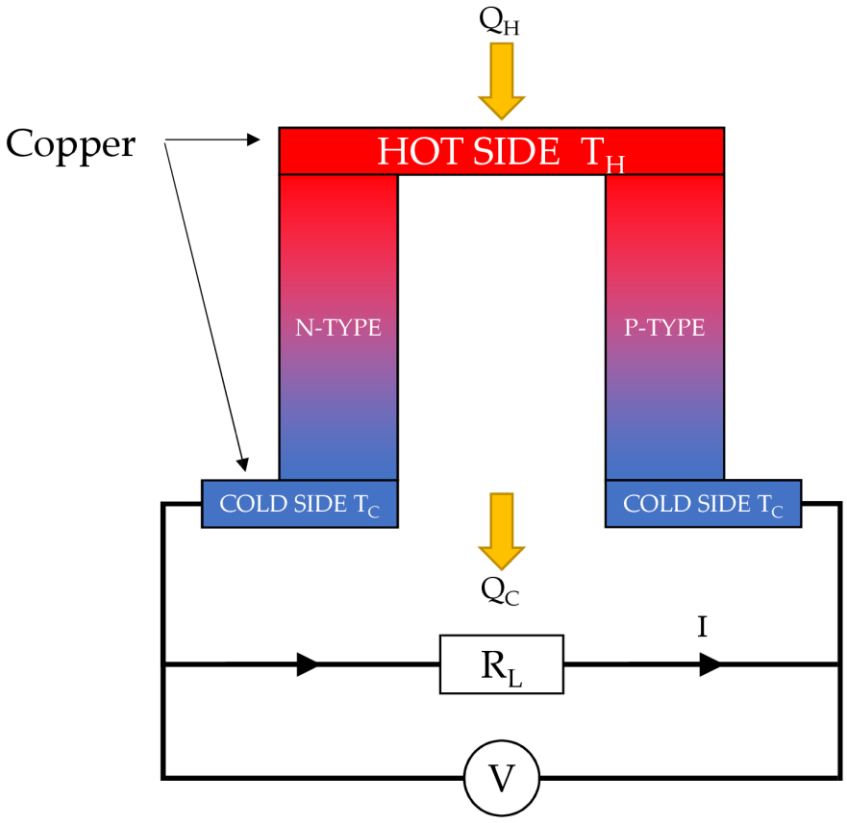

Figure 4.1 Single couple of P-Type and N-Type materials constituting a thermoelectric generator [187].

Considering the heat supplied to the hot side Q_H and the heat released from the cold side Q_C, according to the first law of thermodynamics, it is possible to compute the electric power generated by the thermoelectric n-p couple as follows:

$$\begin{aligned} Q_H &= ST_H I - \frac{1}{2}I^2R + K(T_H - T_C) \\ Q_C &= ST_C I + \frac{1}{2}I^2R + K(T_H - T_c) \end{aligned} \quad \Rightarrow W = Q_H - Q_C = SI\Delta T - I^2R \qquad (4.1.1)$$

where R is the electrical resistance of the thermocouple and K is its thermal conductance.

Since the system is closed to a load, the total electrical power W is also equal to I^2R_L, thus it is possible to express the current and voltage provided by the TEG as follows:

$$V = IR_L = S\Delta T - IR$$
$$I = \frac{S(T_H - T_C)}{R + R_L} \tag{4.1.2}$$

Therefore, the electrical model of a Thermoelectric cell composed by N couples n-doped and p-doped can be simply represented by a voltage generator $V_{TEG} = N \cdot V$ in series with an internal resistance $R_{TEG} = N \cdot R$. However, the Seebeck coefficient S, as well as the thermal conductance K and the internal resistance of the cell are temperature dependent and, therefore, the behavior of the system is non-linear for large temperature variations. On the other hand, if the temperature variation is small, as well as the temperature difference, (as in the case of human body heat energy harvesting) the system can be considered locally linear [188]–[190].

As a second step of this work, a Peltier cell $2 \times 2 \times 0.5$ cm model TEC1-3103 [191] was analyzed with the aim of determining a method to identify a Spice model from the acquired data. A specific test platform was therefore created, which has the role of providing a stable temperature difference between the two sides of the Peltier cell. The system consists mainly of a 22×22 cm printed circuit board on a 2 mm thick thermal-controlled aluminum support, a 5 mm glass plate, an aluminum heat sink to be placed on the cold side of the TEG cell, a model S01138812M fan that has the role of cooling at room temperature the heatsink, and a control system managed by ATMEGA2560 microcontroller from Microchip, which communicates via USB-Serial bus with a Host PC, where it is possible to control all the parameters of the platform and visualize as well as acquire measurement information by means of a LabVIEW-based HMI interface. The Peltier cell is fixed on the glass plate through a 150 μm double-sided thermal conductor, with a thermal conductivity of 1.5 $W(m \cdot K)^{-1}$, also used for fixing and thermally interfacing the cold side of the cell with the aluminum heat sink. In order to prevent the heat, coming from the surface of the aluminum plate surrounding the cell, from affecting the temperature of the heat sink and therefore of

the TEG cold side, the remaining glass surface was covered with an adhesive thermal insulator having a thermal conductivity of 0.0375 $W\ (m \cdot K)^{-1}$. Finally, a 100 kΩ negative temperature coefficient (NTC) thermistor is positioned immediately below the aluminum plate for monitoring and controlling the heater using a PID algorithm implemented on the microcontroller firmware, while a second thermistor of the same type is used to measure the temperature of the heat sink, in order to know and check the temperature difference between the two sides of the cell. The output of the cell is then connected to the programmable DC electronic load BK8600 by B&K Precision, which is controlled by the LabVIEW software and emulates the equivalent output resistive load, performing a resistive sweep and providing instantaneous output voltage and current of the cell under test. The final implementation of the system is illustrated in Figure 4.2.

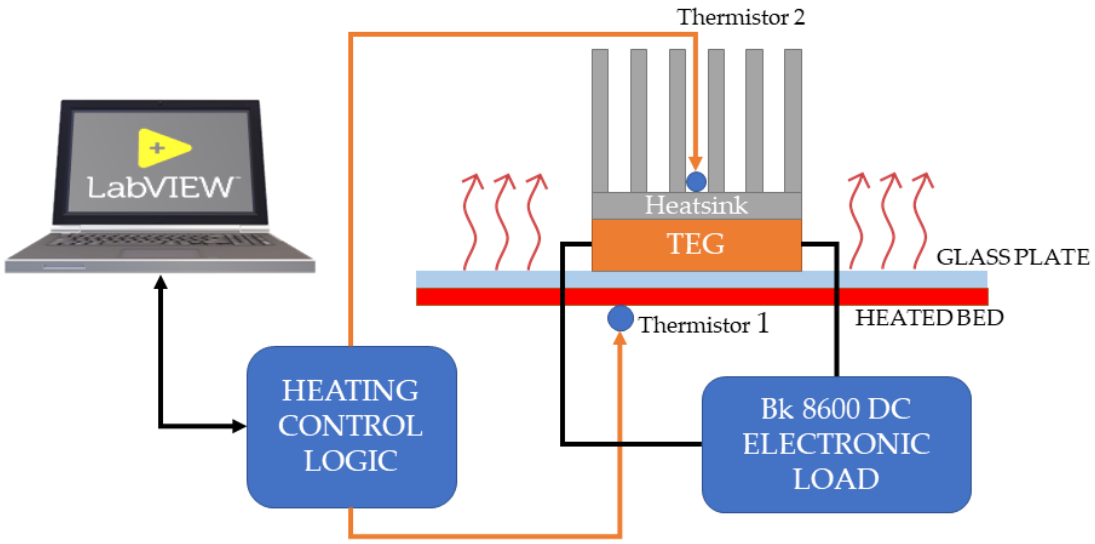

Figure 4.2 Block scheme of the test platform, as reported in [187].

The test system was then employed, to characterize the cell at three values of temperature difference between the aluminum bed and the heatsink:

$$\Delta T1 = T_{bed,1} - T_{heatsink,1} = 4\ °C$$
$$\Delta T2 = T_{bed,2} - T_{heatsink,2} = 8\ °C \qquad (4.1.3)$$
$$\Delta T3 = T_{bed,3} - T_{heatsink,3} = 16\ °C$$

A temperature difference lower than 4 °C was not considered, since the thermal conductance K is not infinite and the temperature between hot and cold side tends to equalize, leading to a system collapse, while temperature differences higher than 16 °C

were not investigated, according to the real scenario of low temperature, low power energy harvesting as from the human body heat, depicted in Chapter 2.

For the Spice model identification, a simple electrical description has been considered here to represent the TEG cell [192], which consists of an ideal generator V_{TEG} in series with an internal resistance R_{TEG} (see Figure 4.3). The equivalent voltage supplied by the internal generator relative to this model is given by the temperature gradient applied between the two faces of the cell multiplied by the Seebeck coefficient S, which should be obtained from the measurements. The internal resistance of the model is also temperature-dependent, as is the resistivity of each material, so it is necessary to calculate its thermal coefficient, which could be positive or negative.

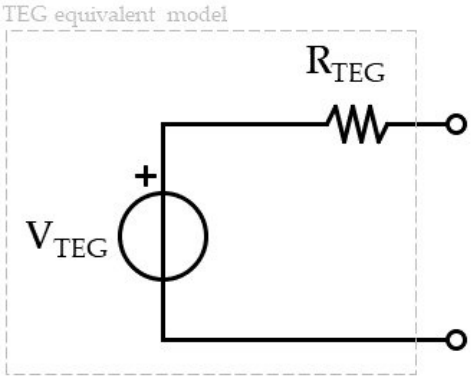

Figure 4.3 Adopted electrical description of the TEG cell [187].

The expressions of V_{TEG} can be identified from the measured data by comparing the measured open-circuit voltages with the values of the chosen temperature differences:

$$S_{TEG,1} = \frac{V_{oc1}}{\Delta T_1}, \qquad S_{TEG,2} = \frac{V_{co2}}{\Delta T_2}, \qquad S_{TEG,3} = \frac{V_{oc3}}{\Delta T_3}$$
$$S_{TEG} = \frac{1}{n}\sum_{i=1}^{n} S_{TEG,i}\,, \qquad n = 3 \tag{4.1.4}$$

where V_{OCi} is the measured open-circuit voltage at the temperature difference i.

The internal resistance R_{TEG} can be computed, at each temperature gradient of analysis, by means of the voltage divider rule, where V_{out} is the output voltage of the cell over the equivalent load:

$$R_{TEG} = \frac{V_{TEG,\Delta Ti} - V_{out,\Delta Ti}}{V_{out,\Delta Ti}} \cdot R_{Load,i}, \qquad i = 1,2,3 \tag{4.1.5}$$

Therefore, measurements are used to obtain a polynomial expression of the first order:

$$R_{TEG,i} = \alpha_i \Delta T_i + \beta_i$$

$$R_{TEG} = \frac{1}{n}\sum_{i=1}^{n} \alpha_i \cdot \Delta T + \frac{1}{n}\sum_{i=1}^{n} \beta_i = \alpha \cdot \Delta T + \beta \qquad n = 3 \tag{4.1.6}$$

where α represents the thermal coefficient while β is a fixed resistive term.

Once the Spice model has been obtained by means of the above-described method, parametric load sweep simulations can be conducted and data can be compared with measurements, in order to validate the model at different temperature differences. The same procedure can be replicated with two or more TEG cells with different interconnection configurations, in order to verify the model validity even for multicell applications.

The final step is to use the aforementioned multicell TEG Spice model for a design example of a DC/DC converter with the MPPT algorithm, in order to maximize the conversion efficiency. For this purpose, a conventional boost converter has been considered, with ideal components, as depicted in Figure 4.4. As for many low-power portable or autonomous applications, it is very important to harvest the maximum available power from the source, in order to guarantee high integrability, with the usage of small batteries. The MPPT here plays this role, therefore a DC/DC with maximum power point track algorithm works more as a power pump, where the output voltage is amplified, with respect to the input, according to the system load, in order to extract the maximum energy from the source [193]–[195]. This can be employed to directly charge a battery or to directly feed digital systems that do not require a stable power supply. If a fixed voltage regulation is also needed, combined with MPPT, usually the latter works as a pre-regulator for a second DC/DC with fixed output voltage [196]. In Figure 4.4, an example of an energy harvesting power management system with both MPPT and regulated voltage is depicted, as S. Alli et all reported in [197]. In this case, the system is composed of a first stage DC/DC converter, which is controlled by an MPPT block that has the role to modulate the PWM of the switching frequency f_l, in order to guarantee the maximum transferred power at the output. The

latter is delivered to a battery and to a storage capacitor *CSTORE*, so as to harvest the maximum available power. The output of this first stage is then delivered to a second standard DC/DC converter, which provides a fixed regulated voltage to the system load. In this case, a bandgap voltage reference is needed for the output voltage regulation loop. Such a configuration allows storing the excess of energy that is not instantly requested by the output load into the battery with the maximum power conversion efficiency, while a fixed voltage $V_{REGULATED}$ is even supplied, together with the MPPT regulated voltage V_{OUT}. Another possibility is to exploit the MPPT algorithms to instantly disable the fixed output voltage when the system load requires higher power than the available energy, in order to perform a sort of PWM output modulation that helps to keep the input voltage near the maximum power point [198]. In this case, usually a supercapacitor is employed to store power to be supplied when the energy source is temporary not available or when the system requires more power.

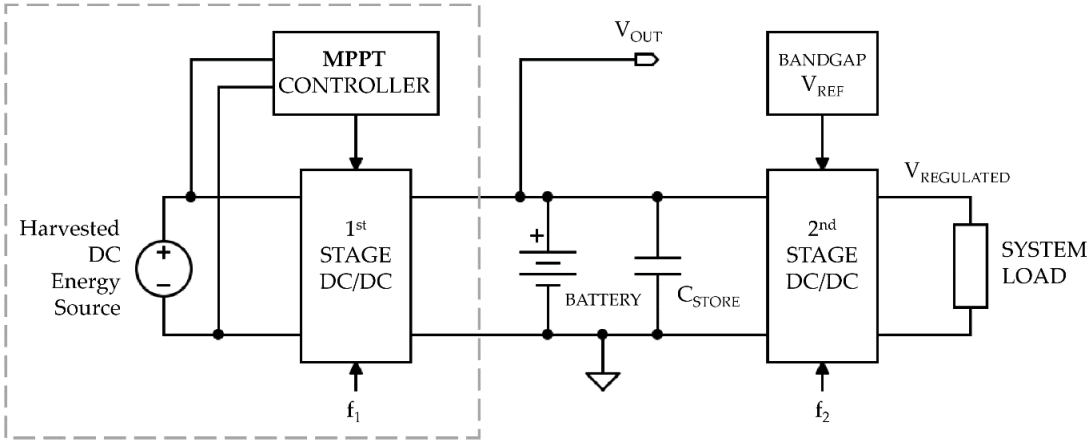

Figure 4.4 An example of a complete energy harvesting power management system with cascaded MPPT and fixed voltage regulated DC/DC converters [187].

Referring to Figure 4.4, the purpose of this contribution is to show how the proposed technique to identify a simple LTSpice model for the TEG cell can improve the design procedure of the first stage MPPT converter, which affects the power conversion efficiency of the harvesting thermal energy. Therefore, a design example of the first DC/DC (grey dashed box) stage is presented in the following pages, since the second conversion stage is considered as standard and not always requested.

As well known, the operation modes of the boost converter can change, based on the current flowing through the inductor *L*. If the current does not go to zero, the converter operates in continuous mode, where:

$$V_{out} = V_{TEG}\frac{1}{1-D}$$
$$I_{TEG} = \frac{I_{OUT}}{1-D} \tag{4.1.7}$$

where D is the Duty cycle of the square wave signal that controls the switch S.

From Equation 4.1.7, it is evident that the equivalent input resistance of the converter that drives an output load R_L is not constant, since:

$$R_{DC/DC} = \frac{V_{TEG}}{I_{TEG}} = \frac{V_{out}(1-D)}{\frac{I_{out}}{1-D}} = \frac{V_{out}}{I_{out}}(1-D)^2 = R_L(1-D)^2 \tag{4.1.8}$$

From Equation 4.1.8 it can be stated that the equivalent input resistance of the DC/DC converter depends on the output load and the switching signal duty cycle. The same dependence of the output voltage and current, thus the equivalent DC/DC input resistance, from the duty cycle and the output load occurs when the converter operates in discontinuous mode, for which the current flowing through the inductor goes to zero during a single operation cycle:

$$V_{out} = V_{TEG} + \frac{V_{TEG}^2 D^2 T}{2LI_{out}}$$
$$I_{out} = \frac{V_{TEG}^2 D^2 T}{2L(V_{out} - V_{TEG})} \tag{4.1.9}$$

where T is the time period of the switching signal.

According to the well-known maximum power transfer theorem, to extract the maximum power from the TEG source, the equivalent input resistance $R_{DC/DC}$ of the converter should be equal to the source resistance R_{TEG}. Therefore, a control algorithm for the DC/DC is needed, in order to dynamically adjust the converter input impedance to guarantee the maximum power transfer. For this reason, many MPPT algorithms have been developed and described in the literature. They differ for complexity, number of sensors or required measured data, efficiency, and hardware, and can be classified into two major categories. The first continuously track voltage and current, in order to dynamically adjust the power operation point, without the need for any empirical information. Algorithms like Perturb and Observe (P&O), Incremental Conductance (InC) or Hill Climbing (HC) belongs to this category [199]–[201] and are characterized by high hardware, complexity, continuous functionality and high,

efficiency, especially if the behavior of the energy source is unknown. Other MPPT techniques like Fractional Open-Circuit Voltage (FOCV) or Fractional Short-Circuit Current (FSCC) requires less complexity and measured data, without the need of continuously track the input voltage and/or current since they rely on a priori information about the source [202], [203]. These algorithms represent the second category of MPPT techniques. The drawback of such type of algorithms is the conversion efficiency, which is affected and lowered if the knowledge and description of the source are not accurate.

The identification of the TEG cell Spice model enables the usage of a priori MPPT techniques for thermal energy harvesting, which are better in terms of occupied hardware area, cost, and complexity. For the purpose of this work, a FOCV technique has been selected for a design example. The technique expects that the source output voltage corresponding to the maximum power point is linearly proportional to the source open-circuit (OC) voltage with a constant *K* coefficient. Therefore, the goal of this algorithm is to measure the open-circuit voltage and modulate the required source current, in order to guarantee the output voltage to be a constant fraction *K* of the OC measured voltage. The adopted scheme is depicted in Figure 4.5.

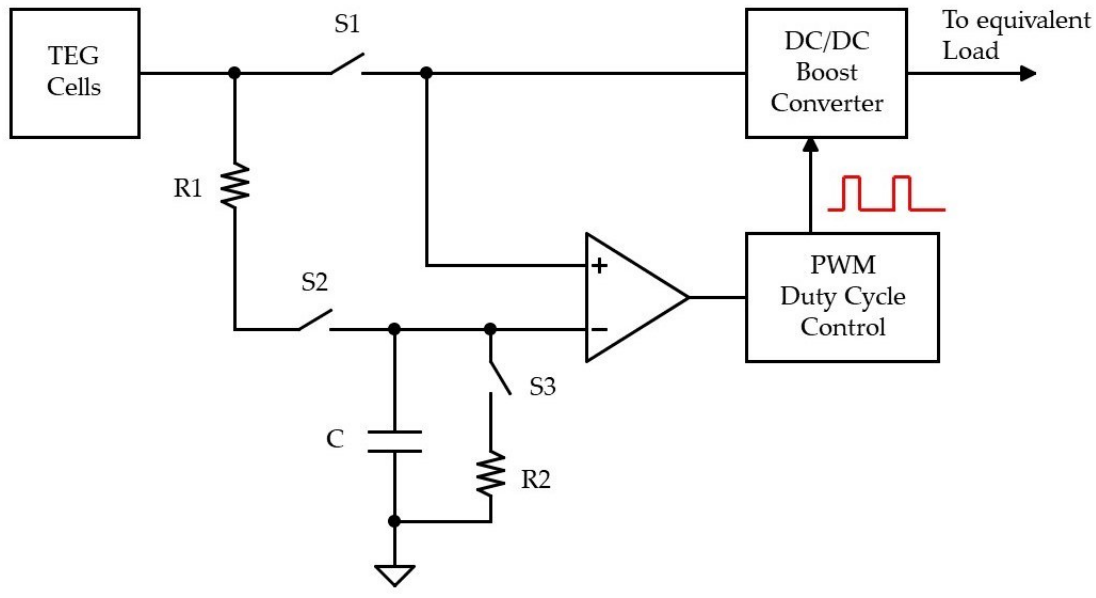

Figure 4.5 Adopted circuital scheme for the implemented FOCV MPPT algorithm [187].

In this scheme, the MPPT algorithm is divided into two working steps, that are repeated over time.

- Step 1:

In the first step, the switch *S1* is open while *S2* and *S3* are closed. The capacitor *C* is then charged at a voltage V_A as follows:

$$V_A = V_{TEG,OC} \frac{R_2}{R_1 + R_2} = K \cdot V_{TEG,OC} \tag{4.1.10}$$

where $V_{TEG,OC}$ is the open-circuit output voltage of the TEG cells, since *S1* disconnects the source from the DC/DC, thus no load is attached. The resistors R_1 and R_2 values should be high enough so as to not affect the open-circuit voltage. In this case, the charging time constant τ is equal to $K \cdot C$, therefore the value of the capacitor should be small, in order to reduce the charging time and, consequently, the duration of the voltage sensing step. On the other hand, if the capacitor value *C* is too small, the charge retention could be affected by the input polarization current of the differential amplifier. Therefore, a compromise should be considered between these two conditions.

The duration of this step should be as low as possible, since the input of the DC/DC converter is disconnected at this stage, in order to properly sense the MPPT information.

- Step 2:

In the second operative step, the switch *S1* is closed while *S2* and *S3* are opened. This constitutes the normal operative condition, where the TEG cells output is connected to the DC/DC for voltage boost. The instantaneous value V_{TEG} is continuously compared with the voltage V_A stored by the capacitor and the difference signal ***e*** represents the error, that is employed to modulate the duty cycle of the DC/DC switching signal, in order to set to zero the difference between the sampled voltage and the output voltage of the source.

4.1.2 Results and Discussion

In this section, experimental data for the description of the Peltier cell and the relative Spice model are reported, as well as a design example of an ideal DC/DC converter with FOCV MPPT algorithm, considering the obtained Spice model for the optimization.

In Table 4.1, information about open-circuit voltage, short circuit current, and maximum power have been measured and reported, for each temperature difference ΔT of analysis.

$\Delta T\ (°C)$	$V_{oc}\ (mV)$	$I_{sc}\ (mA)$	$P_{max}\ (\mu W)$
4	9.25	2.35	9.94
8	20.73	5.2	48.25
16	47.12	13.1	309

Table 4.1 Characterization of a single TEC1-3103 Peltier cell as TEG [187].

Following Equations 4.1.4 and 4.1.6, it is then possible to obtain the Spice model of a single TEG cell once has been characterized, as shown in Figure 4.6.

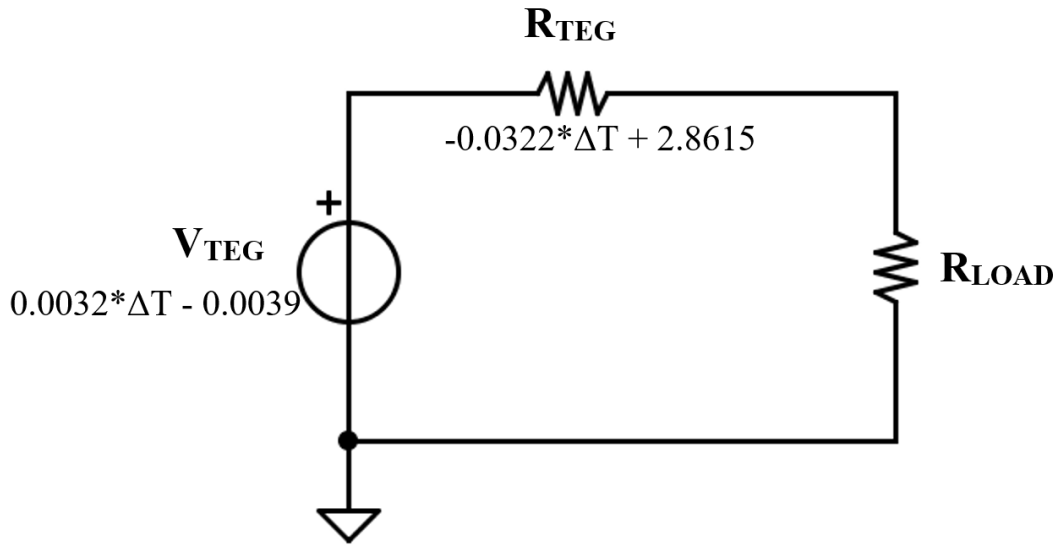

Figure 4.6 Identified Spice model of the single TEG cell [187].

The obtained Spice model is then verified by means of load sweep simulations firstly for the single cell, to relate it with measured data (Figures 4.7a, 4.7b, 4.7c). Consequently, two cells have been connected in parallel and simulations have been compared with real measurements acquired with the test platform, performing a load sweep as in the previous characterization (Figure 4.77d). Results demonstrate that the model is useful even for multicell simulations since the obtained data are in good correspondence with the acquired measures.

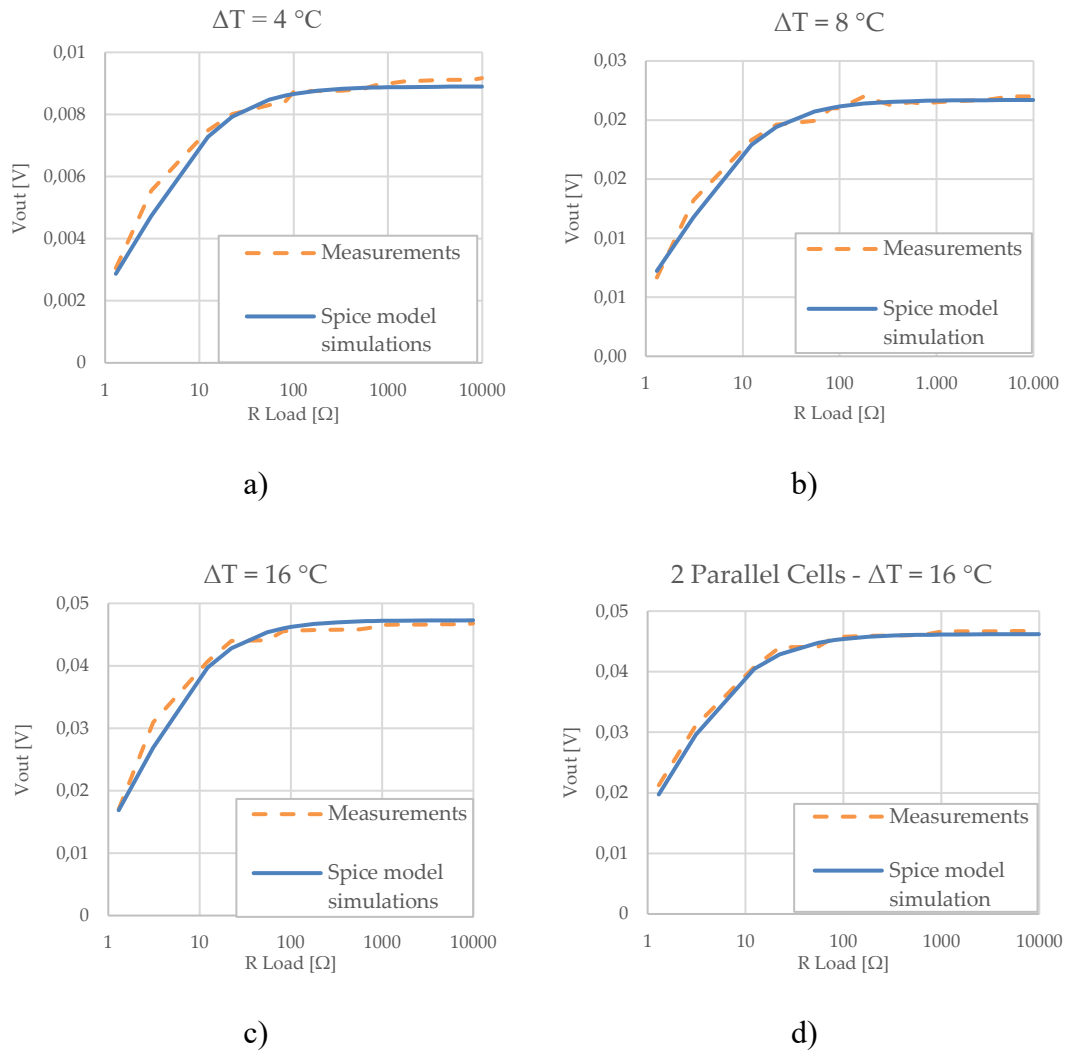

Figure 4.7 Comparison of the obtained Spice model: a) single cell at ΔT = 4 °C, b) single cell at ΔT = 8 °C, c) single cell at ΔT = 16 °C and d) two parallel cells at Δt = 16 °C [187].

For the DC/DC design, a multicell configuration with 12 Peltier modules has been considered. First, it is necessary to analyze the equivalent Spice circuit in order to identify the best connection strategy. Among all the possible configurations, six architectures have been considered, as depicted in Figure 4.8.

For each configuration, a load sweep analysis has been performed, in order to obtain the current-voltage (I-V) characteristic trace, as well as the Power-Voltage (P-V) characteristic curve for a temperature difference of 16 °C. (Figure 4.9).

From the multicell simulation analysis, it can be inferred that the power-voltage curve is a paraboloid, being the equivalent circuital model of a single cell constituted by a simple voltage generator in series with an internal resistor. For 12 cells all connected in series (Figure 4.9a), the maximum power point is located exactly at

$V_{OC}/2$, while this point translates to the left, towards a lower voltage value, as the configuration tends to a parallel connection [204].

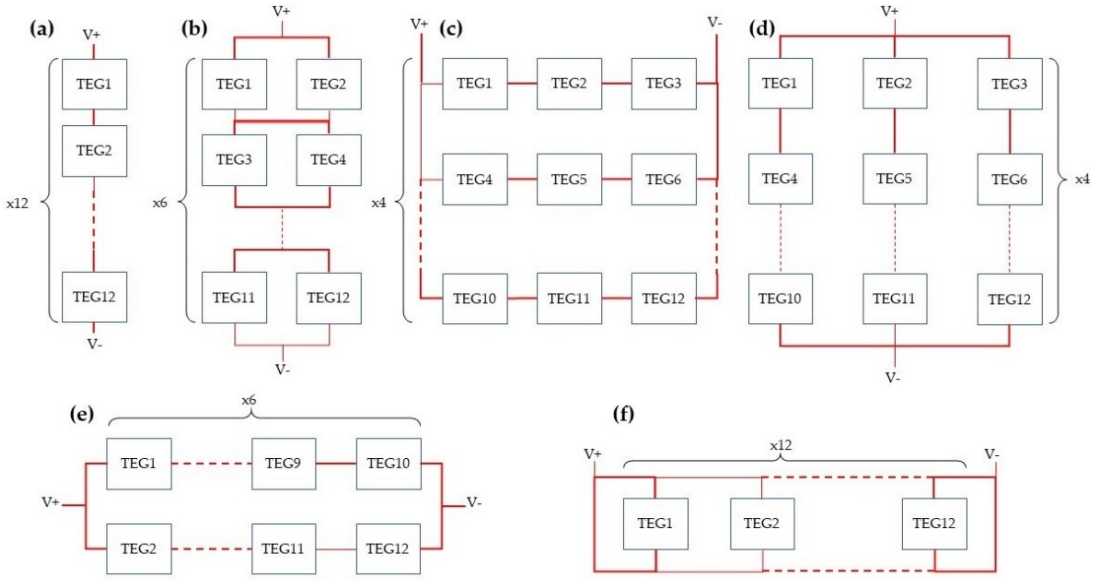

Figure 4.8 Configurations for multicell simulation analysis. a) series of 12 cells, b) 6 series of 2 parallel cells, c) 4 parallels of 3 series cells, d) 3 parallels of 4 series cells, e) 2 parallels of 6 series cells and f) 12 parallel cells.

For 12 cells all connected in parallel, the maximum power point falls out of the lower simulation range for the load sweep. From the obtained results, it can be inferred that the best configurations are the 4×3 or 3×4 since it is a compromise between the output voltage and current, and the loss of conversion efficiency due to a possible heat distribution unevenness for the hot side among the cells. On the other hand, from the electrical point of view, the voltage provided by the TEG array should be as high as possible, in order to reduce the DC/DC design critical issues. For this reason, the full series configuration of the 12 cells has been selected in this case for the DC/DC design example, assuming that the temperature difference is uniform for every cell, since the corresponding voltage of the maximum power point is higher, which helps the DC/DC converter to boost the output voltage. In fact, the lower is the input voltage, the more is the complexity of a real DC/DC converter in order to guarantee the voltage translation, since limitations and parasitic of single electronic devices that constitute the converter architecture can inhibit its functionality when the input voltage is too low.

Once the configuration of operation has been selected, it is necessary to analyze the power-voltage curve at different temperature differences, in order to verify that the

maximum power point condition is constant for every operative condition. According to previous single-cell characterization for Spice model identification, the voltage value of the equivalent circuit is linearly dependent on the temperature gradient, thus the P-V curve shape is expected to remain unaltered, as depicted in Figure 4.10, where a load sweep analysis has been performed for 12 TEG cells connected in series at different ΔT values.

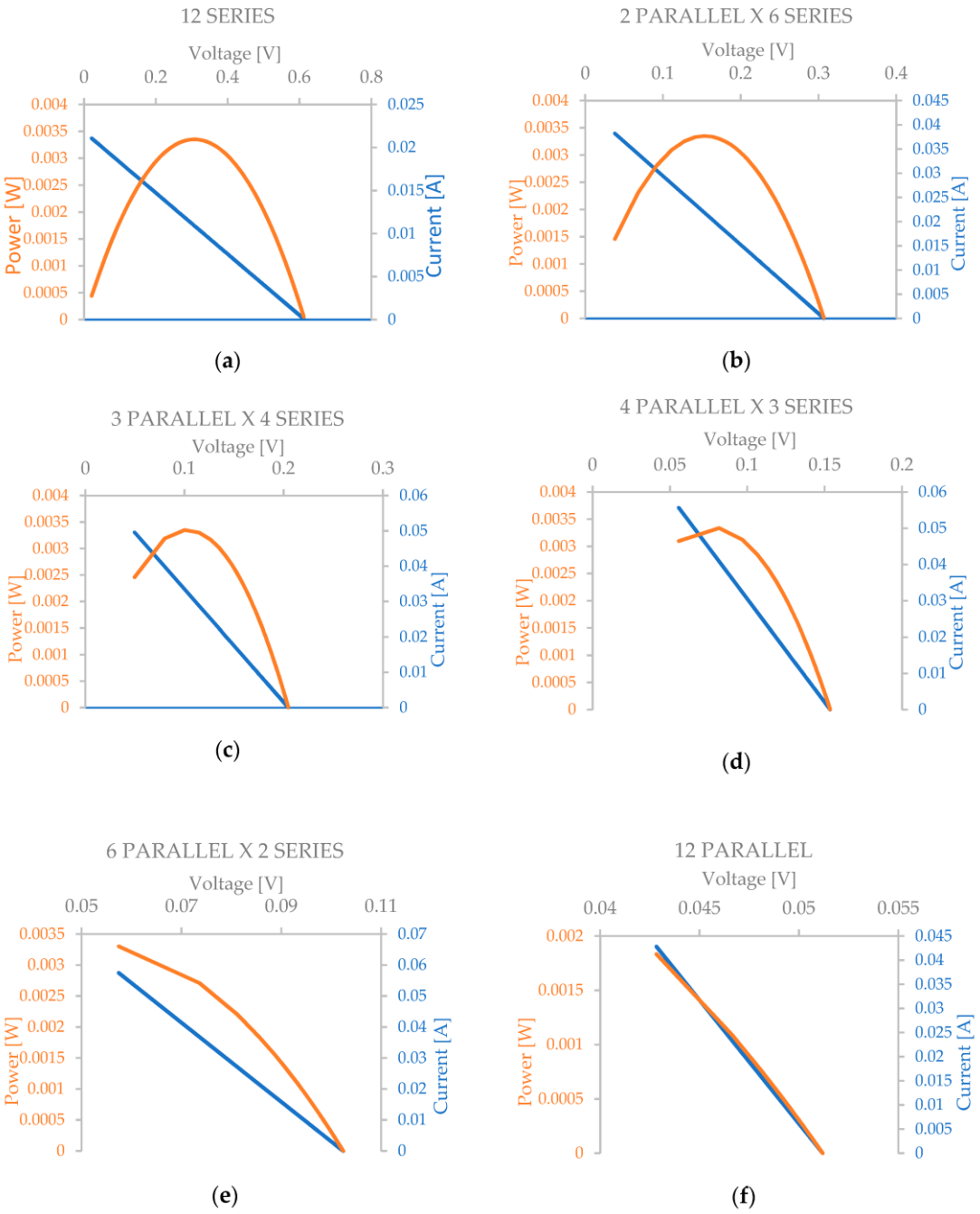

Figure 4.9 Multicell current/voltage (blue trace) and power–voltage (orange trace) simulation analysis with ΔT = 16 °C. (a) series of 12 cells, (b) 6 series of 2 parallel cells, (c) 4 parallels of 3 series cells, (d) 3 parallels of 4 series cells, (e) 2 parallels of 6 series cells, and (f) 12 parallel cells [187].

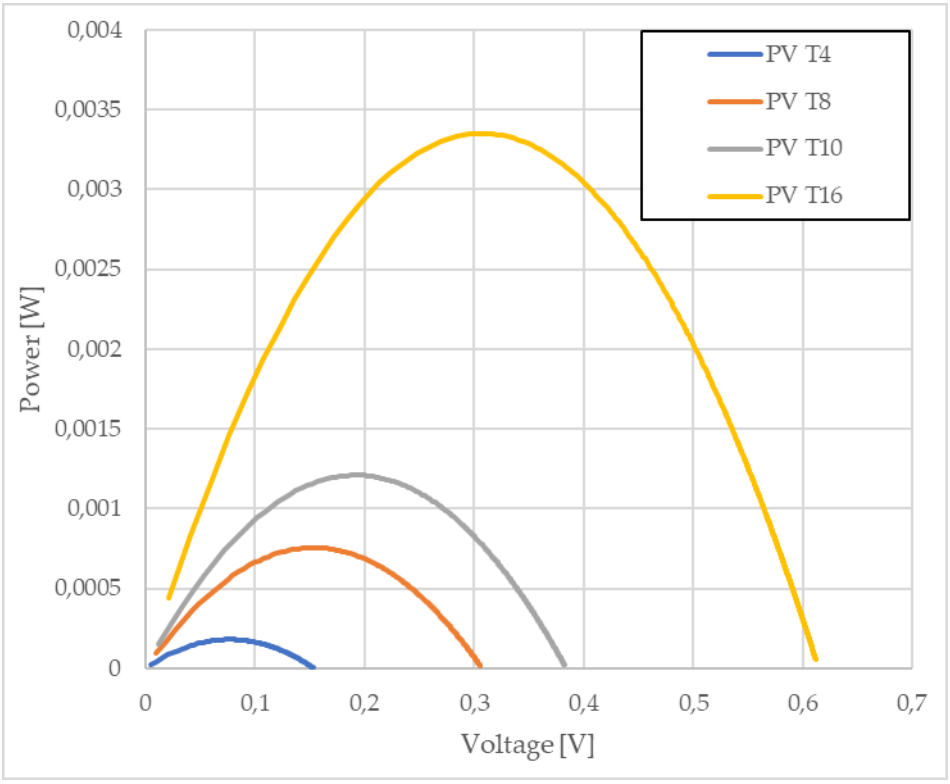

Figure 4.10 Power-voltage simulation analysis for 12 cells connected in series with ΔT = 16 °C (yellow), ΔT = 10 °C (grey), ΔT = 8 °C (orange) and ΔT = 4 °C (blue) [187].

The simulation shown in Figure 4.10 demonstrates that the maximum power point condition for series-connected multicell TEG source, at every temperature difference, is equal to:

$$V_{TEG}(\Delta T)|_{P_{MAX}(\Delta T)} = \frac{1}{2} V_{OC}(\Delta T) \tag{4.1.11}$$

Recalling Equation 4.1.10 for the FOCV MPPT algorithm, the voltage divider coefficient K for the fractional open-circuit voltage sampling should be equal to 0.5, so as to guarantee the maximum power point condition for the selected multicell source.

Finally, the utility and usage of the Peltier cell Spice model have been proved by proposing a design example of a DC/DC boost converter with FOCV MPPT algorithm (Figure 4.11), to demonstrate how the design can be conditioned and optimized by considering a real source model instead of an ideal generator.

In this design, the selected switching frequency of the pulse width modulated (PWM) signal is 200 kHz, which is obtained by means of a sawtooth generator and the

ideal comparator A_3. The latter continuously performs the difference between the reference sawtooth signal and a DC voltage value coming from the MPPT feedforward network, producing an output square wave, that controls the transistor M_1, where its duty cycle is proportional to the V_B voltage level. In this design example, an ideal built-in block of LTSpice has been employed regarding the sawtooth generator, while a reference for a possible real implementation can be found in [205].

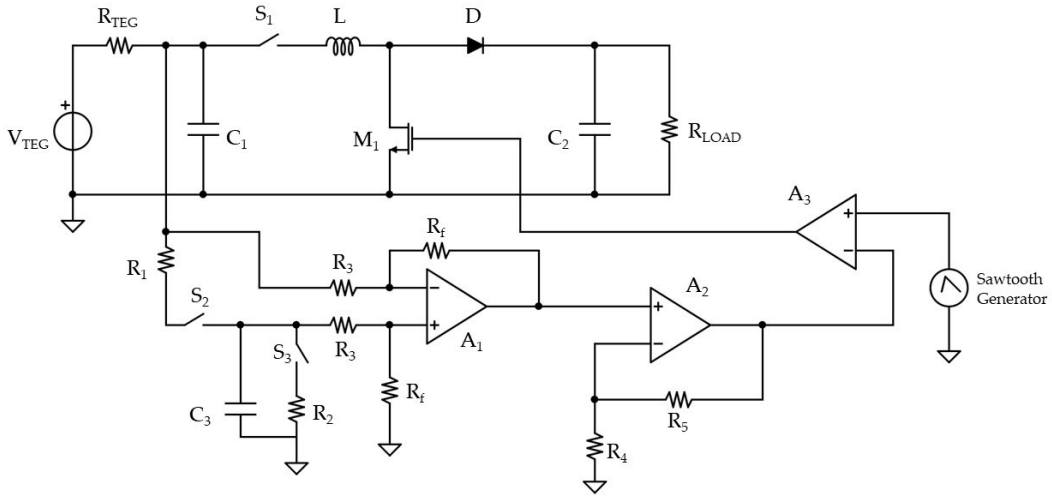

Figure 4.11 Complete scheme of the implemented DC/DC boost converter with the FOCV MPPT algorithm [187].

As mentioned in the previous paragraph, the fractional open-circuit voltage sensing is performed by closing switches S_2 and S_3 and opening the switch S_1, in order to store the maximum power point voltage level by means of the capacitor C_3. Here, an additional 100 nF capacitor C_1 has been added at the output of the TEG source, in order to retain the output voltage during the switching transients. For the capacitor C_3, a value of 1 µF has been chosen, while a resistive value of 10 kΩ has been selected for both resistors R_1 and R_2. The difference between the FOCV value and the instantaneous output voltage of the source is computed by means of the ideal op-amp A_1 in differential amplifier configuration. All the resistors R_3 and R_f have the same value of 200 kΩ. The PID algorithm introduced in the scheme of Figure 4.5 is here simplified to only a proportional contribute, represented by the non-inverting amplifier A_2, where the gain has been set to 3, by means of the resistors R_4 and R_5.

The inductor selection criterion is crucial for the DC/DC functionality. As a rule of thumb, the higher the inductor value, the higher is the maximum achievable current at the output of the converter, thanks to the reduced ripple. On the other hand, if the

inductor value is too high, it can affect the cost and size of the solution, as well as the efficiency, because of the equivalent series resistance. Therefore, the minimum inductor value can be selected as follows, recalling equation 4.1.7 and by considering the desired maximum output current:

$$Lmin = \frac{V_{TEG}(V_{out} - V_{TEG})}{\Delta I_L \cdot f_S \cdot V_{out}} \tag{4.1.12}$$

where f_S is the switching frequency and ΔI_L represents the predictable output ripple current. A good estimation of the ripple value is 20% to 40% of the maximum output current:

$$\Delta I_L = (0.2 \div 0.4) \cdot I_{out,MAX} \cdot \frac{V_{OUT}}{V_{TEG}} \tag{4.1.13}$$

In this design example, by applying equations 4.1.12 and 4.1.13, and considering the multicell source characterization, with a maximum operating temperature difference of 16 °C, the inductor value L has been fixed to 1 mH.

Regarding the Op-Amps A_1, A_2 and A_3, a generic component has been used, with an open-loop gain of 50k and a GBW of 10 MHz. The transistor M_1 was chosen to have an equivalent R_{on} equal to 1Ω and a threshold voltage of 500 mV, while the diode D_1 is a Schottky barrier with a forward voltage of 150 mV at 1 mA.

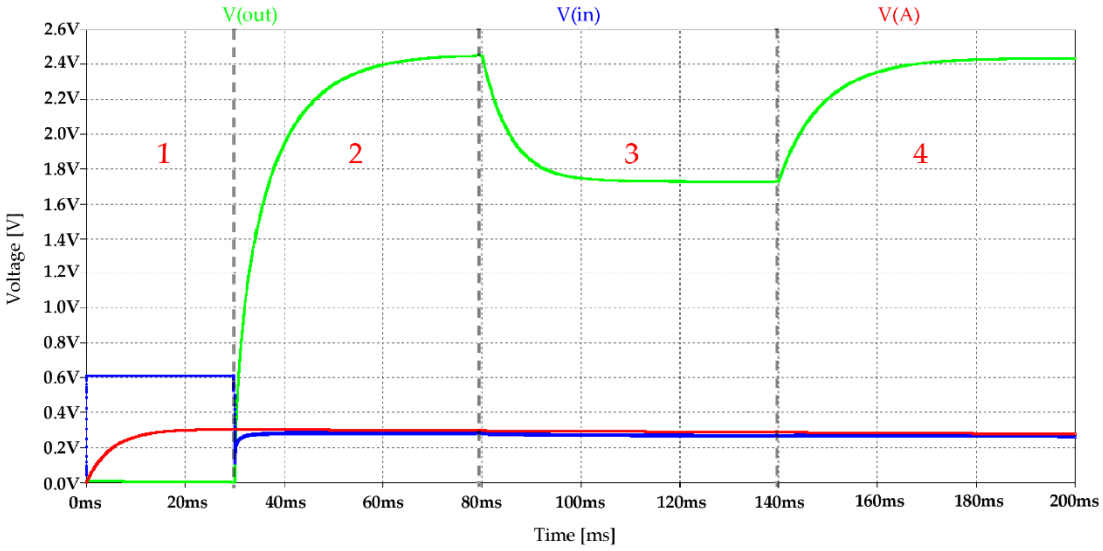

Figure 4.12 DC/DC converter V_{OUT} (green trace), V_{IN} (blue trace) and V_A (red trace) simulation with load step variation. Region 1: input voltage sensing; Region 2: output voltage regulation; Region 3: load changing from 2 kΩ to 1 kΩ and output lowering for MPPT; Region 4: load changing from 1 kΩ to 2 kΩ and output boosting for MPPT [187].

The first system simulation, depicted in Figure 4.12, represents a load variation for 12 teg cells connected in series with a 16 °C temperature difference. In the first Region of the graph, the input is not connected to the DC/DC and the Fractional Open-Circuit Voltage is stored in the capacitor C_3. The sensing time period is fixed to 30 ms, which is enough for the capacitor to be charged at 0.3 V, which is half of the open-circuit output voltage of the source. At the end of this time window, the converter switches from sensing mode to operative mode, thus the MPPT circuit is disconnected from the TEG output, which is attached at the DC/DC input by means of the switch S_1. In order to guarantee the maximum power operative point for the source, considering a DC/DC output load of 2 kΩ, the output voltage is boosted up to 2.4 V. At the end of the region 2, the resistive load changes from 2 kΩ to 1 kΩ. As can be observed, the output voltage is suddenly decreased, in order to keep constant the input voltage and to guarantee the source to operate at the MPP. At the beginning of region 4, the resistive load is reset to 2 kΩ and the output voltage is boosted, accordingly.

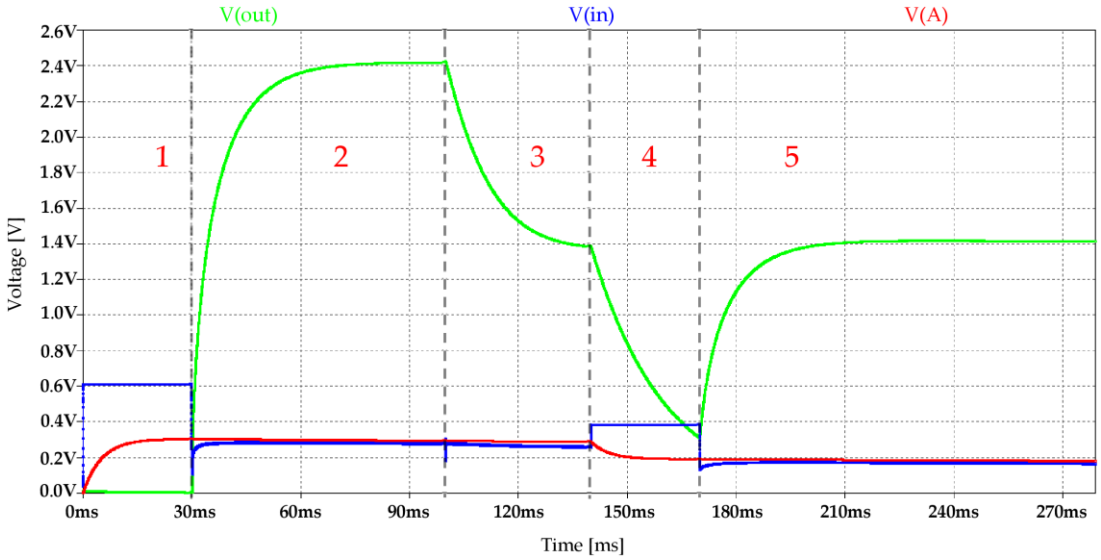

Figure 4.13 DC/DC converter V_{OUT} (green trace), V_{IN} (blue trace) and V_A (red trace) simulation with source temperature difference variation. Region 1: input voltage sensing; Region 2: output voltage regulation; Region 3: temperature difference changing from 16 °C to 10 °C and output lowering; Region 4: new source voltage sensing window and FOCV update; Region 5: output voltage regulation in accordance with the new detected maximum power point [187].

For the second simulation, shown in Figure 4.13, the resistive load has is kept constant, while a source temperature difference changing has been emulated, from 16 °C to 10 °C. As shown in figure 13, in the first two regions the fractional voltage is sensed and the output is regulated, keeping the voltage provided by the TEG source close to the desired MPP. At the end of region 2, the temperature change occurs, thus

the output voltage is lowered but the TEG voltage is still close to the previous maximum power point condition.

At the beginning of region 4, a new voltage sensing is performed and the FPCV value is updated to the correct value. The output of the DC/DC converter falls towards zero in this time window, since the input source is disconnected. After this sensing stage, the output is restored and boosted in accordance with the new MPP reference. In fact, the TEG source voltage is coincident with the reference value.

Finally, Figure 4.14 shows a time window reporting a transition between MPPT input voltage sensing and output voltage regulation modes regarding a load variation simulation. Once the FOCV has been updated, the signal produced by Op-Amp A_2, which is the result of MPPT hardware processing, begins to rise and therefore, the PWM switching signal controlling the transistor M_1 gradually modifies the duty cycle in order to perform the MPPT regulation of the output.

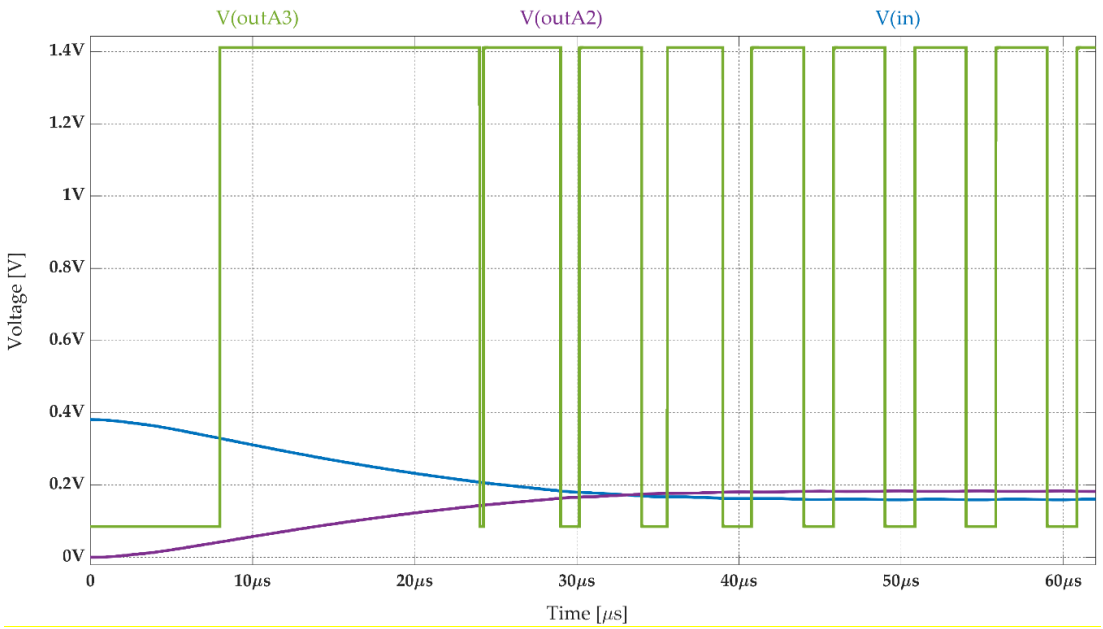

Figure 4.14 Switching signal controlling transistor M_1 (green trace), the MPPT output signal from Op-Amp A_2 (violet trace) and input TEG voltage (blue trace) in a time window reporting the transition between MPPT input voltage sensing and output voltage regulation modes [187].

4.2 HUMAN BODY THERMOELECTRIC ENERGY HARVESTER FOR MULTISENSORY GLOVE

In this contribution, a novel multisensory electronic architecture is reported, which can actually work with very low voltage requirements thus enabling power management directly from harvesting-based low-voltage sources, with no additional voltage conversion requirement. The harvesting system here proposed relays on

thermoelectric generator cells useful for furnishing additional power to an electronic system made of a homemade sensory glove, an inertial measuring unit, and an electromyography device, aimed at providing full measures of the arm-hand dexterities. The thermoelectric generator cells are optimized to work as an array configuration up to 10 cells series-connected and the energy conversion is managed with a commercial DC/DC with MPPT algorithm. This research has been conducted in collaboration with Prof. Saggio and his team, from the University of Rome "Tor Vergata".

4.2.1 Materials and Methods

The multisensory architecture here described is a combination of flex sensors plus an inertial measurement unit, all embedded in a sensory glove, and surface electromyography (sEMG) sensors (Figure 4.15).

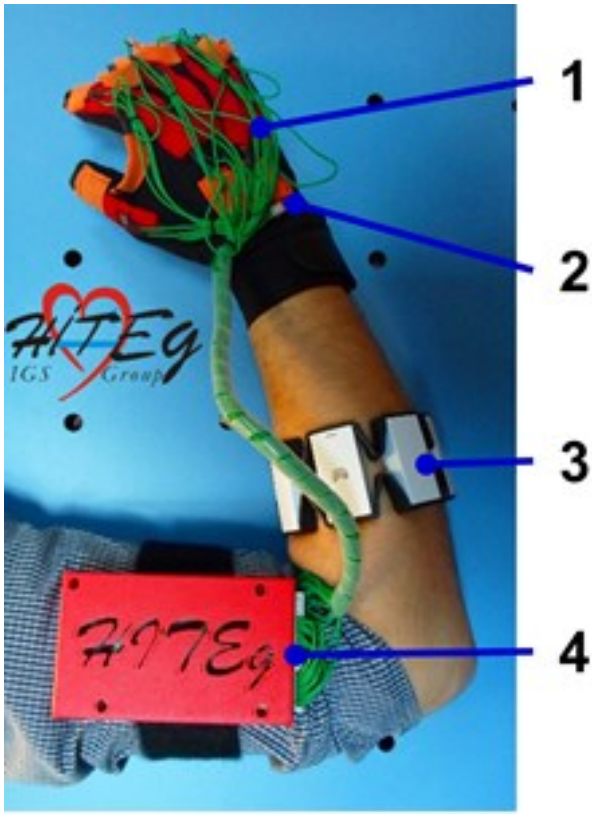

Figure 4.15 The multisensory architecture worn on the right arm. Parts of the architecture: 1 - Hiteglove; 2 - 9DoF Razor IMU M0 (hosted in a pocket of the glove); 3 – MyoTM armband from ThalmiclabsTM; 4 - Hiteg data acquisition board [206].

The sensory glove is a Lycra®-based glove equipped with a total of eighteen flex sensors™ (bend sensor® by Flexpoint Sensor Systems Inc., South Draper USA) [207], fourteen of them over the same number of fingers' joints to measure flex/extension

capabilities, and four of them hosted in pockets between fingers to measure abdu-adduction movements. On the dorsal part of the glove, a pocket hosts a nine degree of freedom (DoF) IMU, (9DoF Razor IMU M0 by SparkFun) used to measure roto-translation movements of the wrist. The sensory glove has been used for a number of different applications, ranging from the dexterity evaluation of surgeons [208] to the remotely driven manipulation [209] to the interfacing of human vs. machine [210], and so ahead.

Electric analog signals from the sensors are conditioned and 10-bit A/D converted by a portable electronic circuitry based on the general-purpose microcontroller PIC24EP512GU810 (by Microchip). The microcontroller can standardly operate with a supply voltage within the 3.0-3.6 V range, draining a current ranging from 12 mA (3.3 V @ 10 MIPS) to 105 mA (3.3 V @ 70 MIPS). Data can be transmitted from the electronic circuitry both via USB cable and wireless via a Bluetooth Low Energy (BLE) module.

The IMU integrates different sensors (a 3D accelerometer, a 3D gyroscope and a magnetometer with a 3.3 V built-in regulator, MPU-9250 by InvenSense®), a LiPo battery charger, a power-control switch and an Arduino-compatible SAMD21 (by Atmel), a low-power high-performance ARM® Cortex®-M0+ based flash microcontroller, with an admissible supply voltage range within 1.62-3.63 V, with a maximum current absorption of 7 mA.

Eight sEMG sensors are hosted in a bracelet termed Myo™ Armband (ThalmicLabs™, Canada), with an NXP® MK22 microprocessor core, an Arm® Cortex® -M4 with math capability. It can operate at a voltage supply within 1.7-3.3 V, with a maximum current of 21 mA in run mode (with all peripheral clocks enabled and code executing from flash), at a frequency up to 120 MHz. The bracelet hosts an InvenSense® MPU-9150 IMU too, which combines the MPU-6050 (3-axis gyroscope, 3-axis accelerometer, a digital motion processor™ to process motion fusion algorithms), plus the AK8975 (a 3-axis digital compass), with operating voltages in the 2.375-3.465 V range, and a maximum current consumption of 9.9 mA (at full power mode and 100% duty cycle conditions). The nRF51822 (by Nordic®) takes care

The paragraph 4.2 is based on the published paper A. Leoni, I. Ulisse, L. Pantoli, V. Errico, M. Ricci, G. Orengo et al., Energy harvesting optimization for built-in power replacement of electronic multisensory architecture, AEU - International Journal Of Electronics And Communications. 107 (2019) 170-176. doi:10.1016/j.aeue.2019.05.002. As the author of this Elsevier article, reuse permissions are not required.

of the communications with a full 2.45 GHz transceiver, which runs off a 32-bit Arm® Cortex® -M0, and supports Bluetooth® low energy, absorbing 6.3 mA at +4 dBm output, with a sensitivity of -93 dBm, and a supply voltage within 1.8-3.6 V.

The thermal energy is collected on the dorsal part of the forearm by means of the so-called Seebeck effect (Figure 4.16). To this aim, we adopted the TEC1-3105 TEG cell [191], as base-block transducers, configured in 10 cells array, as a compromise between the maximization of the covered skin area and the acceptance of the user. Before the adoption on a real human arm, experimental tests were realized with a test-bench made by a controllable 200 mm^2 aluminum-made heated bed (with good mechanical robustness and uniform heat diffusion), over which there were a TEG array and an aluminum heat sink (see Figure 4.17a). The heat was produced by a current flowing into a printed circuit according to the Joule effect, and the consequent electric energy produced by the TEG array was measured by means of a voltmeter and an ammeter.

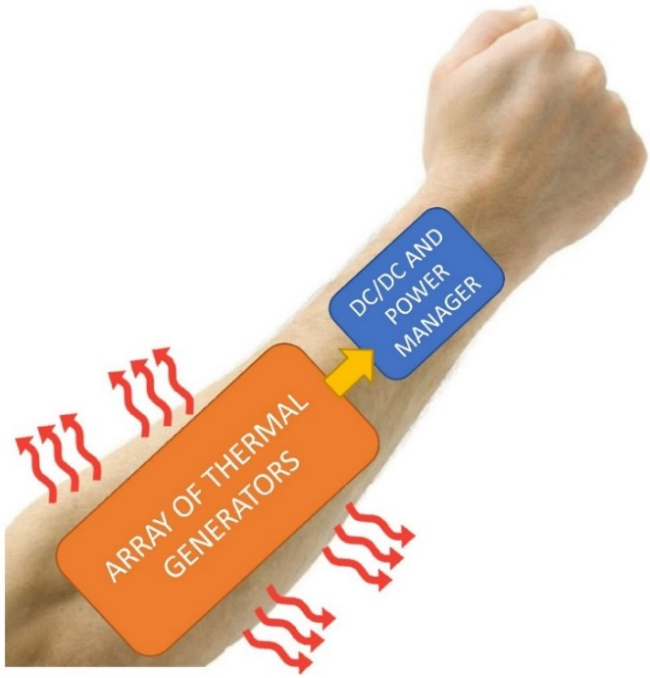

Figure 4.16 Block scheme of the proposed energy harvesting system. It is made on a printed circuit board with an array of thermoelectric generators placed on the front forearm of the user, a DC/DC converter and power manager unit [206].

Moreover, we placed a double-sided adhesive heat conductor (thickness 150 µm) with thermal conductivity of 1.5 $W(m \cdot K)^{-1}$ between heated bed, TEG array and heat sink. The same heat conductor can later easily interface the transducer with the human skin. The $20 \times 10 \times 10$ mm heat sink, depicted in Figure 4.17b,

improved the thermal dissipation capability of the system to assure the maximum thermal gradient between test-bench/room temperatures. Each cell of the array was 1.5 cm spaced, the space filled with a 3 mm adhesive thermal insulator, with thermal conductivity of 0.0375 $W(m \cdot K)^{-1}$.

The control of the heating temperature was assured by a feedback configuration circuitry, which modulated its DC voltage supply on the basis of the temperature values provided by a 100 kΩ negative temperature coefficient (NTC) thermistor placed on the heated bed. A second 100 kΩ NTC thermistor measured the room temperature.

The current-voltage (I-V) curve, parametrized by the temperature, was obtained by varying the DC load connected to the test-bench at different temperature conditions. The resulting I-V characteristic was useful to determine the maximum power point value.

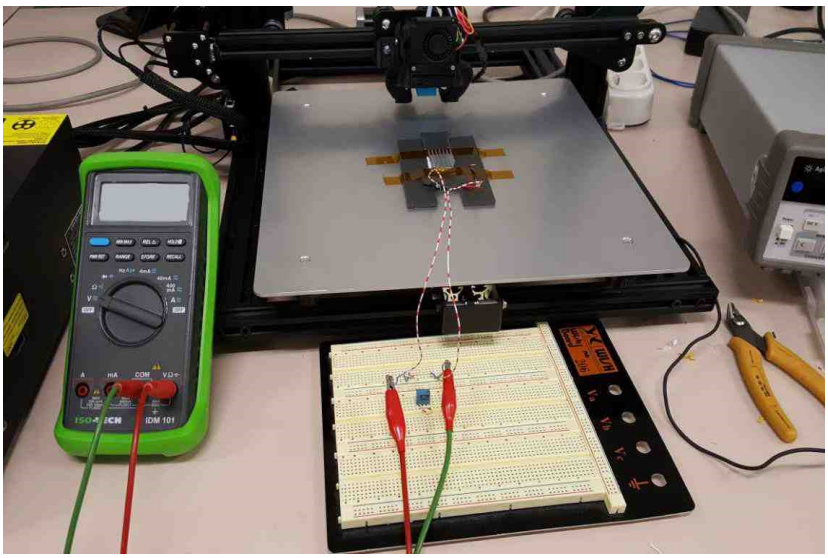

a)

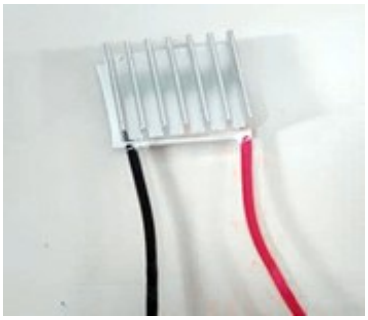

b)

Figure 4.17 Representation of (a) of the test bench for the TEG cells characterization and (b) the adopted TEG cell equipped with low-profile aluminum heat sink [206].

For power recovery and management, the commercial BQ25504 by Texas Instruments has been employed, which is a DC/DC converter and battery charger made with MPPT and power management system. Conveniently, this device is designed to manage from microwatts (μW) to milliwatts (mW) of power generated from a variety of DC sources, among all the thermal electric generators, with a dedicated MPPT algorithm, that allows increasing the energy conversion efficiency by changing the maximum sink current required from the internal battery charge block, so to guarantee high-efficiency operative condition of the TEG cells array. For all the operating conditions, the maximum power point (MPP) of each TEG configuration can be expressed as a percentage of the open-circuit voltage provided by the harvester and can be programmed with a resistive voltage divider across the output of the thermoelectric source. Consequently, the MPPT set-up comes from the results of the TEG cells characterization (as discussed in the following). In addition, the DC/DC conversion allows minimum input voltage, down to 80 mV, suitable for the expected low voltage operation of the device.

4.2.2 Results and Discussion

In order to implement a robust sensory system capable to measure all degree of freedom of the human hand-arm [211], different typologies of sensors can be adopted in the ensemble, such as flex sensors, IMUs, and sEMGs together. However, the power management of such a system has to address power-feeding challenges. Indeed, the sensory system needs for each a specific built-in power board, and each board with different operative voltages. If so, the built-in power source of each component may be inefficient when a harvesting power source is available. Differently, the harvesting-oriented design of the power feeding can be a feasible solution, replacing multiple inefficient built-in sources and providing optimized supply voltage.

Here, we propose the use of an optimized harvesting system that bypasses the USB-oriented 5 V built-in recharge circuits to feed a sensory glove-based system. In particular, we directly harvested energy from the human body heat, so as to increment the lasting time of a standard 3.7 V Li-Po battery. To this aim, with an experimental approach, we characterized the maximum power point value of TEG cells.

Specifically, the maximum power point tracking (MPPT) algorithm was designed according to the experimental results, with a test-bench emulating the human forearm temperature. Moreover, the skin temperature changes depending on the part

of the body, on the age and gender, on the presence of different diseases, on the hour of the day, on the body activity and so ahead [212]. However, we considered the worst case, i.e. the higher mean body temperature (37 °C) that corresponds to less harvested energy. Our first test was made with a single TEG cell with a heated bed at a temperature of 37 °C and a room temperature of 22 °C (Figure 4.18).

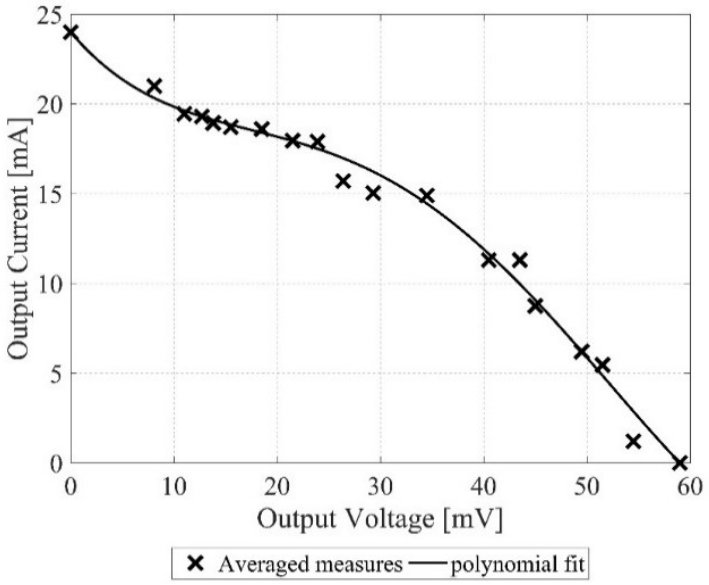

a)

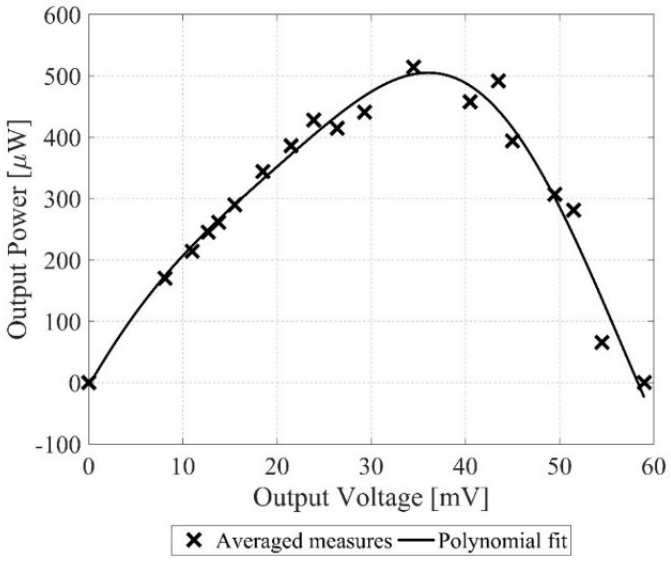

b)

Figure 4.18 (a) Current-voltage characteristic curve for a single TEG cell with a 37 °C hot side temperature and 22 °C cold side temperature. (b) The computed power-voltage characteristic for the single TEG cell [206].

The measure of voltage and current corresponding to a DC load sweep was performed three times, then data were averaged for each DC value and a polynomial fit was calculated to represent the corresponding continuous characteristic trace for the I-V and P-V curves, respectively.

It resulted in a short-circuit current of 24 mA, an open-circuit voltage of 59 mV (see Figure 4.18a), a maximum power point of 500 μW (see Figure 4.18b), corresponding to a voltage of 36 mV, that is 60% of the open-circuit voltage. Consequently, a single cell configuration is not feasible to start the boost action with the chosen DC/DC converter, since the operating voltage is lower than required.

A further test was made using a series of two TEG cells. It resulted in an open-circuit voltage of 120 mV, as shown in Figure 4.19a, double with respect to the single-cell test, as expected, with a short circuit current of 29 mA, and an MPP of 1.55 mW at 82 mV (see Figure 4.19b), which is 68.3% of the open-circuit voltage. Consequently, the series of two TEG cells does not furnish a useful operating voltage to obtain the DC conversion.

Finally, the system has been tested with 10 TEG cells in series. This number of transducers was selected according to human body size study conducted by NASA in [213], demonstrating that it is still suitable for thermal energy harvesting in the front forearm region, in terms of occupied area and considering a gap of 1 cm between each other. This series performed with an open-circuit voltage of 600 mV maximum (see Figure 4.20a), enough for the DC/DC converter to operate, while the short circuit-current was 64 mA and the MPP was 9.9 mW at 305 mV, as shown in Figure 4.20b, roughly 50% of the open-circuit voltage value. The obtained results were in agreement with previously reported works [214], [215] (see Table I).

	This research	**[214]**	**[215]**
Max voltage (mV)	600	-	200
Max current (mA)	64	-	-
Max Power (mW)	9.9	2.5	0.443
Conversion efficiency	70%	68%	48%

Table 4.2 Performance comparison of the proposed system [206].

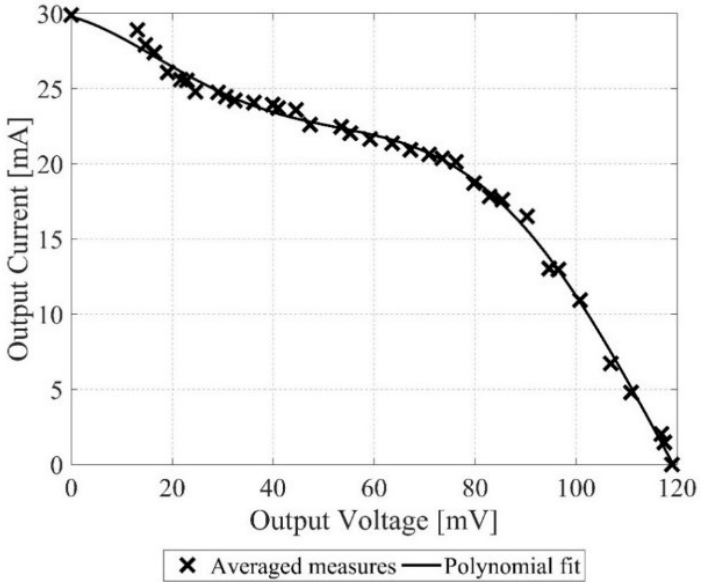

a)

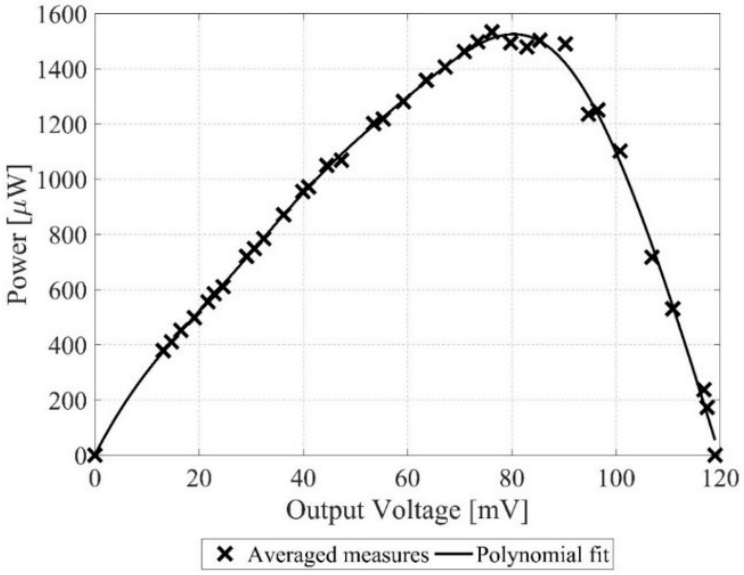

b)

Figure 4.19 (a) Current-voltage characteristic curve for two TEG cells connected in series, with a 37 °C hot side temperature and 22 °C cold side temperature. (b) The computed power-voltage characteristic of two series-connected TEG cells [206].

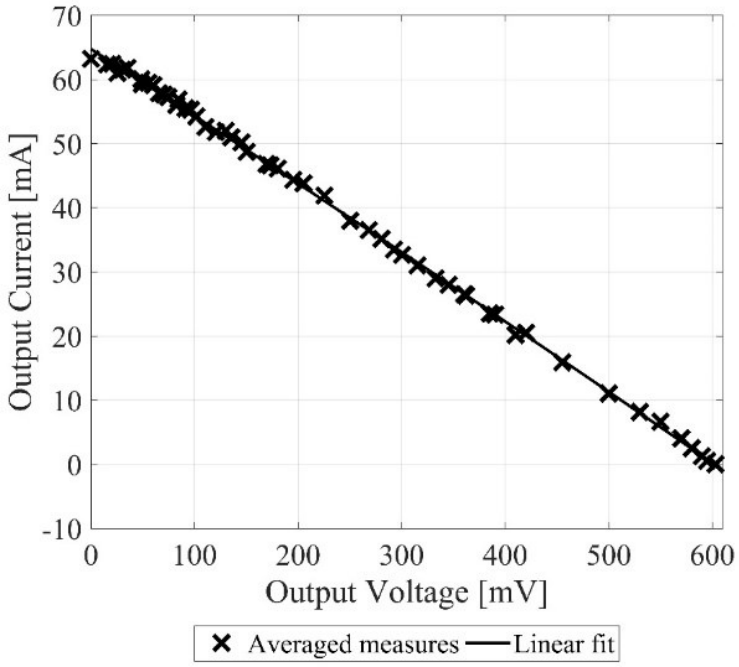

a)

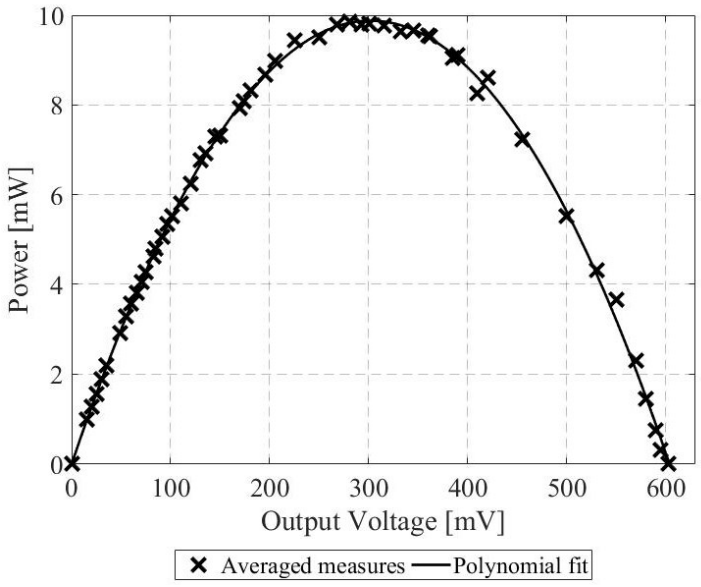

b)

Figure 4.20 (a) Current-voltage characteristic curve for ten TEG cells connected in series, with a 37 °C hot side temperature and 22 °C cold side temperature. (b) The computed power-voltage characteristic of ten series-connected TEG cells [206].

Figures 4.21a and 4.21b show the design of the circuit, using a 50% MPP properly fixed by selecting *R_OC1* and *R_OC2* values. In order to guarantee the fastest recovery of the harvester output voltage to the MPPT level following power withdrawal, the minimum recommended value of 4.7 μF was chosen for *C_HRV*, as

well as *C_STORE* since no large system load are expected during charge tests and also to ensure fast charge time during cold start.

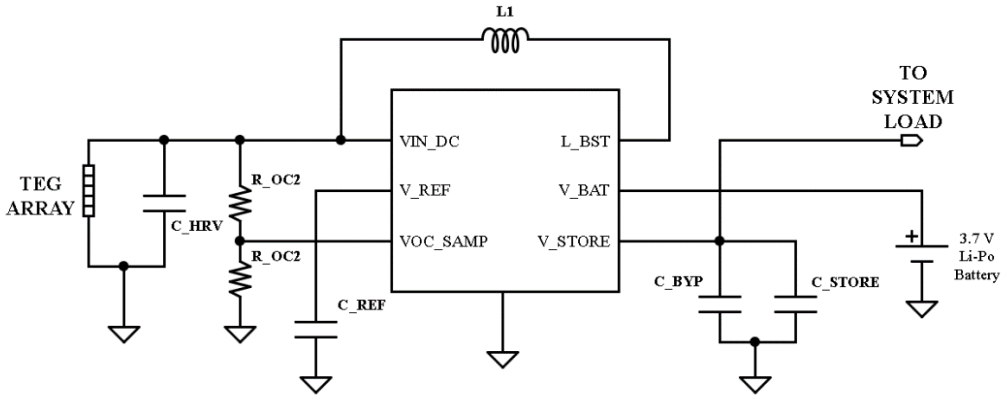

a)

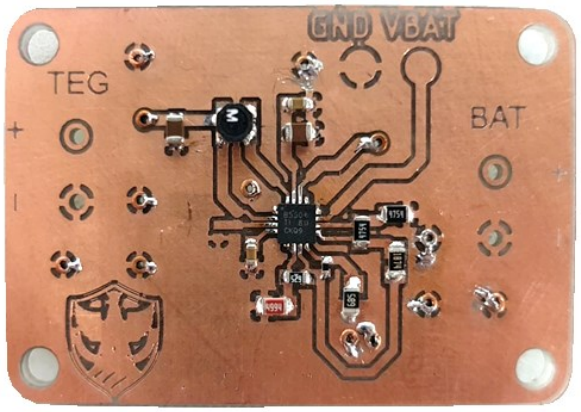

b)

Figure 4.21 (a) Proposed schematic circuit for the thermal energy harvesting power manager test board and (b) the implemented prototype of the EH board [206].

During this test, we also connected a 50 kΩ load in parallel with *C_STORE*, in order to simulate a constant load. As shown in Figure 4.22, the test sequence was as follows: firstly, the battery was connected to the *VBAT* pin, and then ten series-connected TEG cells were connected to the input pin of the power managing circuit. As expected, the circuit was able to manage the TEG cells output voltage for charging a 3.7 V Li-Po battery. The input reached 600 mV periodically, for 250 ms each 16 s, then diminished and self-stabilized at 300 mV. The first of these time windows corresponds to the TEG voltage sampling operation for the MPPT algorithm. In this stage, the open-circuit (OC) voltage of the harvesting source is checked, while in the

remaining time the TEG voltage is kept constant to the selected maximum power point, considered as a percentage of the previously measured OC voltage value, by modulating the current employed for the battery charging process.

As a final test, a fully discharged, 800 mA/h Li-Ion battery powered the system, resulting in 35 hours for a complete charge state. Gathered data allowed to determine the optimal operative condition for the single-cell and for each array configuration, and to optimize the MPPT algorithm in the DC/DC stage of the power management unit. Moreover, according to the experimental results, we designed the power manager selection and realized a custom PB prototype for the thermal energy harvesting and storing process. The proper number of TEG cells ensured sufficient harvested energy and maximum efficiency.

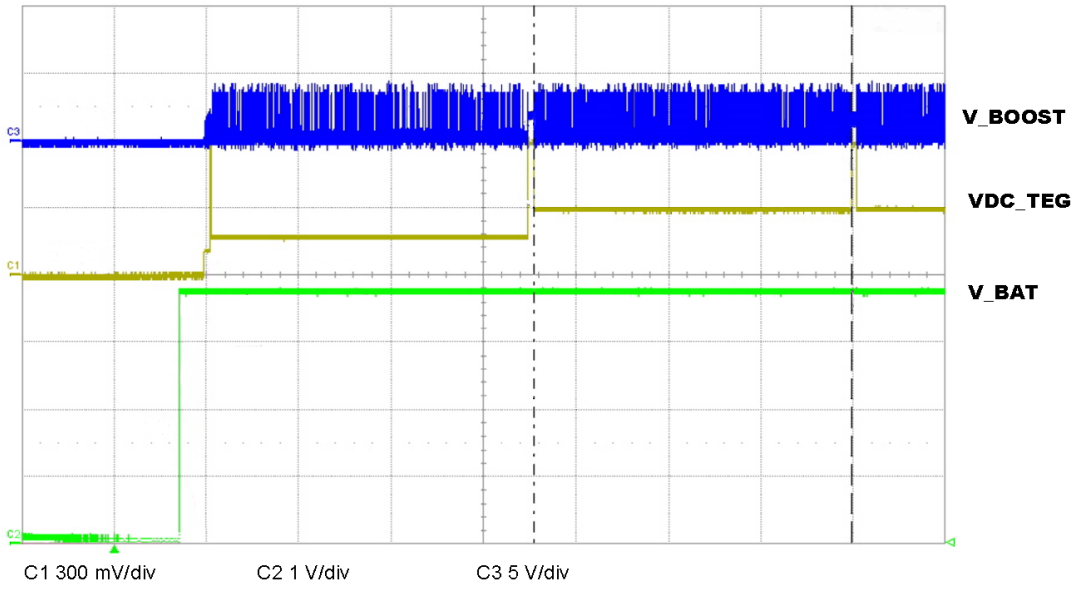

Figure 4.22 Oscilloscope captured image of the start-up sequence and MPPT sampling algorithm [206].

4.3 FLEXIBLE PIEZOELECTRIC EH FOR HUMAN FINGERS: MEASUREMENTS AND APPLICATIONS

This research work reports an extensive set of measurements and suitable consideration on human finger energy harvesting from a mechanically excited piezoelectric element. In particular, a test analysis has been conducted on a harvesting

system composed of a 3D printer finger emulating the human behavior and a piezoelectric strip to be applied in autonomous smart gloves.

In this work, the attention is focused on the capability of human hands to generate energy while moving and on the capability of piezoelectric harvesters to gather this energy [216], [217]. Piezoelectric materials are useful to convert mechanical vibration into electrical energy with a relatively simple structure. Several piezoelectric harvesters have already been presented in the literature review, dealing with different materials that can be categorized into piezoceramics (PZTc) and piezopolymers (PZTp). The PZTc are characterized by a large electromechanical coupling constant and shows high energy conversion capability but are too difficult and fragile to be applied in most applications. On the contrary, PZTp is characterized by a less electro-mechanical coupling constant, compared with PZTc, but are flexible systems so can be used with success in several applications among others those on the human body. EH on the human body, and in particular on human finger motions has been employed in several works [218]–[220]. Also, the EH from several PZT transducers operating simultaneously on the human body has been studied in detail [221] while in [222] studies related to the capability to gather energy from human fingers are shown. In [221] a model analyzing the human finger motion has been investigated and reported following the kinematic framework. In the present research, an investigation has been conducted on the motion of a single finger, reproduced by means of a 3D printed model and actuated by a servo motor, when a PZTp strip is applied along all the finger length (see Figure 4.23).

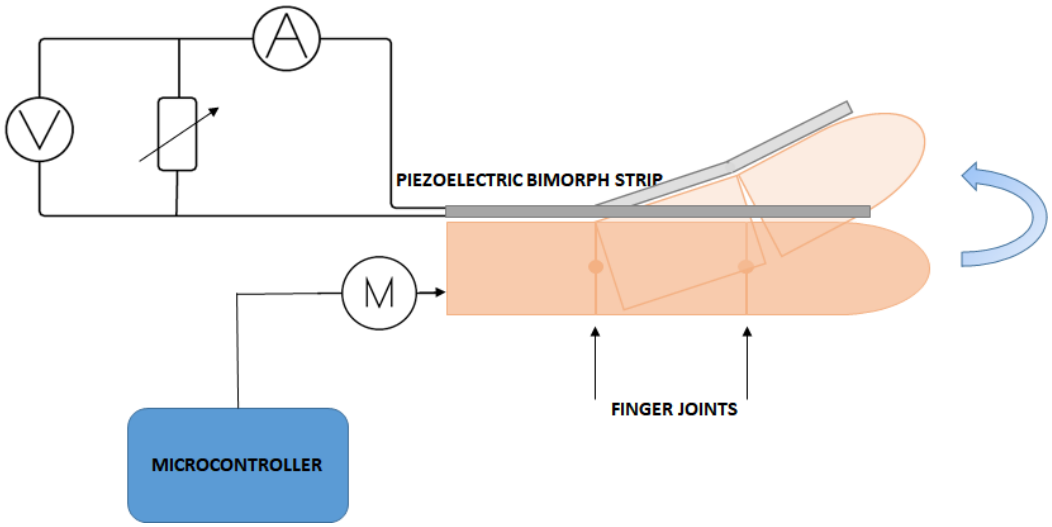

Figure 4.23 Measurements setup for the single finger harvester [223].

Experimental results related to the frequency of operation and harvester load are here given and commented in order to find out the best harvester solution for such a kind of application.

The implemented 3D finger system (see the photo in Figure 4.24), has been designed to reproduce the complete human finger adduction-abduction movements. The 3D architecture is composed of an underactuated mechanism able to implement a motion as similar as possible to the real one when the hand is used for grasping objects or materials. A PZT strip, from TE Connectivity, has been anchored to the finger reproducing the effect of a glove worn on the finger. A microcontroller driven motor is used to move the linkage mechanism activating the finger joints. Measurements have been performed, by means of a digital oscilloscope interfaced with an acquisition tool on the personal computer, activating the finger at different frequencies with different open-close velocity at variable resistive loads. Also, open circuit and shunt measurements have been done on the PZT material. The per-formed experimental shows that the RMS harvested energy at a fixed open-close rate can be maximized for high resistive loads, that match the equivalent PZT internal impedance.

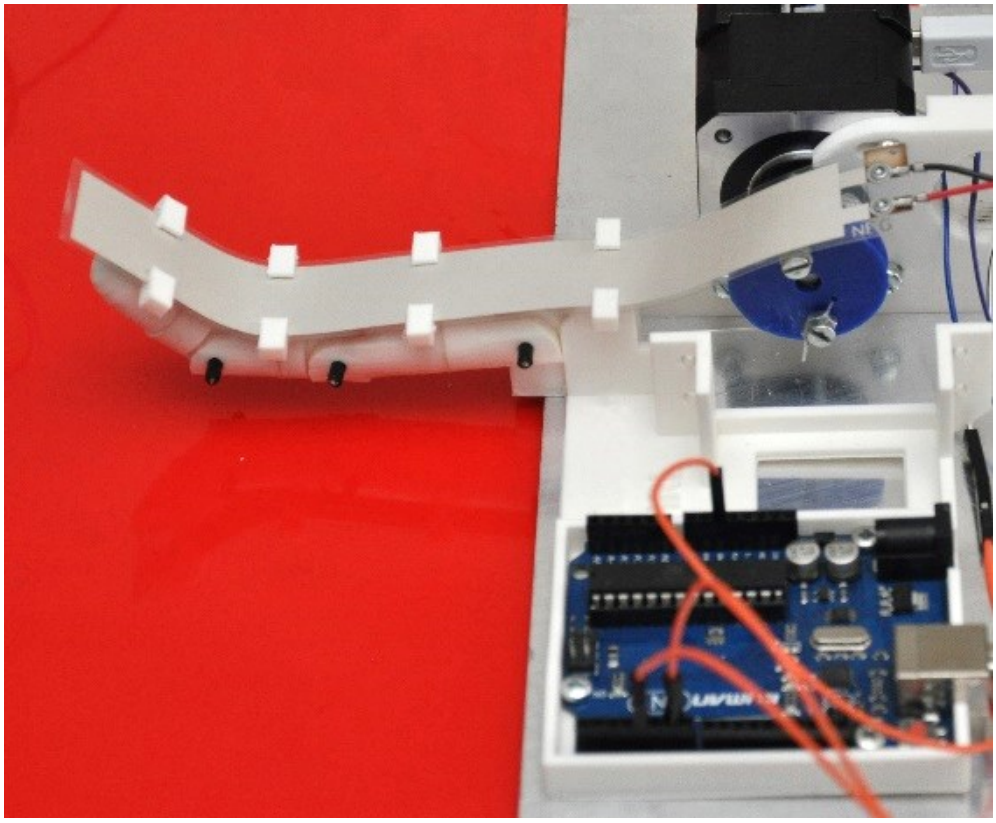

Figure 4.24 The implemented 3D finger system with bimorph PZTb applied to it. The system presents all the human finger joints, that are moved by means of a mechanical structure coupled to a stepper motor [223].

In Figure 4.25 a typical output voltage from the PZT strip is shown with a 1 s open-close finger rate. In this case, in open circuit condition up to 26.8 V peak-to-peak is reached with the utilized PZT material.

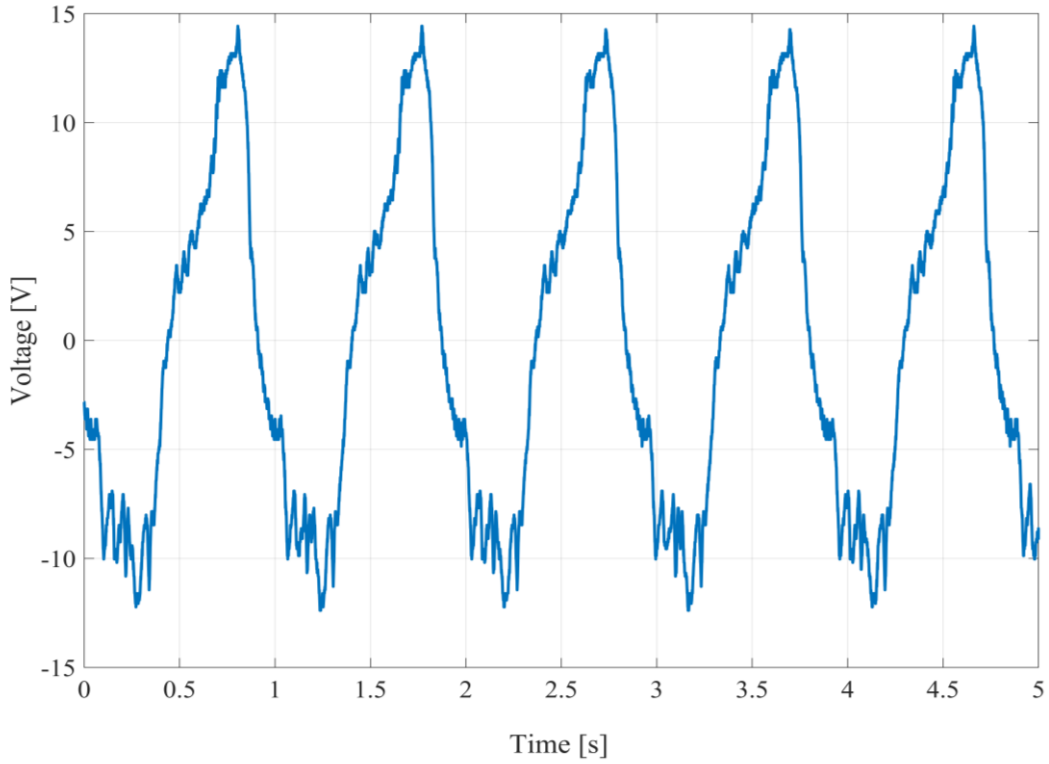

Figure 4.25 Output voltage from the PZT strip with a 1 s open-close finger rate [223].

In Figure 4.26 the measured RMS Voltage - Current and Voltage - Power curves are shown, for a 200 ms abduction-adduction movements.

Finally, the proposed architecture has been used in a practical application to be tested in real conditions. The harvester circuitry has been implemented with a commercial component from Linear Technology conceived for PZT harvesters. This component, equipped with a low-loss full-wave bridge rectifier and a high-efficiency buck synchronous converter, is specially optimized for high impedance generators, such as piezoelectric transducers. The architecture allows transferring energy from a storage device at the input to a regulated voltage output. In this case, a high impedance equivalent load (100kΩ), simulating ultra-low-power devices biasing conditions has been adopted. Results show that with a 1s open-close finger rate the equivalent device can be feed in a continuous way without power interruptions.

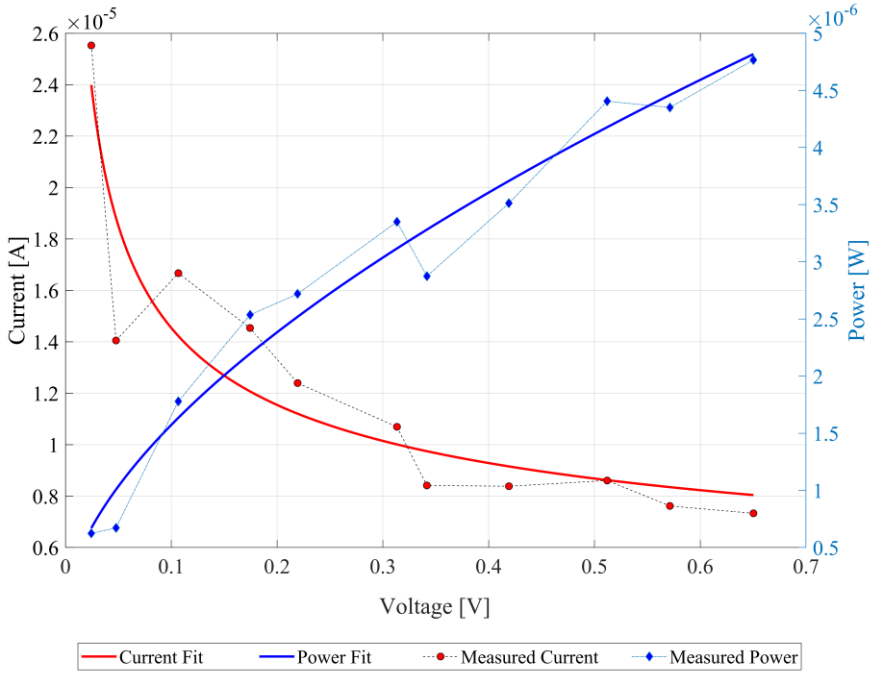

Figure 4.26 RMS Voltage-Current and Voltage-Power curves for a 200 ms abduction-adduction finger movements [223].

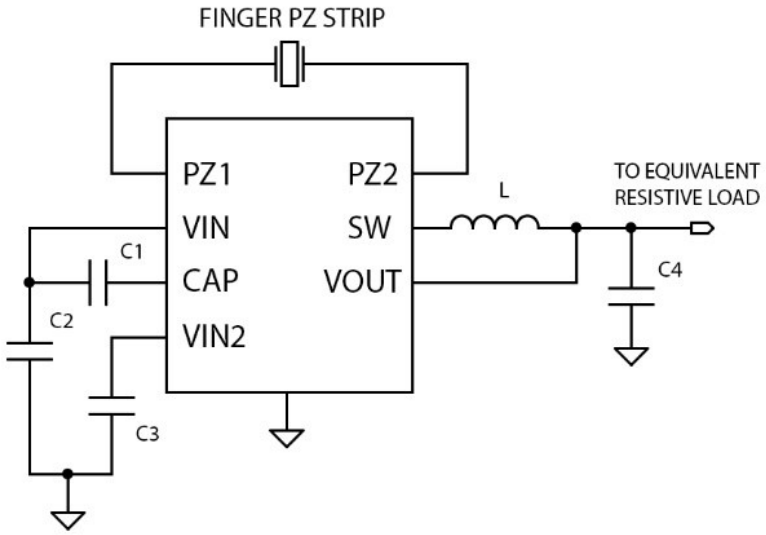

Figure 4.27 Schematic of the adopted testing architecture for the AC to DC energy conversion [223].

4.4 HUMAN BODY MULTISOURCE ENERGY HARVESTER FOR WEARABLE SENSORY GLOVE

In this contribution, the research activity is focused on a multi-source power management system, based on human body energy harvesting, to extend the battery lasting of an electronic sensory glove, used to measure flexion/extension, abduction/adduction movements of fingers of the hand [224], [225]. The system

exploits heat of the human forearm and pressure impressed by the foot heel during walking, so to gather additional energy. The aim is to allow hours of energy-autonomy for the user working with the sensory glove. Such a glove is equipped with a number of flex sensors that furnish data from finger movements, acquired and pre-processed by a microcontroller, and wirelessly sent to a Personal Computer for analysis, visualization and storage purposes. Differing from chapter 4.2, the here proposed power scavenger is based on a multisource biomechanical and thermoelectric energy harvesting method. This research has been conducted in collaboration with Prof. Saggio and his team, from the University of Rome "Tor Vergata".

4.4.1 Sensory Glove Overview

In order to measure the hand gestures, we developed a sensory glove based on acquired experiences. The glove was equipped with 14 flex sensors (Flexpoint Sensor Systems, Inc., Draper, UT) and a 3-axis accelerometer (ADXL335, by Analog Devices, Inc., Norwood, MA) able to measure the flex/ extension capabilities of the finger joints of a human hand, plus the wrist movements.

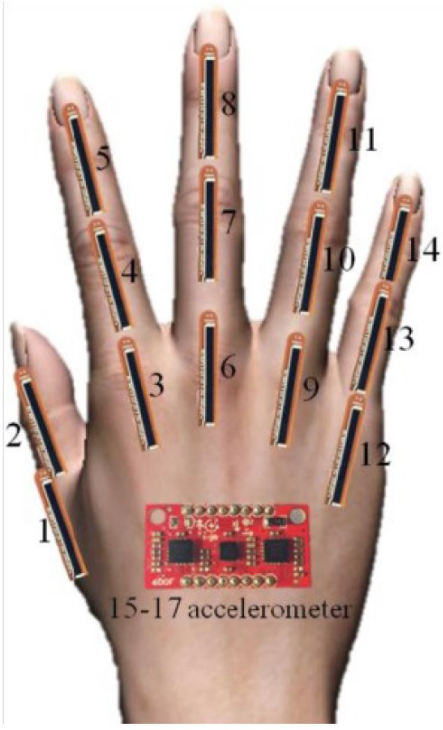

#	Sensor
1	1-MCPJ
2	1-IPJ
3	2-MCPJ
4	2-PIPJ
5	2-DIPJ
6	3-MCPJ
7	3-PIPJ
8	3-DIPJ
9	4-MCPJ
10	4-PIPJ
11	4-DIPJ
12	5-MCPJ
13	5-PIPJ
14	5-DIPJ
15	accelerometer x-axis
16	accelerometer y-axis
17	accelerometer z-axis

Figure 4.28 Flex sensor position on the finger joints, and IMU position on the backside of the hand [224].

The paragraph 4.4 is based on the published papers [224], [225] As the author of this articles, reuse permissions are not required.

Flex sensors were positioned on distal interphalangeal, proximal interphalangeal, and metacarpo-phalangeal finger joints, except for the thumb that has a proximal IP (PIP) sensor and distal IP sensor (DIP), as shown in Figure 4.28.

The accelerometer was positioned on the backside of the hand. In total 17 signals were collected by means of a custom-made prototype board connected to a computer, so to take into account both flexion/extension of the joints of the fingers and rotation/bending of the wrist. The complete wearable system can be seen in Figure 4.29.

The selected resistive sensors are stable, low cost, with a thickness of less than 5 mils, flexible, almost linear [207], [226]. Different sensor sizes can be also selected depending on the application: sensors of 1, 2, 3-inches are available for the finger joints DIP, PIP, MCP, respectively. The influence of fabric composition on sliding and flexion of the sensor has been studied. The glove is made of 88% polyester and 12% Elastane because it provides greater comfort for movement. For the present study, only one medium right-hand glove was sufficient. Additional gloves have been developed for the left hand and the different sizes (small and large).

Figure 4.29 The Lycra glove system: the glove with 14 flex sensors on the DIP, IP and MP joint and the IMU device, and the acquisition and transmission box on the forearm [224].

The selected glove could be best worn by the largest number of participants. The used sensory glove covers all the hand, but it can be modified to let the palmar surface and the fingertips free to maintain the tactile sensitivity. The wiring connection of the sensors to the electronic board is flexible and with a diameter of 1.5 mm and a weight less than 1g/m. The sensory glove has a 50 g weight.

The Arduino Leonardo electronic board allows the management of 14 analog inputs for the bend sensor signals, 2 digital pins for Bluetooth serial communication, and provides ground and voltage reference for the operation of the bend sensors. The transduction takes place via a voltage divider between 0 and 5V with a fixed 18 KΩ resistance, selected because it is the geometric mean between the maximum and minimum sensor resistance, to provide the widest voltage range. The sensor readout circuit is followed by a 10-bit ADC module. The ADC sampling frequency was set to 1 kHz and the transmission frequency was set to 50 Hz, to handle up to 20 multiplexed channels. Once the data are acquired, they are redirected to the Bluetooth module and sequentially to the receiving antenna connected to a PC. For the transmission is used the RN42 mate silver module for low power consumption: a Bluetooth 2.0 dongle is used for the receiving computer. Data missing was not observed during the test. For data transmission on 8-bit serial communication, the 10-bit data from ADC have been decomposed into High and Low byte. Known the high and low part sending sequence, it was able to reconstruct the original given data to 10 bits. The sensory glove can work both alone and within a network of sensors and can be interfaced with mobile devices, smartphones, tablets, and cloud data storage systems. The electronic board has a 250 g. weight, largely due to the Arduino Leonardo board.

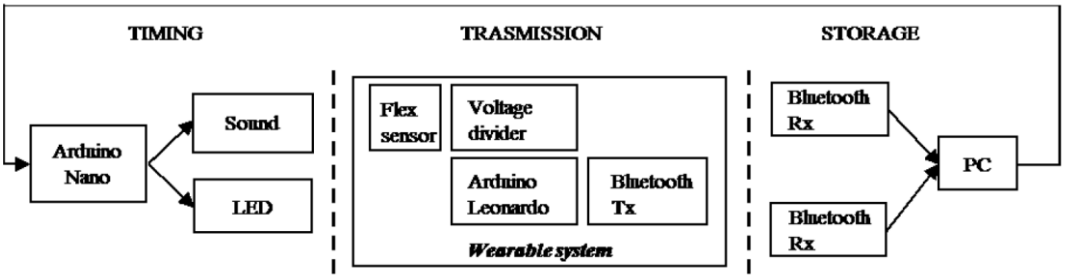

a)

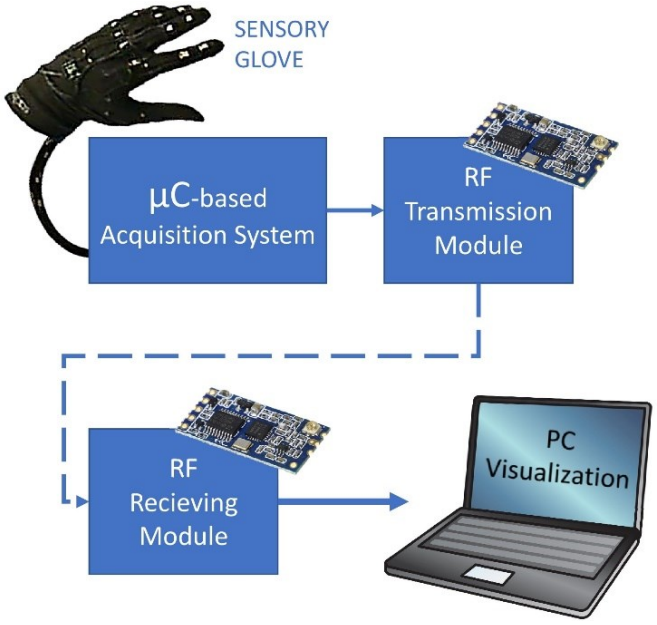

b)

Figure 4.30 (a) Schematic architecture of the glove system with the 3 stages and (b) its visual block scheme. The audio-visual stimulus marks the time and where to place the hand. Synchronously, data are captured and wirelessly transmitted to the receiving antennas connected to the PC. The PC stores the data and redirects the synchronization signal from the acquiring board to the pacing board [224].

The current draw is about 100 mA for the 3D printed glove with 10 flex sensor, and 110 mA for the Lycra glove with 14 flex sensors and the IMU device, but is largely due to the acquisition and transmission board since the bending sensor circuit has resistances of hundreds of kilohms and the IMU unit only absorbs 350 µA. The schematic architecture of the glove system, which is the same for the two types of glove, is shown in Figure 4.30a and 4.30b.

4.4.2 Multisource Harvester Architecture Overview

Evidently, practical reasons impose a wireless transmission system of the sensory gloves. The glove data transmission block scheme trough wireless connectivity is represented in Figure 4.30b. The system is composed of an RF commercial transmitting block driven by a microcontroller and a remote receiving block connected to a data server. In order to guarantee a system battery long lifetime, the overall system includes a multi-harvester block, so as to scavenge free available energy directly from the surrounding environment. The conceived harvesting block is depicted in Figure 4.31, and it relies on a dual-energy source, i.e. the human forearm heat and foot generated pressure (heel strike).

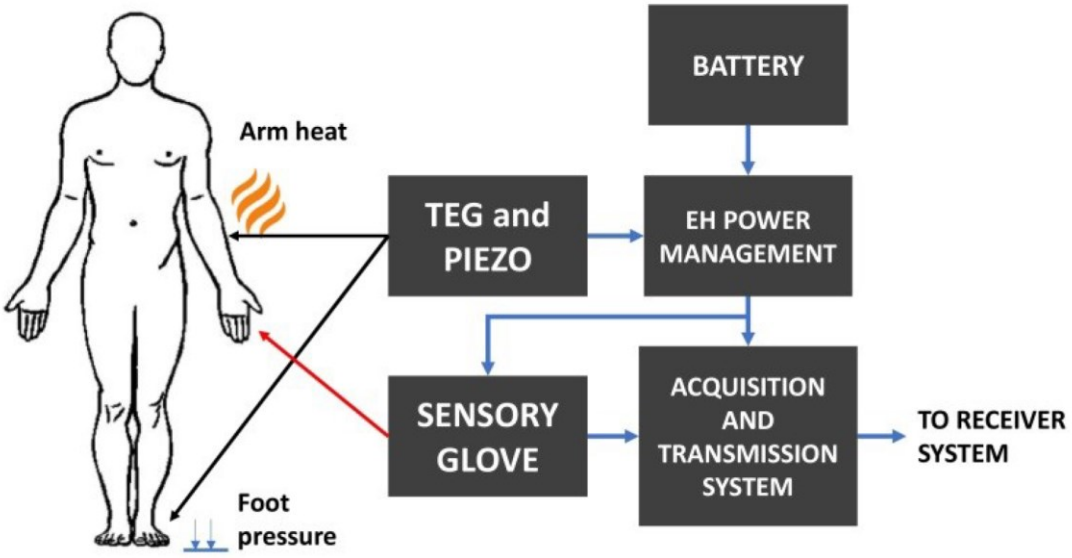

Figure 4.31 The complete multisource energy harvesting architecture [225].

The harvester outputs contribute in parallel to directly power the system circuit. Each harvester sub-system is terminated with an off-chip dual Schottky diode to avoid reverse current flow. Of course, this solution affects the overall harvester efficiency dissipating energy over the diode (even if this phenomenon is mitigated by a low reverse voltage drop of the Schottky barrier) but, usefully, the total amount of collected energy is greater than power coming from a unique energy source.

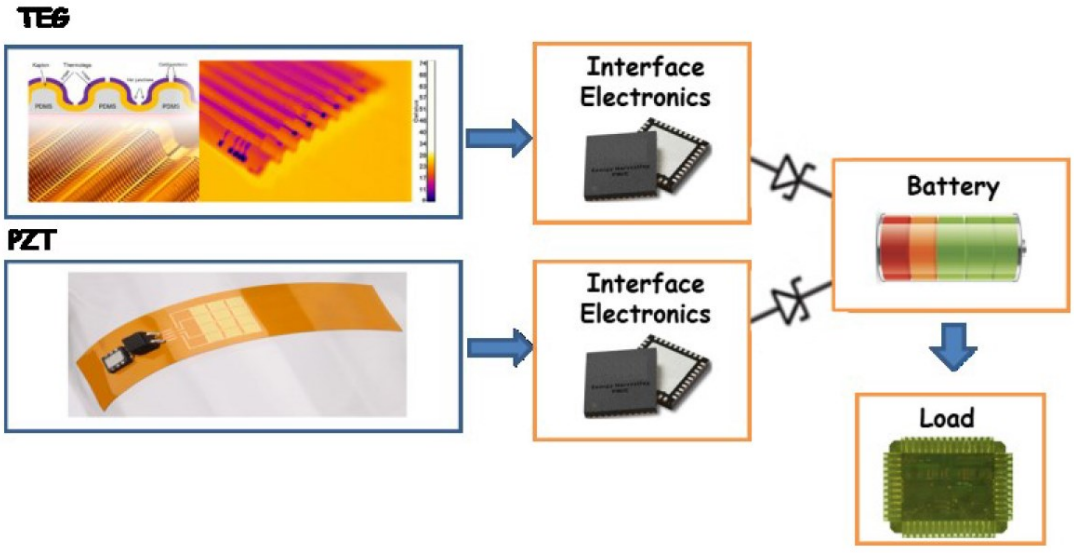

Figure 4.32 Multi-harvester block scheme [225].

As shown in the above Figure 4.32, the EH system is conceived to provide the required current directly from the gathered energy, which is converted in regulated

voltage output. When the energy source is absent or not sufficient to supply the glove, extra current is provided by the battery.

In this discrete prototype, the commercial component LTC3107 from Linear Technology is used to gather energy from a set of TEGs, and to arbitrate the power path with the battery, while the LTC3588 is used to convert the energy obtained by the human walk. In detail, the energy coming from the human heat is collected by means of a set of standard 3cm x 3cm Peltier cells (see Figure 4.33a for the prototype harvester implementation). This is because of the distribution of the heat along the human arm, which is not uniform, thus each cell cannot provide exactly the same output voltage and a parallel connection could cause a dispersion current between cells, reducing the overall efficiency. Since the TEG cells, in this configuration, can provide an output voltage ranging from 20 mV (static arm, rest condition) to 180 mV (movement), a 1:100 transformer has been employed for the fly-back converter, integrated in the LTC3107, in order to allow the DC-DC converter so guaranteeing its functionality with input voltages as low as 20 mV. Concerning the piezo harvesting branch (Figure 4.33b shows the prototype harvester implementation with the connection of multiple stacked disk in parallel), preliminary simulations proved how the amplitude of the voltage signal, obtained with a pressure of 75 kg over a single piezo disk surface, can reach up to 25 Vpp, while the frequency ranges from about 1 Hz (for a normal walk) to 2.5 Hz (for a running session). The first input stage of the LTC3588 chip is composed of a full-wave rectifier bridge, followed by a 20 V clamping Zener diode.

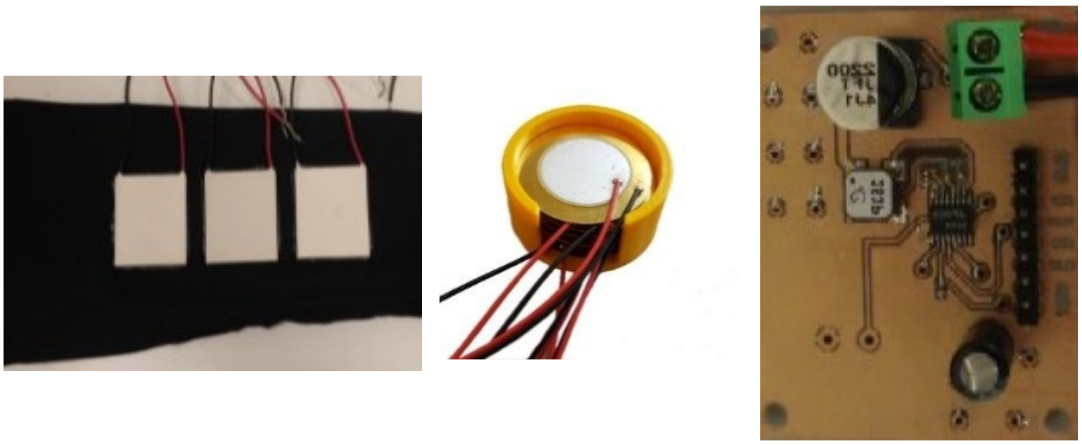

a) b) c)

Figure 4.33 a) TEG Harvester; b) PZT Harvester; c) Electronic board [225].

The final circuit schematic of the designed multisource energy harvesting system is depicted in Figure 4.34.

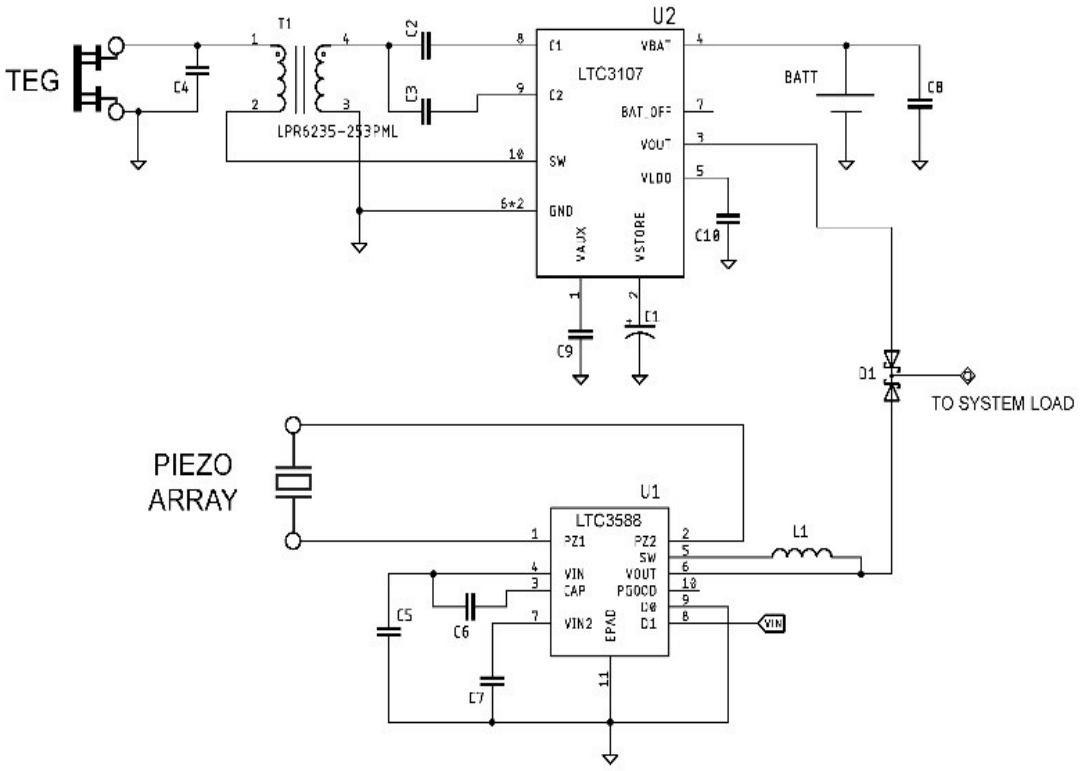

Figure 4.34 Harvesting system electronic scheme [225].

4.4.3 Results and Discussion

A first discrete prototype board (Figure 4.33c), with discrete components mounted both on the top and bottom layer, was designed and fabricated, in order to demonstrate the feasibility of the proposed system. Figure 4.35 shows the TEG and PZT harvester physical implementation. For the TEG harvester, Table 4.3 shows measurement results about conversion efficiency, for a 3.3V regulated output voltage and different loads, without any battery. Results show a relatively high conversion efficiency at lower loads, while the minimum start-up voltage increases as the current requirement rises as well. This problem is mitigated with the introduction of the battery, thus enabling the power path management, which provides as much current as the TEGs can provide by varying the equivalent load seen from the TEG harvester. Also, experimental results proved that the best performance can be achieved by connecting all the cells in series.

Load (kΩ)	Minimum start-up voltage (mV)	Conversion efficiency (%)
100	67	38
82	69	25
68	70	22
47	76	37
39	79	30
33	80	37
27	84	43
10	120	56
4.7	177	43

Table 4.3 Thermoelectric source measured performance [225].

Concerning the piezo harvesting channel, Figure 4.36 shows a typical waveform of a walk, captured with a digital oscilloscope at 20V/div without any load applied to the system. The peak-to-peak voltage value reaches 75V, however, the amplitude drops down to about 18V – for the best case – when a load current is applied, thus avoiding a voltage limitation due to the internal Zener diode of the LTC3588 chip. In Figure 4.37, the overall harvested power is illustrated, considering an equivalent resistive load. Results show a peak of maximum power transfer around 1 kΩ of equivalent resistive load. Another minor peak is located around 82 kΩ of equivalent load.

In order to test the capabilities of the whole harvesting system, a low-power acquisition and transmission board was implemented. The system includes an ARM Cortex M0 and a Si4463 transceiver set up to a short 5 dBm transmission range. The idle current of the system is about 4 mA, while it is as-low-as 10 mA during transmission. According to [227], the acquisition and transmitting rate can go down to 15 ms and 5 ms, respectively, for a mean current consumption of 5.5 mA. In this perspective, results demonstrate that the harvester can extend the battery lifetime up to 20% of the normal duration.

a) b)

Figure 4.35 PZT (left) and TEG (right) harvester physical implementation [225].

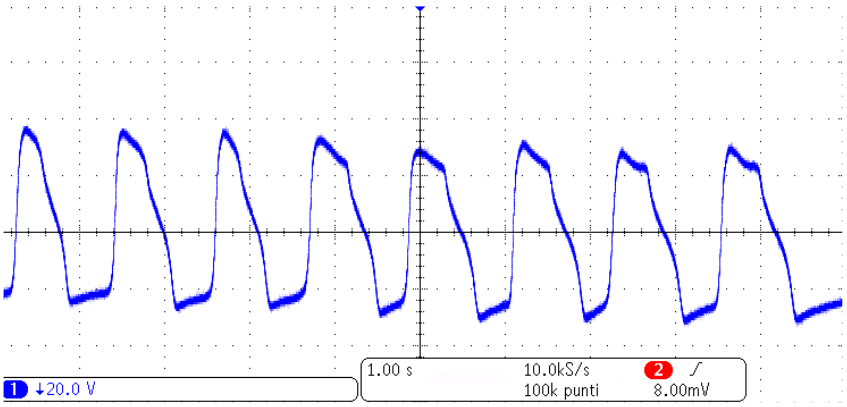

Figure 4.36 Piezoelectric harvester output with no load [225].

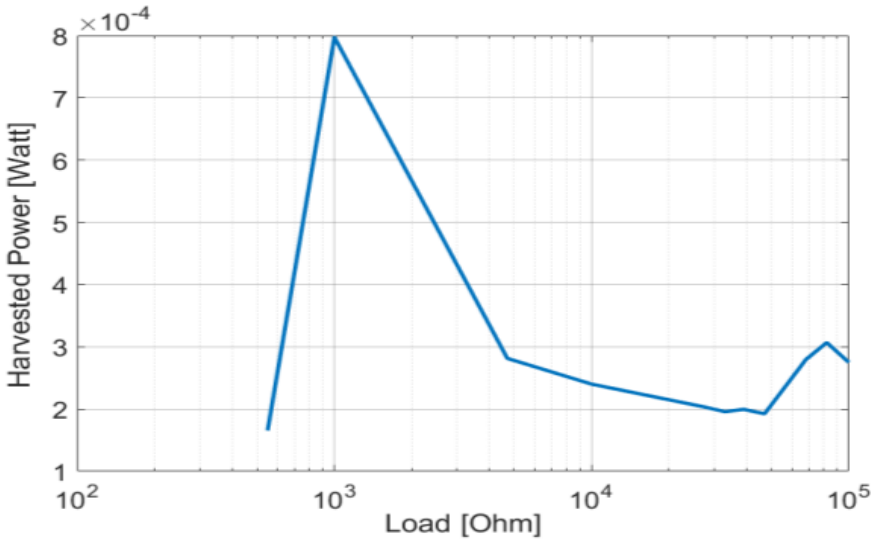

Figure 4.37 Overall piezoelectric heel strike harvested power versus output load [225].

Chapter 5: Conclusions and Future Work

This chapter concludes the dissertation. It briefly restates the motivation of the thesis work, the identified problem areas and the various findings in each problem area. Finally, it shows the direction of future research in this regard.

5.1 CONCLUSIONS

This thesis covers work done on the design and development of various optimized energy harvesting systems for sustaining self-autonomous wireless sensor nodes and wearable devices for biomedical applications, directly exploiting the energy generated from the human body. Nowadays, the continuous and growing development of new electronic technologies is leading to the spread of an enormous number of new generation portable devices that denote an important change and improvement in the wellness of the humankind. In addition to the well-known smartphones and tablets, examples of new generation portable devices are linked to the Internet of Things and the possibility of making smart, remote controlling and monitoring equipment for different applications like home automation, or the new wearable devices for monitoring biomedical parameters or sport activities, or wireless sensor networks (WSNs) and autonomous sensors for environmental monitoring or for improving the supply chain and the efficiency of industrial warehouses. Although the quality of life has greatly improved in this sense, this incessant diffusion of portable electron devices leads to an increase in the need for energy sources capable of sustaining their functionality. Batteries have always been considered the primary source of portable energy and therefore many technological advances have been made in order to improve their performance, in terms of capacity per unit of volume and reliability. However, there are many negative aspects linked to such massive use of batteries for portable applications. First of all, disposal and environmental impact. Although eco-sustainable technologies have recently been developed, the vast majority of batteries currently in circulation constitute a danger to human health and the environment, as they consist of toxic materials that are difficult to dispose of, and an increase in their diffusion would intensify this problem. Secondly, the batteries have a limited duration in time, so they need maintenance for recharging or for replacing them, constituting a cost as well as a limitation for portable devices that benefit from it, especially those sensory

autonomous devices used, for example, for the environmental monitoring, that is dislocated in hostile places and of difficult access.

Therefore, a possible solution to this problem, currently of great scientific interest, is represented by energy harvesting from low-cost alternative sources, with zero environmental impact, that allow to directly supply ideally infinite energy to portable electronic devices, or at least assisting the use of the batteries, prolonging their life and therefore its disposal over time.

There are many alternative energy sources and the related conversion techniques used to date for this purpose. Solar energy, for example, has always been considered one of the most important alternative fonts for both low-power and high-power applications. In this sense, the development of new materials and new technologies for recovering solar energy through photovoltaic panels is constantly evolving, to further improve conversion efficiency and reduce costs. Another promising energy source is vibrational energy, generated for example by natural oscillations of structures such as bridges, frames of industrial equipment but also by the very movement of the human body. The most adopted conversion techniques of this energy are cantilevers with electromagnetic induction or the use of piezoelectric materials. The latter exploit a particular property for which by mechanically altering the crystal lattice of the material itself, a potential difference develops at its ends which is transformed into electric current if closed on a load or, vice versa, it is possible to compress or expand the piezoelectric material subjecting it to a proper voltage. This last effect was the first to be exploited, in the realization of actuators as speakers, but recently is being studied the possibility of applying piezoelectric materials in contact with vibration sources to recover energy from them.

Another important energy recovery technique exploits the known Seebeck effect, for which a thermoelectric material subjected to a thermal gradient generates a potential difference V between the hot and cold ends, proportional to the temperature difference ΔT times the Seebeck coefficient S [29, 30]. Therefore, this method allows for recovering electricity from heat. The reverse phenomenon, or the Peltier effect, has been used for many years for the implementation of electronic systems capable of generating heat or cooling, based on the voltage applied to the device, called the Peltier cell. Recently, the Seebeck effect has been analyzed in new generation materials, with the aim of obtaining higher energy conversion efficiencies. However, due to the still

high cost and the scarce diffusion of such thermoelectric materials, they do not constitute a suitable solution for low-cost applications. On the contrary, the study of the employment of small low-cost Peltier cells as TEG generators for the recovery of thermal energy and how to maximize the conversion efficiency of such devices can be of great interest, as it constitutes a valid source of alternative energy for portable or wearable devices that requires very low power. Among the various applications, the biomedical field is one of the most interesting, since the human body spends energy to maintain constant its temperature level, regardless of the atmospheric conditions of the surrounding environment, within certain limits. It is possible to recover part of this energy dissipated by the human body by using TEG generators, which can supply implantable devices or generic health monitoring sensors. In order to directly feed autonomous, portable devices or to recharge the battery by means of thermoelectric energy harvesting, a constant standard supply voltage should be provided, such as 3.3 V, 1.8 V, etc... However, the output voltage obtained by thermoelectric generators is directly proportional to the temperature gradient and, therefore, it is not fixed to a specific value since it is application dependent. Hence, a DC to DC conversion stage is needed between the source and the equivalent load. This is a key aspect of the thermoelectric energy harvesting system, since the electrical description of the energy source, in terms of Spice model, is crucial to properly design a DC/DC converter, in order to guarantee the maximum efficiency of operation for the whole system by means of Maximum Power Point (MPPT) algorithms.

Finally, one of the latest interesting fields of research is related to the energy harvesting from the radiofrequency electromagnetic field that is spread in the surroundings, mainly due to telecommunication distribution, such as mobile phones networks, TV signals broadcasting, GPS and satellite communication or FM radio, Moreover, short-range communication systems are recently becoming popular for many applications, such as WiFi connections, Bluetooth and others. RF Energy Harvesting generally relies on the amount of available ambient energy levels and converts it into usable electrical energy. Till now, many RF energy harvesters have been presented in the literature, in order to supply autonomous wireless sensors or wearable devices, but only a few of them have been able to harvest energy with good efficiency. There are many causes that limit the collection of these free energy resources, for instance, irregular levels of presence for the EM signals in the

environment during the day and their spectral characteristics, due to modern communication codes, that spread the transmitted energy. The RF EH system design should be carefully done, taking into account requirements for the antenna matching in both frequency of operation an input power range, the proper choice for rectification stage the power management and storage section.

In all, the main objectives as laid out in Chapter.1 of this thesis have been achieved. The findings of this work have been published in scientific journals, research reports, and international technical conferences, for benefit of the future researchers and users of energy harvesting systems for wireless sensor nodes/networks and wearable devices.

5.2 FUTURE RESEARCH WORKS

A broad scope of breath studies has been carried out in this energy harvesting research work, beginning from scrap to what has been done so far, as well as in-depth investigations on critical issues. Nevertheless, there are still rooms for further study, enhancements, and optimization. Some possible future research works include:

- for the RF energy harvesting field, the IC integration of the whole system, including the DC/DC and power management conversion stage can lead to great advantages, such as efficiency improvement, since miniaturization can help to reduce the energy losses due to parasitics, but also a better integration is small, portable devices. However, the RF EH integration is still challenging, since all the needed requirements are too different, therefore it is difficult to identify a suitable technology.
- regarding the human body thermoelectric energy harvesting, the usage of standard TEG cells limits the potential of such energy source, because of the rigidity of these devices, which could be uncomfortable to wear, especially for large body area coverage. On the other hand, novel flexible thermoelectric materials are too expensive and still under research, therefore a study on a novel, low-cost flexible thermoelectric module for thermoelectric energy harvesting is essential for the feasibility of commercial human body EH systems, to support new generation wearables.

- Novel architectures for very low-input voltage DC/DC converters are an important field of research, with the aim to increase the amount of gathered energy from low-power EH systems. Indeed, many energy harvesting devices provide a very low output DC voltage signals, according to the availability of source energy. Although many techniques and design methods have been defined to improve the conversion efficiency from the physical energy source to the electrical domain, the obtained voltage signal must be converted into a standard power supply value, in order to feed electronic devices. If the harvested DC signal is not enough to guarantee the correct functionality of the DC/DC converter, the gathered energy is lost, independently from the harvester conversion efficiency. Therefore, the design of a low-input voltage DC/DC booster, with high efficiency is essential to accomplish the energy harvesting aims.

Bibliography

[1] M. Satyanarayanan, "Mobile computing: The next decade," in *Proceedings of the 1st ACM Workshop on Mobile Cloud Computing and Services: Social Networks and Beyond, MCS'10, Co-located with ACM MobiSys 2010*, 2010.

[2] T. Arampatzis, J. Lygeros, and S. Manesis, "A survey of applications of wireless sensors and wireless sensor networks," in *Proceedings of the 20th IEEE International Symposium on Intelligent Control, ISIC '05 and the 13th Mediterranean Conference on Control and Automation, MED '05*, 2005, vol. 2005, pp. 719–724.

[3] P. A. Di Tore, "Situation awareness and complexity: The role of wearable technologies in sports science," in *Journal of Human Sport and Exercise*, 2015, vol. 10, no. Specialissue1, pp. S500–S506.

[4] I. Korhonen, J. Pärkkä, and M. Van Gils, "Health Monitoring in the Home of the Future," *IEEE Eng. Med. Biol. Mag.*, vol. 22, no. 3, pp. 66–73, May 2003.

[5] "Advantages & Limitations of the Lithium-ion Battery - Battery University." [Online]. Available: https://batteryuniversity.com/learn/archive/is_lithium_ion_the_ideal_battery. [Accessed: 20-Nov-2019].

[6] "Health Concerns with Batteries - Battery University." [Online]. Available: https://batteryuniversity.com/learn/article/health_concerns. [Accessed: 20-Nov-2019].

[7] D. H. P. Kang, M. Chen, and O. A. Ogunseitan, "Potential Environmental and Human Health Impacts of Rechargeable Lithium Batteries in Electronic Waste," *Environ. Sci. Technol.*, vol. 47, no. 10, pp. 5495–5503, May 2013.

[8] M.-A. Bănică, "Energy Harvesting from Renewable Energy Sources," 2020, pp. 247–254.

[9] I. F. Akyildiz, W. Su, Y. Sankarasubramaniam, and E. Cayirci, "Wireless sensor networks: a survey," *Comput. Networks*, vol. 38, no. 4, pp. 393–422, Mar. 2002.

[10] S. R. J. Ramson and D. J. Moni, "Applications of wireless sensor networks — A survey," 2017, pp. 325–329.

[11] F. Karray, M. W. Jmal, M. Abid, M. S. Bensaleh, and A. M. Obeid, "A review on wireless sensor node architectures," in *2014 9th International Symposium on Reconfigurable and Communication-Centric Systems-on-Chip, ReCoSoC 2014*, 2014.

[12] M. O. Farooq and T. Kunz, "Operating systems for wireless sensor networks: A survey," *Sensors*, vol. 11, no. 6, pp. 5900–5930, Jun. 2011.

[13] K. S. Adu-Manu, N. Adam, C. Tapparello, H. Ayatollahi, and W. Heinzelman, "Energy-harvesting wireless sensor networks (EH-WSNs): A review," *ACM Transactions on Sensor Networks*, vol. 14, no. 2. Association for Computing

Machinery, 01-Mar-2018.

[14] T. Ruan, Z. J. Chew, and M. Zhu, "Energy-Aware Approaches for Energy Harvesting Powered Wireless Sensor Nodes," *IEEE Sens. J.*, vol. 17, no. 7, pp. 2165–2173, Apr. 2017.

[15] C. Ó. Mathúna, T. O'Donnell, R. V. Martinez-Catala, J. Rohan, and B. O'Flynn, "Energy scavenging for long-term deployable wireless sensor networks," *Talanta*, vol. 75, no. 3. Elsevier, pp. 613–623, 15-May-2008.

[16] "bPart | TECO – Technology for Pervasive Computing." [Online]. Available: http://www.teco.edu/bpart/. [Accessed: 22-Nov-2019].

[17]. "NOW with eMote." [Online]. Available: https://samraksh.com/products/small-battery-powered-computers/31-product-pages/product-small-battery-powered-computers/60-emote-now. [Accessed: 22-Nov-2019].

[18] D. Riley and M. Younis, "A Modular and Power-Intelligent Architecture for Wireless Sensor Nodes."

[19] "FireFly Real-Time Sensor Networks :: Carnegie Mellon University." [Online]. Available: https://www.archive.ece.cmu.edu/~firefly/. [Accessed: 22-Nov-2019].

[20] Z. Rezaei, "Energy Saving in Wireless Sensor Networks," *Int. J. Comput. Sci. Eng. Surv.*, vol. 3, no. 1, pp. 23–37, Feb. 2012.

[21] P. K. D. Pramanik, B. K. Upadhyaya, S. Pal, and T. Pal, "Internet of things, smart sensors, and pervasive systems: Enabling connected and pervasive healthcare," in *Healthcare Data Analytics and Management*, Elsevier, 2019, pp. 1–58.

[22] T. Starner, "The challenges of wearable computing: Part 1," *IEEE Micro*, vol. 21, no. 4, pp. 44–52, Jul. 2001.

[23] K. J. Kim and D. H. Shin, "An acceptance model for smart watches: Implications for the adoption of future wearable technology," *Internet Res.*, vol. 25, no. 4, pp. 527–541, Aug. 2015.

[24] D. R. Seshadri *et al.*, "Wearable sensors for monitoring the internal and external workload of the athlete," *npj Digit. Med.*, vol. 2, no. 1, Dec. 2019.

[25] T. Starner, "The challenges of wearable computing: Part 2," *IEEE Micro*, vol. 21, no. 4, pp. 54–67, Jul. 2001.

[26] S. Sindhu, S. Vashisth, and S. K. Chakarvarti, "A Review on Wireless Body Area Network (WBAN) for Health Monitoring System: Implementation Protocols," *Commun. Appl. Electron.*, vol. 4, no. 7, pp. 16–20, Mar. 2016.

[27] V. Niemelä, M. Hämäläinen, J. Iinatti, and A. Taparugssanagorn, "P-rake receivers in different measured WBAN hospital channels," in *2011 5th International Symposium on Medical Information and Communication Technology, ISMICT 2011*, 2011, pp. 42–46.

[28] J. Anand and D. Sethi, “Comparative analysis of energy efficient routing in WBAN,” in *3rd IEEE International Conference on*, 2017.

[29] K. C. Liu, C. Y. Hsieh, S. J. P. Hsu, and C. T. Chan, “Impact of Sampling Rate on Wearable-Based Fall Detection Systems Based on Machine Learning Models,” *IEEE Sens. J.*, vol. 18, no. 23, pp. 9882–9890, Dec. 2018.

[30] K. S. Kwak, S. Ullah, and N. Ullah, “An Overview of IEEE 802.15.6 Standard.”

[31] V. Custodio, F. J. Herrera, G. López, and J. I. Moreno, “A review on architectures and communications technologies for wearable health-monitoring systems,” *Sensors (Switzerland)*, vol. 12, no. 10. pp. 13907–13946, Oct-2012.

[32] “MEMS Market Size, Share -2026: Microelectromechanical System Trend.” [Online]. Available: https://www.alliedmarketresearch.com/micro-electromechanical-systems-MEMS-market. [Accessed: 22-Nov-2019].

[33] M. Habibzadeh, M. Hassanalieragh, A. Ishikawa, T. Soyata, and G. Sharma, “Hybrid Solar-Wind Energy Harvesting for Embedded Applications: Supercapacitor-Based System Architectures and Design Tradeoffs,” *IEEE Circuits Syst. Mag.*, vol. 17, no. 4, pp. 29–63, Oct. 2017.

[34] S. J. Roundy, “Energy Scavenging for Wireless Sensor Nodes with a Focus on Vibration to Electricity Conversion,” 1996.

[35] S. Roundy, P. K. Wright, and J. Rabaey, “A study of low level vibrations as a power source for wireless sensor nodes.”

[36] T. Soyata, L. Copeland, and W. Heinzelman, “RF Energy Harvesting for Embedded Systems: A Survey of Tradeoffs and Methodology,” *IEEE Circuits and Systems Magazine*, vol. 16, no. 1. Institute of Electrical and Electronics Engineers Inc., pp. 22–57, 01-Jan-2016.

[37] D. G. F.J. Blatt, P.A. Schroeder, C.L. Foiles, *Thermoelectric power of materials*. New York: Plenum Press, 1976.

[38] O. Mah, *Fundamentals of photovoltaic materials*. National Solar Power Research Institute, 1998.

[39] J.M. Damaschke, “Design of a low-input-voltage converter for thermoelectric generator,” *IEEE Trans. Ind. Appl.*, vol. 33, no. 5, pp. 1203–1207, 1997.

[40] R.L. Myers, *The basics of physics*. Westport, Conn: Greenwood Press, 2006.

[41] R.S. Elliot, *Electromagnetics: history, theory, and applications*. Piscataway: IEEE Press, 1993.

[42] P. Curie, Jacques; Curie, “Development, via compression, of electric polarization in hemihedral crystals with inclined faces,” *Bull. la Société Minérologique Fr.*, vol. 3, no. 4, pp. 90–93, 1880.

[43] N. Tesla, “Experiments with alternate currents of very high frequency and their application to methods of artificial illumination,” *Trans. Am. Soc. Agric. Eng.*, vol. 8, no. 1, pp. 267–319, 1891.

[44] W. Lumpkins, “Nikola Tesla’s Dream Realized: Wireless power energy

harvesting.," *IEEE Consum. Electron. Mag.*, vol. 3, no. 1, pp. 39–42, 2014.

[45] A. Y.-I. T. on antennas and propagation and undefined 1986, "An overview of near-field antenna measurements," *ieeexplore.ieee.org*.

[46] C. Song, Y. Huang, J. Zhou, J. Zhang, S. Yuan, and P. Carter, "A high-efficiency broadband rectenna for ambient wireless energy harvesting," *IEEE Trans. Antennas Propag.*, vol. 63, no. 8, pp. 3486–3495, Aug. 2015.

[47] R. Zaker and A. Abdipour, "A very compact ultrawideband printed omnidirectional monopole antenna," *IEEE Antennas Wirel. Propag. Lett.*, vol. 9, pp. 471–473, 2010.

[48] L.-G. Tran, H.-K. Cha, and W.-T. Park, "RF power harvesting: a review on designing methodologies and applications," *Micro Nano Syst. Lett.*, vol. 5, no. 1, p. 14, Dec. 2017.

[49] P. Momenroodaki, R. Dias Fernandes, and Z. Popovi´cpopovi´c, "Air-substrate Compact High Gain Rectennas for Low RF Power Harvesting."

[50] P. Lu, X. S. Yang, J. L. Li, and B. Z. Wang, "Polarization Reconfigurable Broadband Rectenna With Tunable Matching Network for Microwave Power Transmission," *IEEE Trans. Antennas Propag.*, vol. 64, no. 3, pp. 1136–1141, Mar. 2016.

[51] H. Sun, "An Enhanced Rectenna Using Differentially-Fed Rectifier for Wireless Power Transmission," *IEEE Antennas Wirel. Propag. Lett.*, vol. 15, pp. 32–35, 2016.

[52] H. Sun and W. Geyi, "A New Rectenna with All-Polarization-Receiving Capability for Wireless Power Transmission," *IEEE Antennas Wirel. Propag. Lett.*, vol. 15, pp. 814–817, 2016.

[53] P. Zhu, Z. Ma, G. A. E. Vandenbosch, and G. Gielen, "160 GHz harmonic-rejecting antenna with CMOS rectifier for millimeter-wave wireless power transmission," in *2015 9th European Conference on Antennas and Propagation (EuCAP)*, 2015, pp. 1–5.

[54] J. Zhang, Z. P. Wu, C. G. Liu, B. H. Zhang, and B. Zhang, "A double-sided rectenna design for RF energy harvesting," in *2015 IEEE International Wireless Symposium, IWS 2015*, 2015.

[55] M. K. Hosain, A. Z. Kouzani, M. F. Samad, and S. J. Tye, "A miniature energy harvesting rectenna for operating a head-mountable deep brain stimulation device," *IEEE Access*, vol. 3, pp. 223–234, 2015.

[56] P. Lu, X. S. Yang, J. L. Li, and B. Z. Wang, "A Compact Frequency Reconfigurable Rectenna for 5.2- and 5.8-GHz Wireless Power Transmission," *IEEE Trans. Power Electron.*, vol. 30, no. 11, pp. 6006–6010, Nov. 2015.

[57] T. Matsunaga, E. Nishiyama, and I. Toyoda, "5.8-GHz Stacked Differential Rectenna Suitable for Large-Scale Rectenna Arrays with DC Connection," *IEEE Trans. Antennas Propag.*, vol. 63, no. 12, pp. 5944–5949, Dec. 2015.

[58] J. H. Chou, D. B. Lin, K. L. Weng, and H. J. Li, "All polarization receiving

rectenna with harmonic rejection property for wireless power transmission," *IEEE Trans. Antennas Propag.*, vol. 62, no. 10, pp. 5242–5249, Oct. 2014.

[59] H. Sun, Y. X. Guo, M. He, and Z. Zhong, "A dual-band rectenna using broadband yagi antenna array for ambient rf power harvesting," *IEEE Antennas Wirel. Propag. Lett.*, vol. 12, pp. 918–921, 2013.

[60] H. Sun, Y. X. Guo, M. He, and Z. Zhong, "Design of a high-efficiency 2.45-GHz rectenna for low-input-power energy harvesting," *IEEE Antennas Wirel. Propag. Lett.*, vol. 11, pp. 929–932, 2012.

[61] U. Olgun, C. C. Chen, and J. L. Volakis, "Wireless power harvesting with planar rectennas for 2.45 GHz RFIDs," in *Symposium Digest - 20th URSI International Symposium on Electromagnetic Theory, EMTS 2010*, 2010, pp. 329–331.

[62] Y. J. Ren, M. F. Farooqui, and K. Chang, "A compact dual-frequency rectifying antenna with high-orders harmonic-rejection," *IEEE Trans. Antennas Propag.*, vol. 55, no. 7, pp. 2110–2113, Jul. 2007.

[63] H. A. Wheeler, "Fundamental limitations of small antennas," *Proc. IRE*, vol. 35, no. 12, pp. 1479–1484, 1947.

[64] L. J. Chu, "Physical limitations of omni-directional antennas," *J. Appl. Phys.*, vol. 19, no. 12, pp. 1163–1175, 1948.

[65] C. A. Balanis, *Antenna theory : analysis and design*. .

[66] K. Niotaki, S. Kim, S. Jeong, A. Collado, A. Georgiadis, and M. M. Tentzeris, "A compact dual-band rectenna using slot-loaded dual band folded dipole antenna," *IEEE Antennas Wirel. Propag. Lett.*, vol. 12, pp. 1634–1637, 2013.

[67] C. Song *et al.*, "A Novel Six-Band Dual CP Rectenna Using Improved Impedance Matching Technique for Ambient RF Energy Harvesting," *IEEE Trans. Antennas Propag.*, vol. 64, no. 7, pp. 3160–3171, Jul. 2016.

[68] S. K. Divakaran, D. Das Krishna, and Nasimuddin, "RF energy harvesting systems: An overview and design issues," *Int. J. RF Microw. Comput. Eng.*, vol. 29, no. 1, p. e21633, Jan. 2019.

[69] D. Guha and Y. M. M. Antar, *Microstrip and Printed Antennas New Trends, Techniques and Applications.* Wiley, 2011.

[70] H. C. C. Fernandes, A. R. B. Rocha, and A. Teixeira, "Analysis Of Antennas With Pbg Substrate," in *SBMO/IEEE MTT-S International Microwave and Optoelectronics Conference Proceedings*, 2003, pp. 207–209.

[71] Y. Rahmat-Samii and H. Mosallaei, "Electromagnetic band-gap structures: classification, characterization, and applications," 2001.

[72] F. Yang and Y. Rahmat-Samii, "Applications of electromagnetic band-gap (EBG) structures in microwave antenna designs," in *ICMMT 2002 - 2002 3rd International Conference on Microwave and Millimeter Wave Technology*, 2002, pp. 528–531.

[73] M. K. Khandelwal, B. K. Kanaujia, and S. Kumar, "Defected ground structure:

Fundamentals, analysis, and applications in modern wireless trends," *International Journal of Antennas and Propagation*, vol. 2017. Hindawi Limited, 2017.

[74] N. A. Raj and R. P. Dwivedi, "High gain antenna with DGS for wireless applications," in *2nd International Conference on Signal Processing and Integrated Networks, SPIN 2015*, 2015, pp. 19–24.

[75] N. Engheta and R. W. Ziolkowski, "A positive future for double-negative metamaterials," *IEEE Trans. Microw. Theory Tech.*, vol. 53, no. 4 II, pp. 1535–1555, Apr. 2005.

[76] S. Shrestha, S. K. Noh, and D. Y. Choi, "Comparative study of antenna designs for RF energy harvesting," *International Journal of Antennas and Propagation*, vol. 2013. 2013.

[77] V. Anitha, S. Sri Jaya Lakshmi, M. L. S. N. S. Lakshmi, K. A. Kumar, C. R. Teja, and T. R. Reddy, "A Circularly Polarized Stacked Patch Antenna using Polyflon Substrate for Wireless Applications," *Int. J. Eng. Res. Appl. www.ijera.com*, vol. 2, pp. 903–905.

[78] T. W. Yoo and K. Chang, "Theoretical and Experimental Development of 10 and 35 GHz Rectennas," *IEEE Trans. Microw. Theory Tech.*, vol. 40, no. 6, pp. 1259–1266, 1992.

[79] Y. Sun and J. K. Fidler, "Design of Π impedance matching networks," in *Proceedings - IEEE International Symposium on Circuits and Systems*, 1994, vol. 5, pp. 5–8.

[80] J. Singh, S. Agrawal, M. S. Parihar, and J. S. and M. S. P. Sachin Agrawal, "Performance Analysis of RF Energy Harvesting Circuit with Varying Matching Network Elements and Diode Parameters," *IET Microwaves, Antennas Propag.*, 2015.

[81] H. Bode, "Network analysis and feedback amplifier design," 1945.

[82] R. M. Fano, "Theoretical limitations on the broadband matching of arbitrary impedances," *J. Franklin Inst.*, vol. 249, no. 1, pp. 57–83, 1950.

[83] C. Hoarau, N. Corrao, J. D. Arnould, P. Ferrari, and P. Xavier, "Complete design and measurement methodology for a tunable RF impedance-matching network," *IEEE Trans. Microw. Theory Tech.*, vol. 56, no. 11, pp. 2620–2627, Nov. 2008.

[84] G. Marrocco, "The art of UHF RFID antenna design: Impedance-matching and size-reduction techniques," *IEEE Antennas Propag. Mag.*, vol. 50, no. 1, pp. 66–79, Feb. 2008.

[85] S. Uda and Y. Mushiake, *Yagi-Uda Antenna*. Tokyo: Sasaki Printing and Publishing Co., 1954.

[86] M. Han, S. Jung, and H. Sohn, "High efficient rectenna using a harmonic rejection low pass filter for RF based wireless power transmission," in *2014 11th International Symposium on Wireless Communications Systems, ISWCS 2014 - Proceedings*, 2014, pp. 423–426.

[87] * Rakesh, K. Yadav, S. Das, and R. L. Yadava, “RECTENNAS DESIGN, DEVELOPMENT AND APPLICATIONS.”

[88] C. R. Valenta, “Fundamental limitations for Schottky diode RF energy harvesting,” in *2015 IEEE International Conference on RFID Technology and Applications, RFID-TA 2015*, 2016, pp. 188–193.

[89] “Skyworks SMS7630 Series datasheet.” [Online]. Available: https://www.skyworksinc.com/-/media/SkyWorks/Documents/Products/201-300/Surface_Mount_Schottky_Diodes_200041AE.pdf. [Accessed: 01-Dec-2019].

[90] “Avago HSMS-282x Series datasheet.” [Online]. Available: https://datasheet.octopart.com/HSMS-2820-TR1G-Avago-datasheet-10429945.pdf. [Accessed: 01-Dec-2019].

[91] “Avago HSMS-285x Series datasheet.” [Online]. Available: https://datasheet.octopart.com/HSMS-2850-TR1G-Broadcom-datasheet-87312.pdf. [Accessed: 01-Dec-2019].

[92] “HP HSMS-286x Series datasheet.” [Online]. Available: http://www.hp.woodshot.com/hprfhelp/4_downld/products/diodes/hsms2850.pdf. [Accessed: 01-Dec-2019].

[93] R. D. Shrivastava, D. Deshpande, C. Li, and R. Gale, “An Energy Harvesting System using 3-stage voltage multiplier and MPVD Charge Pump for wireless sensor networks,” in *WiSNet 2013 - Proceedings: 2013 IEEE Topical Conference on Wireless Sensors and Sensor Networks - 2013 IEEE Radio and Wireless Week, RWW 2013*, 2013, pp. 40–42.

[94] G. Gosset and D. Flandre, “Fully-automated and portable design methodology for optimal sizing of energy-efficient CMOS voltage rectifiers,” *IEEE J. Emerg. Sel. Top. Circuits Syst.*, vol. 1, no. 2, pp. 141–149, Jun. 2011.

[95] A. Lamantia, P. Maranesi, and L. Radrizzani, “The dynamics of the Cockcroft-Walton voltage multiplier,” in *PESC Record - IEEE Annual Power Electronics Specialists Conference*, 1990, vol. 2, pp. 485–490.

[96] M. M. Al-Azawy and F. Sari, “Analysis of Dickson Voltage Multiplier for RF Energy Harvesting,” in *Proceedings - 2019 IEEE 1st Global Power, Energy and Communication Conference, GPECOM 2019*, 2019, pp. 10–14.

[97] S. S. Hashemi, M. Sawan, and Y. Savaria, “A high-efficiency low-voltage CMOS rectifier for harvesting energy in implantable devices,” *IEEE Trans. Biomed. Circuits Syst.*, vol. 6, no. 4, pp. 326–335, 2012.

[98] S. S. Chouhan and K. Halonen, “A modified cross coupled rectifier based charge pump for energy harvesting using RF to DC conversion,” in *2013 European Conference on Circuit Theory and Design, ECCTD 2013 - Proceedings*, 2013.

[99] A. P. Sample, D. J. Yeager, J. R. Smith, P. S. Powledge, and A. V. Mamishev, “Energy harvesting in RFID systems,” in *Conference Proceedings - International Conference on Actual Problems of Electrons Devices*

Engineering, APEDE 2006, 2006, pp. 445–449.

[100] K. Y. Lin, T. K. K. Tsang, M. Sawan, and M. N. El-Gamal, "Radio-triggered solar and RF power scavenging and management for ultra low power wireless medical applications," in *Proceedings - IEEE International Symposium on Circuits and Systems*, 2006, pp. 5728–5731.

[101] T. Sogorb, J. V. Llario, J. Pelegrí, R. Lajara, and J. Alberola, "Studying the feasibility of energy harvesting from broadcast RF station for WSN," in *Conference Record - IEEE Instrumentation and Measurement Technology Conference*, 2008, pp. 1360–1363.

[102] Y. Cao, W. Hong, L. Deng, S. Li, and L. Yin, "A 2.4GHz Circular Polarization Rectenna with Harmonic Suppression for Microwave Power Transmission," in *Proceedings - 2016 IEEE International Conference on Internet of Things; IEEE Green Computing and Communications; IEEE Cyber, Physical, and Social Computing; IEEE Smart Data, iThings-GreenCom-CPSCom-Smart Data 2016*, 2017, pp. 359–363.

[103] T. Mitani, S. Kawashima, and T. Nishimura, "Analysis of Voltage Doubler Behavior of 2.45-GHz Voltage Doubler-Type Rectenna," *IEEE Trans. Microw. Theory Tech.*, vol. 65, no. 4, pp. 1051–1057, Apr. 2017.

[104] Y. S. Chen and C. W. Chiu, "Maximum achievable power conversion efficiency obtained through an optimized rectenna structure for RF energy harvesting," *IEEE Trans. Antennas Propag.*, vol. 65, no. 5, pp. 2305–2317, May 2017.

[105] V. Kuhn, C. Lahuec, F. Seguin, and C. Person, "A multi-band stacked RF energy harvester with RF-to-DC efficiency up to 84%," *IEEE Trans. Microw. Theory Tech.*, vol. 63, no. 5, pp. 1768–1778, May 2015.

[106] T. Salter, K. Choi, M. Peckerar, G. Metze, and N. Goldsman, "RF energy scavenging system utilising switched capacitor DC-DC converter," *Electron. Lett.*, vol. 45, no. 7, pp. 374–376, 2009.

[107] F. Kocer and M. P. Flynn, "A new transponder architecture with on-chip ADC for long-range telemetry applications," *IEEE J. Solid-State Circuits*, vol. 41, no. 5, pp. 1142–1148, May 2006.

[108] "Efficient Rectenna Design for Ambient Microwave Energy Recycling." [Online]. Available: https://upcommons.upc.edu/handle/2099.1/7504. [Accessed: 01-Dec-2019].

[109] J. A. Hagerty, F. B. Helmbrecht, W. H. McCalpin, R. Zane, and Z. B. Popović, "Recycling ambient microwave energy with broad-band rectenna arrays," *IEEE Trans. Microw. Theory Tech.*, vol. 52, no. 3, pp. 1014–1024, Mar. 2004.

[110] M. Zeng, A. S. Andrenko, X. Liu, Z. Li, and H. Z. Tan, "A Compact Fractal Loop Rectenna for RF Energy Harvesting," *IEEE Antennas Wirel. Propag. Lett.*, vol. 16, pp. 2424–2427, Jul. 2017.

[111] S. Mandal and R. Sarpeshkar, "Low-power CMOS rectifier design for RFID applications," *IEEE Trans. Circuits Syst. I Regul. Pap.*, vol. 54, no. 6, pp. 1177–1188, Jun. 2007.

[112] K. Kotani, A. Sasaki, and T. Ito, "High-efficiency differential-drive CMOS rectifier for UHF RFIDs," *IEEE J. Solid-State Circuits*, vol. 44, no. 11, pp. 3011–3018, Nov. 2009.

[113] V. Marian, B. Allard, C. Vollaire, and J. Verdier, "Strategy for microwave energy harvesting from ambient field or a feeding source," *IEEE Trans. Power Electron.*, vol. 27, no. 11, pp. 4481–4491, 2012.

[114] G. Singh, R. Ponnaganti, T. V. Prabhakar, and K. J. Vinoy, "A tuned rectifier for RF energy harvesting from ambient radiations," *AEU - Int. J. Electron. Commun.*, vol. 67, no. 7, pp. 564–569, Jul. 2013.

[115] Y. Y. Xiao, Z. X. Du, and X. Y. Zhang, "High-Efficiency Rectifier with Wide Input Power Range Based on Power Recycling," *IEEE Trans. Circuits Syst. II Express Briefs*, vol. 65, no. 6, pp. 744–748, Jun. 2018.

[116] G. J. Snyder, "Thermoelectric energy harvesting," in *Energy Harvesting Technologies*, Springer US, 2009, pp. 325–336.

[117] S. Sieniutycz and J. Jeżowski, "Energy limits for thermal engines and heat-pumps at steady states," in *Energy Optimization in Process Systems*, Elsevier, 2009, pp. 85–126.

[118] D. Allen, R. Haugeto, M. Kajor, and M. Namazian, "Small thermoelectric generators," in *International Conference on Thermoelectrics, ICT, Proceedings*, 2002, vol. 2002-January, pp. 424–426.

[119] T. Hendricks and W. T. Choate, "Engineering Scoping Study of Thermoelectric Generator Systems for Industrial Waste Heat Recovery," Nov. 2006.

[120] B. I. Ismail and W. H. Ahmed, "Thermoelectric Power Generation Using Waste-Heat Energy as an Alternative Green Technology."

[121] D.M. Rowe, *CRC Handbook of Thermoelectrics*, 1st ed. CRC Press, 1995.

[122] H. S. Kim, W. Liu, G. Chen, C. W. Chu, and Z. Ren, "Relationship between thermoelectric figure of merit and energy conversion efficiency," *Proc. Natl. Acad. Sci. U. S. A.*, vol. 112, no. 27, pp. 8205–8210, Jul. 2015.

[123] A. Bitschi, "Modelling of thermoelectric devices for electric power generation," 2009.

[124] "What is a Peltier Cooler | REUK.co.uk." [Online]. Available: http://www.reuk.co.uk/wordpress/thermoelectric/what-is-a-peltier-cooler/. [Accessed: 03-Dec-2019].

[125] K. Uemura, "SCT-93 Short Course on Thermoelectrics." International Thermoelectric Society, Yokohama-shi, Japan, 1993.

[126] J. Martins, L. M. Goncalves, J. Antunes, and F. P. Brito, "Thermoelectric Exhaust Energy Recovery with Temperature Control through Heat Pipes," 2011.

[127] "Voyager - Spacecraft - Radioisotope Thermoelectric Generators (RTG)." [Online]. Available:

https://voyager.jpl.nasa.gov/mission/spacecraft/instruments/rtg/. [Accessed: 03-Dec-2019].

[128] R. Y. Nuwayhid, A. Shihadeh, and N. Ghaddar, "Development and testing of a domestic woodstove thermoelectric generator with natural convection cooling," *Energy Convers. Manag.*, vol. 46, no. 9–10, pp. 1631–1643, Jun. 2005.

[129] M. Azarbayjani and J. Anderson, "Assessment of Solar Energy Conversion Technologies-Application of Thermoelectric Devices in Retrofit an Office Building."

[130] G. J. Snyder, J. R. Lim, C.-K. Huang, and J.-P. Fleurial, "Thermoelectric microdevice fabricated by a MEMS-like electrochemical process," *Nat. Mater.*, vol. 2, no. 8, pp. 528–531, Aug. 2003.

[131] R. Venkatasubramanian, C. Watkins, D. Stokes, J. Posthill, and C. Caylor, "Energy harvesting for electronics with thermoelectric devices using nanoscale materials," in *Technical Digest - International Electron Devices Meeting, IEDM*, 2007, pp. 367–370.

[132] H. Böttner *et al.*, "New thermoelectric components using microsystems technologies," *J. Microelectromechanical Syst.*, vol. 13, no. 3, pp. 414–420, Jun. 2004.

[133] I. Stark and M. Stordeur, "New micro thermoelectric devices based on bismuth telluride-type thin solid films," in *International Conference on Thermoelectrics, ICT, Proceedings*, 1999, pp. 465–472.

[134] B. Gyselinckx, C. Van Hoof, J. Ryckaert, R. F. Yazicioglu, P. Fiorini, and V. Leonov, "Human++: Autonomous wireless sensors for body area networks," in *Proceedings of the Custom Integrated Circuits Conference*, 2005, vol. 2005, pp. 12–18.

[135] Y. Cai, F. Deng, J. Zhao, H. Qiu, X. Fan, and Z. Liang, "The Distributed System of Smart Wearable Energy Harvesting Based on Human Body," in *Chinese Control Conference, CCC*, 2018, vol. 2018-July, pp. 7450–7454.

[136] V. Leonov and R. J. M. Vullers, "Thermoelectric Generators on Living Beings."

[137] Z. Wang, V. Leonov, P. Fiorini, and C. Van Hoof, "Realization of a wearable miniaturized thermoelectric generator for human body applications," *Sensors Actuators, A Phys.*, vol. 156, no. 1, pp. 95–102, Nov. 2009.

[138] W. D. McArdle, F. I. Katch, and V. L. Katch, *Exercise physiology : nutrition, energy, and human performance*. Lippincott Williams & Wilkins, 2010.

[139] L. C. Rome, L. Flynn, E. M. Goldman, and T. D. Yoo, "Biophysics: Generating electricity while walking with loads," *Science (80-.).*, vol. 309, no. 5741, pp. 1725–1728, Sep. 2005.

[140] D. A. Winter, *Biomechanics and Motor Control of Human Movement: Fourth Edition*. John Wiley and Sons, 2009.

[141] R. Riemer and A. Shapiro, "Biomechanical energy harvesting from human motion: theory, state of the art, design guidelines, and future directions," *J.*

Neuroeng. Rehabil., vol. 8, no. 1, p. 22, 2011.

[142] T. Ghomian and S. Mehraeen, "Survey of energy scavenging for wearable and implantable devices," *Energy*, vol. 178. Elsevier Ltd, pp. 33–49, 01-Jul-2019.

[143] S. Mehraeen, S. Jagannathan, and K. A. Corzine, "Energy harvesting from vibration with alternate scavenging circuitry and tapered cantilever beam," *IEEE Trans. Ind. Electron.*, vol. 57, no. 3, pp. 820–830, Mar. 2010.

[144] J. H. Koo, J. Seo, and T. Lee, "Nanomaterials on flexible substrates to explore innovative functions: From energy harvesting to bio-integrated electronics," *Thin Solid Films*, vol. 524. pp. 1–19, 01-Dec-2012.

[145] Z. Li, R. Yang, M. Yu, F. Bai, C. Li, and Z. L. Wang, "Cellular Level Biocompatibility and Biosafety of ZnO Nanowires," *J. Phys. Chem. C*, vol. 112, no. 51, pp. 20114–20117, Dec. 2008.

[146] M.-H. Zhao, Z.-L. Wang, and S. X. Mao, "Piezoelectric Characterization of Individual Zinc Oxide Nanobelt Probed by Piezoresponse Force Microscope," *Nano Lett.*, vol. 4, no. 4, pp. 587–590, Apr. 2004.

[147] K. Miyamoto, M. Sano, H. Kato, and T. Yao, "High-electron-mobility ZnO epilayers grown by plasma-assisted molecular beam epitaxy," *J. Cryst. Growth*, vol. 265, no. 1–2, pp. 34–40, Apr. 2004.

[148] M. O. Kim *et al.*, "Flexible and multi-directional piezoelectric energy harvester for self-powered human motion sensor," *Smart Mater. Struct.*, vol. 27, no. 3, Jan. 2018.

[149] A. Delnavaz and J. Voix, "Energy harvesting for in-ear devices using ear canal dynamic motion," *IEEE Trans. Ind. Electron.*, vol. 61, no. 1, pp. 583–590, 2014.

[150] L. Persano *et al.*, "Shear Piezoelectricity in Poly(vinylidenefluoride-co-trifluoroethylene): Full Piezotensor Coefficients by Molecular Modeling, Biaxial Transverse Response, and Use in Suspended Energy-Harvesting Nanostructures," *Adv. Mater.*, vol. 28, no. 35, pp. 7633–7639, 2016.

[151] J. M. Donelan, R. Kram, and A. D. Kuo, "Mechanical work for step-to-step transitions is a major determinant of the metabolic cost of human walking," *J. Exp. Biol.*, vol. 205, no. 23, 2002.

[152] M. R. Shorten, "The energetics of running and running shoes," *J. Biomech.*, vol. 26, no. SUPPL. 1, pp. 41–51, 1993.

[153] D. A. Winter, A. E. Patla, J. S. Frank, and S. E. Walt, "Biomechanical Walking Pattern Changes in the Fit and Healthy Elderly," *Phys. Ther.*, vol. 70, no. 6, pp. 340–347, Jun. 1990.

[154] J. Kymissis, C. Kendall, J. Paradiso, and N. Gershenfeld, "Parasitic power harvesting in shoes," in *International Symposium on Wearable Computers, Digest of Papers*, 1998, vol. 1998-October, pp. 132–139.

[155] P. Niu, P. Chapman, R. Riemer, and X. Zhang, "Evaluation of motions and actuation methods for biomechanical energy harvesting," in *PESC Record - IEEE Annual Power Electronics Specialists Conference*, 2004, vol. 3, pp. 2100–

2106.

[156] J. M. Donelan, Q. Li, V. Naing, J. A. Hoffer, D. J. Weber, and A. D. Kuo, “Biomechanical energy harvesting: Generating electricity during walking with minimal user effort,” *Science (80-.).*, vol. 319, no. 5864, pp. 807–810, Feb. 2008.

[157] P. Di Marco, V. Stornelli, G. Ferri, L. Pantoli, and A. Leoni, “Dual band harvester architecture for autonomous remote sensors,” *Sensors Actuators, A Phys.*, vol. 247, 2016.

[158] L. Pantoli, A. Leoni, V. Stornelli, and G. Ferri, “An IC architecture for rf energy harvesting systems,” *J. Commun. Softw. Syst.*, vol. 13, no. 2, 2017.

[159] Tashi, M. S. Hasan, and H. Yu, “Design and simulation of UHF RFID tag antennas and performance evaluation in presence of a metallic surface,” in *SKIMA 2011 - 5th International Conference on Software, Knowledge Information, Industrial Management and Applications*, 2011, pp. 13–20.

[160] L. Pantoli, V. Stornelli, G. Leuzzi, and A. Di Carlofelice, “A single transistor post selector active tunable filter for radio receivers applications,” in *International Workshop on Integrated Nonlinear Microwave and Millimetre-Wave Circuits, INMMiC 2014*, 2014.

[161] G. Ferri, V. Stornelli, and A. Celeste, “Integrated rail-to-rail low-voltage low-power enhanced DC-gain fully differential operational transconductance amplifier,” *ETRI J.*, vol. 29, no. 6, pp. 785–792, Dec. 2007.

[162] A. De Marcellis *et al.*, “A CMOS integrable oscillator-based front end for high-dynamic-range resistive sensors,” *IEEE Trans. Instrum. Meas.*, vol. 57, no. 8, pp. 1596–1604, Aug. 2008.

[163] “App note: A microwatt charge pump boosts 1 V to 1.8 V at 90% efficiency, providing ‘Always On’ standby power for microcontrollers – Dangerous Prototypes.” [Online]. Available: http://dangerousprototypes.com/blog/2015/12/20/app-note-a-microwatt-charge-pump-boosts-1-v-to-1-8-v-at-90-efficiency-providing-always-on-standby-power-for-microcontrollers/. [Accessed: 09-Dec-2019].

[164] A. Leoni, L. Pantoli, V. Stornelli, G. Ferri, M. Russo, and P. Šolić, “A combined 90/900 MHz IC architecture for power-assisting in IoT applications,” *J. Commun. Softw. Syst.*, vol. 14, no. 1, pp. 27–32, 2018.

[165] D. M. Pozar, *Microwave Engineering, 4th Edition*. 2012.

[166] “Radio technical reference Design guide - CIRCUIT DESIGN,INC.” [Online]. Available: https://www.cdt21.com/resources/guide2.asp. [Accessed: 09-Dec-2019].

[167] J. J. Shi and X. D. Huang, “Electrostatic energy harvester based on charge-trapping nonvolatile memory structure,” in *2016 IEEE International Conference on Electron Devices and Solid-State Circuits, EDSSC 2016*, 2016, pp. 153–156.

[168] P. Di Marco, V. Stornelli, G. Ferri, L. Pantoli, and A. Leoni, “Dual band

harvester architecture for autonomous remote sensors," *Sensors Actuators, A Phys.*, vol. 247, pp. 598–603, Aug. 2016.

[169] M. Wojnowski, V. Issakov, G. Sommer, and R. Weigel, "Multimode TRL calibration technique for characterization of differential devices," *IEEE Trans. Microw. Theory Tech.*, vol. 60, no. 7, pp. 2220–2247, 2012.

[170] "JTX-4-10T+ datasheet." [Online]. Available: https://www.minicircuits.com/pdfs/JTX-4-10T+.pdf. [Accessed: 10-Dec-2019].

[171] A. Nelson *et al.*, "Wearable multi-sensor gesture recognition for paralysis patients," in *Proceedings of IEEE Sensors*, 2013.

[172] G. Piscitelli *et al.*, "A low-cost energy-harvesting sensory headwear useful for tetraplegic people to drive home automation," *AEU - Int. J. Electron. Commun.*, vol. 107, pp. 9–14, Jul. 2019.

[173] D. Xue, B. A. Garner, and Y. Li, "Investigation of short-range, broadband, on-body electromagnetic wave propagations," *IET Microwaves, Antennas Propag.*, vol. 10, no. 11, pp. 1182–1188, Aug. 2016.

[174] H. W. Silver, *The ARRL Antenna Book*. Newington: The American Radio Relay League, 2015.

[175] D. Bresnahan and Y. Li, "Measurement, simulation and theory of creeping wave propagations around the human head at 2.45 GHz," in *Proceedings of the 2017 Texas Symposium on Wireless and Microwave Circuits and Systems, WMCS 2017*, 2017.

[176] T. Houzen, M. Takahashi, K. Saito, and K. Ito, "Implanted planar inverted F-antenna for cardiac pacemaker system," in *Conference Proceedings 2008 IEEE International Workshop on Antenna Technology: Small Antennas and Novel Metamaterials, IWAT 2008*, 2008, pp. 346–349.

[177] S. Gabriel, R. W. Lau, and C. Gabriel, "The dielectric properties of biological tissues: II. Measurements in the frequency range 10 Hz to 20 GHz," *Phys. Med. Biol.*, vol. 41, no. 11, pp. 2251–2269, Nov. 1996.

[178] H. P. Schwan, "Electrical properties of tissues and cell suspensions: mechanisms and models," 2002, pp. A70–A71.

[179] T. W. Athey, M. A. Stuchly, M. A. Stuchly, and S. S. Stuchly, "Measurement of Radio Frequency Permittivity of Biological Tissues with an Open-Ended Coaxial Line: Part I," *IEEE Trans. Microw. Theory Tech.*, vol. 30, no. 1, pp. 82–86, 1982.

[180] S. M. Abbas, K. P. Esselle, L. Matekovits, M. Rizwan, and L. Ukkonen, "On-body antennas: Design considerations and challenges," in *2016 URSI International Symposium on Electromagnetic Theory, EMTS 2016*, 2016, pp. 109–110.

[181] W. Jeong and J. Choi, "A low profile IR-UWB antenna with conical radiation pattern for on-body communications," in *IEEE Antennas and Propagation Society, AP-S International Symposium (Digest)*, 2015, vol. 2015-October, pp.

2023–2024.

[182] A. Leoni, I. Ulisse, G. Piscitelli, M. Ricci, and V. Errico, “RF energy harvested sensory headwear for quadriplegic people,” in *PRIME 2019 - 15th Conference on Ph.D. Research in Microelectronics and Electronics, Proceedings*, 2019, pp. 257–260.

[183] M. A. Antoniades and G. V. Eleftheriades, “A broadband Wilkinson balun using microstrip metamaterial lines,” *IEEE Antennas Wirel. Propag. Lett.*, vol. 4, no. 1, pp. 209–212, 2005.

[184] U. Park, “A Wilkinson-Type Balun Using a Composite Right/Left-Handed Transmission Line,” *J. Inf. Commun. Converg. Eng.*, vol. 11, no. 3, pp. 147–152, Sep. 2013.

[185] “PowerSpot - Powercast Co.” [Online]. Available: https://www.powercastco.com/products/powerspot/. [Accessed: 10-Dec-2019].

[186] “datasheet HSMS-2852.” [Online]. Available: https://www.digchip.com/datasheets/parts/datasheet/021/HSMS-2852-pdf.php. [Accessed: 10-Dec-2019].

[187] Leoni and Pantoli, “SPICE Model Identification Technique of a Cheap Thermoelectric Cell Applied to DC/DC Design with MPPT Algorithm for Low-Cost, Low-Power Energy Harvesting,” *Appl. Sci.*, vol. 9, no. 18, p. 3744, Sep. 2019.

[188] K. Singkaselit, A. Sakulkalavek, and R. Sakdanuphab, “Effects of annealing temperature on the structural, mechanical and electrical properties of flexible bismuth telluride thin films prepared by high-pressure RF magnetron sputtering,” *Adv. Nat. Sci. Nanosci. Nanotechnol.*, vol. 8, no. 3, Sep. 2017.

[189] M. K. Han, Y. Jin, D. H. Lee, and S. J. Kim, “Thermoelectric properties of Bi2Te3: CuI and the effect of its doping with Pb atoms,” *Materials (Basel).*, vol. 10, no. 11, Oct. 2017.

[190] Y. Pei, H. Wang, Z. M. Gibbs, A. D. LaLonde, and J. G. Snyder, “Thermopower enhancement in Pb1-xMnxTe alloys and its effect on thermoelectric efficiency,” *NPG Asia Mater.*, vol. 4, no. 9, Sep. 2012.

[191] “TEC1-3103 Datasheet.” [Online]. Available: https://download.siliconexpert.com/pdfs/2008/03/05/c/manual/fujtk/htmls/fph112702ac.pdf. [Accessed: 11-Dec-2019].

[192] V. I. Kubov, Y. Y. Dymytrov, and R. M. Kubova, “LTspice-model of thermoelectric Peltier-Seebeck element,” in *2016 IEEE 36th International Conference on Electronics and Nanotechnology, ELNANO 2016 - Conference Proceedings*, 2016, pp. 47–51.

[193] X. Liu, L. Huang, K. Ravichandran, and E. Sanchez-Sinencio, “A Highly Efficient Reconfigurable Charge Pump Energy Harvester with Wide Harvesting Range and Two-Dimensional MPPT for Internet of Things,” *IEEE J. Solid-State Circuits*, vol. 51, no. 5, pp. 1302–1312, May 2016.

[194] X. Liu and E. Sanchez-Sinencio, “A Highly Efficient Ultralow Photovoltaic

Power Harvesting System with MPPT for Internet of Things Smart Nodes," *IEEE Trans. Very Large Scale Integr. Syst.*, vol. 23, no. 12, pp. 3065–3075, Dec. 2015.

[195] S. K. Ram, S. R. Sahoo, K. Sudeendra, and K. Mahapatra, "Energy efficient ultra low power solar harvesting system design with MPPT for IOT edge node devices," in *Proceedings - 2018 IEEE 4th International Symposium on Smart Electronic Systems, iSES 2018*, 2018, pp. 130–133.

[196] Y. P. Cheng, P. C. P. Chao, G. Y. Men, C. C. Yang, and T. W. Wang, "An 80% effeciency and highly adaptable PV energy harvest circuitry with MPPT for IOT devices," in *Proceedings of IEEE Sensors*, 2017, vol. 2017-December, pp. 1–3.

[197] S. S. Alli, S. Jovanovic, P. Poure, and E. Jamshidpour, "MPPT and output voltage control of Photovoltaic systems using a Single-Switch DC-DC converter," in *2016 IEEE International Energy Conference, ENERGYCON 2016*, 2016.

[198] M. K. Rajendran, S. Kansal, A. Mantha, V. Priya, Y. B. Priyamvada, and A. Dutta, "Automated environment aware nW FOCV - MPPT controller for self-powered IoT applications," in *Proceedings - IEEE International Symposium on Circuits and Systems*, 2016, vol. 2016-July, pp. 1818–1821.

[199] T. Selmi, M. Abdul-Niby, L. Devis, and A. Davis, "P&O MPPT implementation using MATLAB/Simulink," in *2014 9th International Conference on Ecological Vehicles and Renewable Energies, EVER 2014*, 2014.

[200] T. M. Chung, H. Daniyal, M. H. Sulaiman, and M. S. Bakar, "Comparative study of p&o and modified incremental conductance algorithm in solar maximum power point tracking," in *IET Conference Publications*, 2016, vol. 2016, no. CP688.

[201] P. Motsoeneng, J. Bamukunde, and S. Chowdhury, "Comparison of Perturb & Observe and Hill Climbing MPPT Schemes for PV Plant under Cloud Cover and Varying Load," in *2019 10th International Renewable Energy Congress, IREC 2019*, 2019.

[202] D. Baimel, S. Tapuchi, Y. Levron, and J. Belikov, "Improved Fractional Open Circuit Voltage MPPT Methods for PV Systems," *Electronics*, vol. 8, no. 3, p. 321, Mar. 2019.

[203] S. K. Kollimalla and M. K. Mishra, "A new adaptive P&O MPPT algorithm based on FSCC method for photovoltaic system," *Proc. IEEE Int. Conf. Circuit, Power Comput. Technol. ICCPCT 2013*, pp. 406–411, 2013.

[204] Q. Wan, Y. K. Teh, Y. Gao, and P. K. T. Mok, "Analysis and Design of a Thermoelectric Energy Harvesting System With Reconfigurable Array of Thermoelectric Generators for IoT Applications," *IEEE Trans. Circuits Syst. I Regul. Pap.*, vol. 64, no. 9, pp. 2346–2358, Sep. 2017.

[205] J. Wittmann and B. Wicht, "A configurable sawtooth based PWM generator with 2 ns on-time for >50 MHz DCDC converters," in *2015 11th Conference on Ph.D. Research in Microelectronics and Electronics, PRIME 2015*, 2015, pp. 41–44.

[206] A. Leoni *et al.*, “Energy harvesting optimization for built-in power replacement of electronic multisensory architecture,” *AEU - Int. J. Electron. Commun.*, vol. 107, pp. 170–176, Jul. 2019.

[207] G. Saggio, F. Riillo, L. Sbernini, and L. R. Quitadamo, “Resistive flex sensors: A survey,” *Smart Materials and Structures*, vol. 25, no. 1. Institute of Physics Publishing, 02-Dec-2015.

[208] G. Saggio *et al.*, “Gesture recognition and classification for surgical skill assessment,” in *MeMeA 2011 - 2011 IEEE International Symposium on Medical Measurements and Applications, Proceedings*, 2011.

[209] G. Saggio and M. Bizzarri, “Feasibility of teleoperations with multi-fingered robotic hand for safe extravehicular manipulations,” *Aerosp. Sci. Technol.*, vol. 39, pp. 666–674, 2014.

[210] G. Saggio, S. Bocchetti, C. A. Pinto, and G. Orengo, “Electronic interface and signal conditioning circuitry for data glove systems useful as 3D HMI tools for disabled persons,” in *HEALTHINF 2011 - Proceedings of the International Conference on Health Informatics*, 2011, pp. 248–253.

[211] V. Stornelli *et al.*, “A Multi-Source Energy Harvesting Sensory Glove Electronic Architecture,” in *2018 3rd International Conference on Smart and Sustainable Technologies (SpliTech)*, 2018.

[212] T. Sakoi, K. Tsuzuki, S. Kato, R. Ooka, D. Song, and S. Zhu, “Thermal comfort, skin temperature distribution, and sensible heat loss distribution in the sitting posture in various asymmetric radiant fields,” *Build. Environ.*, vol. 42, no. 12, pp. 3984–3999, Dec. 2007.

[213] “NASA Technical Reports Server (NTRS) - NASA Anthropometry and Biomechanics Facility Human Modeling.” [Online]. Available: https://ntrs.nasa.gov/search.jsp?R=20170002571. [Accessed: 12-Dec-2019].

[214] V. Jurkans, J. Blums, and I. Gornevs, “Harvesting electrical power from body heat using low voltage step-up converters with thermoelectric generators,” in *Proceedings of the Biennial Baltic Electronics Conference, BEC*, 2019, vol. 2018-October.

[215] V. Leonov and R. J. M. Vullers, “Wearable electronics self-powered by using human body heat: The state of the art and the perspective,” *J. Renew. Sustain. Energy*, vol. 1, no. 6, p. 062701, Nov. 2009.

[216] R. Caliò *et al.*, “Piezoelectric Energy Harvesting Solutions,” *Sensors*, vol. 14, no. 3, pp. 4755–4790, Mar. 2014.

[217] H. S. Kim, J. H. Kim, and J. Kim, “A review of piezoelectric energy harvesting based on vibration,” *Int. J. Precis. Eng. Manuf.*, vol. 12, no. 6, pp. 1129–1141, 2011.

[218] Y. Cha, J. Hong, J. Lee, J. M. Park, and K. Kim, “Flexible piezoelectric energy harvesting from mouse click motions,” *Sensors (Switzerland)*, vol. 16, no. 7, Jul. 2016.

[219] M. Renaud, P. Fiorini, R. Van Schaijk, and C. Van Hoof, “Harvesting energy

from the motion of human limbs: The design and analysis of an impact-based piezoelectric generator," *Smart Mater. Struct.*, vol. 18, no. 3, 2009.

[220] A. Delnavaz and J. Voix, "Flexible piezoelectric energy harvesting from jaw movements," *Smart Mater. Struct.*, vol. 23, no. 10, Oct. 2014.

[221] A. Proto, M. Penhaker, D. Bibbo, D. Vala, S. Conforto, and M. Schmid, "Measurements of generated energy/electrical quantities from locomotion activities using piezoelectric wearable sensors for body motion energy harvesting," *Sensors (Switzerland)*, vol. 16, no. 4, Apr. 2016.

[222] G. De Pasquale, S. G. Kim, and D. De Pasquale, "GoldFinger: Wireless Human-Machine Interface with Dedicated Software and Biomechanical Energy Harvesting System," *IEEE/ASME Trans. Mechatronics*, vol. 21, no. 1, pp. 565–575, Feb. 2016.

[223] A. Leoni, I. Ulisse, V. Stornelli, and G. Ferri, "Flexible Piezoelectric Harvester for Human Fingers: Measurements and Applications," in *FLEPS 2019 - IEEE International Conference on Flexible and Printable Sensors and Systems, Proceedings*, 2019.

[224] V. Stornelli *et al.*, "A 10-17 DOF sensory gloves with harvesting capability for smart healthcare," *J. Commun. Softw. Syst.*, vol. 15, no. 2, pp. 166–172, 2019.

[225] A. Leoni *et al.*, "A human body powered sensory glove system based on multisource energy harvester," in *PRIME 2018 - 14th Conference on Ph.D. Research in Microelectronics and Electronics*, 2018.

[226] G. Saggio and G. Orengo, "Flex sensor characterization against shape and curvature changes," *Sensors Actuators, A Phys.*, vol. 273, pp. 221–231, Apr. 2018.

[227] G. Saggio, M. De Sanctis, E. Cianca, G. Latessa, F. De Santis, and F. Giannini, "Long term measurement of human joint movements for health care and rehabilitation purposes," in *Proceedings of the 2009 1st International Conference on Wireless Communication, Vehicular Technology, Information Theory and Aerospace and Electronic Systems Technology, Wireless VITAE 2009*, 2009, pp. 674–678.